DISSERTATION

BRANCHING RATIO MEASUREMENTS OF $B \rightarrow J/\psi\eta K$ AND $B^{\pm} \rightarrow D^0 K^{\pm}$ WITH $D^0 \rightarrow \pi^+\pi^-\pi^0$

Submitted by
Qinglin Zeng
Department of Physics

In partial fulfillment of the requirements
for the Degree of Doctor of Philosophy
Colorado State University
Fort Collins, Colorado
Summer 2005

ProQuest Information and Learning Company
300 North Zeeb Road
P.O. Box 1346
Ann Arbor, MI 48106-1346

COLORADO STATE UNIVERSITY

summer, 2005

WE HEREBY RECOMMEND THAT THE DISSERTATION PREPARED UNDER OUR SUPERVISION BY QINGLIN ZENG ENTITLED **BRANCHING RATIO MEASUREMENTS OF $B \to J/\psi \eta K$ AND $B^{\pm} \to D^0 K^{\pm}$ WITH $D^0 \to \pi^+\pi^-\pi^0$ BE ACCEPTED AS FULFILLING IN PART REQUIREMENTS FOR THE DEGREE OF DOCTOR OF PHILOSOPHY.**

Committee on Graduate Work

Walter Toki

Walter H. Toki

John L. Harton

Carmen Menoni

Adviser Robert J. Wilson

David A. Krueger

Department Head David A. Krueger

ABSTRACT OF DISSERTATION

Branching ratio measurements of $B \to J/\psi\eta K$ and $B^\pm \to D^0K^\pm$ with $D^0 \to \pi^+\pi^-\pi^0$

Results are presented for the decays of $B \to J/\psi\eta K$ and $B^\pm \to DK^\pm$, respectively, with experimental data collected with *BABAR* detector at PEP-II, located at Stanford Linear Accelerator Center (SLAC).

With 90×10^6 $B\bar{B}$ events at the $\Upsilon(4S)$ resonance, we obtained branching fractions of $\mathcal{B}(B^\pm \to J/\psi\eta K^\pm) = [10.8\pm2.3(stat)\pm2.4(syst)]\times10^{-5}$ and $\mathcal{B}(B^0 \to J/\psi\eta K^0_S) = [8.4\pm2.6(stat)\pm2.7(syst)]\times10^{-5}$; and we set an upper limit of $\mathcal{B}[B^\pm \to X(3872)K^\pm \to J/\psi\eta K^\pm] < 7.7\times10^{-6}$ at 90% confidence level.

The branching fraction of decay chain $\mathcal{B}(B^\pm \to DK^\pm \to \pi^+\pi^-\pi^0K^\pm) = [5.5\pm1.0(stat)\pm0.7(syst)]\times10^{-6}$ with 229×10^6 $B\bar{B}$ events at $\Upsilon(4S)$ resonance, here D represents the neutral D meson. The decay rate asymmetry is $A = 0.02\pm0.16(stat)\pm0.03(syst)$ for this full decay chain. This decay can be used to extract the unitarity angle γ, a weak CP violation phase, through the interference of decay production of D^0 and $\bar{D}^0$ to $\pi^+\pi^-\pi^0$.

Qinglin Zeng
Department of Physics
Colorado State University
Fort Collins, CO 80523
Summer 2005

Acknowledgments

It is a pleasure to thank my advisor Prof. Robert J. Wilson, Prof. Walter H. Toki and Dr. Abner Soffer. Their guidance and continuous support made this work possible.

Prof. Wilson and Prof Toki gave me many suggestions and helpful ideas on the the first project. Their valuable ideas and suggestions led this project into new directions that resulted in publication in a prestigious physics journal. I also thank Dr. Jinlong Zhang for his help and discussion on the details of several techniques used in this project.

Dr. Abner Soffer gave me tremendous help on the second project; his atitude on the work and spirit benefited me a great deal. With his help, this project was finished with ease.

I also would like to thank the CSU group for providing me a friendly work and study environment.

Finally, I would like to thank my wife and my parents for their years of encouragement and help.

Contents

List of Figures

List of Tables

Chapter 1

Introduction

This dissertation documents two analyses the author has performed with the *BABAR* collaboration during 2002-2004. Both analysis topics are related to B decay branching ratio measurements involving the beauty quark to charm quark transition.

The first topic is about the decay $B \rightarrow J/\psi \eta K$, the part the author contributed uses the neutral kaon meson channel. It was finished in the middle of 2003 and published in Physics Review Letter [1]. This decay can be used to elucidate the nature of a new particle, denoted as "X", discovered by *Belle* [2] and confirmed by *CDF II*, *D0* and *BABAR* collaborations.

The X is a new narrow mass width state with a mass of $3.872\,\mathrm{GeV}/c^2$, and is produced in the decay of $B^{\pm} \rightarrow X(3872)K^{\pm}, X(3872) \rightarrow \pi^+\pi^- J/\psi$. This new state could be a $J^{PC} = 2^{--}$ 1^3D_3 charmonium state; a "molecule" state formed with charmed D and D^* mesons; a hybrid charmonium state formed of $c\bar{c}$ + gluon through exclusive B decay; or a diquark-antidiquark state. Details can be found in chapter 2.

1. **Introduction**

If the X is a conventional charmonium state, like $\psi(2S)$ that decays to $J/\psi\pi^+\pi^-$ and $J/\psi\eta$, the exclusive decay channel $B \to J/\psi\eta K$ can be used to search for the X(3872) through the two-body invariant mass of J/ψ and η.

This analysis was performed before 2004, with *BABAR* $89\,\mathrm{fb}^{-1}$ on-peak data, an upper limit for this exclusive $B \to X(3872)K \to J/\psi\eta K$ was set. For the direct channel $B \to J/\psi\eta K$, for both charged and neutral kaon channels, we are the first to measure these exclusive B decay branching ratios. The method for extracting the branching ratio and upper limit measurements is straight forward, using a cut and counting method.

The second analysis topic is about a rare decay chain of $B^\pm \to D^0/\bar{D}^0K^\pm$ with $D^0/\bar{D}^0 \to \pi^+\pi^-\pi^0$, which can be used to extract the weak phase γ through the interferences of D^0 and $\bar{D}^0$ decay to a common final state $\pi^+\pi^-\pi^0$. It was submitted to Physics Review D. The theory and the methods used to extract this weak charge conjugation and parity violation phase γ will be discussed in detail in chapter 2.

As this analysis involves the $\pi^0 \to \gamma\ \gamma$ decay and many radiation processes of charge particles produce low energy photons, the decay chain is not clean as a D^0 decay involving a kaon. The background, which has contributions from continuum and $B\bar{B}$, is a challenge for this analysis and prevents the extraction of γ. However to demonstrate the feasibility of this decay chain, an essential first step is to develop the necessary techniques to control the background, and to measure the branching ratio and the decay rate asymmetry of this decay chain.

To suppress the background while preserving the signal, a nonlinear multidimensional neural network is used, which incorporates many discrimination variables into a single, more powerful, variable. Two neural net variables were used, one to separate signal and $B\bar{B}$ events from continuum background, and the other to separate signal from $B\bar{B}$ and continuum background. To get better sensitivity for this high background analysis, the extended maximum likelihood fit method is adopted.

As these two analyses are quite different in their methodology, to make each analysis self-contained, this document is divided into four parts. Part I contains an introduction (chapter 1), physics overview (chapter 2), *BABAR* detector overview (chapter 3) and an analysis methods overview (chapter 4). Part II contains a description of the analysis process for $B \to J/\psi\eta K$, including the physics motivation, event selection, background estimation, data fit results, systematic error and physics results (chapter 5). Part III describes all parts of the analysis of $B^{\pm} \to DK^{\pm}$ with $D^0/\bar{D}^0 \to \pi^+\pi^-\pi^0$, which has a brief description of the physics motivation, event selection, parameterization for maximum likelihood fit, validation of the parameterization, data fit results, systematic error and physics results (chapter 6). Part IV contains a concluding comment for both analyses (chapter 7).

In chapter 2, a brief description for the nature of X particle, CP violation weak phase γ measurement methods are introduced. For this newly discovered particle

X, several theoretical proposals have been proposed: hybrid state [6], charmonium state [7], molecular meson state [8] or diquark and antiquark state [9]. The nature of X particle is still a mystery, the properties of X remains to be confirmed.

CP violation in quark physics was first discovered in the neutral kaon system [12]. A second independent test may be derived from the properties of the B mesons [13]. A standard parameterization of the CKM (Cabibbo-Kobayashi-Maskawa) matrix [14] introduces a complex quantity such that *CP* violation has a natural place in this theory. The weak phase γ is just one of the three angles of a unitary triangle that can be derived from the CKM matrix columns one and three that are most related to the bottom quark.

In chapter 3, the *BABAR* detector is introduced [16]. The basic components of the detector consists of a five-layer silicon vertex detector (SVT); a forty-layer drift chamber (DCH); a Cherenkov ring imaging detector (DIRC); an electromagnetic calorimeter (EMC); and an instrument flux return detector. The SVT provides the colliding position of the beams, the vertex point of a B meson; and is used with the DCH to provide the tracking and momentum information of the charged particles. The DCH and DIRC provide high performance particle identification of kaon and pion over the essential particle momentum region (0.7 - 4.0 GeV/c); The EMC provides the photon and neutral hadrons information through the energy deposition pattern. The IFR provides information on muons and some long-lived neutral hadrons, such as K_L^0. The author was a commissioner for DIRC for approximately fourteen months, helping to maintain the daily operation of this sub-system with good performance. A short description of positron and electron storage ring (PEP-II) is also included in this chapter.

In chapter 4, analysis methods and some general terminologies for the analysis topics are introduced. The $B \rightarrow J/\psi\eta K$ analysis, a "cut and counting method" is used, while for the $B^{\pm} \rightarrow DK^{\pm}$ analysis an extended maximum likelihood method [18] is used.

In chapter 5, a complete analysis chain for the mode $B \rightarrow J/\psi\eta K$ is described. Data samples, event selection criteria, background estimation, data fit results and systematic errors are listed. A search for $X \rightarrow J/\psi\eta$ is also included in this chapter.

In chapter 6, all the steps for the analysis $B^{\pm} \rightarrow DK^{\pm}$ are discussed. These include: data samples; event selection criteria; fit method; parameterization of the fit input variables; validation of the input variable shapes; Monte Carlo fit; data fit and systematic errors.

Chapter 7 contains a brief conclusion for both analyses.

Chapter 2

Physics overview

In this chapter the nature of the X particle, charge parity (*CP*) violation and the method to extract the *CP* violation weak phase γ are introduced.

2.1. Nature of the X particle

In 2003, the *Belle* Collaboration reported a 10.3σ discovery of a new particle, now denoted X(3872), in its decay $X(3872) \to J/\psi \pi^+\pi^-$, via the decay $B^\pm \to K^\pm X(3872)$ [2]. The particle has a resonance mass $3872.0 \pm 0.6 \pm 0.5$ MeV/c^2 with a width less than 2.3 MeV/c^2. This state has since been confirmed by the *CDF II* [3], the *D0* [4] and *BABAR* [5] collaborations, but still remains something of a mystery. The X(3872) mass is very near the $D^0 D^{*0}$ threshold of 3871.5 ± 0.5 MeV/c^2, which may indicate something important in the structure of X. Several ideas for the nature of this mystery particle have been suggested:

1. A charmonium hybrid state [6];
2. A $1D$ charmonium state [7];
3. A weakly bound state of two mesons, chiefly $D^0\bar{D}^{*0}$ [8];
4. A hidden and open charm diquark-antidiquark state [9].

2.1.1. Hybrid charmonium meson state

Hybrid mesons consist of a $q\bar{q}$ ($q = u, d, s, ...$) pair with an excited gluonic degree of freedom. A hybrid charmonium meson (ψ_g) could be produced in $B-$meson decays. Different theoretical models [19] predict that the low lying states of charmonium hybrid have a mass of 4.0 - 4.5 GeV/c^2 with $J^{PC} = 0^{\pm\mp}, 1^{\pm\mp}, 2^{\pm\mp}$, and $1^{\pm\pm}$, where J is the angular momentum quantum number, C is the charge conjugation, P is space parity. Of these states, the $0^{+-}, 1^{-+}$, and 2^{+-} have exotic quantum numbers that are not consistent with the constituent quark model ($P = (-1)^{l+1}, C = (-1)^{l+s}$, where l is the orbital angular momentum quantum number, and s is the spin of the particle).

There are three decay modes that can be used to search for charmonium hybrids:

1. a Zweig-allowed fall-apart mode, such as $\psi_g \to D^*\bar{D}^*$;
2. a cascade decay to conventional $c\bar{c}$ states, of the type $\psi_g \to (c\bar{c})(gg) \to (c\bar{c})+$(light hadrons), and $\psi_g \to (c\bar{c}) + \gamma$;
3. decays to light hadrons via intermediate gluons, $\psi_g \to (ng) \to$ light hadrons.

Of these modes, ψ_g with exotic J^{PC} quantum numbers offer the most unambiguous signal to search for the hybrid charmonium states. The possible decays $\psi_g \rightarrow D^* D^{*,**}$, $\psi_g(0^{+-}, 2^{+-}) \rightarrow J/\psi + (\pi^+\pi^-, \eta, \eta')$, and $\psi_g \rightarrow (c\bar{c})\gamma$ can be used for this purpose.

The reported properties of X(3872) are consistent with the expectations for 2^{+-} and 0^{+-} hybrids [6], as the lowest lying hybrid charmonium state has a mass above 4.0 GeV/c^2, which is much higher than the mass of X(3872), and the calculation based on the models for hybrid states has a large uncertainty, these states can only be used as a guidance for this X particle.

2.1.2. $1D$ charmonium states

The predictions for $1D$ charmonium states [7] are derived mostly from quark potential models. These models assume a color Coulomb potential plus a linear confining interaction. The expected mass mean value for $1D$ charmonium multiplets is about 3.8 GeV/c^2, Table 2.1 gives the average mass value of the quark model $1D$ and $2P$ $c\bar{c}$ states from several theoretical predictions [20].

Table 2.2 shows a summary of the strong and electromagnetic partial width calculated for all possible $1D$ states [21]. The total widths listed in this table imply that the most plausible $c\bar{c}$ assignments for X(3872) would be $1\,^3D_2$ and $1\,^1D_2$. Both states have no allowed open-charm decay modes due to the parity violation and hence should have narrow decay widths. The $1\,^3D_2$ state has a large branching fraction for the

State	Experiment (MeV)	Average mass value (MeV)
$1\,^3D_3$		3841(22)
$1\,^3D_2$		3827(24)
$1\,^3D_1$	3770	3803(25)
$1\,^1D_2$		3821(32)
$2\,^3P_2$		3990(25)
$2\,^3P_1$		3957(28)
$2\,^3P_0$		3903(40)
$2\,^1P_1$		3964(20)

Table 2.1: Quark model $c\bar{c}$ masses (see Ref. [8]). The number in parenthesis is the error.

radiative decay, which is contrast to *Belle* limit on the radiative decay of X(3872) [2],

$$\frac{B(X(3872) \to \chi_{c1}\gamma)}{B(X(3872) \to J/\psi\pi^+\pi^-)} < 0.89, 90\%\ C.L. \tag{2.1}$$

As there is a large uncertainty on these measurement, the state of $1\,^3D_2$ is not ruled out yet. For $1\,^3D_3$ state, though it has allowed open-charm decay, it is suppressed with high orbital quantum number, it still has a small width. As for the uncertainty in this theoretical prediction, this state might be still a possible assignment for X(3872).

Initial state	Final state	Width (MeV)	BF(%)
1^3D_3	DD	4.04	84.2
	ggg	0.18	3.8
	$J/\psi\pi\pi$	0.21±0.11	4.4
	$\chi_{c_2}(1^3P_2)\gamma$	0.37	7.7
	Total	4.80	100
1^3D_2	ggg	0.08	10.8
	$J/\psi\pi\pi$	0.21±0.11	4.4
	$\chi_{c_2}(1^3P_2)\gamma$	0.09	12.2
	$\chi_{c_1}(1^3P_1)\gamma$	0.36	48.6
	Total	0.74	100
1^3D_1	DD	184	98.9
	ggg	1.15	0.6
	$J/\psi\pi\pi$	0.21±0.11	0.1
	$\chi_{c_2}(1^3P_1)\gamma$	0.20	0.1
	$\chi_{c_1}(1^3P_0)\gamma$	0.44	0.2
	Total	186	100
1^1D_2	DD	0.19	22.2
	$\eta_c\pi\pi$	0.21±0.11	0.1
	$h_c(1^1P_1)\gamma$	0.46	53.5
	Total	0.86	100

Table 2.2: Partial widths and branching fractions (BF) for strong and electric transitions with the initial $c\bar{c}$ state of a mass of X(3872) (see Ref. [8]).

2.1.3. Weakly bound state of two mesons

From Table 2.1, we see that the mass of X(3872) is between $1D$ and $2P$ states but with a discrepancy of 60-100 MeV for either of these two possible states. As the mass of X(3872) is near the threshold of $D^0\bar{D}^{*0}/D^{*0}\bar{D}$ and $D^{\pm}D^{*\pm}$, it fits Törnqvist's prediction of two weakly bound $D\bar{D}^*$ 0^{-+} and 1^{++} states, which have an invariant mass close to 3870 MeV [8,22]. While Swanson argued that it is a state of $J^{PC} = 1^{++}$ $D^0\bar{D}^{*0}$ hadronic resonance, stabilized by an admixture state of $\omega J/\psi$ and $\rho J/\psi$ [8].

If X(3872) really is a weakly bound state of $D^0\bar{D}^{*0}$ as Törnqvist predicted, its properties should be

1. $J^{PC} = 0^{+-}/1^{++}$, for other quantum numbers, the potential is either repulsive or so weak that bound states are not expected;
2. a pure isosinglet with a mass very close to the DD^* threshold;
3. with a width determined mostly by the instability of its components or the D^* width (< 2.1 MeV).

All these properties are based on a pion exchange model.

As branching ratio of $X(3872) \rightarrow J/\psi\pi\pi$ is small, Swanson argued that this may imply a small isovector $\rho J/\psi$ component in X(3872) wave function. He suggested that the wave function of X(3872) may be coupled with six possible decay channels with a threshold close to X(3872). These six channels are

1. $\rho J/\psi$ at 3.8679 GeV/c^2,
2. $\frac{1}{\sqrt{2}}(D^0\bar{D}^{*0} + \bar{D}^0 D^{*0})_S$ at 3.8712 GeV/c^2,
3. $\frac{1}{\sqrt{2}}(D^0\bar{D}^{*0} + \bar{D}^0 D^{*0})_P$ at 3.8712 GeV/c^2,
4. $\frac{1}{\sqrt{2}}(D^+\bar{D}^{-*} + \bar{D}^- D^{+*})_S$ at 3.8793 GeV/c^2,
5. $\frac{1}{\sqrt{2}}(D^+\bar{D}^{-*} + \bar{D}^- D^{+*})_P$ at 3.8793 GeV/c^2,
6. $\omega J/\psi$ at 3.8795 GeV/c^2

where S (P) stands for S (P) wave for orbital quantum number $l = 0(1)$. Fig. 2.1 shows the wave function coefficients (defined as $\int |\varphi_\alpha|^2 d^3x$, α is a channel index) as a function of binding energy. From Fig. 2.1, if X(3872) is really a weakly bound state of mesons, $D^0\bar{D}^{*0}$ is the main component.

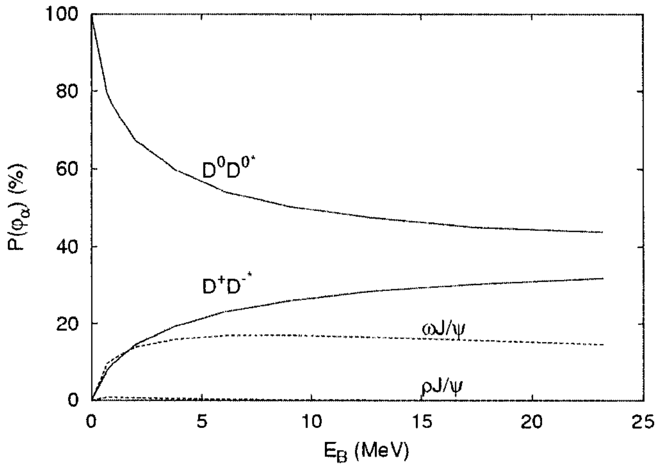

Figure 2.1: Component strength vs. binding energy.

2.1.4. Diquark-antidiquarks

As the X(3872) does not fit in a $c\bar{c}$ assignment very well, Maiani *et al.* [9] argued that it might be a 4-quark bound state: a $J^{PC} = 1^{++}$ state with the symmetric spin distribution $[cq]_{S=1}[\bar{c}\bar{q}]_{S=0} + [cq]_{S=0}[\bar{c}\bar{q}]_{S=1}$, where $q = u, d$ quarks.

In ref. [9], they studied two aspects of diquark-antidiquark state, constituent diquark mass and spin-spin interaction. For hadrons, the mass of a particle originates from: quark composition, constituent quark masses and spin-spin interactions. The mass Hamiltonian can be written as

$$H = \sum_i m_i + \sum_{i<j} 2\kappa_{ij}(S_i S_j), \tag{2.2}$$

where i, j are the indices of the constituent quarks, S_i, S_j are the spins for quarks i and j, and the coefficients κ_{ij} depend on the flavor of the constituents i, j and on the particular color state of the pair. Fig. 2.2 shows the mass spectrum for the X particles with X(3872) mass set to 3.872 GeV/c^2. The 2^{++} state is a possible assignment for the observed X(3940) state through $e^+e^- \to J/\psi X(3940), X(3940) \to D\bar{D}^*$ [10] or the resonance of $J/\psi\omega$ with decay channel $B \to J/\psi\omega K$ [11]. The search for 1^{+-} state can be done through the channels $J/\psi + \pi(\eta)$ and $\eta_c + \rho(\omega)$. The particle X might be a mixture of two neutral mass eigenstates $X_u = [cu][\bar{c}\bar{u}]$ and $X_d = [cd][\bar{c}\bar{d}]$ $(c\bar{c}u\bar{u}(c\bar{c}d\bar{d}) = \frac{1}{\sqrt{2}}c\bar{c}\left(\frac{u\bar{u}+d\bar{d}}{\sqrt{2}} + (-)\frac{u\bar{u}-d\bar{d}}{\sqrt{2}}\right) = \frac{1}{\sqrt{2}}(|I_S = 0> +(-)|I_S = 1>)$, I_S is the

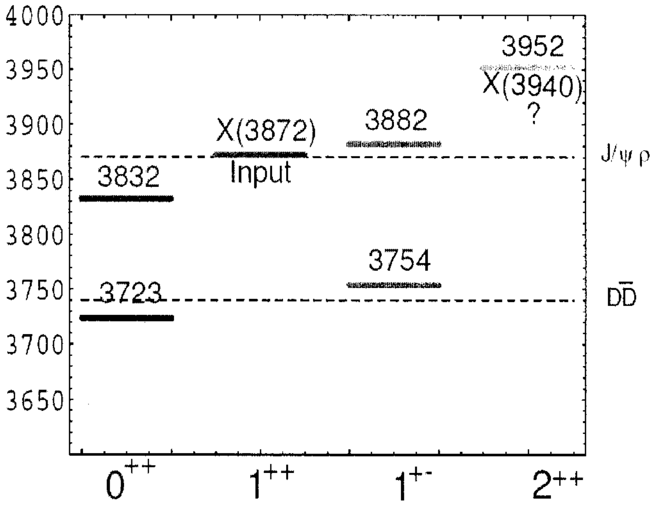

Figure 2.2: Full spectrum of the X particles.

spin). This would lead to isospin breaking in their mass eigenstates and strong decays. With this assumption, a heavy X_h and a light X_l, both may decay into $J/\psi\omega$.

With this diquark-antidiquark model, there is no limitation on the X charged partner (X^+, $[cu][\bar{c}\bar{d}]$, X^-, $[cd][\bar{c}\bar{u}]$). Maiani *et al.* predicted that if particle X_u (X_d) dominates final production of B^+, X_d (X_u) will dominate the neutral B^0. A precise measurement of the X mass in B^+ and B^0 decay should reveal the mass difference between X_h and X_l.

2.2. Charge conjugation and parity violation

Charge conjugation(C), space parity(P) and time reversal (T) are three discrete symmetries in the universe. For a particle with momentum $\vec{p}$, charge Q, spin $\vec{S}$ and

Energy E, Charge conjugation operation changes this particle to its corresponding anti-particle that has charge -Q. Space-parity operation changes the position $\vec{x}$ of the particle to $-\vec{x}$. Time reversal operation leads to the interchange between the initial state and the final state. The combined CP transformation changes a particle to its antiparticle and flips its momentum and helicity (basically it is the inner product of the spin and momentum of the particle). The product transformation CPT, in any order, is an exact symmetry for a local field that is a Lorentz invariant and meets the spin-statistics requirement (boson fields obey commutation rules and fermion field obey anti-commutation rules).

The earliest discovery of CP violation was found in neutral K-meson system [12] by Cronin, Fitch and co-workers. They observed that there is a small but finite probability for the decay $K_L^0 \to \pi^+\pi^-$, in which the final state has $CP = +1$, while K_L^0 also decays into 3 pions state which is CP = -1. All these are due to that K_L^0 is a mass eigenstate but not a CP eigenstate.

For the origin of the CP violation in hadronic physics, the Standard Model of the electroweak interaction provides a good explanation.

In the Standard Model, there are three generation of quarks: $\begin{pmatrix} u \\ d \end{pmatrix}$, $\begin{pmatrix} c \\ s \end{pmatrix}$,

$\begin{pmatrix} t \\ b \end{pmatrix}$. The flavor of the quarks involve in the weak interaction. As the flavor eigenstate is not a physics quantity, such as mass, the weak transitions of the states (d, s, b) to (u, c, t) obey mixing rules that can be described by the Cabibbo-Kobayashi-Maskawa (CKM) mixing matrix [14] to get physics measurement. The CKM matrix in general can be written as:

$$U = \begin{bmatrix} U_{ud} & U_{us} & U_{ub} \\ U_{cd} & U_{cs} & U_{cb} \\ U_{td} & U_{ts} & U_{tb} \end{bmatrix} . \qquad (2.3)$$

where U_{ij} is the quark coupling constant between quark i and quark j. Usually the diagonal term is Cabibbo-favored and the non-diagonal terms are Cabibbo-suppressed.

This is a unitary 3×3 matrix which can be fully parameterized by 3 real and 1 imaginary parameters. An instructive parameterization of the CKM matrix is

Wolfenstein expression [23]

$$U = \begin{bmatrix} 1-\lambda^2/2 & \lambda & \lambda^3 A(\rho - i\eta) \\ -\lambda & 1-\lambda^2/2 & \lambda^2 A \\ \lambda^3(1-\rho-i\eta) & -\lambda^2 A & 1 \end{bmatrix}, \tag{2.4}$$

where $\lambda = \sin\theta_c \simeq 0.22$, and θ_c is the Cabibbo angle.

The amplitude for a process $ab \rightarrow cd$ is [24]

$$\begin{aligned} \mathcal{M} &\propto \mathcal{J}^{\mu}_{ca}\mathcal{J}^{\dagger}_{\mu bd} \\ &= (\bar{u}_c\gamma_\mu(1-\gamma^5)U_{ca}u_a)(\bar{u}_b\gamma_\mu(1-\gamma^5)U_{bd}u_d)^\dagger \qquad (2.5) \\ &= U_{ca}U^*_{db}(\bar{u}_c\gamma_\mu(1-\gamma^5)u_a)(\bar{u}_d\gamma_\mu(1-\gamma^5)u_b), \end{aligned}$$

where charge current $J^{\mu}_{ca} = \bar{u}_c\gamma_\mu(1-\gamma^5)U_{ca}u_a$.

The CP-transformed amplitude is

$$\begin{aligned} \mathcal{M}_{CP} &\propto (\mathcal{J}^{\mu}_{ca})_{CP}(\mathcal{J}^{\dagger}_{\mu bd})_{CP} \\ &= U_{ca}U^*_{db}(\bar{u}_a\gamma_\mu(1-\gamma^5)u_c)(\bar{u}_b\gamma_\mu(1-\gamma^5)u_d). \qquad (2.6) \end{aligned}$$

if we find $\mathcal{M}_{CP} = \mathcal{M}^\dagger$, then CP is conserved, otherwise CP is violated. From Eqn. 2.5

amplitude $\mathcal{M}^\dagger$ is then

$$\mathcal{M}^\dagger \sim U_{ca}^* U_{db} (\bar{u}_c \gamma_\mu (1-\gamma^5) u_a)(\bar{u}_d \gamma_\mu (1-\gamma^5) u_b). \tag{2.7}$$

Due to the two complex elements of matrix (see Eqn. 2.4), it is easy to show that for some processes,

$$\mathcal{M}_{CP} \neq \mathcal{M}^\dagger. \tag{2.8}$$

then CP symmetry violation in the SM model is mainly due to the complex coupling constants that can not be removed by any choice of phase redefinition.

2.3. Charge conjugation and parity violation in B physics

B meson decays provide a second and independent set of tests of the Standard Model's CP violation mechanism [13]. The best determination of CP violating parameters in the Standard Model comes from neutral B mesons with a mixing between B^0 and $\bar{B}^0$ [25]. Also with a large data sample, it is possible to explore the CP violation without B mixing [26].

In the neutral $B^0 - \bar{B}^0$ system, the mass eigenstates are not flavor eigenstates. As CP is not a good symmetry, the mass eigenstates are also not CP eigenstates. The mass eigenstate of a neutral B is a mixture of the two flavor states, $|B^0>$ and $|\bar{B}^0>$, can be written as:

$$
\begin{aligned}
|B_L> &= p|B^0> + q|\bar{B}^0> \\
|B_H> &= p|B^0> - q|\bar{B}^0>
\end{aligned}
\tag{2.9}
$$

where H(L) stands for the Heavy(Light). p and q are complex coefficients, and governed by the time-dependent Schrödinger equation

$$
i\frac{d}{dt}\begin{pmatrix} p \\ q \end{pmatrix} = H\begin{pmatrix} p \\ q \end{pmatrix} = (M - \frac{i}{2}\Gamma)\begin{pmatrix} p \\ q \end{pmatrix}. \tag{2.10}
$$

Here M and Γ are 2×2 Hermitian matrices, $-i\Gamma$ describes the exponential decay of the $B^0 - \bar{B}^0$ system, M is the mass matrix of this B_d system. CPT invariance guarantees $H_{11} = H_{22}$, and the non-diagonal terms are crucial for CP violation

Defining $M = (M_H + M_L)/2$, $\Gamma = (\Gamma_H + \Gamma_L)/2$ and $\Delta u = \Delta M - i\Delta\Gamma = (M_H - M_L) - i(\Gamma_H - \Gamma_L)$, with Eqn. 2.10, the ratio of q/p is

$$
\frac{q}{p} = \frac{-\Delta u}{2(M_{12} - \frac{i}{2}\Gamma_{12})} = -\frac{2(M_{12}^* - \frac{i}{2}\Gamma_{12}^*)}{\Delta u}. \tag{2.11}
$$

The amplitudes for $B^0(\bar{B}^0)$ decays into a CP eigenstate f are

$$A =< f|H|B^0 >, \bar{A} =< f|H|\bar{B}^0 > . \tag{2.12}$$

Defining

$$r(f) = \frac{q}{p}\frac{\bar{A}}{A}, \tag{2.13}$$

the time-dependent rates for initially pure $|B^0>$ or $|\bar{B}^0>$ states to decay into a final CP eigenstate at time t can be written as

$$\begin{aligned} \Gamma(B^0(t) \to f) &= |A|^2 e^{-\Gamma t} \times (\frac{1+|r(f)|^2)}{2} \qquad (2.14) \\ &+ \frac{1-|r(f)|^2}{2}\cos(\Delta M t) - Im[r(f)]\sin(\Delta M t)) \\ \Gamma(\bar{B}^0(t) \to f) &= |A|^2 e^{-\Gamma t} \times (\frac{1+|r(f)|^2)}{2} \qquad (2.15) \\ &- \frac{1-|r(f)|^2}{2}\cos(\Delta M t) + Im[r(f)]\sin(\Delta M t)) \end{aligned}$$

The time-dependent CP asymmetry is then defined

$$a_f(t) \equiv \frac{\Gamma(B^0(t) \to f) - \Gamma(\bar{B}^0(t) \to f)}{\Gamma(B^0(t) \to f) + \Gamma(\bar{B}^0(t) \to f)}. \tag{2.16}$$

2.3.1. Prototypical CP violation mechanisms in B decay

There are three prototypical conditions by which a process may exhibit CP violation in the $B\bar{B}$ system.

(i) CP violation in decay

In general, amplitude A ($\bar{A}$) can be factorized to three parts: the absolute value of A ($\bar{A}$), a strong phase shift δ (CP invariant), and a weak phase ϕ (CP violating). If several amplitudes contribute to the decay $B \to f$,

$$A = \sum_i A_i e^{i\delta_i} e^{i\phi_i}, \bar{A} = \sum_i A_i e^{i\delta_i} e^{-i\phi_i} \tag{2.17}$$

$$\left|\frac{\bar{A}}{A}\right| = \left|\frac{\sum_i A_i e^{i\delta_i} e^{-i\phi_i}}{\sum_i A_i e^{i\delta_i} e^{i\phi_i}}\right|. \tag{2.18}$$

When CP is conserved, the weak phases ϕ_i are all equal. Therefore, CP violation implies

$$\left|\frac{\bar{A}}{A}\right| \neq 1 \tag{2.19}$$

(ii) CP violation in mixing

Considering Eqn. 2.11, if CP is conserved the relative phase between M_{12} and Γ_{12} vanishes, So that CP violation implies

$$|\frac{q}{p}| \neq 1. \tag{2.20}$$

(iii) CP violation in the interference of mixing and decay

In this case $|q/p| = 1$ and $|\bar{A}/A| = 1$, but $(p/q) \neq 1$, *i.e.*, p/q has a CP-violating phase.

Potentially, CP violation can be found in the neutral B system through any of these three types. As in charged B mesons, there is no mixing, CP violation may be discovered only through the type (i) processes.

2.4. The unitarity triangle

As the CKM matrix is a unitary matrix, there are three useful relations among its elements:

$$V_{ud}V_{us}^* + V_{cd}V_{cs}^* + V_{td}V_{ts}^* = 0, \tag{2.21}$$

$$V_{us}V_{ub}^* + V_{cs}V_{cb}^* + V_{ts}V_{tb}^* = 0, \tag{2.22}$$

$$V_{td}V_{tb}^* + V_{cd}V_{cb}^* + V_{ud}V_{ub}^* = 0. \tag{2.23}$$

In the complex plane, the above three relations can be represented as triangles. The Unitarity triangle, which represents Eqn 2.23, is shown in Fig. 2.3. The three angles of this triangle are given by:

$$\alpha = arg(-\frac{V_{td}V_{tb}^*}{V_{ud}V_{ub}^*}) \tag{2.24}$$

$$\beta = arg(-\frac{V_{cd}V_{cb}^*}{V_{td}V_{tb}^*}) \tag{2.25}$$

$$\gamma = arg(-\frac{V_{ud}V_{ub}^*}{V_{cd}V_{cb}^*}). \tag{2.26}$$

One of the analyses described in this thesis will ultimately lead to the measurement of the angle γ, as described in the next section.

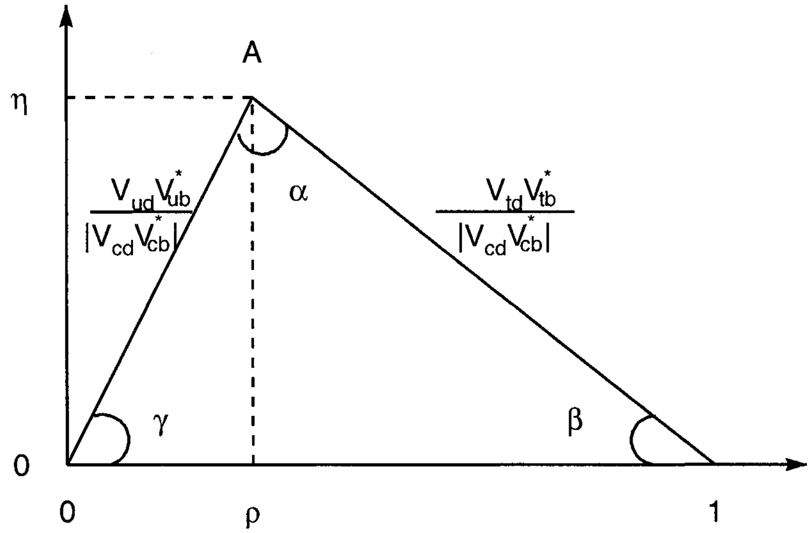

Figure 2.3: Unitarity triangle.

2.5. Measurements of the angle γ with charged B mesons

In this section we give an overview of γ measurements using charged B decays. More detail about these measurement methods is given in the subsequent subsections.

The first proposal to extract γ by using charged B meson decays, suggested by Gronau and Wyler (GW) [27], is to use the interference of two b quark transitions, $B^- \to D^0K^-$ and $B^- \to \bar{D}^0K^-$ with $D^0/\bar{D}^0$ decaying into common CP eigenstates. $B^- \to D^0K^-$ ($b \to c\bar{u}s$ transition) is flavor favored decay, which includes two decay processes, color allowed and color suppressed. For $B^- \to \bar{D}^0K^-$ ($b \to u\bar{c}s$ transition), it is a color and Cabibbo suppressed decay. Due to the color and Cabibbo suppression of transition involving in the decay $B^- \to \bar{D}^0K^-$, the interference magnitude between these two decay channels is at a level of 10%, determined by the ratio of the decay amplitudes of these two transitions [28]. With the GW method, the measurement of γ is also dependent on all the transition branching ratios. As Atwood, Dunietz and Soni (ADS) [29] pointed out, the GW method has some difficulty in measuring the branching ratio of $B^- \to \bar{D}^0K^-$. The contribution from $B^- \to D^0K^-$ with D^0 undergoing a doubly Cabibbo suppressed decay into the same final state is at the same order as the amplitude of $B^- \to \bar{D}^0K^-$ with a Cabibbo allowed $\bar{D}^0$ decay, and these two channels interference. Therefore, it is hard to distinguish these two contributions.

The ADS method makes use of the full interference of these two channels, *i.e.*,

$B^- \to D^0K^-$ with the D^0 undergoing a doubly Cabibbo suppressed decay to final states, such as $K^+\pi^-$, $B^- \to \bar{D}^0K^-$ with $\bar{D}^0$ undergoing Cabibbo favored decay into the same final states. The full rates of these two process are similar, and they can interfere at a level of O(1).

To circumvent the color suppression of $b \to u\bar{c}s$ transition in the GW and ADS methods, Aleksan *et. al.* have suggested using 3-body B decays, $B^- \to DK^-\pi^0$, which have color-allowed $b \to u\bar{c}s$ contributions [30]. Despite this advantage, the sensitivity of this method is limited by "Dalitz plot suppression", in which the $b \to c\bar{u}s$ and $b \to u\bar{c}s$ amplitudes populate mostly different regions of the Dalitz plot, reducing the level of interference between them.

With the data accumulated with *BABAR* (about 210 fb^{-1}) to date , the statistics is still not enough to get a good measurement on γ with above introduced methods. To make maximal use of the current data, many variants of the ADS and GW methods have been developed [31]. One of the most promising methods is to use multi-body D decay with full D Dalitz analysis [35].

There are also proposals to use neutral B mesons to extract γ. Dunietz suggested to use the so-called self-tagging B_d modes $B_d \to D^0/\bar{D}^0K^{*0}$ with $K^{*0} \to K^+\pi^-$ (which tags the B flavor) [33]. Gronau *et. al.* suggested using untagged $B^0 \to DK_S$ modes [34].

In the following several sections, we focus on the use of charged B decay modes.

2.5.1. Gronau-Wyler method

The decay modes $B^- \to D^0K^-$, $B^- \to \bar{D}^0K^-$, $B^\pm \to D^0_{1,2}K^\pm$, together with their charge-conjugate counterparts can be used to determine the value of γ, with 8-fold discrete ambiguity. Here $D^0_1(D^0_2) = (D^0 + (-)\bar{D}^0)/\sqrt{2}$ is a CP-even(odd) state,

Let us first consider the decay $B^\pm \to D^0_1(D^0_2)K^\pm$. This decay can be identified by the CP decay products of the D^0_1/D^0_2. For instance, $K_s\pi^0$, $K^0_S\rho^0$, and $K^0_S\phi$ can be used to identify the CP-odd state D^0_2, while $\pi^+\pi^-, K^+K^-$ indicate the CP-even state D^0_1.

The decay amplitudes of the charged B decay, $B^\pm \to D^0_1K^\pm$ can be written as

$$\sqrt{2}A(B^+ \to D^0_1K^+) = |A|e^{i\gamma+i\delta} + |\bar{A}|e^{i\bar{\delta}},$$

$$\sqrt{2}A(B^- \to D^0_1K^-) = |A|e^{-i\gamma+i\delta} + |\bar{A}|e^{i\bar{\delta}}. \tag{2.27}$$

where A and $\bar{A}$ are the two weak amplitudes, with CKM factor $V^*_{ub}V_{cs}$ and $V^*_{cb}V_{us}$, respectively. $|A| = |A(B^+ \to D^0K^+)| = |A(B^- \to D^0K^-)|$, $|\bar{A}| = |A(B^+ \to \bar{D}^0K^+)| = |A(B^- \to \bar{D}^0K^-)|$. δ and $\bar{\delta}$ are the final state interaction phases; generally $\delta \neq \bar{\delta}$. The expression for D^0_2 are obtained by replacing the "+" signs with "-" signs in Eqn. 2.27.

Eqn. 2.27 also can be written as

$$\sqrt{2}A(B^+ \to D^0_1K^+) = A(B^+ \to D^0K^+) + A(B^+ \to \bar{D}^0K^+),$$

$$\sqrt{2}A(B^- \to D_1^0 K^-) = A(B^- \to D^0 K^-) + A(B^- \to \bar{D}^0 K^-). \tag{2.28}$$

Eqn. 2.27 and 2.28 can be pictured as two triangles in the complex plane (Fig. 2.4). Note here

$$\begin{aligned} A(B^+ \to \bar{D}^0 K^+) &= A(B^- \to D^0 K^-) \\ A(B^+ \to D^0 K^+) &= e^{2i\gamma} A(B^- \to \bar{D}^0 K^-) \\ |A(B^+ \to D_1^0 K^+)| &\neq |A(B^- \to D_1^0 K^-)| \end{aligned} \tag{2.29}$$

In Eqn. 2.29, $\gamma \neq 0$, $\delta \neq \bar{\delta}$ are assumed. We may define a partial decay rate asymmetry by

$$\begin{aligned} a_{cp} &= \frac{|A(B^+ \to D_1^0 K^+)|^2 - |A(B^- \to D_1^0 K^-)|^2}{|A(B^+ \to D_1^0 K^+)|^2 + |A(B^- \to D_1^0 K^-)|^2} \\ &= \frac{2r_B \sin\gamma \cos(\bar{\delta} - \delta)}{1 + r_B^2 + 2r_B \cos\gamma \cos(\bar{\delta} - \delta)} \end{aligned} \tag{2.30}$$

where

$$r_B = \frac{|A(B^- \to \bar{D}^0 K^-)|}{|A(B^- \to D^0 K^-)|}, \tag{2.31}$$

it is expected to be around 0.1. Measuring the magnitudes of the six amplitudes in

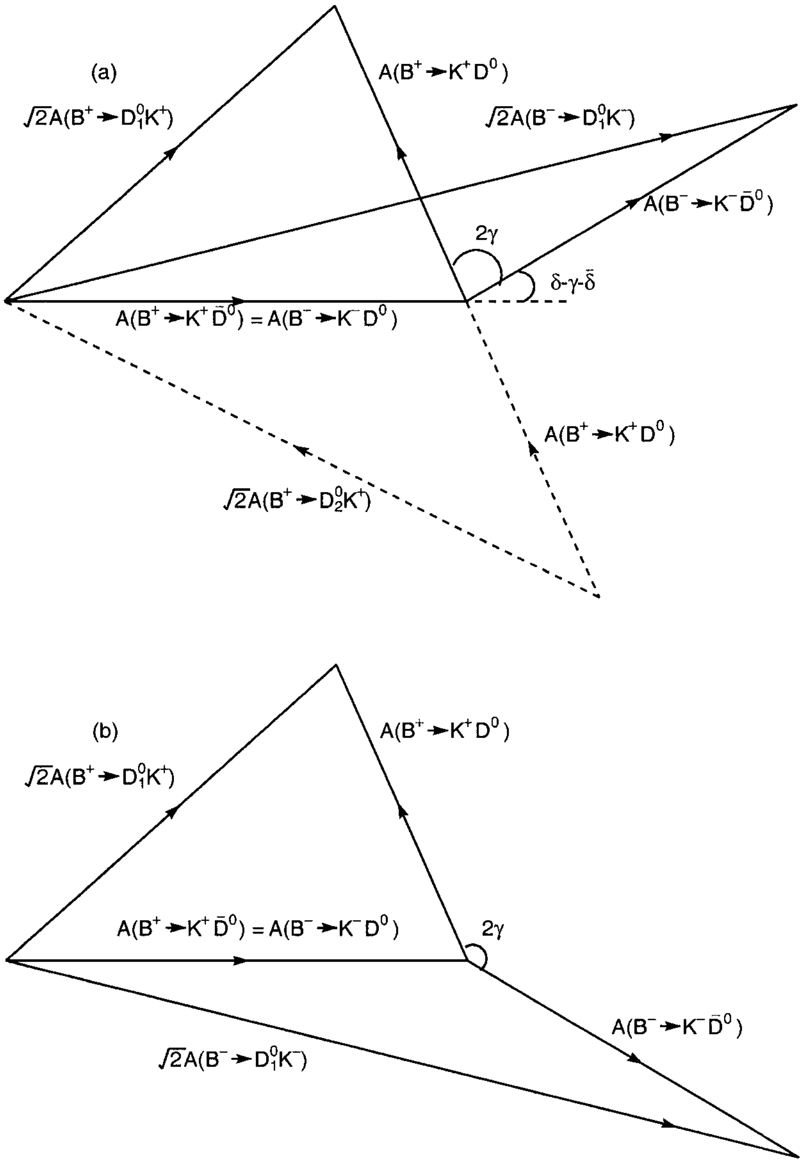

Figure 2.4: Representation of Eqns. 2.27 and 2.28 in the complex plane: (a) and (b) describe two possible solutions for γ.

Eqn. 2.29, $\sin\gamma$ is given by

$$\sin\gamma = \frac{1}{4|A||\bar{A}|}\{\pm\sqrt{[(|A|+|\bar{A}|)^2 - 2|A_1^+|^2][2|A_1^-|^2 - (|A| - |\bar{A})^2]} \\ \pm\sqrt{[(|A|+|\bar{A}|)^2 - 2|A_1^-|^2][2|A_1^+|^2 - (|A| - |\bar{A})^2]}\}, \qquad (2.32)$$

where $A_1^+ = A(B^+ \to D_1^0 K^+)$, $A_1^- = A(B^- \to D_1^0 K^-)$. The value for γ has an 8-fold discrete ambiguity [36] due to invariance of the measured decay rates under the three operations:

$$\begin{aligned} \textit{exchange} &: (\gamma, \delta - \bar{\delta}) \to (\delta - \bar{\delta}, \gamma) \\ \textit{sign} &: (\gamma, \delta - \bar{\delta}) \to (-\gamma, -\delta + \bar{\delta}) \\ \pi &: (\gamma, \delta - \bar{\delta}) \to (\pi + \gamma, \pi + \delta - \bar{\delta}) \end{aligned} \qquad (2.33)$$

This can be seen from Eqn. 2.32, which involves $\cos(\gamma \pm (\delta - \bar{\delta}))$ in A_1^+/A_1^-.

The amplitudes of the six processes (see Eqn. 2.29) are needed in order to extract γ. But experimentally, it is difficult to measure the branching ratios of $B^- \to \bar{D}^0 K^-$ and its charged partner. Experimentally, there are only two possible ways to tag the flavor of a $\bar{D}^0$: a) through semi-leptonic decays; b) through hadronic decays.

Using the semi-leptonic decay $\bar{c} \to l^- \bar{s} \bar{\nu}_l$ to tag the D flavor in the decay $B^- \to \bar{D}^0 K^-$ suffers from an overwhelming combinatoric background

For hadronic D decay, one would detect the decay of $B^- \to \bar{D}^0 K^-$ through a

Cabibbo-allowed $\bar{D}^0$ decay into a state with a K^+. However $B^- \rightarrow D^0K^-$ can also decay into a state with a K^+ through a double Cabibbo-suppressed D^0 decay. As $r_B \sim 0.1$, $\lambda^2 \sim 0.05$, the final production rates from the above two contributions are of same order and they interfere quantum mechanically, it is not easy to identify whether one had a D^0 or a $\bar{D}^0$.

2.5.2. Atwood-David-Soni method

ADS method makes use of the interference of the same D final states of $B^- \rightarrow D^0K^-$ through a double Cabbibo-suppressed D decay and $B^- \rightarrow \bar{D}^0K^-$ through a Cabibbo-allowed D decay. Let us define this D final state to be X, where X is a non-CP eigenstate of D.

Let us take the conventions of ref. [29], using the same definition of the branching ratios.

$$\begin{aligned} a(k) = Br(B^- \rightarrow K^-D^0),\ \bar{a}(k) = Br(B^+ \rightarrow K^+\bar{D}^0), \\ b(k) = Br(B^- \rightarrow K^-\bar{D}^0),\ \bar{b}(k) = Br(B^+ \rightarrow K^+D^0), \\ c(X) = Br(D^0 \rightarrow X),\ \bar{c}(X) = Br(\bar{D}^0 \rightarrow X), \\ c(\bar{X}) = Br(D^0 \rightarrow \bar{X}),\ \bar{c}(\bar{X}) = Br(\bar{D}^0 \rightarrow \bar{X}), \\ d(k,X) = Br(B^- \rightarrow K^-[X]),\ \bar{d}(k,\bar{X}) = Br(B^+ \rightarrow K^+[\bar{X}]), \end{aligned} \tag{2.34}$$

In the Standard Model, $a(k) = \bar{a}(k) = |A|^2$, $b(k) = \bar{b}(k) = |\bar{A}|^2$ and $\bar{c}(X) = c(\bar{X})$. Now write $d(k,X)$ and $\bar{d}(k,\bar{X})$ in terms of a, b and c

$$\begin{aligned} d(k,X) &= a(k)c(X) + b(k)c(\bar{X}) \\ &+ 2\sqrt{a(k)b(k)c(X)c(\bar{X})}\cos(\zeta_k + \delta_X + \gamma), \\ \bar{d}(k,\bar{X}) &= a(k)c(X) + b(k)c(\bar{X}) \\ &+ 2\sqrt{a(k)b(k)c(X)c(\bar{X})}\cos(\zeta_k + \delta_X - \gamma), \end{aligned} \tag{2.35}$$

where $\zeta_k = \delta - \bar{\delta}$, δ_X is the strong phase difference between $D \to X$ and $D \to \bar{X}$. In general, if $\gamma \neq 0$, $d(k,X) \neq d(k,\bar{X})$.

Let us consider the case where $b(k)$ is not known (hard to get a measurement) and $d(k,X_{1,2})$, $\bar{d}(k,\bar{X}_{1,2})$, $a(k)$, $c(X_{1,2})$ and $c(\bar{X}_{1,2})$ are known, where $X_{1,2}$ is two different final non-CP state from D decay. There are four unknowns to solve for: $\{b(k), \xi_1, \xi_2, \gamma\}$, where $\xi_i \equiv \zeta_k + \delta_{X_i}$.

Here the quantities defined in ref. [29] are used:

$$\begin{aligned} u_i = \frac{b(k)c(\bar{X}_i)}{a(k)c(X_i)}; y_i &= \frac{d(k,X_i) - \bar{d}(k,\bar{X}_i)}{2a(k)c(X_i)}; \\ z_i &= \frac{d(k,X_i) + \bar{d}(k,\bar{X}_i)}{2a(k)c(X_i)} - 1; \\ \rho &= \frac{c(X_1)c(\bar{X}_2)}{c(\bar{X}_1)c(X_2)} = \frac{u_2}{u_1}; \\ \varsigma = z_1^2 - z_2^2/\rho - 2(z_1 - z_2)u_1 &+ (1-\rho)u_1^2; \end{aligned}$$

$$\vartheta = y_1^2 - y_2^2/\rho; \tag{2.36}$$

here y_i, z_i, ϑ and ρ can be measured directly from experiment, u_i is unknown. It is easy to derive

$$4u_1\varsigma\vartheta = (\vartheta - \varsigma)(y_1^2\varsigma - (z_1 - u_1)^2\vartheta). \tag{2.37}$$

This equation in general is a quartic equation of u_1 (ς is second order in u_1) which may have up to 4 real roots. $\sin^2\gamma$ is then given by

$$\sin^2\gamma = \frac{\vartheta}{\vartheta - \varsigma}. \tag{2.38}$$

As $\sin^2\gamma$ can't distinguish between the solutions $\{\pm\gamma, \pi \pm \gamma\}$, each u_1 solution has 4-fold ambiguities, observations of at least 3 modes of D^0 decay are needed to reduce these 16 possible ambiguities to 4.

2.5.3. Multi-body D decay with full Dalitz analysis

As the sensitivity of the γ measurement is severely limited by the available statistics, it is important to develop new methods that use as many modes as possible. Grossman *et al.* [32] developed the idea of using Non-CP eigenstate D decay modes that have singly Cabibbo-suppressed amplitudes for both D^0 and $\bar{D}^0$ decays. They suggested to use the decays $D \to K^{\pm}K^{*\mp}$ or $D \to \rho\pi$. The idea is that both D^0

and $\bar{D}^0$ decay into these final states with similar yet unequal amplitudes. In this way, the final states like $K^{\pm}K^{*\mp}$ serve as two separate states and provide enough observables to extract a solution for $\cos^2\gamma$. This requires that the branching ratios $Br(D^0 \rightarrow K^+K^{*-})$ and $Br(\bar{D}^0 \rightarrow K^+K^{*-})$ be known. Since both have the same final state, they interfere, it is hard to distinguish without a full D Dalitz plot analysis. Aware of this problem, Giri *et al.* [35] developed a new way to extract γ by a full D Dalitz plot analysis. This approach allows D decay mode with enough statistics, can be used to extract γ.

Similarly, for the decay of $D \rightarrow \pi^+\pi^-\pi^0$, there are two contributions, one from D^0 and another from $\bar{D}^0$, the amplitude of this decay to a point (s_{12}, s_{13}) in the Dalitz plot (see Fig. 2.5) is

$$\begin{aligned} A_D(s_{12}, s_{13}) &= A_{12,13}e^{i\delta_{12,13}} \\ &= A(D^0 \rightarrow \pi^0(p_1)\pi^+(p_2)\pi^-(p_3)) \\ &= A(\bar{D}^0 \rightarrow \pi^0(p_1)\pi^-(p_3)\pi^+(p_2)), \end{aligned} \tag{2.39}$$

where $s_{ij} = (p_i + p_j)^2$, and p_1, p_2, p_3 are the momenta of the π^0, π^+ and π^-, respectively. $A_{12,13}$ is defined to be real and positive, and δ takes any value between 0 and 2π.

The amplitude for $B^- \to D(\pi^+\pi^-\pi^0)K^-$ with spin $J = 0$ D final state is

$$
\begin{aligned}
A(B^- \to (\pi^+\pi^-\pi^0)_D K^-) &= A(B^- \to D^0 k^-)A(D^0 \to \pi^+\pi^-\pi^0) \\
&+ A(B^- \to \bar{D}^0 K^-)A(\bar{D}^0 \to \pi^+\pi^-\pi^0) \\
= A_B P_D(A_D(s_{12}, s_{13}) &+ r_B e^{i(\zeta_k-\gamma)} A_D(s_{13}, s_{12})), \qquad (2.40)
\end{aligned}
$$

where r_B is the ratio between $A(B^- \to \bar{D}^0 K^-)$ and $A(B^- \to D^0 K^-)$, $A_B = |A(B^- \to D^0 K^-)|$, P_D is the D meson propagator, which may very accurately be set to 1, given the narrow width of the D meson. The reduced partial decay width is

$$
\begin{aligned}
d\hat{\Gamma}(B^- \to (\pi^+\pi^-\pi^0)K^-) &= |A(B^- \to K^-(\pi^+\pi^-\pi^0)_D)|^2 dp \\
\propto \{A^2_{12,13} + r_B^2 A^2_{13,12} &+ 2r_B Re[A_D(s_{12}, s_{13})A^*_D(s_{13}, s_{12})e^{-i(\zeta_k-\gamma)}]\}dp, (2.41)
\end{aligned}
$$

where $A_{12,13} = |A_B A(s_{12}, s_{13})|$, dp is the phase space term, and the product of $A_D(s_{12}, s_{13})A^*_D(s_{13}, s_{12})$ is symmetric under the exchange $s_{12} \leftrightarrow s_{13}$ followed by a complex conjugation. The last term of Eqn. 2.41 can be written as

$$
\begin{aligned}
&Re[A_D(s_{12}, s_{13})A^*_D(s_{13}, s_{12})e^{-i(\zeta_k-\gamma)}] \\
&= A_{12,13}A_{13,12}[\cos(\delta_{12,13} - \delta_{13,12})\cos(\zeta_k - \gamma) \\
&+ \sin(\delta_{12,13} - \delta_{13,12})\sin(\zeta_k - \gamma)]. \qquad (2.42)
\end{aligned}
$$

Now, it is necessary to extract γ with Eqn. 2.41 and 2.42. The Dalitz plot is partitioned into n bins with identical division on both sides of the $s_{12} \leftrightarrow s_{13}$ symmetry axis. Define quantities integrated over the phase space of the jth bin:

$$\begin{aligned} c_j &= \int_j \mathrm{d}p A_{12,13} A_{13,12} \cos(\delta_{12,13} - \delta_{13,12}), & (2.43) \\ s_j &= \int_j \mathrm{d}p A_{12,13} A_{13,12} \sin(\delta_{12,13} - \delta_{13,12}), & (2.44) \\ T_j &= \int_j \mathrm{d}p A_{12,13}^2. & (2.45) \end{aligned}$$

The variables c_j and s_j contain the difference of strong phases and are unknown in the analysis, while T_j can be measured through flavor tagged D decays, which are achieved by using the charge of the soft pion in the decay $D^{*+} \rightarrow D^0\pi^+$. The c_j is unchanged with the exchange $s_{12} \leftrightarrow s_{13}$, while the s_j undergoes a sign flip. In a Daltiz plot with variables s_{12} and s_{13}, as the D decay is ρ-like decay, there must be a line which makes c_i symmetric and s_j anti-symmetric (see Fig. 2.5). Let us define this symmetry axis and consider a case of $n = 2k$ bins, the k bins on one side above the axis (denoted by the index j) and the remaining k bins lying under the axis (denoted by $\bar{j}$), so $c_{\bar{j}} = c_j$ and $s_{\bar{j}} = -s_j$, while there is no relation between T_j and $T_{\bar{j}}$. Considering these special bins j and $\bar{j}$, we can get the decay rates for bin j:

$$\begin{aligned} \hat{\Gamma}_j^- &= \int_j d\hat{\Gamma}(B^- \rightarrow (\pi^0\pi^+\pi^-)_D K^-) \\ &= T_j + r_B^2 T_{\bar{j}} + 2r_B[\cos(\zeta_k - \gamma)c_j + \sin(\zeta_k - \gamma)s_j], & (2.46) \end{aligned}$$

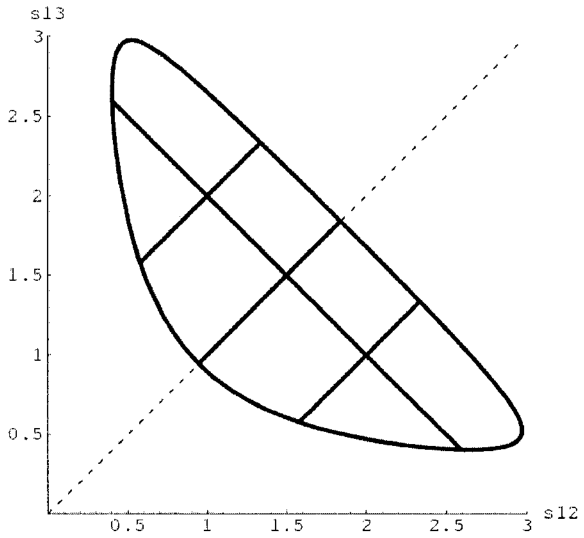

Figure 2.5: The partitions of the Dalitz plot as discussed in the text. The dashed line is the symmetry axis.

$$\begin{aligned}\hat{\Gamma}_{\bar{j}}^{-} &= \int_{\bar{j}} d\hat{\Gamma}(B^- \to (\pi^0\pi^+\pi^-)_D K^-) \\ &= T_{\bar{j}} + r_B^2 T_j + 2r_B[\cos(\zeta_k - \gamma)c_j - \sin(\zeta_k - \gamma)s_j], \qquad (2.47)\\ \hat{\Gamma}_{j}^{+} &= \int_{j} d\hat{\Gamma}(B^+ \to (\pi^0\pi^+\pi^-)_D K^+) \\ &= T_j + r_B^2 T_{\bar{j}} + 2r_B[\cos(\zeta_k + \gamma)c_j - \sin(\zeta_k + \gamma)s_j], \qquad (2.48)\\ \hat{\Gamma}_{\bar{j}}^{+} &= \int_{\bar{j}} d\hat{\Gamma}(B^+ \to (\pi^0\pi^+\pi^-)_D K^+) \\ &= T_{\bar{j}} + r_B^2 T_j + 2r_B[\cos(\zeta_k + \gamma)c_j + \sin(\zeta_k + \gamma)s_j], \qquad (2.49)\end{aligned}$$

From Eqn. 2.46 to 2.49, we can see that the five unknown variables are c_j, s_j, r_B, ζ_k and γ. Increasing one more bin only adds two more unknown variables: c_j and s_j, but four more equations like Eqn. 2.49. So there will be $4j$ equations and $2j+3$

unknown variables. If $4j >= 2j + 3$, all these unknown parameters can be solved. In other words, The determination of γ without hadronic uncertainties only needs a partition of the D meson Dalitz plot to four or more bins ($k >= 2$). In this method, γ is obtained with a 4-fold ambiguity.

Also, if using the properties of the symmetry axis and combining j and $\bar{j}$ into one bin j', then $s_{j'} = 0$, the $4j$ equations will reduce to $2j$ equation. To determine γ in this case requires $j' \geq 3$, and there is an 8-fold ambiguity.

As three-body D decays involve many resonances, $c_j = 0$ or $s_j = 0$ are not expected for all j. Therefore γ can be extracted even if $\zeta_k = 0$, if some of the c_j or s_j are measured independently at a charm factory.

If we know a functional dependence of both the moduli and the phases of the D^0 meson decay amplitudes $A_D(s_{12}, s_{13})$, there are only 3 unknown variables, r_B, δ_B, and γ, but this will introduce model dependence. As most of $D^0 \to \pi^+\pi^-\pi^0$ decay proceeds via ρ resonances [56], the decay amplitude can be fitted to a sum of Breit-Wigner functions plus a constant term:

$$\begin{aligned} A_D(s_{12}, s_{13}) &= A(D^0 \to \pi^0(p_1)\pi^+(p_2)\pi^-(p_3)) \\ &= a_0 e^{i\delta_0} + \sum_r a_r e^{i\delta_r} A_r(s_{12}, s_{13}), \end{aligned} \tag{2.50}$$

where the first term is the non-resonant term and the second is the resonant contributions. the Breit-Wigner function is

$$A_r(s_{12}, s_{13}) = M_r^J \times F_{BW}^r, \tag{2.51}$$

where r represents one resonance in any two of these three pions, M_r^J accounts for the angular distribution that depends on the spin J of the r resonance ($M_r^0 = 1$, $M_r^1 = -2\vec{p}_1 \cdot \vec{p}_3$, where $\vec{p}_1$, $\vec{p}_3$ are, respectively, the momentum of one of the particle from the r^{th} resonance and of the remaining particle.). F_{BW}^r is the relative Breit-Wigner function

$$F_{BW}^r(s) = \frac{1}{s - M_r^2 + iM_r\Gamma_r(\sqrt{s})}, \tag{2.52}$$

where M_r is the mass of the rth resonance and $\Gamma(\sqrt{s})$ is the mass dependent width, with s being the square of the invariant mass of the resonance.

2.5.4. Effect of D^0-$\bar{D}^0$ mixing on the measurement of γ

In the discussion of the methods used to extract γ, we neglect all the effects due to the mixing of D^0 and $\bar{D}^0$. In this section, only the final results will be given, the detail can be found in ref [37].

In general, the mixing in the $D^0 - \bar{D}^0$ system can be parameterized by two variables: $x_D = \Delta m_D/\Gamma_D$ and $y_D = \Delta\Gamma_D/(2\Gamma_D)$, where Δm_D is the difference between two mass eigenstate of the D, Γ_D is the average width of two D states, and $\Delta\Gamma_D$

is the difference between them. In the Standard Model, $x_D \sim y_D \sim 10^{-2}$ (upper bound). The effect on extraction of γ is proportional to x_D/r_B, y_D/r_B, x_D/r_D or y_D/r_D, which is expected to be at order of at most 10% for the expected value of $r_B \sim 0.1$ or $r_D \sim 0.1$. However, this effect can be eliminated by incorporating $D^0-\bar{D}^0$ mixing in the formalism, using mixing parameters measured in D decay.

2.5.5. Existing results on γ

With the ADS method, the *BABAR* collaboration uses the decay of $B^\pm \to D^0K^\pm$ with $D^0 \to K^\pm\pi^\mp$ to set the upper limit, $r_B = \frac{|A(B^-\to\bar{D}^0K^-)|}{|A(B^-\to D^0K^-)|} < 0.22$ (90% $C.L.$) [38], which is consistent with the value $r_B = 0.118^{+0.093}_{-0.092}$ given by *BABAR*'s full Dalitz plot anlysis of $B^- \to DK^-$ with $D \to K^0_S\pi^+\pi^-$ [39] and with the value $r_B = 0.26^{+0.11}_{-0.15}$ given by *Belle* [40].

Both *BABAR* and *Belle* conducted the full Dalitz analysis on $D^0 \to K^0_S\pi^+\pi^-$ from $B^\pm \to D^{(*)}K^\pm$, where $D^* \to D^0\gamma$ or $D^0\pi^0$ by using the method introduced in ref. [35]. For the weak phase γ, *Belle*'s result [40]: $\gamma = (77^{+17}_{-19}(stat.) \pm 13(syst.) \pm 11(model))^\circ$, the corresponding two standard deviation interval is $26^\circ < \gamma < 126^\circ$; *BABAR*'s result [39] is $\gamma = (70 \pm 31(stat)^{+12}_{-10}(syst.)^{+14}_{-11}(model))^\circ$, the two standard deviation interval is $12^\circ < \gamma < 137^\circ$.

Chapter 3

BABAR Detector

The primary motivation for the *BABAR* experiment is to study CP asymmetries in the decays of neutral B mesons [15]. If the Standard Model holds, a large asymmetric effect is expected in B meson decays and many different B decay modes can be used. Besides the CP study, *BABAR* also can be used to precisely determine the value of the CKM matrix elements and search for rare B decay processes when a high integrated luminosity is available.

The *BABAR* detector is located at one of the intersection regions of the PEP-II B Factory, which is an asymmetric e^+e^- energy collider designed to operate at a center-of-mass energy of 10.58 GeV, the mass of $\Upsilon(4S)$ resonance. The data collected on the $\Upsilon(4S)$ resonance is called the on-peak data, while the data collected about 40 MeV below the resonance peak is called the off-peak data. The 9.0 GeV e^- beam collides head-on with the 3.1 GeV e^+ beam at an interaction point (IP) inside *BABAR* detector.

The asymmetric beam energy results in a Lorentz boost to the $\Upsilon(4S)$ resonance of $\beta\gamma = 0.56$. This enables the decay times of the B mesons to be inferred from their measurable decay lengths, thus to measure the time dependence of their decay rates.

3.1. Electron and positron storage rings

A schematic representation of the PEP-II storage ring is shown in Figure 3.1. An electron gun is used to create two bunches of electrons that are accelerated to about 1 GeV before entering one of the damping rings, whose purpose is to reduce the dispersion of beams. These electrons are accelerated in the linac and one of the bunches is diverted to collide with a tungsten target to create a position beam, which in turn passes through the damping ring and is accelerated in the linac. At the end of the linac, they are fed into the PEP-II storage rings. There these two beams collide at IP head-on.

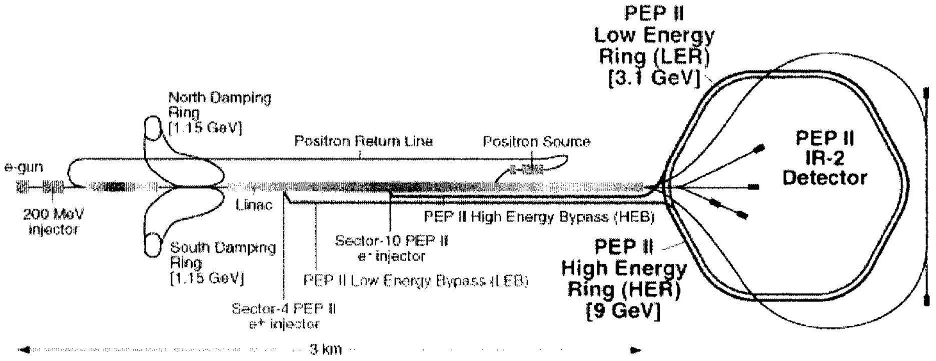

Figure 3.1: The schematic view of PEP-II.

The design luminosity is 3×10^{33} cm^{-2}s^{-1}, now the peak luminosity is above 8×10^{33} cm^{-2}s^{-1}, with a high (low) energy ring current 1.3A (2.2A), and 1034 bunches. Some parameters of these energy asymmetric storage rings are summarized in Table 3.1.

Table 3.1: PEP-II beam parameters.

Parameters	Design	Typical
Energy HER/LER(GeV)	9.0/3.1	9.0/3.1
Current HER/LER(A)	0.75/2.15	1.3/2.2
# of bunches	1658	1034
Bunching spacing (ns)	4.2	6.3-10.5
σ_{L_x} (μm)	110	120
σ_{L_y} (μm)	3.3	5.6
σ_{L_z} (μm)	9	9

3.2. Interaction region

Figure 3.2 shows the IR layout. The bunches collide head-on and are separated magnetically in the horizontal plane by a pair of dipole magnets (B1), followed by a series of offset quadrupoles, which are used to focus the beam. The collision axis is off-set from z-axis of the *BABAR* detector by about 20 mrad in the horizontal plane to minimize the perturbation of the beams by the solenoidal field.

The interaction region is enclosed by a double-layer beryllium beam pipe of about 2.8 cm outer radius. The pipe is cooled by water flowing between these two layers.

The beam pipe, some focusing magnets and the silicon vertex detector (SVT) were

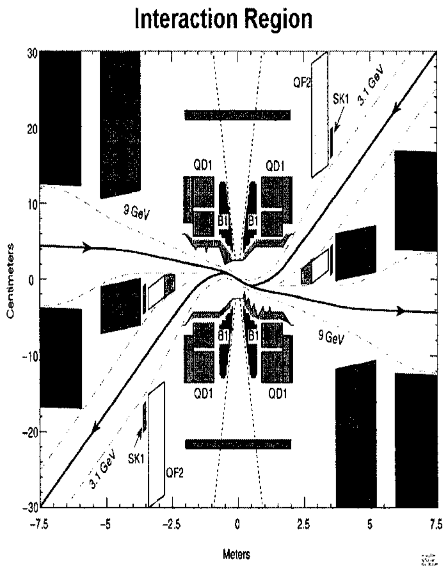

Figure 3.2: The interaction region, X and Y axes are with different scales.

assembled and aligned as one unit, and enclosed in a 4.5 m long support tube that spans the IP.

3.3. Detector overview

The *BABAR* detector was designed and built by a large international team of scientists and engineers including members of the high energy physics group at Colorado State University. Figure 3.3 shows a longitudinal section through the detector center. The detector surrounds the PEP-II interaction region. To maximize the geometric acceptance for the boosted $\Upsilon(4S)$ decays, the whole detector is offset relative to the beam-beam IP by 0.37 m in the direction of the lower energy beam.

The inner detector consists of a silicon vertex tracker, a drift chamber, a ring-

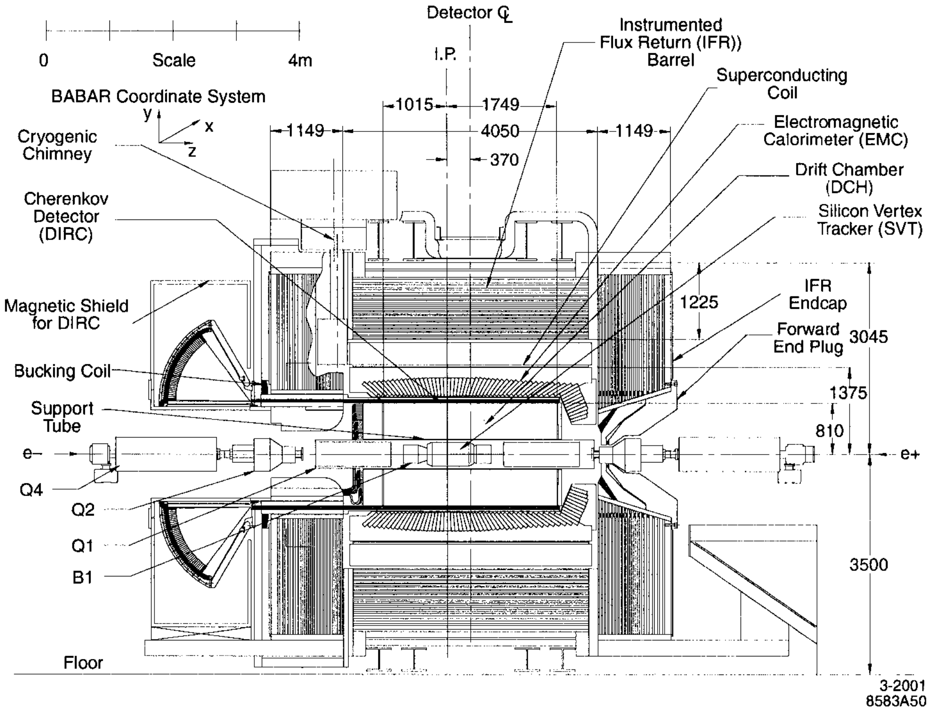

Figure 3.3: *BABAR* detector longitudinal section (dimension in mm).

imaging Cherenkov detector, and a CsI (cesium iodide) calorimeter. These detectors are surrounded by a superconducting solenoid that is designed to produce a field of 1.5 T in the central region of the apparatus. the steel magnetic flux return is instrumented for muon and neutral hadron detection. The detector polar angle acceptance is $17^o < \theta_{lab} < 150^o$ in the laboratory frame ($-0.95 < \cos\theta_{CM} < 0.87$ in the center mass frame).

The charged particle tracking system is made of two components, the silicon vertex tracker (SVT) and the drift chamber (DCH). The SVT has been designed to measure angles and positions of the charged particles precisely just outside the beam pipe.

The role of the DCH is to measure the momentum of the charged particles and also supplies information for the charged particle trigger and particle identification.

The DIRC, the Detector of Internally Reflected Cherenkov light [67], is a novel particle identification device providing powerful separation of pions and kaons from about 500 MeV/c to the kinematic limit of 4.5 GeV/c.

The electromagnetic calorimeter (EMC) is designed to detect electromagnetic showers, associated with incident electrons, positions, and photons, with excellent energy and angular resolution over the energy range from 20 MeV to 4 GeV. This coverage allows the detection of low energy π^0s and ηs from B decays and higher energy photons and electrons from electromagnetic, weak, and radiative process.

The instrumented flux return (IFR) is designed to identify muons and to detect neutral hadrons.

In the following sections, we provide a short description of the major detector sub-systems. The details can be found in Ref. [16].

3.4. Silicon vertex tracker

The SVT is composed of five layers of double-sided silicon strip detectors that are assembled from modules with readout at each end (see Fig. 3.4). The inner three layers primarily provide position and angle information for the measurement of the vertex position. This is critical for the measurement of the time-dependent

CP asymmetry. They are mounted as close to water-cooled beryllium beam pipe as practical. The outer two layers are at a bigger radii, providing coordinate and angle measurements needed for linking SVT and DCH tracks and for pattern recognition.

For a full reconstructed B decay, the mean vertex resolution along z-axis is better than 80 μm, in the x-y plane, it is about 100 μm. For the analysis $B^- \to DK^-$, the variable Δz is used, which is the distance between the vertex point of the signal B meson and the vertex point of the rest of the event.

The SVT can provide standalone tracking for particles that cannot reach the central tracking device (DCH), *i.e.* a particle with transverse momentum p_t less than 120 MeV/c .

As the SVT is the closest device to the beam pipe, the tolerance of ionizing radiation is critical for long term operation; it must withstand 2 Mrad dose life time. Also due to the inaccessibility during the normal operation, a high level of reliability and robustness are essential.

The SVT has a combined hardware and software reconstruction efficiency of 97%, calculated for each half-module by comparing the number of associated hits to the number of tracks crossing the active area of the module. This number excludes the defective readout sections (9 out of 208).

The double-sided sensor provides up to ten measurement of dE/dx per track. The SVT provides a 2σ separation between the kaons and pions up to momentum of 500

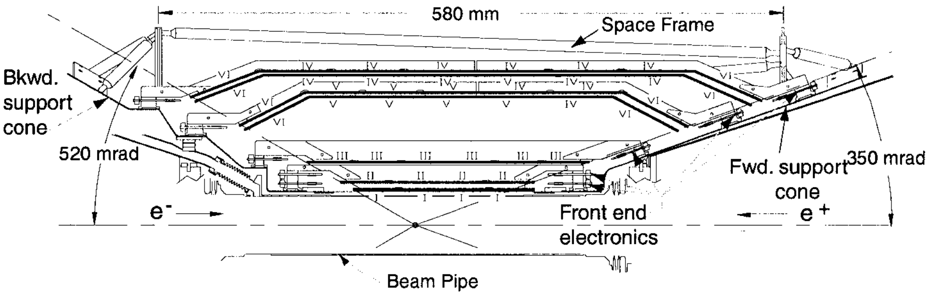

Figure 3.4: Schematic view of SVT: longitudinal section.

MeV/c, and between kaons and protons beyond 1 GeV/c.

3.5. Drift chamber

The DCH is a 276.4 cm long concentric cylinders with a relative small diameter (inner radius is 23.6 cm and outer radius is 80.9 cm). A longitudinal cross-section and dimensions of the DCH are shown in Fig 3.5. It is asymmetrically located with respect to the IP, the forward-backward coverage is $-1.01 < z < 1.75$ m along the z axis. It is full of a gas mixture of helium and isobutane at one atmospher and operated at high voltage.

It has 40 layers of small hexagonal cells. Each drift cell contains one gold-plated tungsten-rhenium sense wire surrounded by six gold-plated aluminum field wires (see Fig. 3.6). 1900-1960 V high voltage is applied on the sense wire, while the field wire is grounded. An avalanche gain of approximately 5×10^4 is obtained at an operation

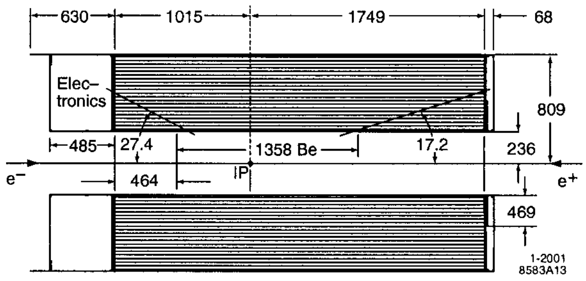

Figure 3.5: Longitudinal section of the DCH with principal dimensions.

voltage of 1600 V and a 80:20 helium:isobutane gas mixture.

Two guard wires are added at the inner or outer boundary of a superlayer to improve the electrostatic performance of the cell and to match the gain of boundary cells to those of cells in the inner layers. At the innermost boundary of layer 1 and the outmost layer 40, two clearing wires have been added per cell to collect charges created through photon conversion in the material of walls.

The DCH provides up to 40 spatial and ionization loss measurements for charged particles with $p_t > 180$ MeV. The ionization energy loss dE/dx is obtained from the measurement of total charge deposited in each drift cell and for a single track the energy loss is computed as a truncated mean from the lowest 80% of the individual dE/dx measurement. Fig 3.7 shows the distribution of dE/dx measurements as a function of track momenta after all corrections. The resolution for dE/dx is about 7.5%.This dE/dx measurement of ionization loss provides useful particle identification.

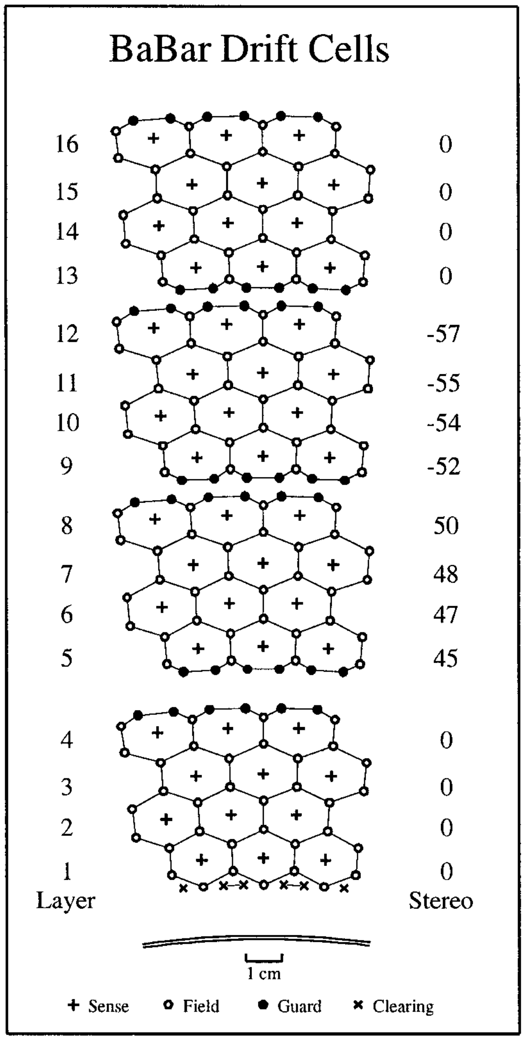

Figure 3.6: Schematic layout of the drift cells for the four innermost superlayers.

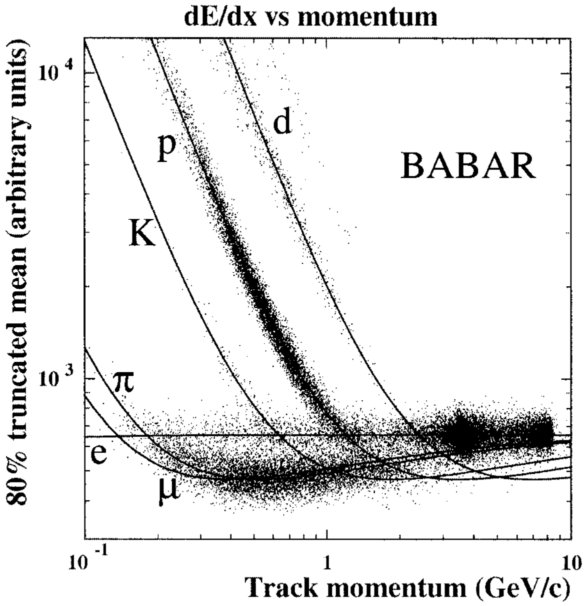

Figure 3.7: Measurement of dE/dx in the DCH as a function of track momenta. The curves show the Bethe-Bloch predictions.

For the spatial measurements, they help to complement the measurements of vertex for the decay and interaction outside of the SVT volume.

The DCH tracking efficiency is determined as the ratio of the number of reconstructed DCH tracks to the number of tracks detected in the SVT within the acceptance of the DCH. Fig 3.8 shows the track reconstruction efficiency as a function of transverse momentum and polar angle. At the operating voltage of 1960 V the efficiency averages $98 \pm 1\%$ per track above 200 MeV/c and polar angle $\theta > 500$ mrad.

For transverse momentum measurement, the resolution can be obtained from a

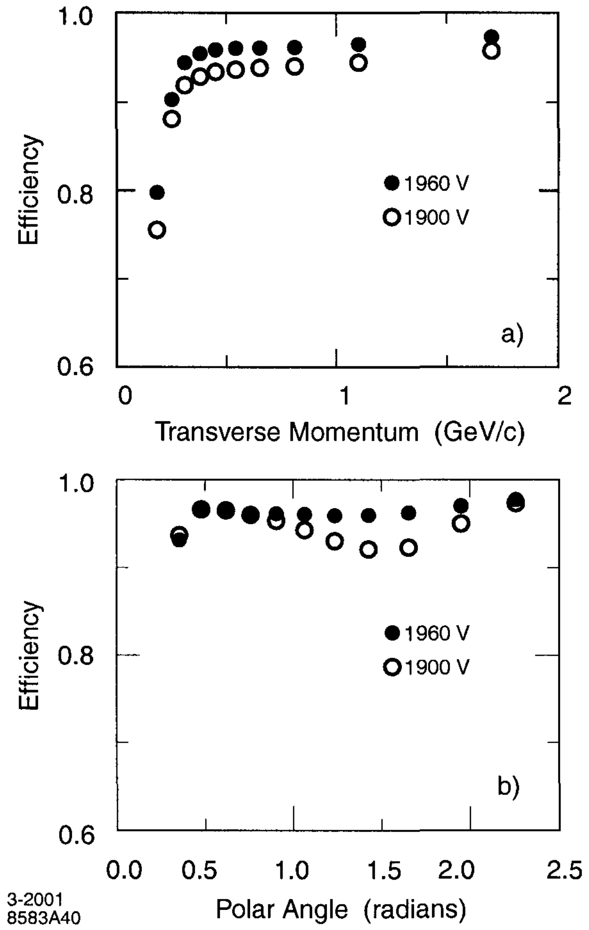

Figure 3.8: The track reconstruction efficiency in the DCH at operating voltage 1900 and 1960 V for multi-hadron events, as function of (a) transverse momentum, and (b) polar angle.

linear function (Fig 3.9)

$$\sigma_{p_t}/p_t = (0.13 \pm 0.01)\% \bullet p_t + (0.45 \pm 0.03)\% . \qquad (3.1)$$

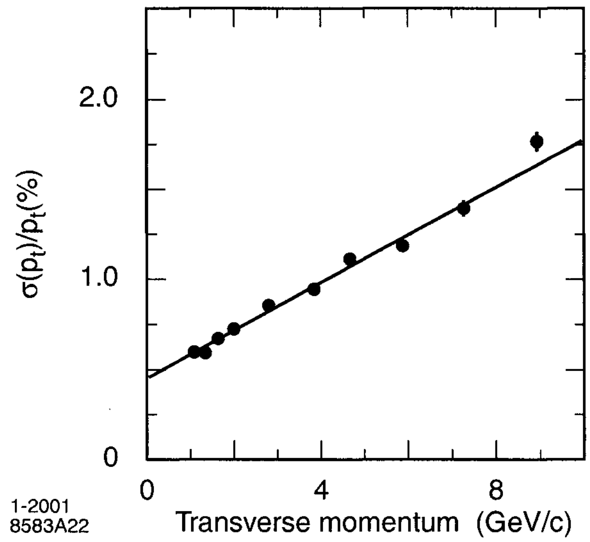

Figure 3.9: Resolution in the transverse momentum p_t determined from cosmic ray muons transversing the DCH and SVT.

3.6. Detector of internally reflected Cherenkov light

DIRC is the acronym for Detector of Internally Reflected Cherenkov light. It is a subtype of Ring Imaging Cherenkov counter, which uses the Cherenkov light cone from a radiator to deduce the velocity of a charge particle [67]. With this property and combined with the high precision momentum measurement of DCH, the mass of the particle can be obtained.

As shown in Fig 3.10, this sub-system is a 12-sided polygon around PEP-II interaction region with a total 144 long fused silica bars ($1.7 \times 3.5 \times 490$ cm^3). These bars are coupled to a $\sim 11,000$ photomultiplier tubes (PMTs) array through a 120 cm standoff region filled with purified water in the backward side.

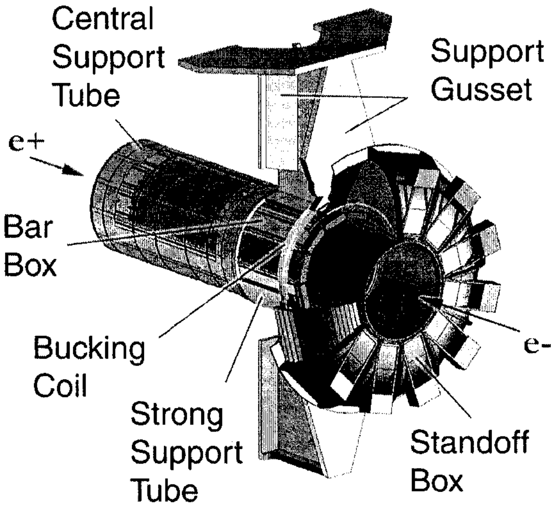

Figure 3.10: Exploded view of the DIRC.

Figure 3.11 shows the principle of light production, transport, and imaging of the DIRC and geometry with a single bar. The bar is assembled from four 1.225 m pieces that are glued end-to-end, and has a fused silica wedge glued to it at the readout end and mirror attached at the forward end. The PMTs at the rear of the standoff box (SOB) lie on a surface is approximately toroidal. They are grouped into 12 sector associated with these 12 bar box. Each sector contains 896 PMTs, in a closely packed array inside the water volume.

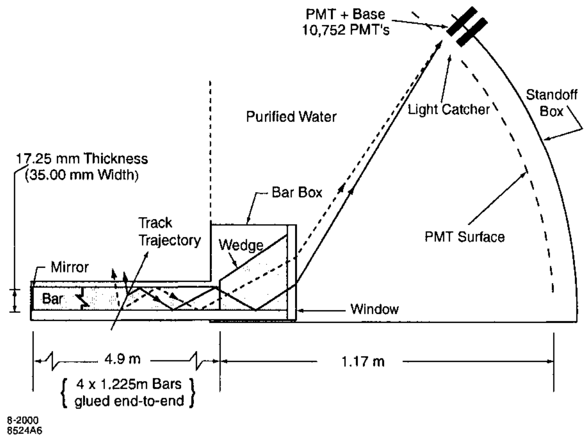

Figure 3.11: Schematics of the DIRC fused silica radiator bar and imaging region.

The DIRC is intrinsically a three-dimensional imaging device: the position (two cherenkov emission angles, θ_c, ϕ_c) and arrival time of the PMT signals. This redundancy is extremely useful to reject backgrounds and ambiguities, and perhaps put constraints on the Cherenkov angle measurement.

The single photon angular resolution ($\sigma_{C,\gamma}$) obtained from di-muon event is about 10.2 mrad. The track Cherenlov angle resolution can be scaled as $\sigma_{\mathrm{C,track}} = \sigma_{\mathrm{C},\gamma}/\sqrt{N_{\mathrm{pe}}}$, where N_{pe} is the number of photons detected. For a $\beta(v/c) = 1$ particle entering normal to the surface at the center of the bar, N_{pe} is about 28.

Fig 3.12 shows the kaon selection efficiency and pion misidentification as a function of track momentum from a particle selection criteria based on DIRC information.

The DIRC provide up to 4σ separation between pion and kaon with momentum range from 700 MeV/c to 4.2 GeV/c. This is very important to clean the background

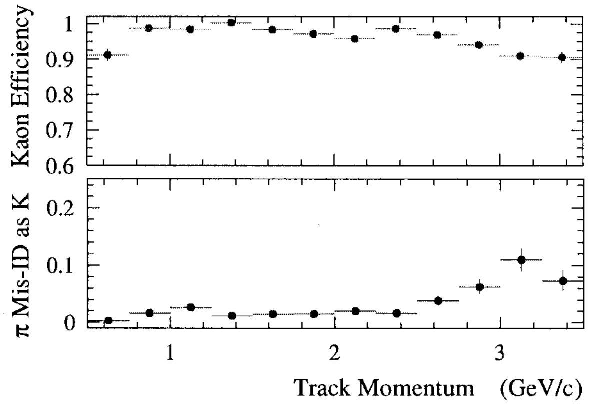

Figure 3.12: Efficiency and misidentification probability for the selection of charged kaons as a function of track momentum, determined using $D^o \rightarrow K^-\pi^+$ decays selected kinematically from inclusive D^* production.

for the charged kaon from the charged pion.

3.7. Electromagnetic calorimeter

The electromagnetic calorimeter (EMC) used by *BABAR* detector is a hermetic, total-absorption calorimeter. It was composed of a finely array of 6580 pieces of thalium-doped cesium idiode (CsI(Tl)) crystals. These crystals have short radiation length, high light yield and small *Moliére* radius. This sub-system has excellent energy and angular resolution and is compact.

Pattern recognition algorithms are used in EMC to identify a shower whether it is caused by a neutral or charged particle. It is capable to detection of photons, which are from π^0 and η decays as well as electromagnetic and radiative processes, and electrons.

EMC consists of a cylindrical barrel and conical forward endcap. The barrel has 48 distinct rings and the endcap holds eight rings (see Fig. 3.13).

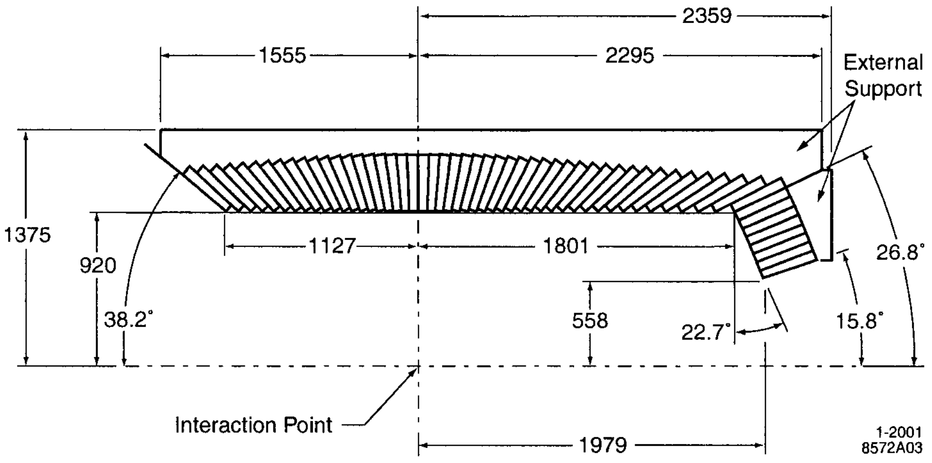

Figure 3.13: A longitudinal cross-section of the EMC (top half). All dimensions are given in mm.

The EMC has 90% solid angle coverage in the *c.m.* system with full coverage in azimuth and from 15.8° to 141.8° in polar angle.

The EMC in *BABAR* detector has a good performance in the energy range from 20 MeV to 9 GeV. At low energy the resolution (σ_E/E) is $5.0 \pm 0.8\%$ at 6.13 MeV (measured from radioactive source). At high energy, the resolution is $1.9 \pm 0.07\%$ at 7.5 GeV (measured from Bhabha scattering). The resolution as a function of energy is:

$$\sigma_E/E = (2.32 \pm 0.03)\%/\sqrt[4]{E} \bigoplus (1.85 \pm 0.12) \tag{3.2}$$

Fig 3.14 shows the angular resolution as function of photon energy. It is based on the analysis of π^0 and η decays to two photons of approximately equal energy. The resolution can be parameterized as

$$\sigma_\theta = \sigma_\phi = (3.87 \pm 0.07/\sqrt{E} + 0.00 \pm 0.04) \text{ mrad} \tag{3.3}$$

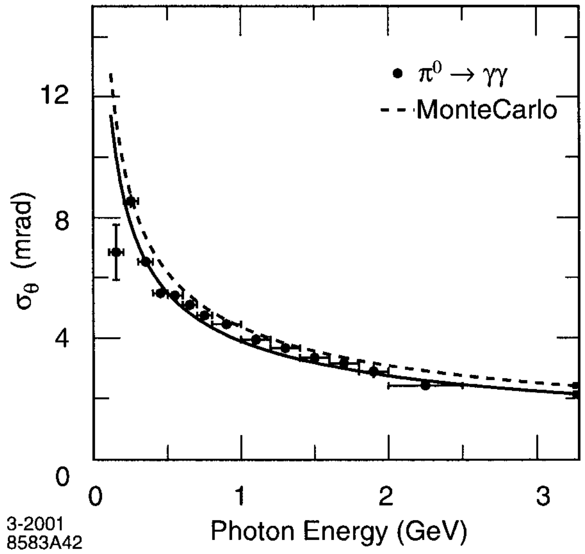

Figure 3.14: The angular resolution of the EMC for photons from π^0 decay.

3.8. Instrumented flux return

The main purpose of this sub-system is to identify muons with high purity and neutral hadrons with wide momentum range.

The IFR uses the steel flux return of the magnet as muon filter and hadron absorber. Single gap resistive plate chambers (RPCs) with two coordinate readout are used as detectors. They are operated in limited streamers and the signals are read out capacitively.

Fig 3.15 shows overview of the IFR. It consists of a barrel and two end doors. 19 RPC layers are in the barrel, 18 are in the endcaps. Two more layers of cylindrical RPCs are between EMC and magnet cryostat. The total active area is about 2000 m^2

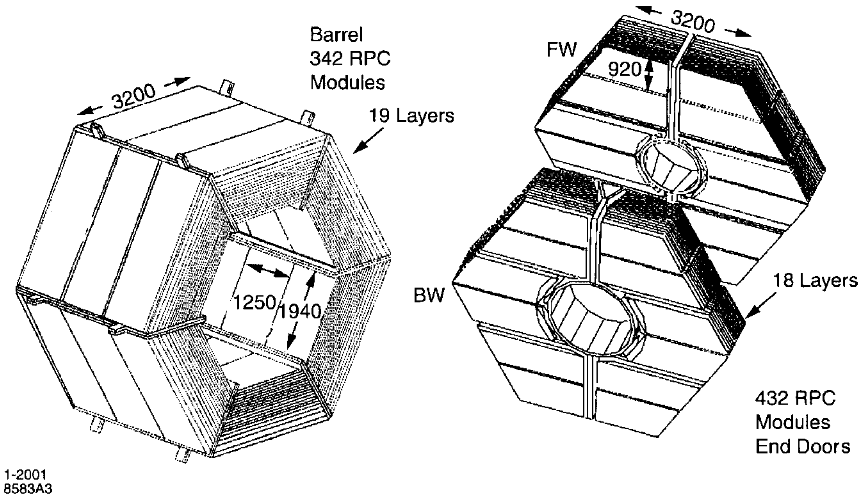

Figure 3.15: Overview of the IFR: Barrel sectors and forward and backward end doors; the shape of the RPC modules and their dimensions are indicated.

In the momentum range of $1.5 < p < 3.0$ GeV/c, the efficiency of detecting of a muon is close to 90% with $6 - 8\%$ pion misidentification (Fig 3.16).

This sub-detector plays a specific role in the reconstruction of J/ψ with $J/\psi \to \mu^+\mu^-$.

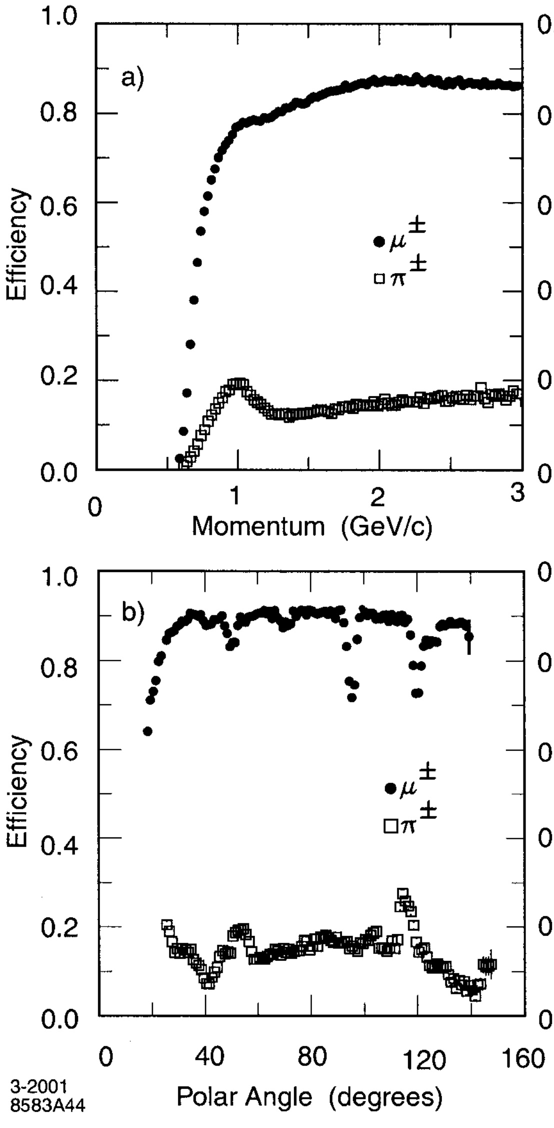

Figure 3.16: Muon efficiency (left scale) and pion misidentification probability (right scale) as a function of (a) the laboratory track momentum, and (b) the polar angle (for $1.5 < p < 3.0$ GeV/c momentum), obtained with loose selection criteria.

Chapter 4

Analysis Methods

Two analysis methods are introduced, a cut and counting method and a maximum likelihood fit method. The first of these methods is straightforward to implement and understand, the second is significantly more complicated but gives a better sensitivity for low signal, high background analysis. In this chapter, we also included some general terminologies to help establish the concepts needed in the following chapters.

4.1. General terminology

4.1.1. Event thrust angle

The thrust axis of an event, $\hat{T}$, is defined to be the direction that maximizes thrust

$$T = \frac{\sum_i |\hat{T} \cdot \vec{p_i}|}{\sum_i |\vec{p_i}|}. \tag{4.1}$$

where p_i is the longitudinal momentum of the i^{th} particle [17]. The allowed range for T is [0.5 1.0].

The thrust angle θ_T is defined as the angle between the thrust axis of a reconstructed B and the thrust axis of the rest of event. For signal-type events, the distribution of $|\cos\theta_T|$ is flat, while for continuum events the distribution is more piled up near 1. Fig. 4.1 shows the distribution of $|cos\theta_T|$ from the decay of $B^0 \to J/\psi\eta K^0_S$.

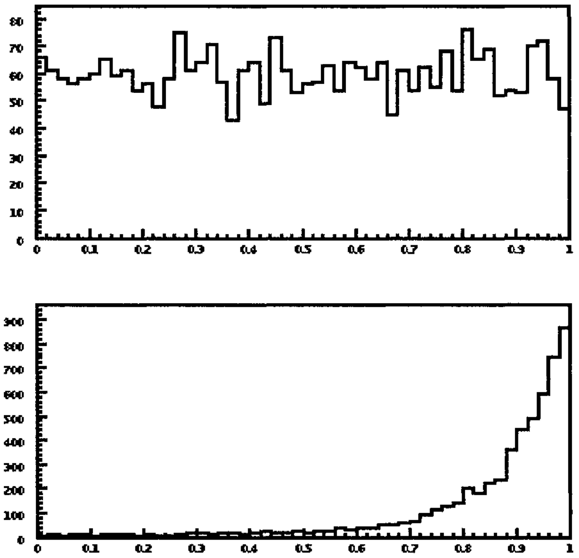

Figure 4.1: Distribution of $|\cos\theta_T|$ for $B^0 \to J/\psi\eta K^0_S$, the top plot is for signal Monte Carlo, the bottom plot is for continuum Monte Carlo.

4.1.2. Helicity angle

Generally, helicity angle is used as a discriminant in two-body decays. For example, a decay chain of $X \to Y + \cdots$, $Y \to a + b$. The helicity angle θ_H of particle a is defined as the angle between the direction of itself and the direction of grandparent particle X in the rest frame of the parent particle Y. The shape of $\cos\theta_H$ is dependent on angular momentum of particle Y, a and b. Fig. 4.2 shows the cosine distribution of the helicity angle between the direction of photon and the direction of B^0 in the rest frame of η. In this case, the distribution of signal Monte Carlo is flat, however it peaks near ±1 for continuum Monte Carlo.

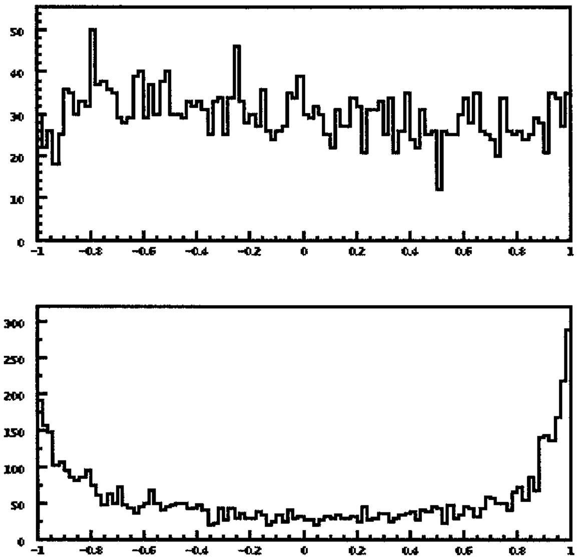

Figure 4.2: Distribution of $\cos\theta_\eta^\gamma$ in the decay $B^0 \rightarrow J/\psi\eta K_S^0$, the helicity angle θ_η^γ between the direction of photon and the direction of B^0 in the rest frame of η. The top plot is for signal Monte Carlo, the bottom plot is for continuum Monte Carlo.

4.1.3. Fox-Wolfram moments

These moments are mainly used to distinguish continuum and $B\bar{B}$ events. Continuum events are more like jet like, while $B\bar{B}$ events are more spherical. The l-th

Fox-Wolfram moment [41] is defined by the charged tracks as

$$H_l = \sum_{ij} \frac{|\vec{p_i}||\vec{p_j}|}{s} P_l(\cos\phi_{ij}) \tag{4.2}$$

here $\vec{p_i}$, $\vec{p_j}$ is the momenta of the i^{th} and the j^{th} in the event and ϕ_{ij} is the angle between them. $P_l \cos\phi_{ij}$ is the Legendre polynomial and $\sqrt{s}$ is the center-of-mass energy. The ratio of the second order to the zeroth order of Fox-Wolfram moments, used frequently in the B decay analyses, is defined as

$$R_2 = \frac{H_2}{H_0} \tag{4.3}$$

4.1.4. Fisher discriminant

Fisher discriminant uses a linear function to maximally distinguish two populations or categories based on the same quality measurements [42].

Let two populations have k measurable characteristics: $x_1^{1,2}$, $x_2^{1,2}$, $\cdots$, $x_k^{1,2}$ and linear function, $X^{1,2} = \sum_i \lambda_i x_i^{1,2}$, λ_i is the coefficient. Define $D = \sum_i \lambda_i d_i$, where $d_i = x_i^1 - x_i^2$, $S^j = \sum_p \sum_q \lambda_p \lambda_q (< x_p^j x_q^j > - \bar{x}_q^j \bar{x}_p^j), j = 1, 2$. The particular linear function, X, which best discriminates the two populations will be one for which the ratio of D^2/S is greatest, by variation of the coefficients, λ_i. The coefficient can be found

$$\lambda_i = \sum_{j=1}^{k} (U_{ji}^1 + U_{ji}^2)^{-1} \times (\bar{x}_i^2 - \bar{x}_i^1), \tag{4.4}$$

where $U_{ij}^{1,2}$ and $\bar{x}_i^{1,2}$ are the covariant matrices and average value for population 1(2) input variables vector $x^{1,2}$ and $x_i^{1,2}$, respectively.

In the $B \to DK$ analysis, we use four measurable quantities

1. $|\cos\theta_C|$, the unsigned cosine of the angle between the chosen B candidate thrust axis and the beam axis(z),
2. $|\cos\theta_T|$, the unsigned cosine of the thrust angle,
3. 0^{th} (L_0) and 2^{nd} (L_2) oder of Legendre moments, which are

$$\begin{aligned} L_0 &= \sum_{i_{track}} \sum_{n=0} P_n(\cos\theta_{i_{track}}), \\ L_2 &= \sum_{i_{track}} \sum_{n=0} P_n(\cos\theta_{i_{track}}) p_{i_{track}}^2. \end{aligned} \tag{4.5}$$

From these measurable quantities, we generate the Legendre-based Fisher discriminant function:

$$F_{LGD} = 0.367 \times (1.60287|\cos\theta_C| + 1.89495|\cos\theta_T| + 0.66531 L_0 + 2.6685 L_2) - 1.3. \tag{4.6}$$

4.1.5. Vertexing

Vertexing is the process of finding the best estimate of the three-dimensional point of intersection of a number of tracks. In this subsection, general principle of vertexing is described, the details can be found in ref. [43].

A vertex usually is reconstructed by minimizing the sum of the squares of the distance of closest approach of a set of tracks to a point. *BABAR* takes a track in a magnetic field as a helix and uses kinematic fitting – a process of using kinematic constraints, such as masses, and energy and momentum conservation, to improve the knowledge of an event – to find a vertex.

Definition of the distance of Δz between two Bs

In the $B^- \to D^0 K^-$ analysis, we used the variable of Δz, which is the distance difference in z direction between one full reconstructed B (signal B) and the other B. The full reconstructed B meson is kinematically reconstructed and the decay vertex position can be measured using all the particles of the decay chain. The other B vertex is reconstructed with the remaining charged tracks in the event. By convention, Δz is defined as

$$\Delta z = z_{sig} - z_{other}, \tag{4.7}$$

where z_{sig} (z_{other}) is the coordinate of signal B (other B) in z-axis of laboratory system.

4.1.6. B flavor tagging

The purpose of b quark flavor tagging is to identify whether the decay product from B^0 or $\bar{B}^0$, by using the correlation between the charge of the b quark and signed characteristics of the decay products. Leptons and kaons are the main sources for B flavor tagging in *BABAR*. Here only the basic principle and lepton tagging are introduced. The details can be found in Ref. [44].

Fig. 4.3 shows correlation between the charge of the b quark and the charge of the lepton from a semi-leptonic decay of the B meson. If the lepton stems from a semi-leptonic decay of the B meson (see Fig. 4.3a), the sign of the charge of the lepton is identical to the sign of the b quark. A lepton may originate from a cascade, in which case the sign of its charge may be opposite to the sign of the b quark (see Fig. 4.3b) or may be have the same sign as the b quark (see Fig. 4.3c). In this example, the distinction between the two cascade leptons and a direct lepton lies in the momentum in the rest frame of $\Upsilon(4S)$. The momentum spectrum of the direct lepton is harder than the spectrum of the lepton from a cascade decays. The final value are based on the probability.

4.1.7. Particle identification

Most of the final decay products of a compound particle, like B meson, D meson and J/ψ meson, are some detectable relatively long-lived charged particle such as

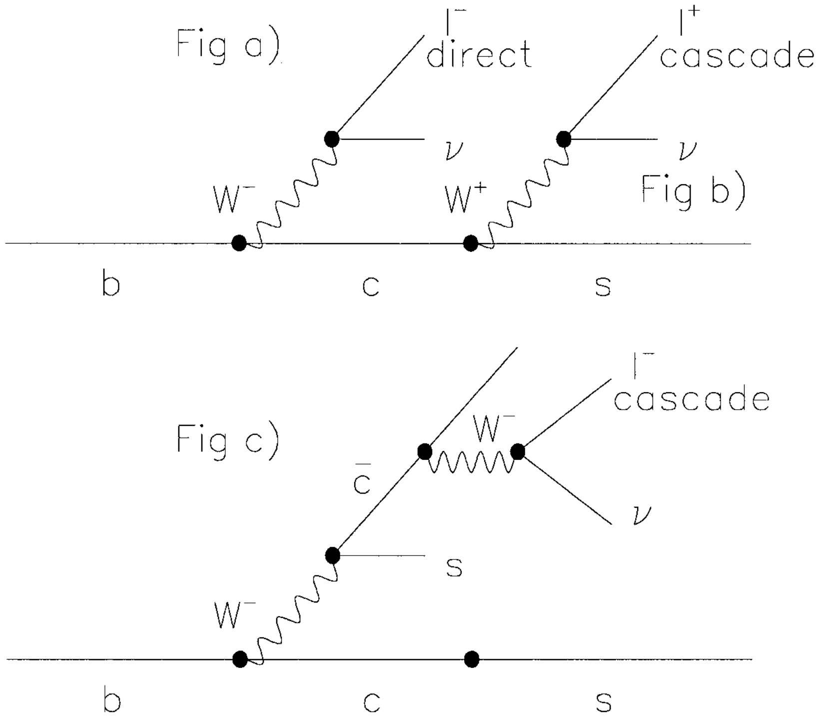

Figure 4.3: (a) Direct production of a lepton. (b) Cascade production of a lepton with a reversed sign. (c) Cascade production of a lepton with direct sign.

kaon, pion, electron, muon and proton, and neutral particles like photon. Exclusively reconstruction of an initial or an intermediate state out of these particles benefits from good particle identification with good efficiency within the fiducial detector volume (for charged tracks, the polar angle $20.6^o < \theta_{lab} < 135.9^o$).

Electron

Here a cut-based electron identification is introduced [45]. This identification is base on the information from subdetectors of EMC, DIRC, and energy loss measurements dE/dx from the tracking devices. Different criteria from subdetectors forms different cut selectors. Tab. 4.1 shows the cut selectors and their efficiencies. There are five selectors, denoted as *NoCal, VeryLoose, Loose, Tight* and *VeryTight.* The numbers in parentheses are for a range.

Selector	E/p	LAT	A_{42}	N_{cry}	ϕ	$N_\gamma > 9$	dE/dx	efficiency
NoCal	-	-	-	-	-	-	(540, 860)	-
VeryLoose	(0.50, 5.0)	(-10.0,10.0)	(-10.0,10.0)	3	no	no	(500,1000)	>97%
Loose	(0.65,5.0)	(-10.0,10.0)	(-10.0,10.0)	3	no	no	(500,1000)	>97%
Tight	(0.75,1.3)	(0.0,0.6)	(-10.0,10.0)	3	no	no	(500,1000)	95%
VeryTight	(0.89,1.2)	(0.0,0.6)	(-10.0,0.11)	3	yes	yes	(540,860)	88%

Table 4.1: The selectors and efficiencies of the cut based electron identification. Column headings are defined in the text.

The details of the criteria from the subdetectors are listed as following.

1. the ratio E/p of the measured energy E of a shower deposited in EMC crystals and measured momentum p of the corresponding charged track. For electrons and positrons, E/p is centered at 1 with a width of $0.02 \sim 0.03$ after calibration, while for other charged particles, E/p is centered far below 1 with a long tail.

2. Lateral shower shape (LAT). This shape will compensate E/p for those hadrons that have hadronic showers. The shape (LAT) is defined as [46]

$$LAT = \frac{\sum_{i=3}^{N} E_i r_i^2 + E_1 r_0^2 + E_2 r_0^2}{\sum_{i=4}^{N} E_i r_i}, E_1 > E_2 > \cdots > E_N, \tag{4.8}$$

here r^0 is the average distance between two neighbor crystals front-face (about

5 cm for *BABAR* calorimeter), r_i is the distance between i^{th} crystal and the shower center. In general, LAT for electrons is smaller than LAT for hadrons that shower.

3. Zernike-Moment A42. The Zernike-moment [47], is a polynomial function of ratio of r_i and corresponding polar angle ϕ_i. It is used to describe the shape variation of the EMC shower. For hadronic shower, A42 is more irregular compare to the one caused by electron shower.
4. N_{cry}, number of EMC crystals associated with a shower.
5. DIRC photon number (N_γ) for a charged track.
6. the average range of DCH dE/dx value (generally dE/dx has a Gaussian distribution that peaks at about 650 with a width about 50, with arbitrary unit)
7. ϕ_i, it is the polar angle for the shape of EMC shower.

To reconstruct the intermediate state J/ψ in the decay $B \rightarrow J/\psi\eta K$, both electron and positron from J/ψ are required to have a "Tight" selector.

Muon identification

Here also a cut-based muon identification is used [48]. *BABAR* uses the IFR and EMC system to identify muons and reject pions. Table. 4.2 shows the muon cut selectors and their efficiencies.

Selector	E_{cal}	N_L	$\Delta\lambda$	λ	χ^2_{trk}	χ^2_{fit}	T_c	$\bar{m}$	σ_m	efficiency
MIP	< 0.5	-	-	-	-	-	-	-	-	100%
VeryLoose	< 0.5	≥ 2	< 2.5	> 2	-	-	> 0.1	< 10	< 6	92%
Loose	< 0.5	≥ 2	< 2	> 2	< 7	< 4	$> .2$	< 10	< 6	86%
Tight	(0.05,0.4)	≥ 2	< 1	> 2.2	< 5	< 3	> 0.3	< 8	< 4	70%
VeryTight	(0.05,0.4)	≥ 2	< 0.8	> 2.2	< 5	< 3	> 0.34	< 8	< 4	67%

Table 4.2: The criteria for cut-based muon identification and efficiency, MIP stands for minimum ionizing particle.

The detailed variables associated with Tab. 4.2 are

1. E_{cal}, the total energy deposited in the showered EMC crystals for a muon.
2. N_L, the number of hit layers in IFR for a cluster.
3. λ, the number of interaction lengths traversed in *BABAR*.
4. $\Delta\lambda$, the difference between λ and the expected number of interaction lengths traversed in *BABAR*.
5. χ^2_{trk}, the $\chi^2/d.o.f$ of the IFR hit strips in the cluster with the track extrapolation fit.
6. χ^2_{fit}, the $\chi^2/d.o.f.$ of the IFR hit strips with a three order polynomial fit.
7. T_c, a function of N_L, F_h(first hit layer) and L_h(last hit layer).

$$T_c = \begin{cases} N_L/(L_h - F_h + 1), \text{if no hit in the inner RPC} \\ N_L/(L_h - F_h), \quad \text{if a hit in the inner RPC} \end{cases} \tag{4.9}$$

8. $\bar{m}$, the average multiplicity of hit strips per layer.

9. σ_m, the standard deviation of $\bar{m}$, $\sigma_m = \sqrt{< m >^2 - \bar{m}^2}$, where m is the multiplicity of hit strips per layer.

For the $J/\psi \rightarrow \mu^+\mu^-$ process, both tracks are required to satisfy the "Tight" muon selector.

Kaon and pion identification

To identify a charged kaon, information from subdetectors SVT, DCH and DIRC is needed. *BABAR* uses two different kaon identification selectors called PidKaonSMSSelector and PidKaonMicroSelector [49]. Both selectors use dE/dx from these two tracking devices (for those particles, whose momentum does not reach the threshold of DIRC), but different approaches on the information from DIRC. PidKaonSMSSelector uses relative likelihood ratio of kaon and pion strategies; PidKaonMicroSelector uses hit-by-hit global likelihood algorithm with a neural network based approach. Both selectors give comparable performance concerning efficiency and misidentification for hadrons.

PidKaonSMSSelector is used as a cut-based selector. The criteria used by this selector are the momentum of particle and the relative likelihood ratio of kaon and pion which is based on the Cherenkov angle from DIRC.

For a particle $i \in \{e, \mu, \pi, k, p\}$, The DIRC likelihood l_i is defined as

$$l_i = g_i \cdot p_i / \sum_{i=e}^{p} g_i \cdot p_i, \tag{4.10}$$

and assumes that the Gaussian probability part g_i and Poisson probability part p_i are uncorrelated. Here $g_i = \frac{e^{-\frac{(\theta-\theta_i)^2}{2\sigma_\theta}}}{\sqrt{2\pi}\sigma_\theta}$. θ, δ_{theta} and θ_i are the measured angle, its error, and the expected angle for particle i, respectively.

The DIRC Poisson probability p_i is

$$p_i = Poisson(N_s + N_b, N^i_{exp} + N_b), \tag{4.11}$$

where N_s, N_b and N^i_{exp} are signal photons, background photons and expected number of photons for particle i, respectively. Both p_i and g_i are normalized independently. To separate particle i and j ($j \in \{e, \mu, \pi, k, p\}$ and $j \neq i$), a relative likelihood ratio r_{ij} is used and defined as

$$r_{ij} = l_i / l_j \tag{4.12}$$

Tab. 4.3 shows the summary of requirements on the likelihood ratio and the particle momentum. Generally, for tracks with lab momentum less than 3 GeVc, the efficiency is about 70 - 90% for all the criteria except for *NotApion*, which is > 90%.

For PidKaonMicroSelector, a single continuous variable is used to quantify the kaon. This variable is the output of a track-based neural net K-Net after combined

Selector	Momentum p range(GeV/c)			Likelihood cut
	SVT	DCH	DIRC	
NotAPion	< 0.5	< 0.6	> 0.6	$r_{K\pi} < 0.1$ if $p \leq 0.5$
VeryLoose	< 0.6	< 0.6	> 0.6	$r_{Kp} > 1$; $r_{K\pi} > 3$ if $p < 2.5$, $r_{K\pi} > 20$ if $0.4 < p < 0.7$
Loose	< 0.7 or > 1.5	< 0.7 or > 1.5	> 0.6	$r_{Kp} \geq 1$ or no DIRC;$r_{K\pi} > 1$ if $p < 2.7$, $r_{K\pi} > 80$ if $p > 2.7$, $r_{K\pi} > 15$ if $0.5 < p < 0.7$
Tight	< 0.7	< 0.7	> 0.6	$r_{Kp} > 1$; $r_{K\pi} > 1$ if $p < 2.7$, $r_{K\pi} > 80$ if $p > 2.7$, $r_{K\pi} > 15$ if $0.5 < p < 0.7$
VeryTight	< 0.6	< 0.6	< 0.6	$r_{Kp} > 1$; $r_{K\pi} > 3$ if $p < 2.5$, $r_{K\pi} > 200$ if $p > 2.5$, $r_{K\pi} > 20$ if $0.4 < p < 0.7$

Table 4.3: The criteria for cut-based kaon identification.

input variables (limited to kaons and pions)

1. $L_x = \frac{L_{K_x} + L_{\pi_x}}{L_{K_x}}$, $x \in \{SVT, DCH, DIRC\}$,

2. track laboratory momentum P_{lab}.

For $x \in \{SVT, DCH\}$, likelihood L_{i_x} is obtained from dE/dx as for the PidKaonSMSSeletor, where $i \in \{K, \pi\}$. While for DIRC, L_i is obtained from a global likelihood, which is based on the photomultiplier tube hit and all the tracks in an event and the machine background.

Analogous to PidKaonSMSSelector cut-based criteria, *veryTight, Tight, Loose, veryLoose* and *notApion* are set as selectors based on a cut on this single output variable at > 0.68, > 0.62, > 0.50, > 0.45 and > 0.06 respectively.

For charged pions, there is no dedicated selector. Usually, the pion selector is just to reverse the kaon selector, i.e., a logical **NOT**.

For the $B \to J/\psi\eta K$ analysis, a cut-based selector is used. For the $B \to DK$ analysis, both selectors are used, for the pions from D decay, a cut-based logic **Not** *Loose* kaon is used, for the bachelor kaon, which is directly from B meson, a neural network based *Loose* kaon is used.

4.1.8. Signal region

The signal region is used in the cut and counting method, which will be described later. For reconstructed B meson, there are two minimally correlated variables that help to isolated it from the background, the energy and momentum of B meson. Based on the energy and momentum of the reconstructed B meson, two signature variables, ΔE and m_{ES}, can be used to identify a B meson. The energy difference is defined as

$$\Delta E = E_B^* - E_{beam}^*, \tag{4.13}$$

where E_B^* and E_{beam}^* are the energy of reconstructed B meson and the energy of each e^+e^- beams in center mass frame, respectively. E_{beam}^* is half of the total energy of e^+e^- beam system in the center mass frame, conventionally, it is called beam energy.

Energy substitute mass (also known as the beam constrained mass) m_{ES} is defined as

$$m_{ES} = \sqrt{E_{beam}^{*2} - P_B^{*2}} \tag{4.14}$$

where P_B^* is the momentum of reconstruct B in the center mass frame.

For signal B mesons, ΔE is a Gaussian distribution with a mean at ~ 0.0 and a width dependent on decay mode, m_{ES} is also a Gaussian distribution with a mean around 5.279 GeV/c^2 and a width about 3 MeV.

The signal region is defined with these two B meson signature variables, typically $m_{ES} > 5.2725$ GeV/c^2 and $|\Delta E| < 0.04$ GeV for the $B \rightarrow J\psi\eta K$ analysis.

4.1.9. Best B candidate selection

As a B meson is reconstructed from all possible measured charged tracks and neural photons of one colliding event, different combinations of these tracks and photons cause one event to have several versions of reconstructed B candidates, but a B candidate only has one "true" reconstruct B candidate. To select this "true" reconstructed B candidate, there are several common methods used in *BABAR*.

1. Select the B candidate with a minimum ΔE in all the reconstruction of one B event.

2. Random selection, randomly select one of B candidates.

3. Least χ^2 selection, combined several selection criteria $\hat{sc} = \{sc_1, sc_2, \cdots, sc_k\}$ and use

$$\chi^2 = \sum_i^k \frac{(sc_i - sc_i^{exp})^2}{\sigma_{mc_i}^2} \tag{4.15}$$

here σ_{mc_i} and sc_i^{exp} are the error and expectation value for selection criteria i, respectively.

In fact, after all selection criteria have been applied to the reconstructed B candidates, a big fraction of B events have only one reconstructed B candidate.

4.2. Extended maximum likelihood definition

4.2.1. Maximum likelihood principle

Joint-likelihood function for an observation $\underline{x} = (x_1, x_2, \cdots, x_n)$ for a given θ is defined as

$$L(\underline{x}|\theta) = \prod_{i=1}^{n} f(x_i;\theta), \tag{4.16}$$

where $f(x_i;\theta)$ is a probability density function (p.d.f) for x_i at given θ. $f(x_i;\theta)$ is a p.d.f properly normalized to one, therefore the likelihood function is also normalized to one.

According to the maximum principle [50], there is a particular $\hat{\theta}$, for all values of θ, it satisfies

$$L(\underline{x}|\hat{\theta}) \geq L(\underline{x}|\theta). \tag{4.17}$$

This principle requires the first derivative of eq. 4.16 to be 0 and the second derivative to be negative with respect to the variable θ.

Since L and logarithm of L attain their maximum for the same value of θ, from the principle of maximum theory

$$\frac{\partial}{\partial\theta}\ln L(\underline{x}|\theta) = \frac{\partial}{\partial\theta}\sum_{i}^{n}\ln f(x_i|\theta) = 0, \tag{4.18}$$

$$\frac{\partial^2}{\partial\theta^2}\ln L(\underline{x}|\theta)|_{\theta=\hat{\theta}} = \frac{\partial^2}{\partial\theta^2}\sum_{i}^{n}\ln f(x_i|\theta)|_{\theta=\hat{\theta}} < 0. \tag{4.19}$$

For a general case, while there are several parameters $\underline{\theta} = \{\theta_1, \theta_2, \cdots, \theta_k\}$, a set of logarithm likelihood equations

$$\frac{\partial}{\partial\theta_j}\ln L(\underline{x}|\underline{\theta}) = 0, j = 1, 2, \cdots, k, \tag{4.20}$$

can be used to find maximum likelihood estimates $\hat{\underline{\theta}} = \{\hat{\theta_1}, \hat{\theta_2}, \cdots, \hat{\theta_k}\}$. The definite negative of the quadratic matrix $U(\hat{\underline{\theta}})$ with elements

$$U_{ij}(\hat{\underline{\theta}}) = \frac{\partial^2 \ln L}{\partial\theta_i\partial\theta_j}|_{\underline{\theta}=\hat{\underline{\theta}}} \tag{4.21}$$

will affirm that the $\hat{\underline{\theta}}$ are for the absolute maximum of the likelihood.

4.2.2. Extended maximum likelihood

From Eq. 4.16, $f(x_i;\theta)$ is properly normalized to one. For the extended maximum likelihood [18], this requirement is not that strict, but is normalized to a number.

This extended maximum likelihood function is defined as

$$L(\underline{x}|\underline{\theta}) = \prod_{i}^{N} P(x_i;\theta)\frac{e^{-N}}{N!} \tag{4.22}$$

with $P(x_i;\theta) = Nf(x_i;\theta)$.

To find the estimates $\hat{\theta}$,

$$\langle\frac{\partial lnL}{\partial\theta_i}\rangle = 0, \tag{4.23}$$

$$\langle(\frac{\partial lnL}{\partial\theta_i})(\frac{\partial lnL}{\partial\theta_i})\rangle = -\langle\frac{\partial^2 lnL}{\partial\theta_i\partial\theta_j}\rangle, \tag{4.24}$$

are required.

4.3. Cut and counting method

This method is very straightforward; all the criteria of the cuts are applied to select the B candidate in a data sample, then the number remaining left in the signal region is accounted.

The procedure is essentially as follows: for a branching ratio measurement, the cuts are optimized with a maximum ratio of

$$R = \frac{N_{Sig}}{\sqrt{N_{Sig} + N_{Bk}}}, \tag{4.25}$$

where N_{Sig} and N_{Bk} stand for the number for signal events and the number for background events, and usually in signal region. For an upper limit, the cuts are optimized with a maximum ratio of

$$R = \frac{N_{Sig}}{\sqrt{N_{Bk}}}. \tag{4.26}$$

Usually, N_{Sig} and N_{Bk} are estimated from Monte Carlo (MC) samples. For N_{Bk} if the number is too small in the signal region, it may cause a big fluctuation in the maximization of R. In this case, the region out of signal region (the sideband region) is used and scaled to the signal region to get an more accurate estimate of N_{Bk}.

Chapter 5

Analysis of $B \to J/\psi\eta K$

In this chapter, the whole analysis process for $B \to J/\psi\eta K$ is introduced, including data samples, event selection, background estimation, data fit and physics results.

5.1. Physics motivation

Fig. 5.1 shows the Feynman diagram for decay $B \to J/\psi\eta K$. From the two body resonance (a), we can use it to search for the X(3872) through $X \to \eta J/\psi$. Also if the mass of X is heavy enough (above 4.0 GeV/c^2), it is possible to be used to search for the hybrid charmonium state ($c\bar{c}g$).

5.2. Data samples

Data samples used for $B \to J/\psi\eta K$ are Monte Carlo (MC) samples and collected e^+e^- beam colliding experimental data. These MC samples, generated by Geant4

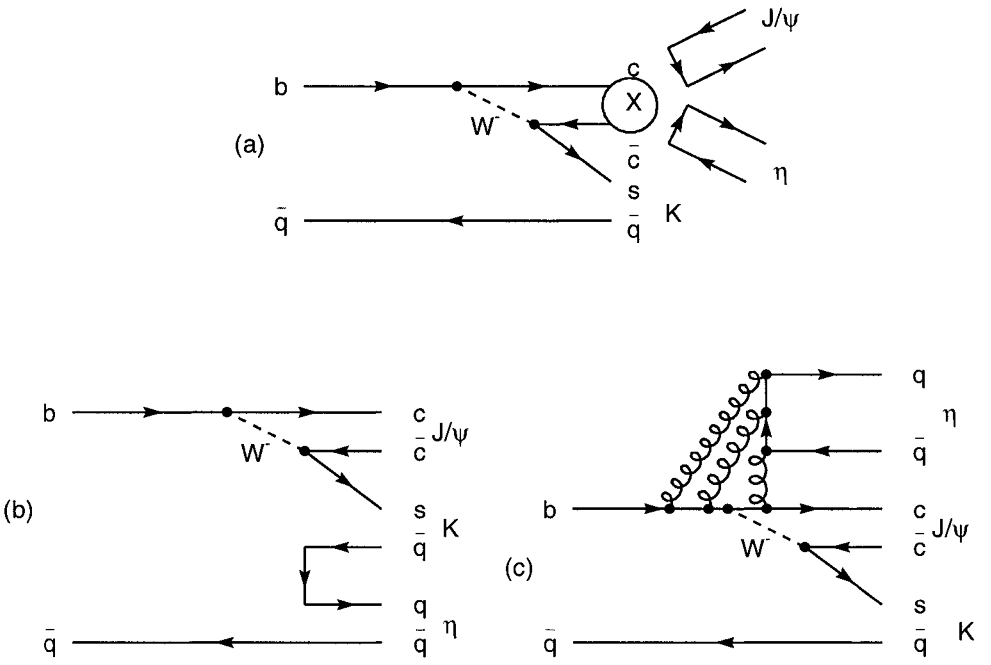

Figure 5.1: The Feynman diagrams for $B \to J/\psi\eta K$. (a) two body resonance, (b) sea quark and (c) gluon coupling.

simulation package and used to estimate the yield and shapes of the signal and background, are MC signal, generic B^+B^-, generic $B^0\bar{B}^0$, continuum $c\bar{c}$ and continuum *uds* samples; the beam colliding data are on-peak data and off-peak data samples. Off-peak data is about 10% of the on-peak data.

The analysis $B \to J/\psi\eta K$ mainly used the colliding data before 2003, and SP3 and SP4 MC samples (SP stands for MC simulation production, 3 or 4 is just the number for SP cycle).

The numbers of total integrated luminosity L ($L = \frac{\text{number of events}}{\text{cross section}}$) of all the samples are listed in Table 5.2 except MC signal samples. For signal MC samples, $B \to J/\psi\eta K$ has 30,000 events for charged kaon channel and 24,000 events for neutral kaon channel.

Data Sample	$B \to J/\psi\eta K(\text{fb}^{-1})$
B^+B^-	62.9
$B^0\bar{B}^0$	62.8
$c\bar{c}$	62.9
uds	61.8
Inclusive J/ψ	86.2
on-peak data	81.9
off-peak data	9.8

Table 5.1: Data samples used for the analysis $B \to J/\psi\eta K$.

5.3. Event selection

Two decay channels are used in this analysis, charged and neutral B mesons. My work is mainly on neutral B, which will be described in more detail in the following sections.

5.3.1. Reconstruction of B candidate

We reconstructed the neutral (charged) B meson from particles like J/ψ, η and K^0_S (charged kaon) with secondary decay of $J/\psi \to e^+e^-/\mu^+\mu^-$, $\eta \to \gamma\gamma$ and $K^0_S \to$

$\pi^+\pi^-$.

1. J/ψ, which is reconstructed from e^+e^- or $\mu^+\mu^-$ pairs. As the electron (positron) is a light lepton, it will have Bremsstrahlung radiation loss while it travels inside the detector. A calculation procedure is taken to estimate energy loss, and the invariant mass of J/ψ reconstructed from a e^+ and e^- pair is low due to the loss, thus has a long tail in the low mass band. The criteria to identify electron and muon, which is described in section 4.1.7, were used here.

2. η, which is reconstructed from a photon γ pair. The main background for this photon pair is from the decay of π^0. A specific π^0-veto is developed to eliminate this background. This π^0-veto is used to eliminate photon pair combinations for which one of the photons forms an invariant mass with any other photon in the event within some range of the nominal π^0 mass, *i.e.*, 135 MeV/c^2. In this analysis, the range of ± 10 MeV/c^2 (± 17 MeV/c^2) is used for neutral (charged) kaon mode; the energy of each photon to form η is require to be greater than 150 MeV/c^2. Another useful tool to reject continuum background, is the helicity angle θ_η^γ of photon in the η frame. The distribution of $|\cos\theta_\eta^\gamma|$ is flat for signal MC, while is more peaking around ± 1 for continuum (see Fig. 4.2).

3. K_S^0, which is reconstructed from a $\pi^+\pi^-$ pair. As the K_S^0 is a relative long life time particle, the flight length of K_S^0 ($c\tau \sim 2$ cm) can be used to reject fake particles.

4. B meson, which is reconstructed from the reconstructed J/ψ, η, and kaon candidates. The momentum and energy of this B meson in the e^+e^- machine central mass frame are used to construct the B signature variables of m_{ES} and ΔE (defined in section 4.1.8). Also the thrust angle of this colliding beams event is used to reject jet-like continuum event.

5.3.2. Cuts optimization

The procedure of optimization of cuts is based on maximizing the ratio of $\frac{N_{Sig}}{\sqrt{N_{Sig}+N_{Bk}}}$ by varying all possible the criteria used to get a clean B meson signal. The criteria (cuts) involved in neutral B are:

1. Invariant mass of J/ψ, η, K^0_S (J/ψ mass range is fixed);
2. Decay length of K^0_S (this cut is fixed);
3. Identification of electron, muon (kaon for charged B meson channel);
4. Helicity angle and π^0-veto of η candidate;
5. Thrust angle of the event.

The branching ratio for the charged mode is estimated to be 5×10^{-5} [68] as the quark components in the mesons ϕ and η are similar. The neutral mode is expected to be half of this value since half of K^0s decay into K^0_S.

The signal box is defined in the plane of m_{ES} and ΔE. Both channels consist of common ΔE window which is $|\Delta E| \leq 0.04$ GeV and a common m_{ES} window:

1. $B^{\pm} \to J/\psi\eta(\gamma\gamma)K^{\pm}$, $5.272 \leq m_{ES} \leq 5.289$ GeV/c^2;

2. $B^0 \to J/\psi\eta(\gamma\gamma)K^0_S$, $5.272 \leq m_{ES} \leq 5.289$ GeV/c^2.

In the signal region, for events with multi-reconstructed B candidates, only one candidate is chosen, that with the smallest $|\Delta E|$.

In the plane of ΔE and m_{ES}, all the region excluding the signal region is defined to be a sideband. This region is used to get an accurate number of events to estimate the background when the estimated background events number from the signal region has a big fluctuation.

Table 5.2 shows the detail of all the optimized cuts used for $B \to J/\psi\eta K$. Table 5.3 shows the raw efficiency and the optimized ratio for these two channels. Fig. 5.2 and 5.3 show the the signal region (with a rectangle box) and the projection on each B meson signature variables for these $B \to J/\psi\eta K$ channels.

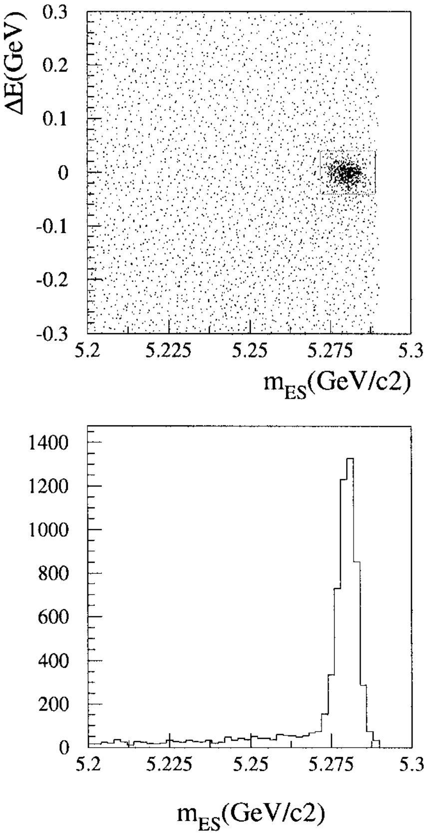

Figure 5.2: $B^{\pm} \longrightarrow J/\psi\eta(\gamma\gamma)K^{\pm}$ signal MC: plot of ΔE *vs.* m_{ES} with a signal region box overlaid (top left); the ΔE projection of m_{ES} signal band (top right); the m_{ES} projection of ΔE signal band (bottom left).

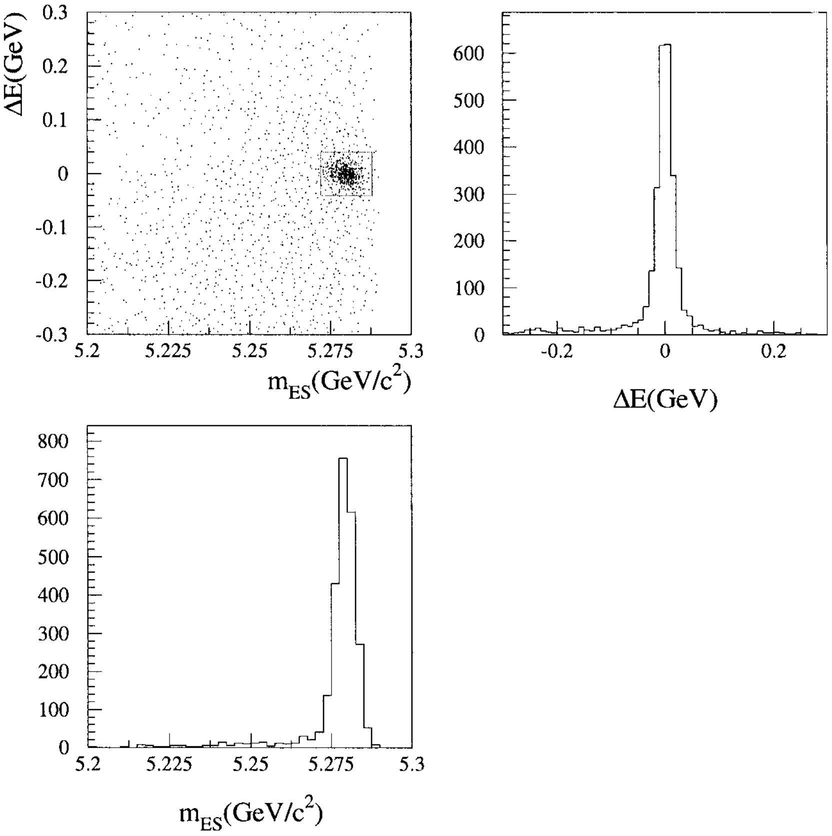

Figure 5.3: $B^0 \to J/\psi\eta(\gamma\gamma)K^0_S$ signal MC: plot of ΔE *vs.* m_{ES} with a signal region box overlaid (top left); the ΔE projection of m_{ES} signal band (top right); the m_{ES} projection of ΔE signal band (bottom left).

Criteria	$B^{\pm} \to J/\psi\eta(\gamma\gamma)K^{\pm}$	$B^{0} \to J/\psi\eta(\gamma\gamma)K^{0}_{S}$
J/ψ:		
e^+e^- channel	PID: Tight, Loose	PID: Tight, Tight
mass (GeV/c^2)	$2.95 < M_{J/\psi} < 3.14$	
$\mu^+\mu^-$ channel	PID: Loose, Loose	PID: Loose, Loose
mass (GeV/c^2)	$3.06 < M_{J/\psi} < 3.14$	
η:		
$\|M_\eta - 0.547\| \leq$	0.023 GeV/c^2	0.023 GeV/c^2
π^0-veto if $\|M(\gamma_\eta\gamma) - 0.135\| \leq$	0.017 GeV/c^2	0.010 GeV/c^2
Kaon:	PID: Loose	$\|M_{K^0_S} - 0.489\| \leq 0.09$ GeV/c^2
		K^0_S decay length ≥ 0.1 cm
Helicity: $\|\cos(\theta^{\gamma}_{\eta})\| \leq$	0.93	0.81
Thrust: $\|\cos(\theta_T)\| \leq$	0.8	0.9

Table 5.2: Optimized cuts for $B \to J/\psi\eta K$.

Channel	Efficiency	$\frac{N_{Sig}}{\sqrt{N_{Sig}+N_{Bk}}}$
$B^{\pm} \to J/\psi\eta(\gamma\gamma)K^{\pm}$	14.1%	2.0
$B^{0} \to J/\psi\eta(\gamma\gamma)K^{0}_{S}$	9.8%	1.1

Table 5.3: Raw efficiency and and the optimized ratio for $B \to J/\psi\eta K$ channels.

5.4. Background overview

The background for $B \to J/\psi\eta K$ is estimated with MC, off-peak and on-peak data samples, including background from continuum, $B\bar{B}$ without a J/ψ (all B candidate whose decay product contains a J/ψ is removed), inclusive $B \to J/\psi X$ (X stands for other non-signal particles). The background is categorized into two types, for example in the frame of m_{ES}:

1. "flat background", the shape is described by an Argus function [51];
2. "peaking background", the shape is described by a Gaussian function with a mean around the mass of the B meson

The method used to estimate the backgrounds is based on an exclusive charmonium model [52]. In this model, the flat background is from continuum (N_{cont}), from $B \to J/\psi X$ non-peaking events ($N_{J/\psi Arg}$) and from non-J/ψ $B\bar{B}$ events ($N_{B\bar{B}}$); the peaking background is from inclusive $B \to J/\psi X$ peaking part ($N_{J/\psi Gauss}$).

There are six flat background quantities that need to be determined from MC samples and on-peak data,

1. Monte Carlo continuum (uds and $c\bar{c}$), N^{MC}_{cont};
2. the Argus-shape component of the Monte Carlo generic $B\bar{B}$ with a $J/\psi \to l^+l^-$ $(l = e^+ or \mu^+)$, $N^{MC}_{J/\psi Arg}$;
3. Monte Carlo generic $B\bar{B}$ without a $J/\psi \to l^+l^-$, $N^{MC}_{B\bar{B}}$;

4. Off-peak data, $N_{cont}^{off-peak}$;
5. On-peak data J/ψ mass sideband, $N_{J/\psi side}^{on-peak}$;
6. the Argus-shape component of on-peak data ΔE sideband, $N_{\Delta E side}^{on-peak}$.

These six quantities satisfy

1. $N_{cont}^{MC} = N_{cont}$;
2. $N_{J/\psi Arg}^{MC} = N_{J/\psi Arg}$;
3. $N_{B\bar{B}}^{MC} = N_{B\bar{B}}$;
4. $N_{cont}^{off-peak} = N_{cont}$;
5. $N_{J/\psi side}^{on-peak} = N_{cont} + N_{B\bar{B}}$;
6. $N_{\Delta E side}^{on-peak} = N_{cont} + N_{B\bar{B}} + N_{J/\psi Arg}$.

Based on these six quantities, the three flat background types are determined with a minimum χ^2 fit with associated errors.

Another method used to estimate background is with the experimental on-peak and off-peak data, which used the sideband of some variables, for our case, like η mass, ΔE. In this way, we scaled the background level we got from the sideband to signal region to get the level or shape of the background.

In our analysis, we first tried the exclusive charmonium model and found that the inclusive J/ψ background is not fit very well and is mode dependent. Subsequently we used the second method to estimate our background and use the first as a cross check except inclusive J/ψ background.

5.5. Inclusive charmonium model

In our analysis, the $m_{\rm ES}$ distribution is used to estimate the background. The procedures to get the background for inclusive charmonium model are

1. First to get the Argus shape fit parameters from a "fake" J/ψ sample in the $m_{\rm ES}$ distribution within signal region. A fake J/ψ candidate is constructed by using the identical selection criteria except for logically reversing the lepton PID which is used for a "true" J/ψ candidate. This will provide a sufficient statistics to do the background fitting most of the time.

2. Second the shape parameters for the Argus function (except the normalization) are used to fit the sample with corrected lepton PID. The number of background events are calculated as the integral of the Argus function defined by this fit in the $m_{\rm ES}$ signal region.

5.5.1. Continuum MC, N_{cont}^{MC}

About 61.8 fb^{-1} *uds* and 62.9 fb^{-1} *cc* were used. Fig. 5.4 shows the plots of the *uds* (left-hand column) and $c\bar{c}$ (right-hand column) backgrounds. The numbers of the continuum background N_{cont}^{MC} from the fit function are 4.23±0.87 and 1.16±0.41

for $B^{\pm} \to J/\psi\eta K^{\pm}$ and $B^0 \to J/\psi\eta K^0_S$, respectively. All numbers are scaled to the total on-peak data luminosity.

5.5.2. Off-peak data, $N_{cont}^{off-peak}$

About 9.8 fb^{-1} off-peak data was used. The expected background $N_{cont}^{off-peak}$ are 1.09±1.02 and 1.22±1.08 for $B^{\pm} \to J/\psi\eta(\gamma\gamma)K^{\pm}$ and $B^0 \to J/\psi\eta(\gamma\gamma)K^0_S$, respectively. Fig. 5.5 shows $m_{\rm ES}$ distribution from off-peak data for both channels.

5.5.3. Generic $B\bar{B}$ MC without J/ψ, $N_{B\bar{B}}^{MC}$

About 62.8 fb^{-1} $B^0\bar{B}^0$ and 62.9 fb^{-1} B^+B^- MC samples are used. The expected backgrounds for this source are 2.67±0.74 and 1.48±0.48 for $B^{\pm} \to J/\psi\eta(\gamma\gamma)K^{\pm}$ and $B^0 \to J/\psi\eta(\gamma\gamma)K^0_S$, respectively. Fig. 5.6 shows the $m_{\rm ES}$ distributions for both channels from generic $B\bar{B}$ background.

5.5.4. Inclusive J/ψ, $N_{J/\psi Arg}^{MC}$

About 86.2 fb^{-1} inclusive J/ψ MC sample was used. In this sample, the signal modes were removed. As the fake J/ψ sample for this background has lower statistics than the real sample, we did not use "fake" J/ψ reference shape to extract the background, instead, we extracted the background from the direct fit on the real J/ψ sample with an Argus function plus a Gaussian function centered at

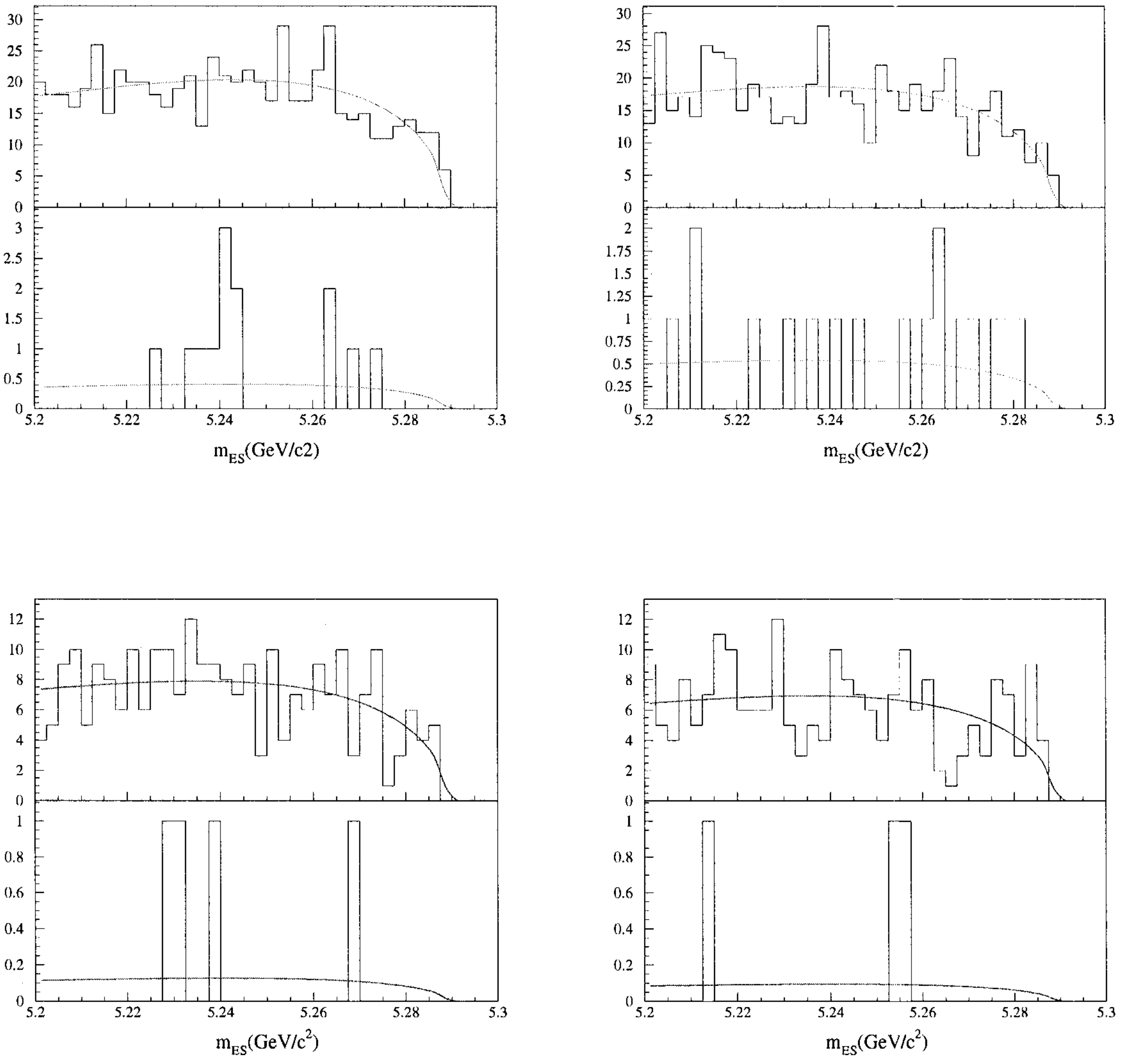

Figure 5.4: Continuum background estimate from *uds* (left column) and $c\bar{c}$ (right column) Monte Carlo samples. The two signal modes are $B^{\pm} \to J/\psi\eta(\gamma\gamma)K^{\pm}$ (top) and $B^0 \to J/\psi\eta(\gamma\gamma)K^0_S$ (bottom).

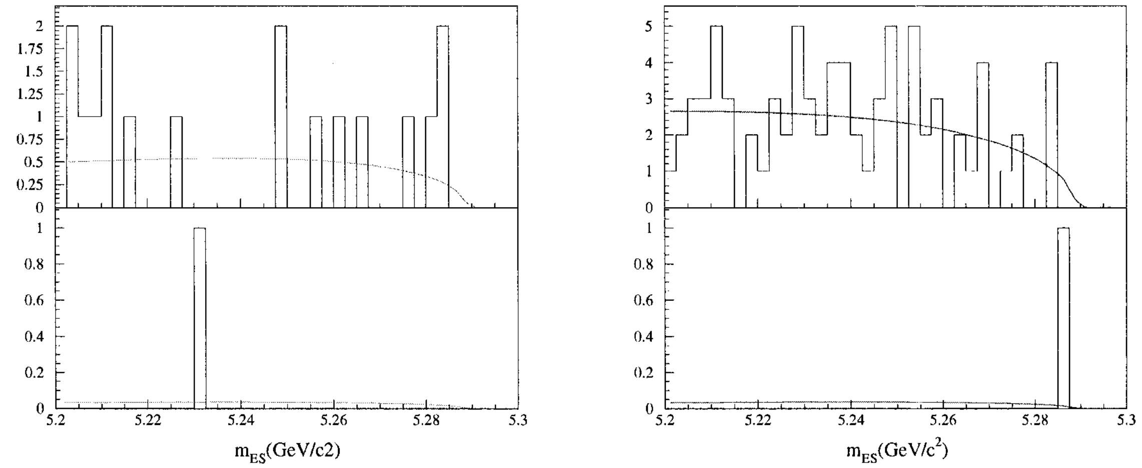

Figure 5.5: Off-peak data background estimate. The two signal modes are $B^{\pm} \to J/\psi\eta(\gamma\gamma)K^{\pm}$ (right) and $B^0 \to J/\psi\eta(\gamma\gamma)K^0_S$ (left).

B mass. The fit results for flat background are 38.69±12.70 and 25.93±4.61, while for peaking background are 56.35±16.30 and 0.2 ± 0.8, for $B^{\pm} \to J/\psi\eta(\gamma\gamma)K^{\pm}$ and $B^0 \to J/\psi\eta(\gamma\gamma)K^0_S$, respectively. Fig. 5.7 shows the $m_{\rm ES}$ distribution for both channels from inclusive J/ψ background.

5.5.5. J/ψ mass sideband, $N^{on-peak}_{J/\psi side}$

On-peak data sample was used for this source. The number of events with J/ψ mass falling into the following region is counted:

1. $J/\psi \to e^+e^-$ channel, $3.156 < m_{J/\psi} < 3.300$ GeV/c^2;

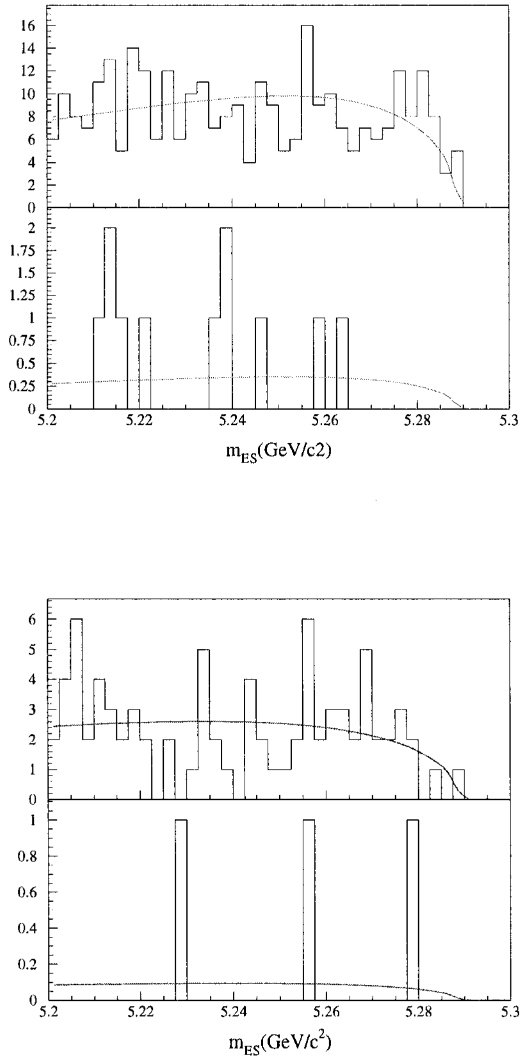

Figure 5.6: Generic $B\bar{B}$ without a J/ψ candidate background from B^+B^- (left column) and $B^0\bar{B}^0$ (right column) Monte Carlo samples. The two signal modes are $B^\pm \to J/\psi\eta(\gamma\gamma)K^\pm$ (right) and $B^0 \to J/\psi\eta(\gamma\gamma)K^0_S$ (left).

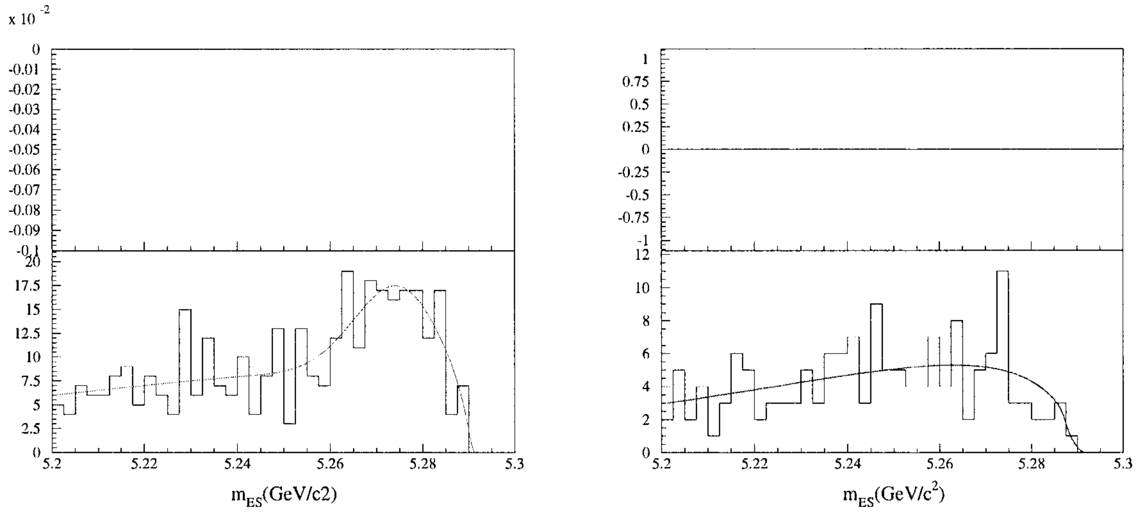

Figure 5.7: Inclusive J/ψ background from inclusive J/ψ Monte Carlo samples. The two signal modes are $B^{\pm} \to J/\psi\eta(\gamma\gamma)K^{\pm}$ (right) and $B^0 \to J/\psi\eta(\gamma\gamma)K^0_S$ (left).

2. $J/\psi \to \mu^+\mu^-$ channel, $2.980 < m_{J/\psi} < 3.024$ GeV/c^2 or $3.156 < m_{J/\psi} < 3.300$ GeV/c^2.

Two scaling factors were used, 1.42 and 0.46 for $J/\psi \to e^+e^-$ and $J/\psi \to \mu^+\mu^-$ respectively. A fit to J/ψ invariant mass from inclusive J/ψ data sample with a one-order linear function plus a Gaussian is used to estimate the scaling factor. The background is modeled by a linear function, the events for background in the two sidebands and signal region are counted. The scaling factor is just the ratio between the two numbers in sideband and signal region. The expected background event numbers are 5.14±0.88 and 2.57±0.46 for $B^{\pm} \to J/\psi\eta(\gamma\gamma)K^{\pm}$ and $B^0 \to J/\psi\eta(\gamma\gamma)K^0_S$, respectively. Fig. 5.8 shows the m_{ES} distributions for both channels from J/ψ mass sideband.

5.5.6. ΔE sideband, $N^{on-peak}_{\Delta Eside}$

On-peak data sample was used. The sideband region for ΔE is defined as

1. $0.10 < |\Delta E| < 0.14$ GeV for $B^{\pm} \to J/\psi\eta(\gamma\gamma)K^{\pm}$;
2. $0.04 < |\Delta E| < 0.30$ GeV for $B^0 \to J/\psi\eta(\gamma\gamma)K^0_S$.

Since we assumed that the distribution for background in ΔE is one order polynomial, the background in signal region can be scaled with the ratio of ΔE sideband region to the signal region. The factors used are 1.0 and 0.154 for $B^{\pm} \to J/\psi\eta(\gamma\gamma)K^{\pm}$ and $B^0 \to J/\psi\eta(\gamma\gamma)K^0_S$, respectively. The numbers of the background of this source are estimated to be 27.10 ± 7.3 and 16.12 ± 0.57 for $B^{\pm} \to J/\psi\eta(\gamma\gamma)K^{\pm}$ and $B^0 \to J/\psi\eta(\gamma\gamma)K^0_S$, respectively. Fig. 5.9 shows the $m_{\rm ES}$ distributions for both channels from ΔE sideband.

5.5.7. Summary of the six correlated backgrounds results.

Table 5.4 shows the fit results with the six inputs from Sections 5.5.1 - 5.5.6, using the χ^2 fit method. The background is dominated by the inclusive J/ψ background type. By checking the numbers from continuum background (section 5.5.1) and from off-peak data (section 5.5.2), they agree well; as so does the number from

Source	$B^{\pm} \to J/\psi\eta(\gamma\gamma)K^{\pm}$	$B^0 \to J/\psi\eta(\gamma\gamma)K^0_S$
N_{cont}	2.51 ± 0.61	1.13 ± 0.35
$N_{b\bar{b}}$	2.79 ± 0.57	1.37 ± 0.45
$N_{J/\psi\, Arg}$	26.00±6.34	13.8±0.68
Total	31.29±6.33	16.31±0.57

Table 5.4: Summary of the background fit results

on-peak data J/ψ sideband (section 5.5.5) and the sum of background from MC continuum (section 5.5.1) and MC generic $B\bar{B}$ without J/ψ (section 5.5.3). There is more than one sigma difference between the sum of background event numbers from Sections 5.5.1, 5.5.3 and 5.5.4 and the estimated background from ΔE sideband (section 5.5.6). This difference most comes from inclusive J/ψ sample. As the inclusive J/ψ sample depends on the input from different analysis needs, it has strong model dependence.

5.6. Model dependent background in J/ψ inclusive

In the previous sections, we showed that the main background is from inclusive J/ψ, and there is about one sigma difference on the background between data and MC. The difference indicates the inclusive J/ψ background Monte Carlo model does not fit well for this analysis, and it is likely due to large correlated J/ψ backgrounds.

We studied the backgrounds by identifying the direct parent of the J/ψ, such as χ_1, χ_2, ψ' and B meson, using the inclusive J/ψ background samples.

Fig. 5.10 shows the distributions of the two-body invariant mass of $J/\psi\eta$ and ηK_S^0, using the events satisfying our optimized cuts. The top three plots are for the J/ψ events whose direct parent was a χ_1, χ_2, or ψ', by using the MC truth. Compared to the distribution of signal MC events, these backgrounds tend to have a $J/\psi\eta$ mass below 4 GeV/c^2. The lower three plots are for the J/ψ events whose direct parent is B; these backgrounds tend to have a ηK_S^0 invariant mass > 1.5 GeV/c^2. For $B^\pm \to J/\psi\eta(\gamma\gamma)K^\pm$, the two-body invariant mass of $J/\psi\eta$ tend to be below 4 GeV/c^2 and the invariant mass of ηK tend to below 1.5 GeV/c^2, too.

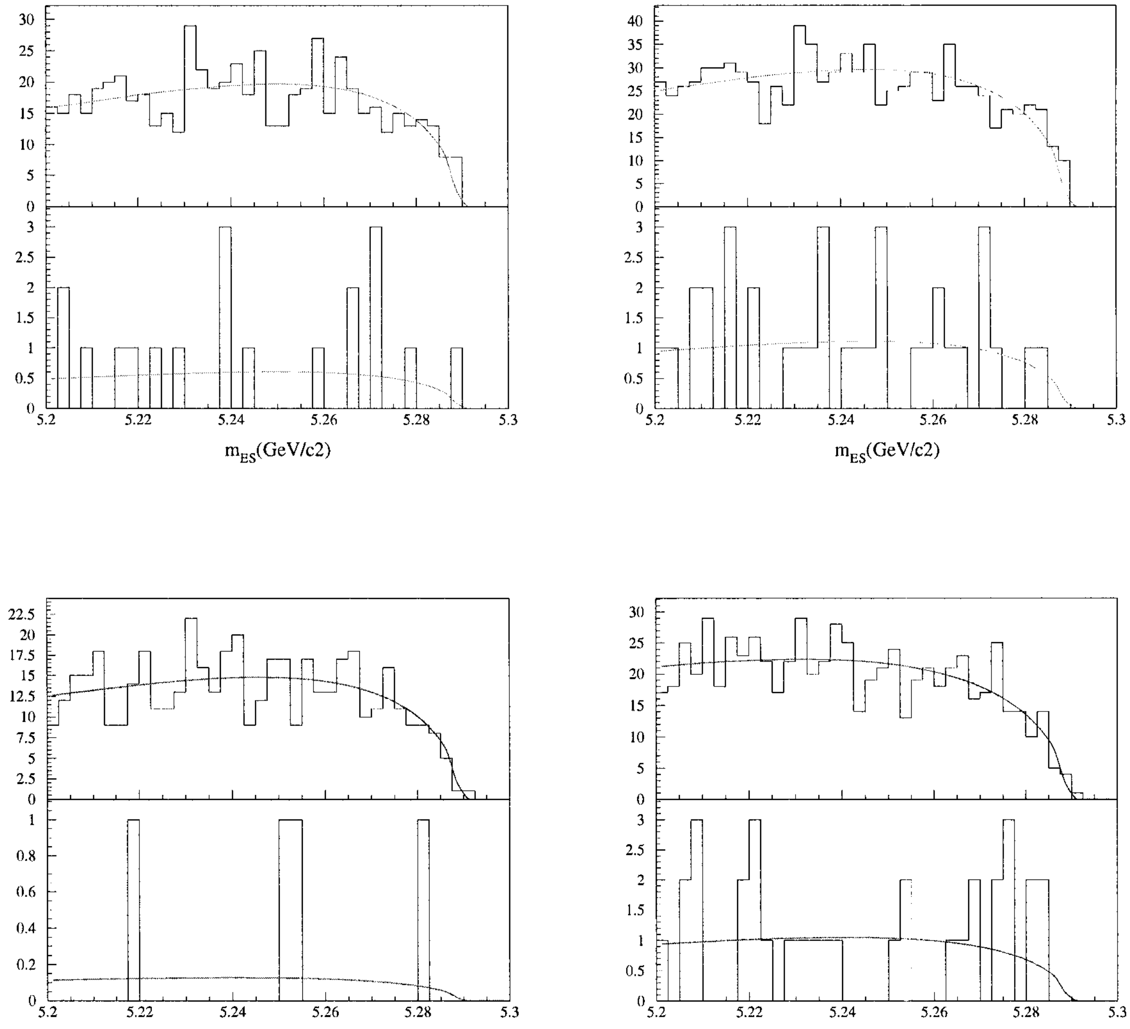

Figure 5.8: Background estimate from data using the J/ψ sidebands in the ee (left column) and $\mu\mu$ (right column) channels. The two signal modes are $B^{\pm} \to J/\psi\eta(\gamma\gamma)K^{\pm}$ (right) and $B^0 \to J/\psi\eta(\gamma\gamma)K^0_S$ (left).

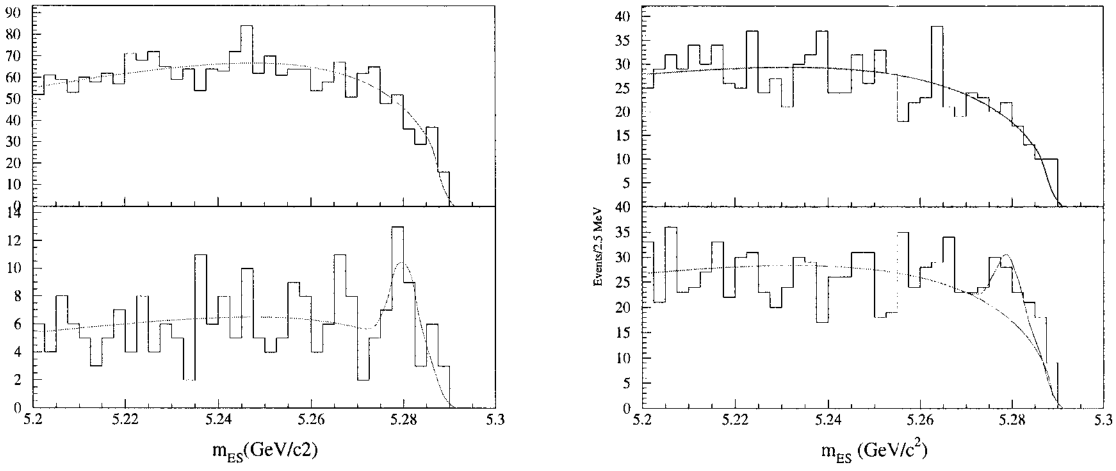

Figure 5.9: Background estimate from data using the ΔE sideband. The two signal modes are $B^{\pm} \rightarrow J/\psi\eta(\gamma\gamma)K^{\pm}$ (right) and $B^0 \rightarrow J/\psi\eta(\gamma\gamma)K_S^0$ (left).

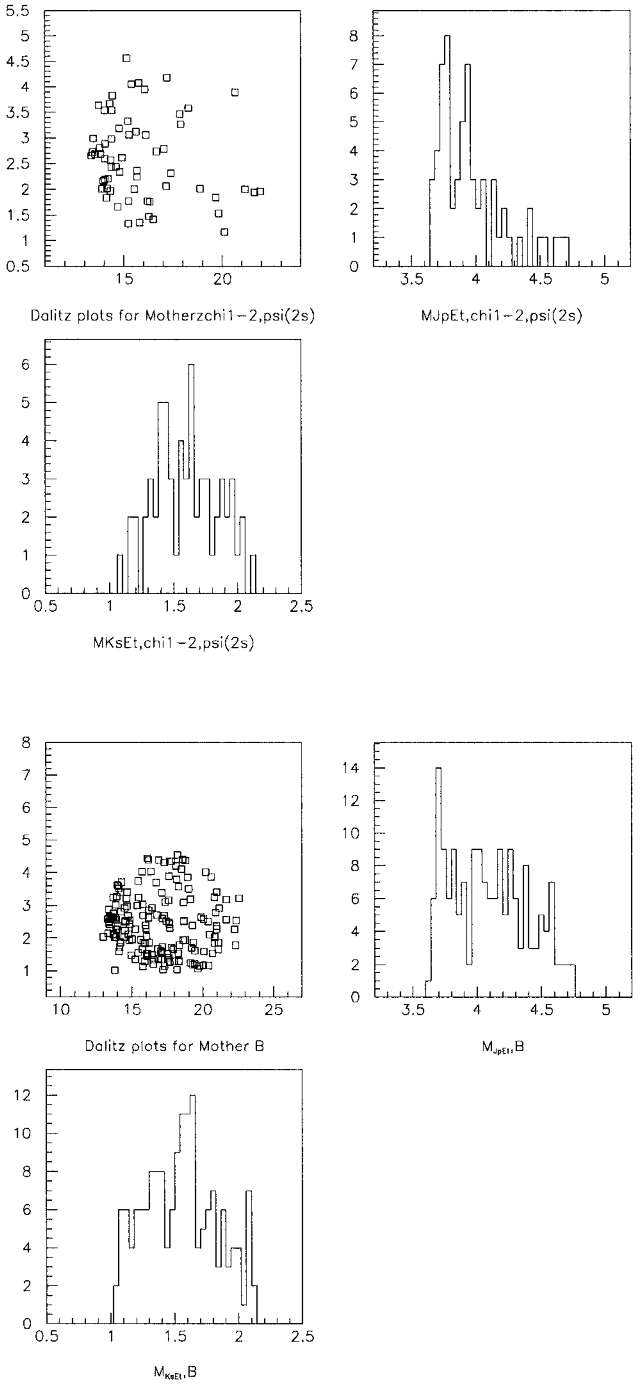

Figure 5.10: Reconstructed Monte Carlo $B^0 \to J/\psi\eta(\gamma\gamma)K^0_S$ events in which the J/ψ parent is a χ_1, χ_2 or a ψ' (upper three plots) and those in which the J/ψ parent is a charged or neutral B meson (lower three plots). The three plots in each group consist of the Dalitz plot for J/$\psi\eta$ (vertical axis) and ηK (horizontal axis) combinations, along with the corresponding mass distributions.

5.7. Data fit procedure

The signal region is slightly modified to accommodate all the bins without crossing the edge, $|\Delta E| < 0.04$ GeV and $5.2725 < m_{\rm ES} < 5.2875$ GeV/c^2. The data is fitted in the $m_{\rm ES}$ distribution in forty 2.5 MeV/c^2 bins in the range of $5.2 - 5.3$ GeV/c^2. The fit function is the sum of Gaussian (signal) and a background line shape determined from the fits to the $m_{\rm ES}$ distributions from two different background parameterizations: (1) $|\Delta E|$ sidebands from data and (2) η sidebands from data. In the fits to these sidebands, the free parameters are the Argus shape parameter, the Argus normalization, the Gaussian normalization, the Gaussian mean and the Gaussian width. For the data fit, we fixed the signal Gaussian width which is determined from the signal *MC* and the Argus shape parameter from the sideband fits.

5.8. Data fit

The data was fitted with the shape parameters determined from the ΔE and η sidebands.

The η sideband region is defined in invariant mass of η, $0.47 < M(\eta) < 0.49$ GeV/c^2 or $0.59 < M(\eta) < 0.62$ GeV/c^2 (the region is limited by the initial cut for η mass region).

The two background shapes were initially found with an Argus function and a Gaussian (peaking background). Fig. 5.11 shows the background fit and data fit for mode $B^0 \to J/\psi\eta(\gamma\gamma)K^0_S$, here we did not give the plots for charged kaon. The fit results are shown in Table 5.5 ($B^0 \to J/\psi\eta(\gamma\gamma)K^0_S$) and 5.6 ($B^\pm \to J/\psi\eta(\gamma\gamma)K^\pm$). These tables includes the data fit result with J/ψ inclusive shape parameters, which is used as a comparison. From these fit results, we found that the $|\Delta E|$ sideband and η sideband shapes are similar and the resulting number of signal events are close.

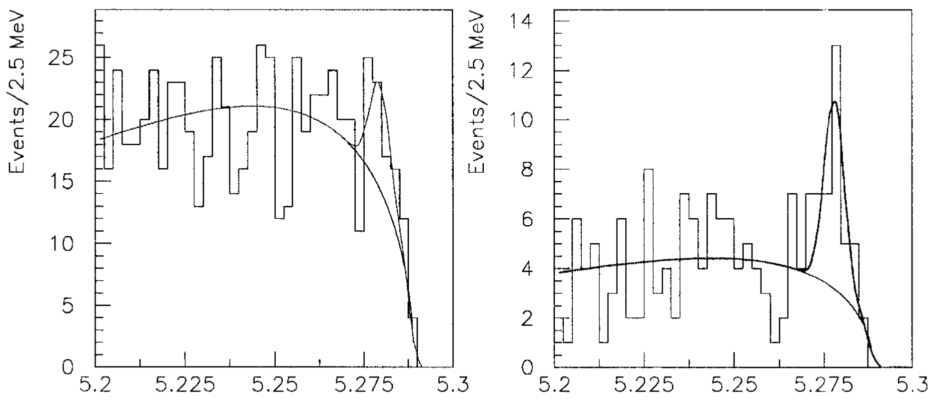

m$_{ES}$,ΔE sideband--opt

m$_{ES}$--opt

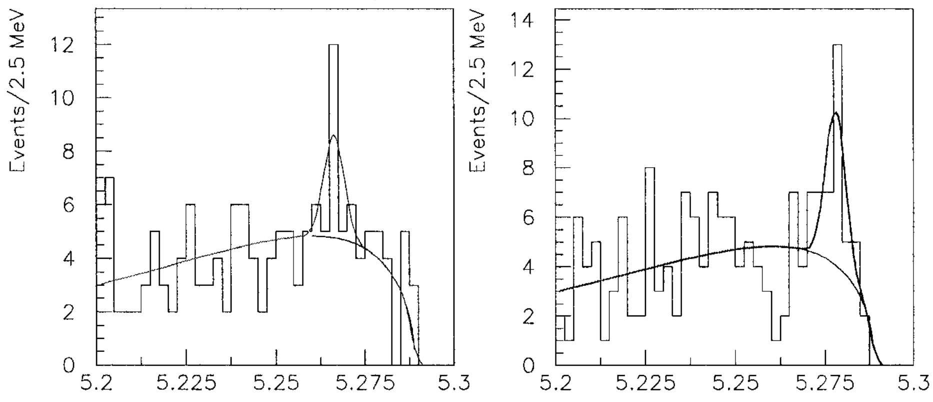

m$_{ES}$,eta sideband--opt

m$_{ES}$--opt

Figure 5.11: Data fit with Argus + Gaussian for $B^0 \to J/\psi\eta(\gamma\gamma)K^0_S$, the Argus shape parameters are got from ΔE and η sidebands, which are fitted with Argus function + Gaussian. top row, ΔE sideband (left), data fit (right); bottom row, η sideband (left, the peaking bin is due to fluctuations), data fit (right).

Bkgd	vary	Fit results						
		$M_B(MeV/c^2)$	$\sigma(M_B)$	χ^2	N_{bkg}	$\sigma(N_{bkg})$	N_{sig}	$\sigma(N_{sig})$
η SB	M_B	5281.1±1.27	2.82	1.54	21.7	1.94	17.3	6.54
ΔE SB	M_B	5278.0±1.22	2.82	1.67	16.8	1.52	22.2	6.43
J/ψ incl	M_B	5278.1±1.30	2.82	1.56	19.8	1.87	19.2	6.49

Table 5.5: Data fits for $B^0 \to J/\psi\eta(\gamma\gamma)K^0_S$ with Argus+Peaking background using η sideband, ΔE sideband and J/ψ inclusive background shapes. The signal width is fixed and the mass of B meson is allowed to vary.

Bkgd	vary	Fit results						
		$M_B(MeV/c^2)$	$\sigma(M_B)$	χ^2	N_{bkg}	$\sigma(N_{bkg})$	N_{sig}	$\sigma(N_{sig})$
η SB	M_B	5279.9±0.72	2.8	1.30	57.7	3.5	41.3	10.5
ΔE SB	M_B	5279.9±0.66	2.8	1.08	51.5	3.1	47.5	10.4
J/ψ incl	M_B	5279.9±0.79	2.8	1.37	69.1	4.2	29.9	10.8

Table 5.6: Data fits for $B^\pm \to J/\psi\eta(\gamma\gamma)K^\pm$ with Argus+Peaking background using η sideband, ΔE sideband and J/ψ inclusive background shapes. The signal width is fix and the mass of B meson is allowed to vary.

For the η sideband, there are some restrictions on the mass region, we have chosen the ΔE sideband to represent the background shape. In both modes, we find that the Gaussian or peaking background is very small relative to the Argus flat background, therefore the background shapes used were only with the Argus function on the ΔE sideband.

Fig. 5.12 shows the final data fit without and with Dalitz plot cuts, Fig. 5.13 shows the data fit without and with Dalitz plot cuts. These fit results with and without

without Dalitz cuts are listed in Table 5.7. How N_{sig} is determined will be discussed

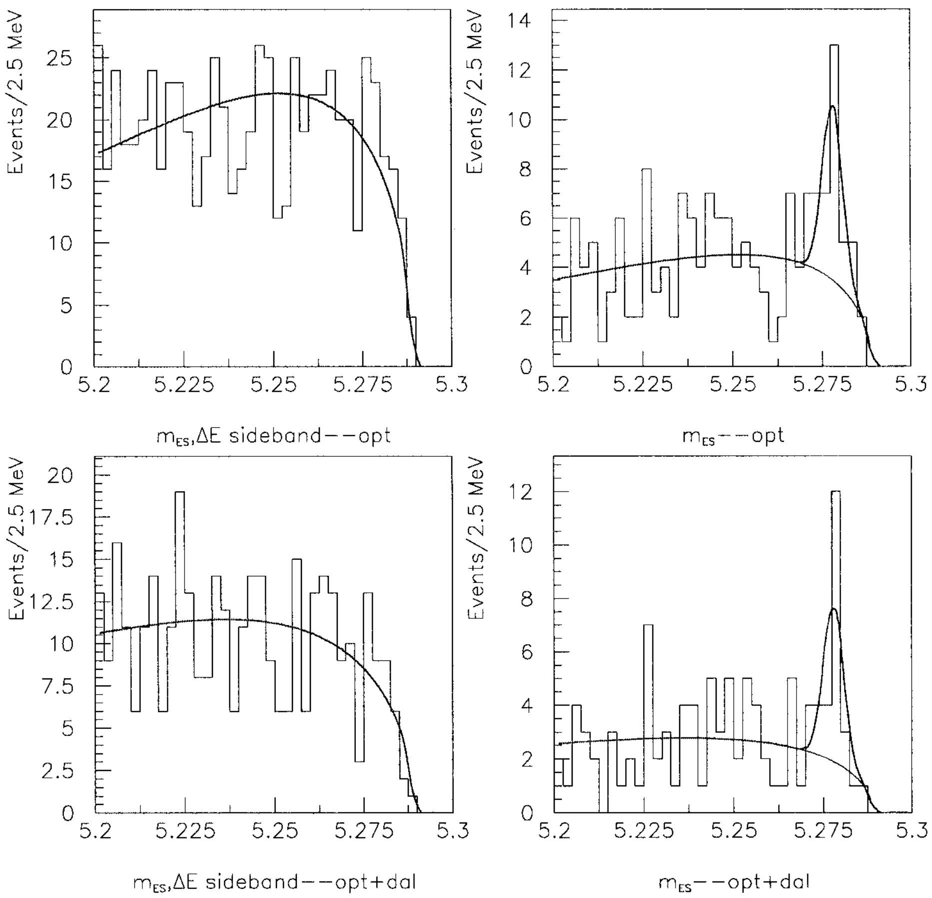

Figure 5.12: Data fit on $B^0 \to J/\psi\eta(\gamma\gamma)K^0_S$ with Argus + Gaussian function, Argus shape parameters are got from ΔE sideband, which is fitted only with Argus function. Top row is without Dalitz plot cuts, ΔE sideband (left), data fit (right); bottom row is with Dalitz plot cuts, ΔE sideband (left), data fit (right).

later (section 5.10.1).

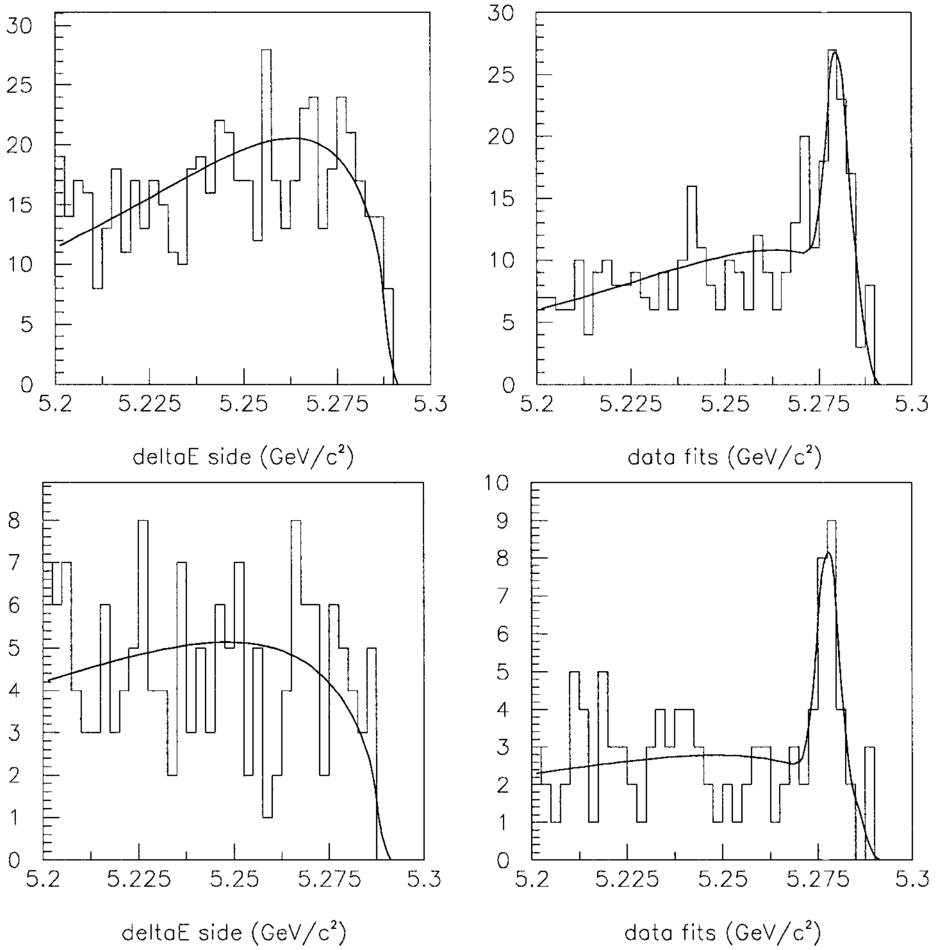

Figure 5.13: Data fit on $B^{\pm} \to J/\psi\eta(\gamma\gamma)K^{\pm}$ with Argus + Gaussian function, Argus shape parameters are got from ΔE sideband, which is fitted only with Argus function. Top row is without Dalitz plot cuts, ΔE sideband (left), data fit (right); bottom row is with Dalitz plot cut, ΔE sideband (left), data fit (right).

mode	Fit results						
	$M_B(MeV/c^2)$	$\sigma(M_B)$	χ^2	N_{bkg}	$\sigma(N_{bkg})$	N_{sig}	$\sigma(N_{sig})$
K^+	5279.9±0.57	2.8	1.15	50.3	3.0	48.7	10.4
K^+ Dalitz	5277.8±0.9	2.8	0.79	11.1	1.3	15.9	5.3
K_S^0	5278.0±1.18	2.82	1.59	18.53	1.66	20.47	6.46
K_S^0 Dalitz	5277.9±0.97	2.82	1.22	9.95	1.21	15.05	5.14

Table 5.7: Data fits with only Argus background shape from ΔE sideband for $B^\pm \to J/\psi\eta(\gamma\gamma)K^\pm$ and $B^0 \to J/\psi\eta(\gamma\gamma)K_S^0$ without and with Dalitz plot cuts. The signal width is fix and the mass of B meson is allowed to vary.

5.9. Systematic Errors

In this section, the systematic errors on the branching ratios are discussed. Included in this study are the uncertainties on the number of $B\bar{B}$ pairs, the branching ratios of the secondary particles, MC efficiency, π^0-veto, mass cut of the η candidate and background parameterization.

5.9.1. Number of $B\bar{B}$ pairs

The total integrated luminosity used for $B \to J/\psi\eta K$ (Table 5.2) is 81.87 fb^{-1}, which corresponds to 89,956,344 $B\overline{B}$ events with statistical, systematic and combined errors of 22,806, 989,520 and 989,782, respectively. This gives a fractional error of 1.10%.

5.9.2. Secondary branching fraction uncertainties

The secondary particle like J/ψ and η in the decay $B \to J/\psi\eta K$, has its own uncertainty in its decay branching ratio. This uncertainty should be propagated into the branching ratio measurement of $B \to J/\psi\eta K$. The uncertainty due to the J/ψ leptonic decays are about 1.68% for electrons and about 1.70% for muons; it is about 0.66% on the decay of $\eta \to \gamma\gamma$; on the decay of $K_S^0 \to \pi^+\pi^-$, the uncertainty is about 0.39%. So the combined systematic error for $B^\pm \to J/\psi\eta(\gamma\gamma)K^\pm$ and $B^0 \to J/\psi\eta(\gamma\gamma)K_S^0$ are 2.48% and 2.52%, respectively.

5.9.3. Monte Carlo statistics

For signal MC, the largest uncertainty is from the limited statistics of reconstructed events from the total signal MC. For $B^{\pm} \rightarrow J/\psi\eta(\gamma\gamma)K^{\pm}$, 3114 (1723) events were reconstructed without (with) Daltiz plot cuts, which gives about 1.79% (2.41%) fractional uncertainty. For $B^0 \rightarrow J/\psi\eta(\gamma\gamma)K^0_S$, 2114(1558) events were reconstructed without (with) Dalitz plot cuts, this gives about 2.17% (2.53%) fractional uncertainty.

5.9.4. Tracking and particle ID

Table 5.8 shows the systematic errors due to the lepton selection of J/ψ taken from Ref. [53], the combined error for both channels is about 1.8%. Table 5.9 shows the systematic errors due to the charged kaon selection following the *BABAR* PID group procedure, the systematic error is about 1.5%. The neutral kaon systematic errors, shown in Table 5.10, are determined by the *BABAR* track efficiencies presented by the track efficiency task force for K^0_S [54]. The systematic error is about 3.0%.

5.9.5. η detection systematics

The η detection systematics are determined from the neutral killing procedure presented on the tools group web page [55], the systematic error is 5.0%. The tracking systematic errors are determined by the track efficiencies presented by the track efficiency task force, a workgroup of *BABAR*, a flat correction factor 0.8% was applied per charged track. For $B^{\pm} \to J/\psi\eta(\gamma\gamma)K^{\pm}$, 3 tracks give a systematic error of 2.4%, while for $B^0 \to J/\psi\eta(\gamma\gamma)K^0_S$, it is about 1.6% for the two tracks.

Lepton (PID selection)	Systematic Error
J/ψ η K+: ee (tight-loose)	2.0%
J/ψ η K+: $\mu\mu$ (loose-loose)	1.6%
J/ψ η K+: Combined	1.8%
J/ψ η Ks: ee (tight-tight)	1.9%
J/ψ η Ks: $\mu\mu$ (loose-loose)	1.6%
J/ψ η Ks: Combined	1.75%

Table 5.8: J/ψ-Lepton PID systematics.

Systematic	Systematic Error
Fitting/counting correction	0.8%
MC truth difference	1.1%
MC statistics	0.2%
Background subtraction	0.56%
Control sample statistics	1.0%
Total $K^{\pm}$ mode PID systematic	1.48%

Table 5.9: Charged Kaon PID systematics.

Systematic	Systematic Error
Tracking error, no DCH hit cut	2.6%
Difference between momentum ≥ 1 GeV/c and no momentum cut	1.5%
Total K^0_S mode PID systematic	3.0%

Table 5.10: Neutral Kaon PID systematics.

5.9.6. π^0-veto

The η candidates are identified by their decay into two photons. π^0-veto is the most effective cut to remove backgrounds to the η selection by eliminating photon pair combinations for which one of the photons forms an invariant mass with any other photon in the event within some range of π^0 nominal mass, 0.135 GeV/c^2. A range of $\pm$ 10 MeV/c^2 ($\pm$ 17 MeV/c^2) is used for $B^0 \to J/\psi\eta(\gamma\gamma)K^0_S$ ($B^\pm \to J/\psi\eta(\gamma\gamma)K^\pm$). Each photon from η is required to have energy $>$ 150 MeV.

Inclusive η with a J/ψ candidate on-peak data (13 fb^{-1}) and Monte Carlo (238,000 events) samples were used to investigate the systematic effects on the π^0-veto cut. For this study the details can be found in Ref. [58].

The procedure used here is:

1. Momentum of the η candidate is divided into 3 bins, (0.3 - 0.6) GeV/c, (0.6 - 0.9) GeV/c and (0.9 - 1.5) GeV/c
2. Each momentum bin, the range cuts of 2, 5, 10, 17, 20 and 25 MeV/c^2 are applied. η signal events number ($N^i_\eta, i = MC, data$), its error ($\sigma^i_\eta, i = MC, data$)

are extracted by a fit for each veto mass range cut with both on-peak data and Monte Carlo samples. Then these numbers are normalized by the number of events without π^0-veto for mid and high momentum ranges, while for low momentum range, it is normalized by 2 Mev/c^2 mass range cut. The numbers of signal and background were extracted by a Gaussian plus polynomial fit in the η mass range of 0.48-0.60 GeV/c^2, The η signal part is extracted only from the Gaussian part of the fit.

3. The ratio of signal events from on-peak data and Monte Carlo sample for each mass range cut is $CF = \frac{N_\eta^{data}}{N_\eta^{MC}}$, and it is used as a correction factor for this cut. The error is $CFErr = CF \times \sqrt{\sum_i (\frac{\sigma_\eta^i}{N_\eta^i})^2}$. Fig. 5.14 shows CF as function of mass range cuts.

4. Signal MC of $B \to J/\psi\eta K$ is divided into three η momentum bins and each bin holds a fraction (f_j, $j = 1,2,3$) for the whole signal sample. The total correction factor is $\sum_j f_j \times CF_j \pm \sqrt{\sum_j (f_j \times CFErr_j)^2}$. The systematic error is just its error over its center value.

The fractions are 20% (18%), 33% (33%), and 46% (48%) for the low, middle, high momentum ranges for charged kaon mode (neutral kaon mode). Table 5.12 (Table 5.11) shows particular CF for the π^0-veto used for $B^\pm \to J/\psi\eta(\gamma\gamma)K^\pm$ ($B^0 \to J/\psi\eta(\gamma\gamma)K_S^0$). The overall correction factor is 1.01 ± 0.08 (0.96 ± 0.08). The systematic error is about 0.8% for both modes.

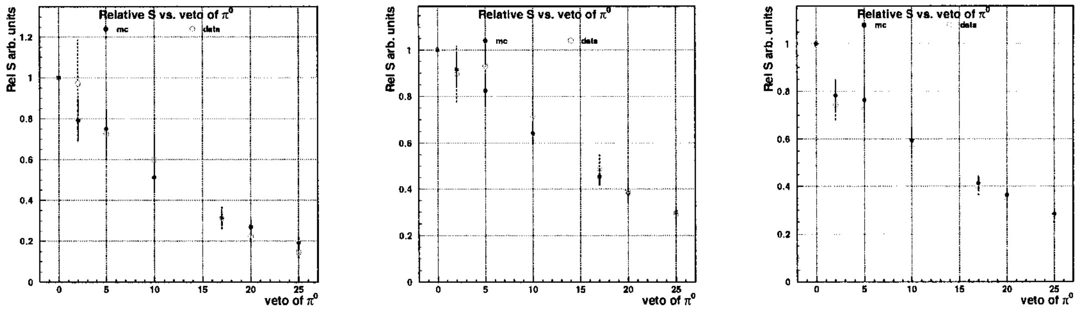

Figure 5.14: Relative signal ratio as a function of the π^0-veto range cut for η candidates in the low (left), middle (middle) and high (right) momentum ranges. middle and high momentum ranges are normalized to non π^0-veto signal event, while for low momentum range, it is normalized to 2 MeV/c^2 cut range.

Momentum Range	Relative signal		Correction Factor
	MC	data	
Low(0.3 - 0.6 GeV/c)	0.512±0.066	0.600±0.120	0.85±0.20
Mid(0.6 - 0.9 GeV/c)	0.642±0.051	0.712±0.091	0.90±0.14
High(0.9 - 1.5 GeV/c)	0.595±0.044	0.565±0.042	1.05±0.11

Table 5.11: Relative ratio of η number in MC and data and correction factor for $B^0 \to J/\psi\eta(\gamma\gamma)K^0_S$.

5.9.7. η mass cut

Table 5.13 shows the Gaussian mean and width of η mass from above inclusive η with a J/ψ study. η mass mean value and width does not agree between Monte Carlo and data.

The procedure to extract the systematic error of η mass cut is (a.) divide the

Momentum Range	Relative Signal		Correction Factor
	MC	data	
Low(0.3 - 0.6 GeV/c)	0.314±0.040	0.313±0.050	1.00±0.20
Mid(0.6 - 0.9 GeV/c)	0.453±0.038	0.485±0.060	0.93±0.14
High(0.9 - 1.5 GeV/c)	0.414±0.032	0.393±0.030	1.05±0.11

Table 5.12: Relative number of the η in MC and data and correction factor for $B^{\pm} \to J/\psi\eta(\gamma\gamma)K^{\pm}$.

Momentum Range	mean	width	mean	width
	Data(GeV/c^2)		MC(GeV/c^2)	
0.6 - 0.9 GeV/c	0.5451	0.0147±0.007	0.5473	0.0120±0.007
0.9 - 1.5 GeV/c	0.5429	0.0175±0.017	0.5475	0.0127±0.008

Table 5.13: Fit parameters for two-photon invariant η mass, which was obtained from a Gaussian plus a polynomial fit on η different momentum ranges.

signal MC into two η momentum ranges, 0.0 - 0.9 GeV/c and 0.9 - 1.5 GeV/c; (b.) varying the width of η invariant mass by one sigma with the on-peak data parameters to get the cut efficiency for each momentum range.

Table 5.14 shows the cut efficiency with the on-peak data fit parameters. The systematic error is determined by a ratio of the half of the difference between efficiencies with ±1 standard deviation on the η mass cut over the efficiency without a variation on the η mass cut. From Table 5.14, the systematic error is 2% for η momentum range of (0.0 - 0.9) GeV/c, and 5% for rest of the η momentum range.

η mass width (MeV/c^2)	fraction
14.7	0.881
14.7 + 0.7	0.864
14.7 - 0.7	0.899
17.5	0.810
17.5 + 1.7	0.854
17.5 - 1.7	0.77

Table 5.14: Fraction of η candidates in the analysis with ± 23 MeV/c^2 mass cut window as the η mass width is varied.

5.9.8. ΔE cut

The systematic errors on the ΔE cut are estimated using the cut variation studies. The cut is varied from 25 MeV to 40 MeV for the charge kaon mode, for the neutral kaon is from 26 MeV to 54 MeV.

The procedure is as the following: a). vary the applied cut and recalculate signal MC efficiency; b). refit the background and data distributions to extract the number of signal events. The systematic error is just half of the maximum difference of ratios of the signal events over signal efficiency divided by the ratio without a variation.

The systematic error for the charged kaon mode is about 7.4%, for the neutral kaon mode is about 8.5%. Table 5.15 (Table 5.16) shows the results of the cut variation with ΔE cuts for charged (neutral) kaon.

ΔE cut (MeV)	N_{bkg}	N_{sig}	eff.	N_{sig}/eff
40	50.7	59.3	0.129	458.7
35	45.7	50.3	0.126	397.7
30	40.0	48.0	0.123	391.6
25	32.3	45.7	0.117	390.8

Table 5.15: Results of the cut variation for ΔE cut for $B^{\pm} \to J/\psi\eta(\gamma\gamma)K^{\pm}$.

ΔE cut (MeV)	# in Sig. Region	N_{sig}	eff(%)	N_{sig}/eff
54	47.0	23.7	10.0	237.0
47	45.0	25.1	9.9	253.5
40	40.0	22.4	9.7	230.9
33	37.0	20.6	9.6	214.6
26	35.0	21.0	9.5	221.1

Table 5.16: Results of the cut variation for ΔE cut for $B^0 \to J/\psi\eta(\gamma\gamma)K^0_S$.

5.9.9. Background parameterization

The uncertainty on the background parameterization was estimated with two different data sidebands sources. For ΔE sideband, the parameter that controls the Argus function shape was varied by ±1 standard deviation. The resulting number of the signal events is determined by this new Argus plus a Gaussian fit on the data. Table 5.17 shows the signal events change and systematic error due to this variation of the Argus shape.

For the second one, the background shape is determined by using an Argus func-

Mode	N_{sig}	ΔN_{sig}	syst. err.
$B^{\pm} \to J/\psi\eta(\gamma\gamma)K^{\pm}$	48.7±10.4	3.3	6.8%
$B^{\pm} \to J/\psi\eta(\gamma\gamma)K^{\pm}$ w/Dalitz	15.9±5.2	1.5	9.4%
$B^{0} \to J/\psi\eta(\gamma\gamma)K^{0}_{S}$	20.5±6.5	1.2	5.7%
$B^{0} \to J/\psi\eta(\gamma\gamma)K^{0}_{S}$ w/Dalitz	15.1±5.1	0.9	6.4%

Table 5.17: Signal events change on the data fit with a standard deviation on the Argus shape parameter using ΔE sideband.

tion fit to an η sideband and refit the data m_{ES} distribution to extract the signal events. The difference between the numbers of signal events with the fits from ΔE sideband Argus shape and η sideband Argus shape is assigned as an additional systematic error. Table 5.18 shows the data fit results, the Argus shape parameter and the systematic error using η sideband.

Mode	N_{sig}	N_{bkg}	Argus shape	syst. err.
Charged Kaon	41.3	57.7 ± 3.1	-60.1±6.1	15.3%
Neutral Kaon	15.1	23.9 ± 2.1	-52.1±9.0	26.4%

Table 5.18: Data fit results using η sideband Argus background shape parameter and the systematic error.

5.9.10. Systematic error from J/ψ polarization and two-body resonance

The MC modeling assumed phase space decay for the three body decay of $B \to J/\psi\eta K$. We do not know if the decay is polarized or if there are quasi-two body resonances in this decay. Since the reconstruction efficiency is likely to vary with a different model, we estimate this uncertainty in the section by calculating the raw efficiency for two different lepton polarizations and the three different Dalitz plot regions. The following situations are considered:

1. 3 body phase space;
2. $\sin^2\theta_l$ for the decay $J/\psi \rightarrow l^+l^-$ polarization, $l = e$ or μ;
3. $1 + \cos^2\theta_l$ for the decay $J/\psi \rightarrow l^+l^-$ polarization, $l = e$ or μ;
4. $20 < M^2(J/\psi\eta) < 22$ (GeV/c^2)^2, $1.5 < M^2(\eta K) < 2.5$ (GeV/c^2)^2;
5. $14 < M^2(J/\psi\eta) < 16$ (GeV/c^2)^2, $2.0 < M^2(\eta K) < 3.0$ (GeV2/c^2)^2;
6. $16 < M^2(J/\psi\eta) < 18$ (GeV/c^2)^2, $3.5 < M^2(\eta K) < 4.5$ (GeV/c^2)^2;

These three different regions of the Dalitz plot are shown in Fig. 5.15. The efficiency of each of these three regions are listed in Table 5.19. The systematic uncertainty is estimated as the difference between the minimum and maximum efficiencies divided by two. The fractional uncertainty is the ratio of the above difference over the phase space efficiency. Table 5.20 shows the systematic errors due to these two sources.

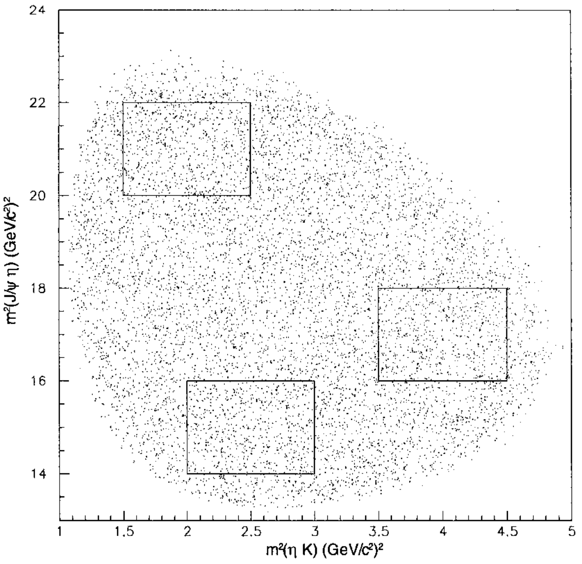

Figure 5.15: Dalitz plot of phase space for the three body decay of $B \to J/\psi\eta K$ showing three regions used for efficiency calculations.

5.9.11. Summary of the systematic errors

Table 5.21 summarized all the above systematic error we discussed above. The errors are assumed to be uncorrelated and they all are added in quadrature.

5.10. Analysis results for branching fraction

5.10.1. Data event yields

The signal events yields are counted as

$$N_{sig} = N_0 - N_{bkg} \tag{5.1}$$

Model	$B^{\pm} \to J/\psi\eta(\gamma\gamma)K^{\pm}$	$B^{0} \to J/\psi\eta(\gamma\gamma)K^{0}_{S}$
Phase Space(flat angle)	$13.49 \pm 0.21\%$	$9.38 \pm 0.20\%$
$20 < M^2_{J/\psi\eta} < 22$, $1.5 < M^2_{\eta\mathrm{K}} < 2.5$	$12.54 \pm 0.74\%$	$9.03 \pm 0.70\%$
$14 < M^2_{J/\psi\eta} < 16$, $2 < M^2_{\eta\mathrm{K}} < 3$	$12.96 \pm 0.77\%$	$9.52 \pm 0.73\%$
$16 < M^2_{J/\psi\eta} < 18$, $3.5 < M^2_{\eta\mathrm{K}} < 4.5$	$13.88 \pm 0.78\%$	$10.82 \pm 0.79\%$
$sin^2\theta_{J/\psi \to ll}$	13.61%	9.41%
$(1 + cos^2\theta_{J/\psi \to ll})/2$	13.43%	9.31%

Table 5.19: Model-dependent efficiency.

Syst.Err.	$B^{\pm} \to J/\psi\eta(\gamma\gamma)K^{\pm}$	$B^{0} \to J/\psi\eta(\gamma\gamma)K^{0}_{S}$
J/ψ Pol.	1.3%	0.5%
2-body res.	5.0%	9.5%

Table 5.20: J/ψ polarization and two-body resonance systematic.

where the variables in Eq. 5.1 are defined as,

- N_{sig} = number of signal events
- N_0 = number of events in the signal box
- N_{bkg} = number of events integrated over an Argus fit to m_{ES} in the signal region

The error on N_{sig} is

$$\sigma(N_{sig}) = \sqrt{N_0 + \sigma^2(N_{bkg})}. \tag{5.2}$$

N_{bkg} and its error ($\sigma(N_{bkg})$) are determined by following the procedure listed in section 5.7 and all the fit results and data yields are tabulated in Table 5.7.

sources/mode	$K^{\pm}$	$K^{\pm}$ w/Dalitz	K^0_S	K^0_S w/Dalitz
No. B decays	1.10	1.10	1.10	1.10
Prod.BF	2.48	2.48	2.52	2.52
MC stat.	1.77	2.40	2.17	2.53
Lepton PID	1.75	1.75	1.75	1.75
Charged K PID	1.79	1.79		
Neutral K PID			3.0	3.0
$\eta(2\gamma)$ detection	5.0	5.0	5.0	5.0
π^0 veto	8.1	8.1	8.3	8.3
Charged tracking	2.4	2.4	1.6	1.6
J/ψ pol.	1.3	1.3	0.5	0.5
2 body res.	4.9	0	9.5	0
η mass cut	3.40	3.40	3.14	3.14
Argus param. var.-ΔE	6.8	9.4	5.7	6.4
Argus param. diff.-η SB	15.3	-	26.4	-
ΔE cut	7.4	7.4	8.5	8.5
TOTAL(quadrature)	22.0	16.5*	32.0	15.7*

Table 5.21: Tabulation of systematic errors (%) for the $B^{\pm} \to J/\psi\eta(\gamma\gamma)K^{\pm}$ and $B^0 \to J/\psi\eta(\gamma\gamma)K^0_S$ modes (* The Dalitz total does include an η sideband contribution).

5.10.2. Efficiency correction

The signal efficiency is determined by the signal Monte Carlo events left after the selection criteria are applied. As the data and Monte Carlo events are slight different, these differences are assigned as a correction factor on the signal efficiency. Table 5.22 (Table 5.23) shows the possible sources for the correction factor for charged (neutral) kaon mode. The final signal efficiencies for both modes are in Table 5.24

	Optimized cuts	Optimized + Dalitz cuts
	correction factor	
PID killing	0.88	0.90
Neutral smearing	0.93	0.93
Tracking killing	1.00	1.00
π^0-veto	1.01	1.01
total correction factor	0.83	0.85

Table 5.22: Efficiency correction for $B^{\pm} \to J/\psi\eta(\gamma\gamma)K^{\pm}$.

	Optimized cuts	Optimized + Dalitz cuts
	correction factor	
PID killing	0.98	0.98
Neutral smearing	0.91	0.91
K_S^0 efficiency correction	1.05	1.05
Tracking killing	1.02	1.02
π^0-veto	0.96	0.96
total correction factor	0.92	0.92

Table 5.23: Efficiency correction for $B^0 \to J/\psi\eta(\gamma\gamma)K_S^0$.

5.10.3. Branching fractions and upper limits

The branching fraction and its statistical error are determined from

$$\begin{aligned} BF &= \frac{N_{sig}}{N_{B\bar{B}} \times \varepsilon \times f}, \\ \sigma(BF) &= \frac{\sigma(N_{sig})}{N_{B\bar{B}} \times \varepsilon \times f}. \end{aligned} \tag{5.3}$$

	Optimized cuts	Optimized + Dalitz cuts
	final efficiency(%)	
$B^{\pm} \longrightarrow J/\psi\eta(\gamma\gamma)K^{\pm}$	10.75	6.00
$B^{0} \longrightarrow J/\psi\eta(\gamma\gamma)K^{0}_{S}$	8.53	6.34

Table 5.24: Final Monte Carlo efficiency after all the correction factors.

where ε is the Monte Carlo final efficiency (see Table 5.24) and f is the product of secondary branching fractions. For $B^{\pm} \longrightarrow J/\psi\eta(\gamma\gamma)K^{\pm}$, $f_{K^+} = 0.04657$, which consists of J/ψ lepton decays and $\eta \longrightarrow 2\gamma$; for $B^{0} \longrightarrow J/\psi\eta(\gamma\gamma)K^{0}_{S}$, $f = 0.03194$, which comes from the secondary decay of $K^{0}_{S} \longrightarrow \pi^{+}\pi^{-}$ and the other two secondary decays like charged modes. Table 5.25 shows the branching fraction for each mode of $B \longrightarrow J/\psi\eta K$. The upper limit on the branching fraction is defined in the presence of background and with a confidence level. If the total number of events observed in the signal box is N_0 and the estimated error on the background is σ_b (combining both statistical and systematic error), then the number of signal events, N, that represents

	$BF(10^{-5})$
$B^{\pm} \longrightarrow J/\psi\eta(\gamma\gamma)K^{\pm}$	$10.81 \pm 2.31(stat.) \pm 2.37(syst.)$
$B^{\pm} \longrightarrow J/\psi\eta(\gamma\gamma)K^{\pm}$ w/Dalitz cut	$6.31 \pm 2.11(stat.) \pm 1.04(syst.)$ *
$B^{0} \longrightarrow J/\psi\eta(\gamma\gamma)K^{0}_{S}$	$8.35 \pm 2.64(stat.) \pm 2.67(syst.)$
$B^{0} \longrightarrow J/\psi\eta(\gamma\gamma)K^{0}_{S}$ w/Dalitz cut	$8.26 \pm 2.82(stat.) \pm 1.30(syst.)$ *

Table 5.25: Measured branching fractions for $B \longrightarrow J/\psi\eta K$ (* The Dalitz total does include an η sideband contribution).

a $(1-\epsilon)$ upper limit confidence level, is determined from

$$\epsilon = \frac{\sum\limits_{n=0}^{N_0} \frac{1}{\sqrt{2\pi}\sigma_N} \int\limits_0^{\infty}\int\limits_0^{\infty} e^{-\left(\widetilde{n}_{\mathrm{b}}+\widetilde{n}_{\mathrm{s}}\right)} \frac{\left(\widetilde{n}_{\mathrm{b}}+\widetilde{n}_{\mathrm{s}}\right)^n}{n!} e^{-\frac{\left(N_{\mathrm{bkg}}-\widetilde{n}_{\mathrm{b}}\right)^2}{2\sigma_{\mathrm{b}}^2}} e^{-\frac{\left(N-\widetilde{n}_{\mathrm{s}}\right)^2}{2\sigma_N^2}} d\widetilde{n}_{\mathrm{b}} d\widetilde{n}_{\mathrm{s}}}{\sum\limits_{n=0}^{n_0} \int\limits_0^{\infty} e^{-\widetilde{n}_{\mathrm{b}}} \frac{\left(\widetilde{n}_{\mathrm{b}}\right)^n}{n!} e^{-\frac{\left(N_{\mathrm{bkg}}-\widetilde{n}_{\mathrm{b}}\right)^2}{2\sigma_{\mathrm{b}}^2}} d\widetilde{n}_{\mathrm{b}}}, \tag{5.4}$$

where σ_N is the total fractional systematic error (see Table 5.21) $\times N$. This assumes the statistical and systematic errors are Gaussian and the upper limit is formed by convoluting the Poisson distribution of the number of observed events with two Gaussians that represent the background and acceptance uncertainties.

We also calculate the probability for a null hypothesis (P-value), which is defined as the Poisson probability that the estimated number of background events fluctuates to the observed number of events N_0 or greater,

$$P = \sum_{n=N_0}^{\infty} \frac{(N_{bkg})^n e^{-N_{bkg}}}{n!} \tag{5.5}$$

Table 5.26 shows a P-Value range with a variation of background $(\sigma(N_{bkg}))$ and at 90% confidence level $(\epsilon = 0.1)$, the signal events number N and its upper limit for each mode of $B \to J/\psi\eta K$.

	N_0	$N_{bkg} \pm \sigma(N_{bkg})$	P-value	N	90% C.L. upper limit
$B^{\pm} \to J/\psi\eta(\gamma\gamma)K^{\pm}$	99	50.3 ± 3.0	(0.09 - 1.42)$\times 10^{-8}$	70.0	15.5×10^{-5}
$B^{0} \to J/\psi\eta(\gamma\gamma)K^{0}_{S}$	39	18.5 ± 1.7	(0.23 - 1.3)$\times 10^{-4}$	34.5	14.1×10^{-5}

Table 5.26: The P-value for null hypothesis, the number of signal events N and its branching fraction upper limit at the 90% confidence level for each mode of $B \to J/\psi\eta K$.

5.11. X particle search

In this section, search for $X \to J/\psi\eta$ is performed by using the same dataset and selection criteria as the decay $B \to J/\psi\eta K$.

X particle search is conducted with charged and neutral $B \to J/\psi\eta K$ channels with decay of $X(3870) \to J/\psi\eta(\gamma\gamma)$. Fig. 5.16 shows the invariant two body mass of $J/\psi\eta$ for each mode, and Fig. 5.17 shows the summary plot for both modes. These plots are made without a Dalitz plot cut and are plotted in 6 MeV/c^2 bins.

From Fig. 5.17, there is no evidence for X(3872). Also since there are very few events for neutral channel in X(3872) mass region, only the charged mode is used to set the upper limit for $B^- \to X(3872)K^-, X(3872) \to J/\psi\eta$.

5.11.1. Monte Carlo efficiency

10,000 Monte Carlo signal events were generated, with all the cuts listed in Table 5.2 and $3.850 < M(J/\psi\eta(\gamma\gamma)) < 3.890$ GeV/c^2, about 1417 are left in the signal

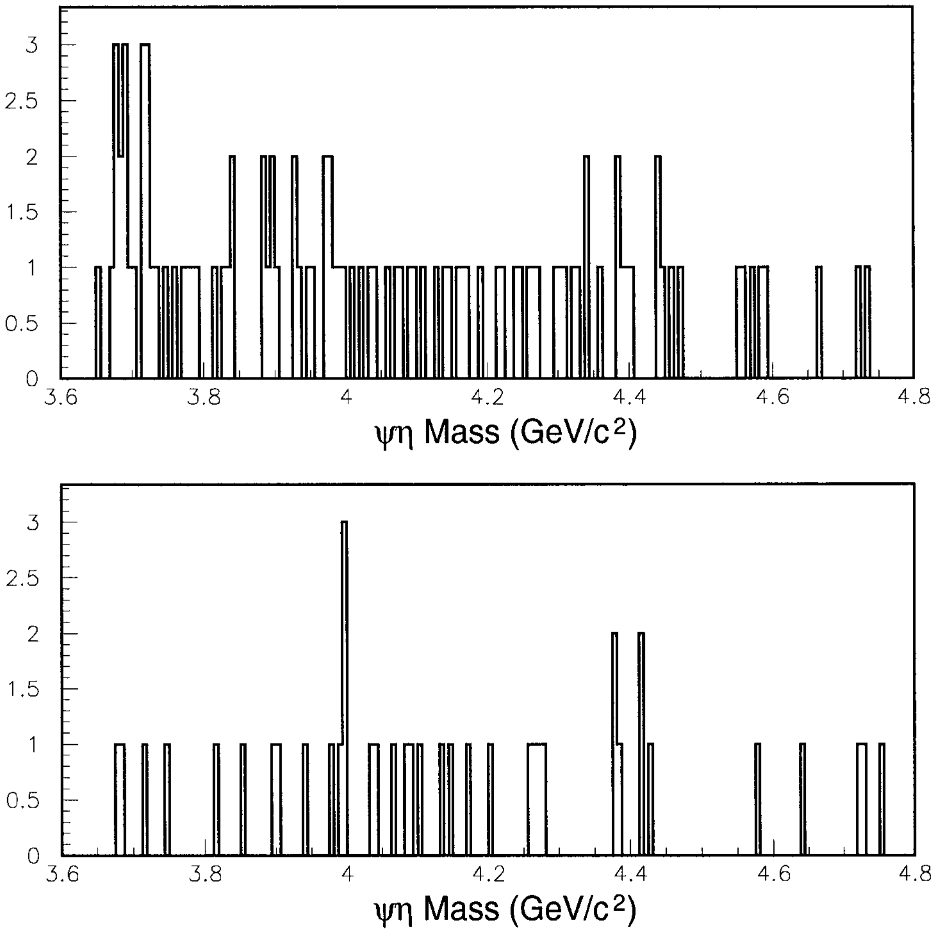

Figure 5.16: The $J/\psi\eta$ distribution of the charged (upper) and neutral (lower) B modes.

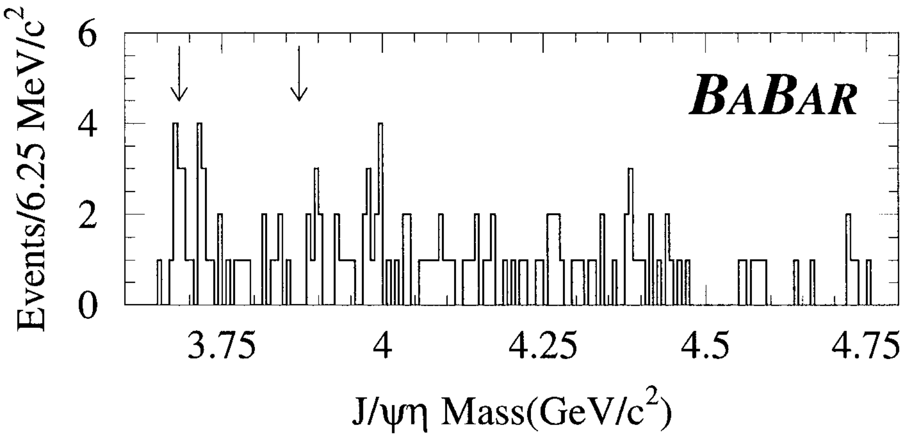

Figure 5.17: The summed $J/\psi\eta$ mass distributions from the charged and neutral B modes.

region. This results in the raw efficiency of $(14.17 \pm 3.8)\%$. Fig. 5.18 shows the distribution of signal MC two-body invariant mass of $J/\psi\eta$. With the efficiency correction factor from Table 5.22 the final Monte Carlo efficiency is $(11.73 \pm 3.8)\%$.

5.11.2. Fit results

The procedure used here is the same as the analysis $B \to J/\psi\eta K$. We fit the m_{ES} distribution of on-peak data with an Argus plus a Gaussian function, and the Argus shape parameters are determined from the ΔE sideband. Fig 5.19 shows Argus shape overlaid with ΔE sideband (left) and a fit with on-peak data (right) with shape parameters from ΔE sideband. The background events are estimated to be 3.066 ± 0.704 and in the signal box there are only 3 events.

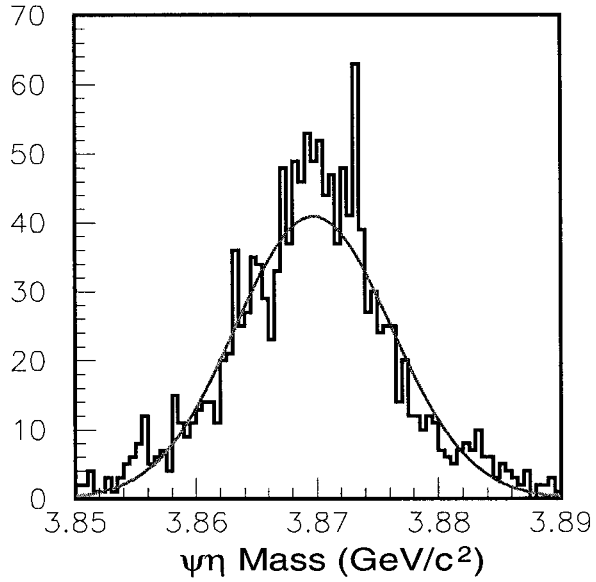

Figure 5.18: The Monte Carlo $J/\psi\eta$ mass distributions for $X(3872) \to J/\psi\eta(\gamma\gamma)$.

5.11.3. Systematic error

Compared to the main $B \to J/\psi\eta K$ analysis, only the $J/\psi\eta$ signal mass region is used in the search of X(3872) analysis. Due to the similarities, the systematic error for X(3872) analysis should be almost the same as for analysis $B^{\pm} \to J/\psi\eta(\gamma\gamma)K^{\pm}$, the only difference for these two analyses appears in the signal Monte Carlo events. The final total systematic error is 22.3%.

5.11.4. Upper limit for $X(3872) \to J/\psi\eta$

Followed the procedure introduced in section 5.10.3, at 90% confidence level, the number of signal events is about 3.77 with a systematic error 22.3%, $N_0 = 3$ and $N_{bkg} = 3.07 \pm 0.70$. The resulting 90% C.L. branching fraction upper limit is

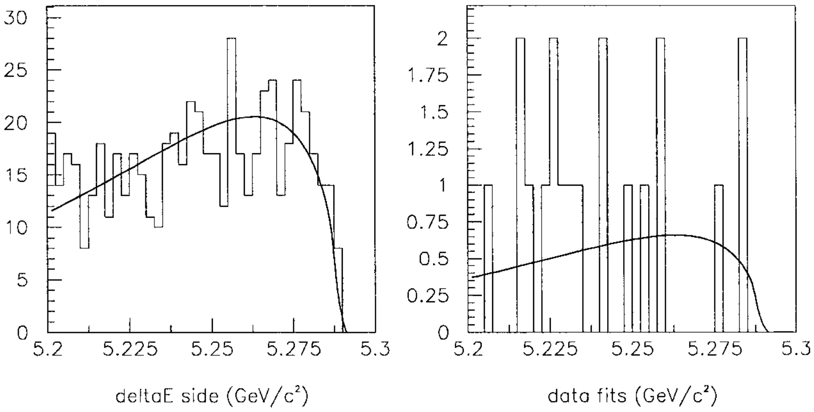

Figure 5.19: The $m_{\rm ES}$ distributions for ΔE sideband (left) and on-peak data (right) for the events in the X(3872) mass region, both with fit overlaid.

7.67×10^{-6}.

5.11.5. Some cross checks with two body invariant mass of $\eta J/\psi$

Check of $\psi(3680) \to \eta J/\psi$

Signal Monte Carlo of $B^{\pm} \to \psi(3680)K^{\pm}$ with $\psi(3680) \to \eta J/\psi$ is used to estimate optimized cuts efficiency. The raw Monte Carlo efficiency is about 17% with an additional $M(\eta J/\psi) < 3.71$ GeV/c^2 cut. With the correction factors, the final Monte Carlo efficiency is about 14%. This results in about 12.1 signal events expected in the two body mass region $M(\eta J/\psi) < 3.71$ GeV/c^2 with optimized cuts. We observed about 15 events in the signal box. Data and Monte Carlo expectation are in good agreement.

We also check the yields of $\psi(3680)$ from inclusive J/ψ Monte Carlo sample. The total inclusive J/ψ Monte Carlo yield is about 347 events. As data luminosity is about half of the inclusive J/ψ Monte Carlo sample, the yield on the data is expected to be half of the 347 events. In data, we only observed 99 events in data. This might be due to mode dependence as discussed in section 5.6.

Check of $J^{PC} = 1^{--}\eta J/\psi$

To search for $J^{PC} = 1^{--}\eta J/\psi$ states and to verify the existence of $B^{\pm} \to \psi(3680)K^{\pm}$, $\psi(3860) \to \eta J/\psi$, the helicity angle cuts are applied. These can exactly determine a parity conserving decay of a $J^{PC} = 1^{--}$ resonance into $\eta J/\psi$ and a J/ψ decay into leptons. The square of the amplitude is,

$$|M|^2 = (\sin\theta_{J/\psi})^2(\cos^2(\phi_{e/\mu}) + \cos^2\theta_{e/\mu}\sin^2(\phi_{e/\mu})), \tag{5.6}$$

where $\theta_{J/\psi}$ is the helicity angle of the J/ψ in the rest frame of $\psi(3680)$ and $(\theta_{e/\mu}, \phi_{e/\mu})$ are the helicity angles of the lepton in the J/ψ rest frame. As the acceptance of the $\cos_{J/\psi}$ and $\sin_{J/\psi}$ for vector 1^{--} component is flat, non-$1^{--}\eta J/\psi$ vector background can be reduced by using the cuts of $|\cos\theta_{e/\mu}| > 0.8$ and $|\cos\theta_{J/\psi}| < 0.8$. Fig 5.20 shows the distribution of two body invariant mass of $\eta J/\psi$ after these two helicity angles cuts (combined with the helicity angle cut of photon in η frame (upper plot) and lepton ID requirements cut (bottom plot for both cuts applied), other regular cuts are removed). From Fig. 5.20, there are some $\psi(3680)$ events, but few events are

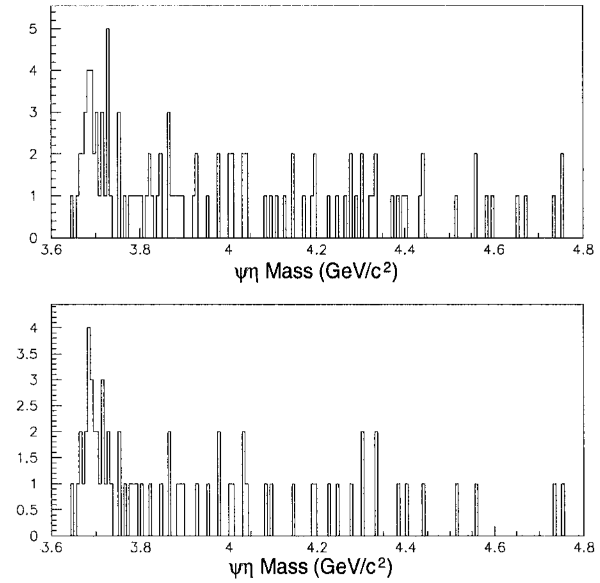

Figure 5.20: The distribution of two body invariant mass of $\eta J/\psi$ with helicity angle cuts. The upper plot is combined with only photon helicity angle cut, the bottom one is combined with photon helicity angle cut and lepton PID cut.

above $\psi(3680)$.

5.12. Some additional studies

5.12.1. Removing $B \to \psi' K$ events

In this study, $\psi' \to J/\psi\eta$ events (the intermediate resonance of two body mass of $\eta J/\psi$) are removed. An additional cut of $M(\eta J/\psi) > 3.75$ GeV/c^2 is applied to both channels along with other optimized cuts. We refit the $m_{\rm ES}$ plots using backgrounds shape determined by ΔE sideband. The results are shown in Table 5.27.

mode	$K^{\pm}$	K^0_S
N_0	84	35
N_{bkg}	45.4 ± 2.9	18.5 ± 0.5
N_{sig}	37.5	16.5
P-Value	2.0×10^{-6}	5.6×10^{-5}
Significance	4.75σ	4.1σ

Table 5.27: Data fit results for $B \to J/\psi\eta K$ without intermediate two body resonance of ψ'.

The number of signal events for both modes decreases about 20%, which is consistent with the PDG value. For the neutral mode, the statistical significance increases, in fact this is due to its low statistics.

5.12.2. η signal check

To make sure $\eta \to 2\gamma$ signal events exist after final selection for $B \to J/\psi\eta K$, we used a logic "NOT" on the η mass sideband. We know there are not many η

signal events in the mass sideband of η. If we can verify that there are not many $B \to J/\psi\eta K$ signal events left with η sideband, then the signal events appearing with η signal region are really true η signal events.

As the mass region for an η candidate is limited ($0.470 < M(2\gamma) < 0.620$ GeV$/c^2$), two very narrow η mass region are used, $0.470 < M(2\gamma) < 0.493$ GeV$/c^2$ and $0.597 < M(2\gamma) < 0.620$ GeV$/c^2$. With these two sideband regions, the total area used to estimate the background is approximated to the area used for the background under the signal region $|M(2\gamma) - 0.547| < 0.023$ GeV$/c^2$. Fig. 5.21 and 5.22 shows the results got from the these two sideband windows for ΔE and m_{ES}. We observed the signal events peak disappears when the η mass sidebands were used.

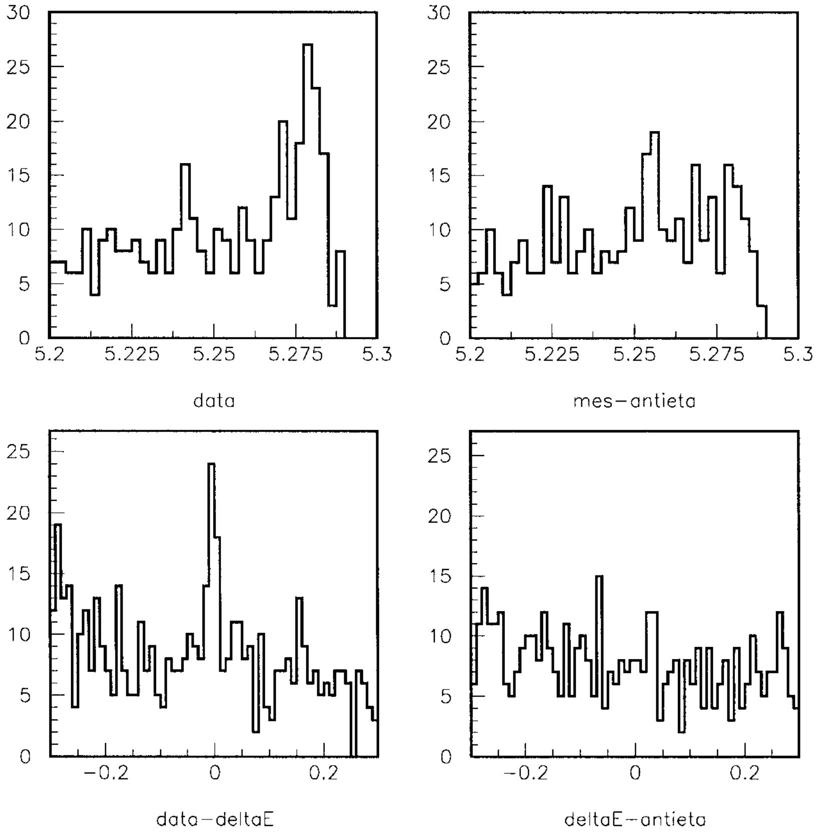

Figure 5.21: The charged decay mode plots for m_{ES} (both upper plots) and ΔE (both lower plots) with the 2γ invariant mass in the η signal region (both left plots) and sideband region (both right sideband plots).

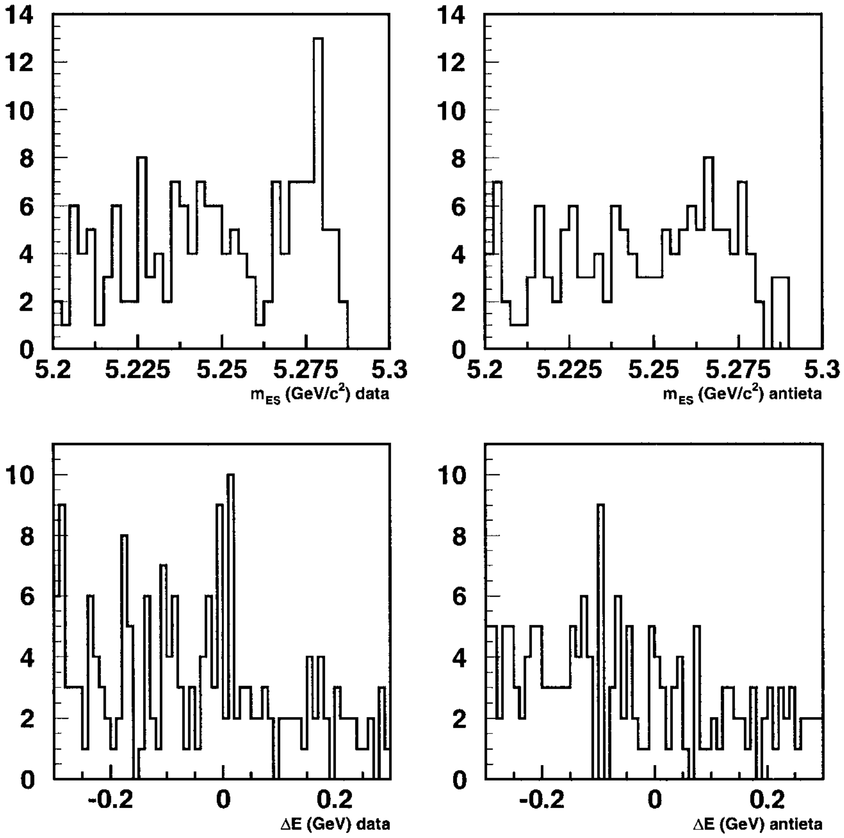

Figure 5.22: The neutral decay mode plots for m_{ES} (both upper plots) and ΔE (both lower plots) with the 2γ invariant mass in the η signal region (both left plots) and sideband region (both right sideband plots).

Chapter 6

Analysis of $B^{\pm} \to DK^{\pm}$

In this chapter, the analysis of the decay $B^{\pm} \to DK^{\pm}$ with $D^0/\bar{D}^0 \to \pi^+\pi^-\pi^0$ is described. Data samples, event selection criteria, parameterization of the maximum likelihood fit, data fit, and systematic errors are included.

6.1. Physics motivation

This decay mode can be used to measure CP angle γ (see chapter 2), due to the interference between $b \to c\bar{u}s$ and $b \to u\bar{c}s$ decays into a common final state. As this mode has a high background, an essential first step is to develop the techniques necessary to suppress the background, and to get the branching ratio and decay rate asymmetry of this decay chain.

6.2. Data samples

Table 6.2 shows the data and Monte Carlo samples used in this analysis. The signal MC events are generated according to the measured D^0 Dalitz plot distribution [56]. In addition, about 70,000 signal MC events are generated with flat phase space distribution for the D^0 decay. The analysis procedure was developed using *BABAR*'s first 168.3 fb^{-1}. Additional dataset of 39.0 fb^{-1} was added later, for which the whole data was refitted. but the systematic errors used were obtained only from the 168.3 fb^{-1} sample.

Event sample	$B^{\pm} \to DK^{\pm}$
B^+B^-	509.2 fb^{-1}
$B^0\bar{B}^0$	513.0 fb^{-1}
$c\bar{c}$	165.9 fb^{-1}
uds	170.0 fb^{-1}
On-peak data	207.3 fb^{-1}
Off-peak data	21.1 fb^{-1}
$B^{\pm} \to DK^{\pm}$ signal	80,000

Table 6.1: Data samples used for $B \to DK$ with $D \to \pi^+\pi^-\pi^0$.

6.3. Event selection

We first started with four D decay modes: $D \to K^{\pm}\pi^{\mp}K^0_S$, $D \to K^+K^-\pi^0$ and $D \to \pi^+\pi^-\pi^0$, however the first three modes have very low statistics, we only focus on the last one. Although this mode has more statistics, it also has more background due to the fact that most e^+e^- events are dominated by pions, as well as the high combinatoric background associated with π^0 reconstruction.

6.3.1. Reconstruction of B candidate

Of the particles involved in this analysis, the π^0, $D^0/\bar{D}^0$ and $B^{\pm}$ are composite particles that need to be reconstructed from their decay products. The π^0 is reconstructed from its decay to two photons. A $D^0/\bar{D}^0$ candidate is reconstructed from two charged pion tracks and a reconstructed π^0. These two charged tracks must not be identified as loose kaons and must be in the fiducial volume of the *BABAR* detector. A B candidate is reconstructed from a reconstructed $D^0/\bar{D}^0$ particle and a charged kaon track. This track must satisfy the fiducial volume and loose kaon ID criteria.

6.3.2. Event pre-selection

To reduce the size of the raw data sample, we apply some initial cuts which keep most of the signal but remove a large fraction of the background. The cuts we apply are:

1. $|\cos\theta_T| < 0.8$;
2. $R_2 < 0.5$;
3. $5.2 \leq m_{ES} \leq 5.3$ GeV/c^2;

4. $-0.07 < \Delta E < 0.14$ GeV;
5. $1.805 < m_D < 1.924$ GeV/c^2, where m_D is the $D^0/\bar{D}^0$ candidate's invariant mass;
6. all tracks are in the fiducial volume of the detector;
7. the bachelor kaon track has at least 5 DIRC photons;
8. the bachelor kaon candidate passes loose kaon criteria;
9. neither of the $D^0/\bar{D}^0$ daughter tracks meets the loose kaon criteria of the cut-based kaon identification.

In events with multiple B candidates, we select one candidate at random. With all the pre-selection criteria and best candidate selection, about 74% of the events of signal MC, 67% of the $B\bar{B}$ generic MC, 77% of the continuum MC, and 77% of the on-peak data sample, respectively, have only one reconstructed B candidate.

6.4. Analysis strategy

The challenge of the mode $D^0/\bar{D}^0 \to \pi^+\pi^-\pi^0$ is to separate a small number of the signal B events from a much larger background. With a rough study of this mode, we find that the background is mostly dominated by events associated with badly reconstructed π^0. The biggest contribution is the continuum background. To suppress this background, we use a nonlinear multidimensional neural network to combine several variables that have separation power between $B\bar{B}$ and continuum events into a new variable that maximizes the separation of these two populations. We called this variable $N1$.

We also developed another neural network variable ($N2$) to distinguish fake π^0/D^0 candidates from well-reconstructed ones.

With these two variables providing strong separation power to suppress the background, we further maximize the signal sensitivity by using a maximum likelihood fit as the final stage of the analysis.

6.5. Neural network

6.5.1. General principle of neural network

The basic building block of the Neural Network is referred to as a "neuron", in analogy with the human brain. A single neuron j is associated with N input variables x_k and a response, the output z_j. The N inputs are linearly combined according to some weights w_{jk}, giving a signal Z_j that will activate the neuron:

$$Z_j = \sum_{k=1}^{N} w_{jk} x_k + \theta_j, \tag{6.1}$$

where θ_j is the threshold (bias) of the neuron j. The activation is simulated by a nonlinear function which is generally given by the sigmoid function

$$z_j = \frac{1}{1+e^{-Z_j}}. \tag{6.2}$$

We use a multilayer perceptron architecture, where the neurons are put into three layers: an N-node input layer, an N_h-node hidden layer, and a 1-node output layer. The weights giving the strengths of the connections between neurons of adjacent layers are determined by minimizing the error function

$$E = \frac{1}{2n}\sum_{p=1}^{n}(X_{NN} - X_1^p)^2 \tag{6.3}$$

where n is the number of patterns (events in our case), X_1^p is the desired value of the output,

$$X_1^p = \begin{cases} 0 & \text{background} \\ 1 & \text{signal} \end{cases}, \tag{6.4}$$

and X_{NN} is the output, which is defined as a function of the input x_k:

$$X_{NN} = \frac{1}{1+e^{-\sum_{j=1}^{N_h} w_{1j}z_j+\theta_1}}. \tag{6.5}$$

Here θ_1 is the bias of the output layer.

The analysis uses the neural net implementation of the SNNS package [57].

6.5.2. Continuum background suppression

As described in section 6.4, the neural net output variable $N1$ is used to separate continuum background from the signal. The input variables used for $N1$ all provide such separation to some degree. These variables are

1. Legendre Fisher discriminant F_{LGD} (see Fig. 6.1 (left)),
2. $log(|\Delta Z|)$ (see Fig. 6.1 (right)),
3. $|\cos(\theta_T)|$ (see Fig. 6.2),
4. $log(l_{DOCA})$ (see Fig. 6.2),
5. An integer variable T based on electron and muon B flavor tagging. For $\ell = \{e, \mu\}$ we calculate the B^0 flavor probability $P^{\ell}_{B^0}$ in the events in which a tagging lepton was found. T is defined as

$$T = \left\{ \begin{array}{cc} 3 & |P^{\ell}_{B^0} + 0.5| > 0.4 \\ 2 & 0.1 < |P^{\ell}_{B^0} + 0.5| < 0.4 \\ 1 & |P^{\ell}_{B^0} + 0.5| < 0.1 \\ 0 & \text{no lepton was found} \end{array} \right\}, \tag{6.6}$$

where the condition must be satisfied for either $\ell = \mu$ or $\ell = e$. When more than one lepton is found, the largest value of T is used. See Fig. 6.3.

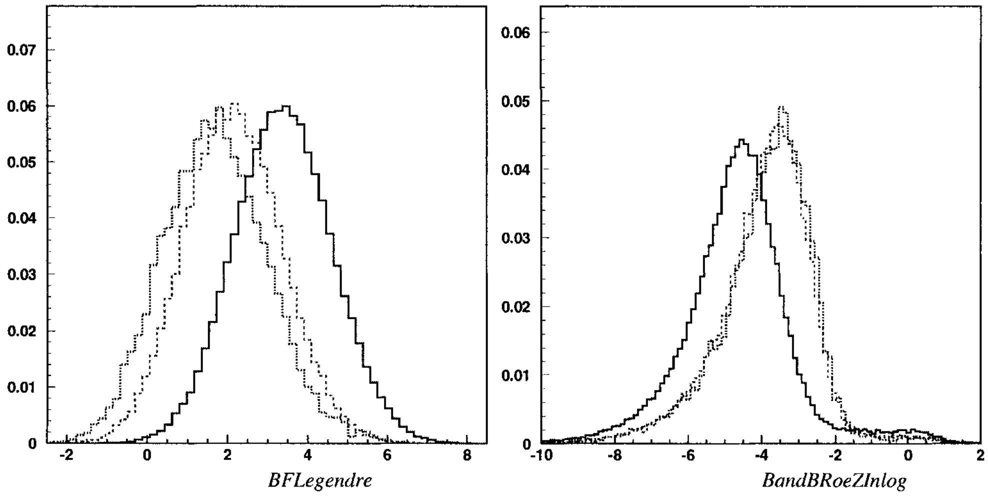

Figure 6.1: The Legendre polynomial Fisher discriminant (left) and $\log(\Delta z)$ (right) distributions of signal (dotted), $B\overline{B}$ background (dashed), and continuum background (solid).

About 13,500 MC signal events and 13,700 continuum events (5700 $c\bar{c}$, 8000 $u\bar{u}/d\bar{d}/s\bar{s}$) were used to train this continuum suppression neural work. Fig. 6.4 shows the $N1$ distribution for all MC samples. Fig. 6.5 shows the efficiency variation by adding the $N1$ variables one by one. These plots are obtained with test samples, which consist of about 3000 MC signal events and about 12,000 events continuum MC samples .

6.5.3. Combinatoric background suppression

The variables used for $N2$ provide separation between badly and well reconstructed π^0 and D^0 candidates, providing separation between signal and background. These

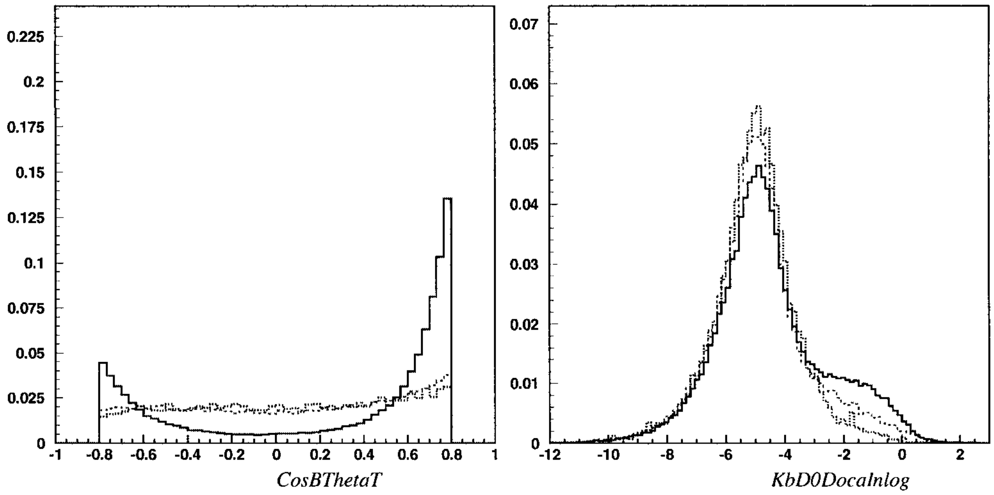

Figure 6.2: $|\cos\theta_T|$ (left) and $\log(l_{DOCA})$ (right) distributions of signal (dotted), $B\overline{B}$ background (dashed), and continuum background (solid). All plots are normalized to unit area.

variables are

1. the invariant mass, laboratory momentum and helicity angle $\theta^{\gamma}_{\pi^0}$ of π^0 (see Fig 6.6), where $\theta^{\gamma}_{\pi^0}$ is the angle between the direction of a photon and the direction of the center-mass-frame in π^0 frame (see Fig. 6.6);
2. the invariant mass m_h of a π^0_h, which is a reconstructed "π^0-like" candidate with a higher energy photon γ_h from the π^0 and any other photons from this event (except the lower energy photon γ_s comes from this π^0) (see Fig. 6.7 and 6.8);
3. the invariant mass m_s of a π^0_s (which is calculated similarly to π^0_h (see Fig. 6.7 and 6.8);

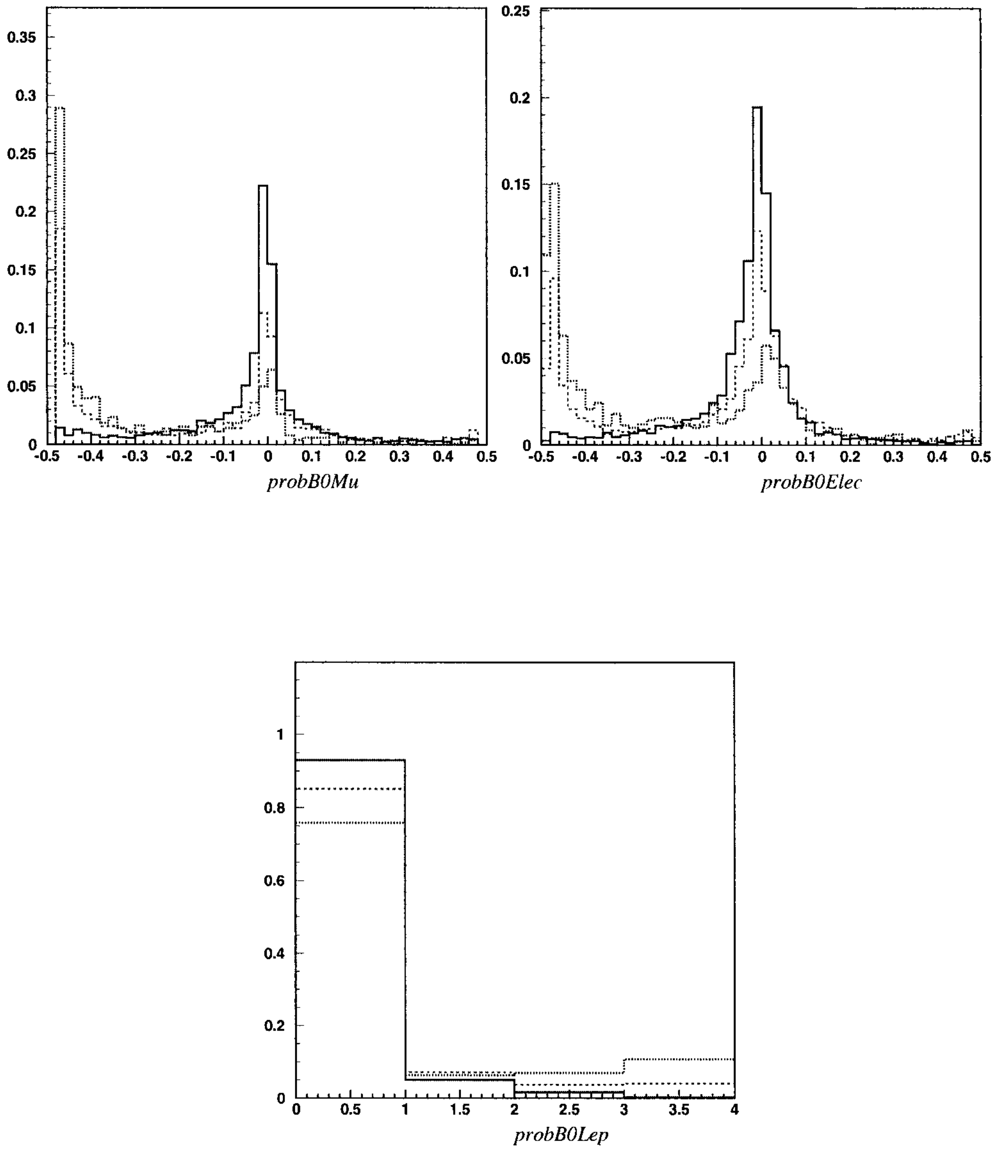

Figure 6.3: Signal (dotted), $B\overline{B}$ background (dashed), and continuum background (solid, blue) distributions of $(P^{\ell}_{B^0} + 0.5)$ multiplied by the reconstructed B charge for $\ell = \mu$ (left) and $\ell = e$ (center), and the integer variable T (right) constructed from $P^{\ell}_{B^0} + 0.5$. All plots are normalized to unit area.

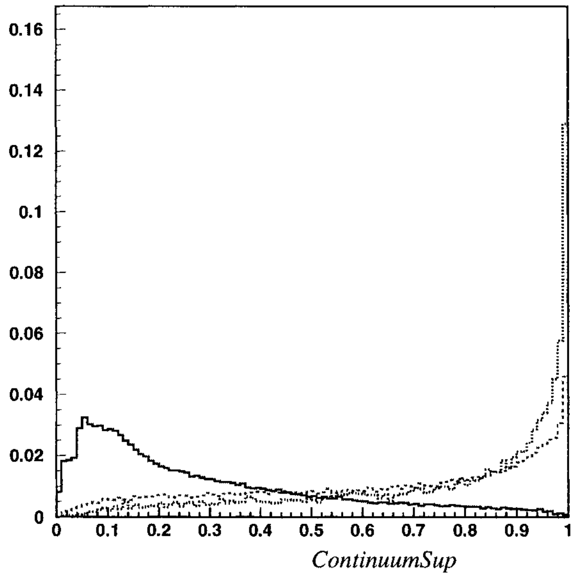

Figure 6.4: The distributions for MC signal (dotted), $B\overline{B}$ background (dashed), and continuum background (solid). All plots are normalized to unit area.

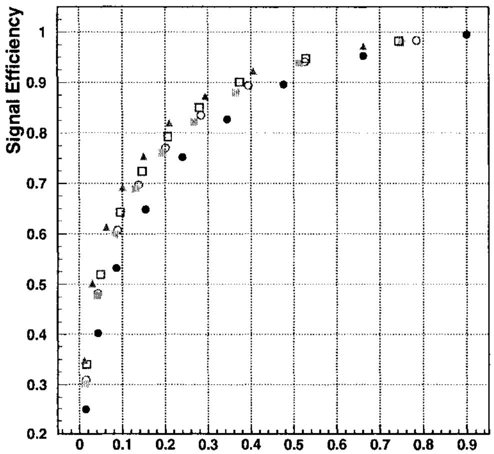

Figure 6.5: The efficiency plot for $N1$ obtained by adding discrimination variables one by one from Fisher (solid circle), ΔZ (empty circle), $\cos\theta_T$ (solid square), l_{DOCA} (empty square), B flavor tagging T (triangle).

4. two cosine values of helicity angles (θ_h,θ_s) from the reconstructed (π^0_h,π^0_s) candidates (see Fig. 6.9);

5. $|\cos\theta_D|$ and $|\cos\theta_{BD}|$ (see Fig. 6.10);

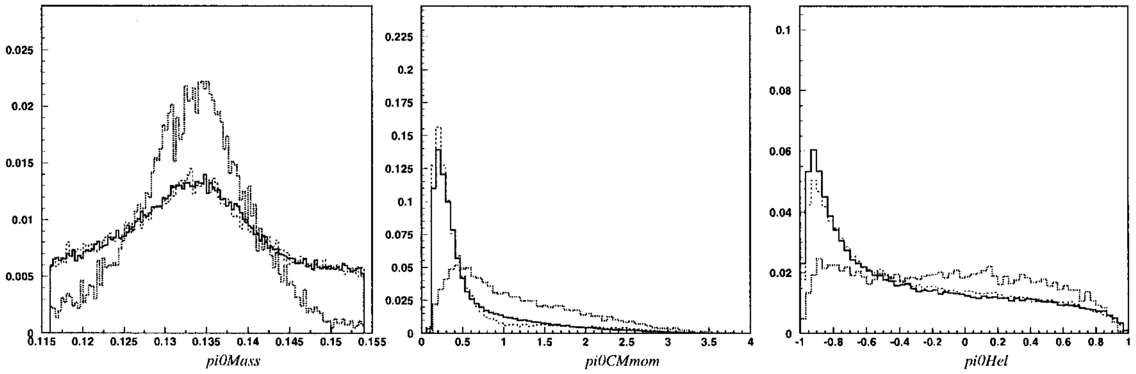

Figure 6.6: π^0 invariant mass (left), lab momentum (middle) and cosine of the π^0 "helicity angle" (right) distributions of signal (dotted), $B\overline{B}$ background (dashed), and continuum background (solid). All plots are normalized to unit area.

$N2$ is trained with about 13,000 signal MC events, 3000 B^+/B^- MC events and 10,000 continuum MC events. Fig 6.11 shows a complete MC result, and Fig 6.12 shows the efficiency by adding additional variables to the first six variables. The test samples are described in section 6.5.2.

6.6. Unbinned maximum likelihood fit

The purpose of this fit is to extract the signal yield with the highest possible sensitivity despite the high background. The fit was performed using the standard

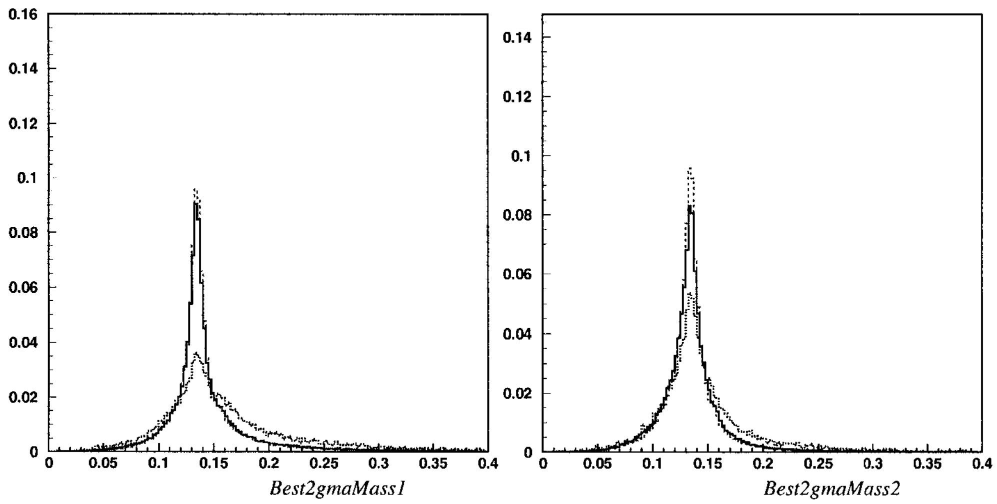

Figure 6.7: m_h (left) and m_s (right) distributions of signal (dotted), $B\overline{B}$ background(dash), and continuum background (solid). All plots are normalized to unit area.

BABAR fit package RooFit [59], which uses Minuit [60] to perform the maximization of the likelihood function numerically.

6.6.1. Event types for maximum likelihood fit

Ten event types were used for categorizing the events. Doing this helps to understand the background and estimate the systematic error.

The ten types are:

1. "DK_D": $B^- \rightarrow DK^-$ signal event with a good (correctly reconstructed) D candidate. These are the only events that are useful for the γ measurement, and hence are the only ones we consider as our true signal.

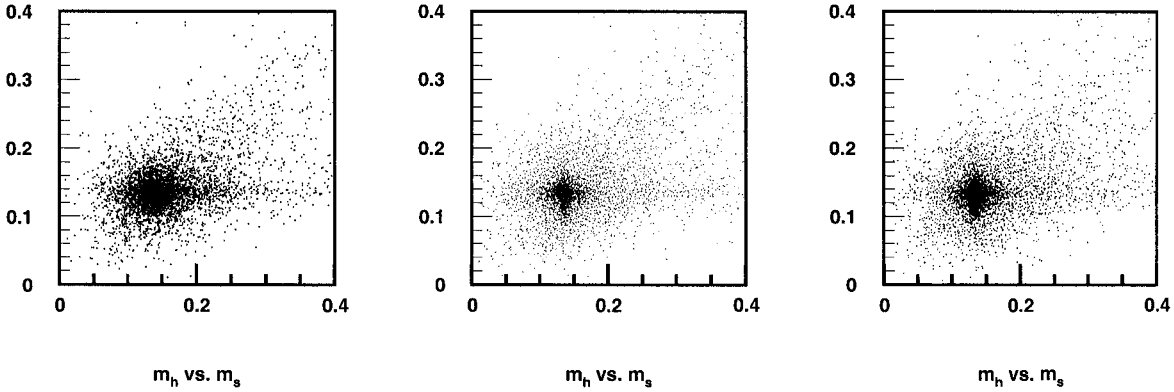

Figure 6.8: m_h vs. m_s distributions of signal (left), $B\overline{B}$ background (center), and continuum background (right).

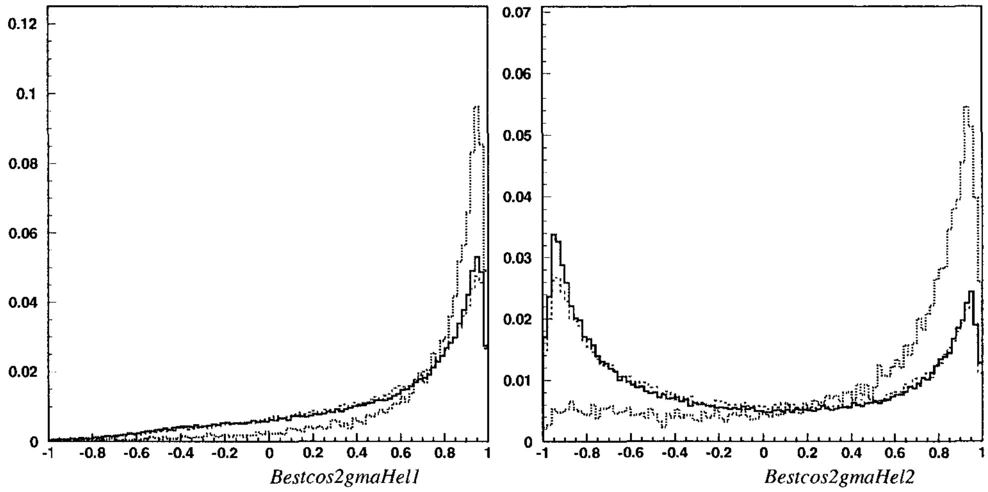

Figure 6.9: $\cos(\theta_h)$ (left) and $\cos(\theta_s)$ (right) distributions of signal (dotted), $B\overline{B}$ background (dashed), and continuum background (solid). All plots are normalized to unit area.

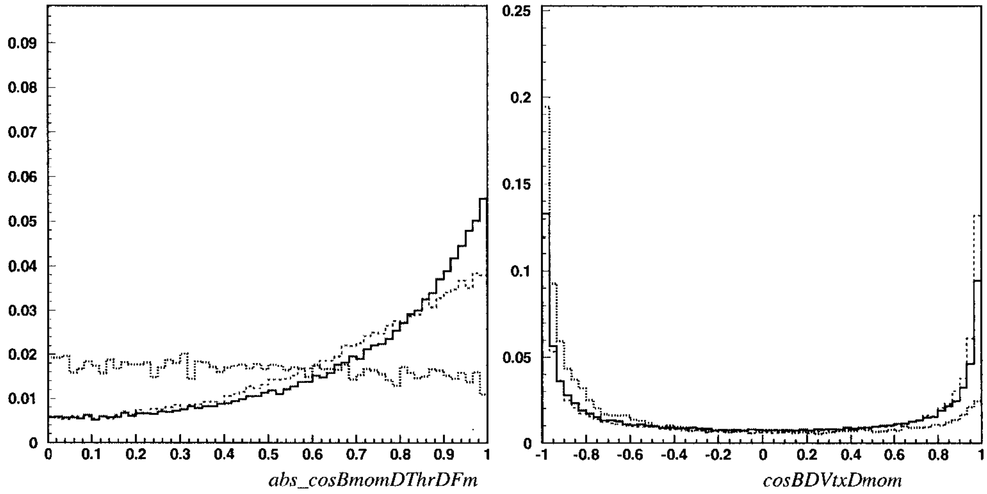

Figure 6.10: $|\cos\theta_D|$ (left) and $\cos\theta_{BD}$ distributions of signal (dotted), $B\overline{B}$ background (dashed), and continuum background (solid). All plots are normalized to unit area.

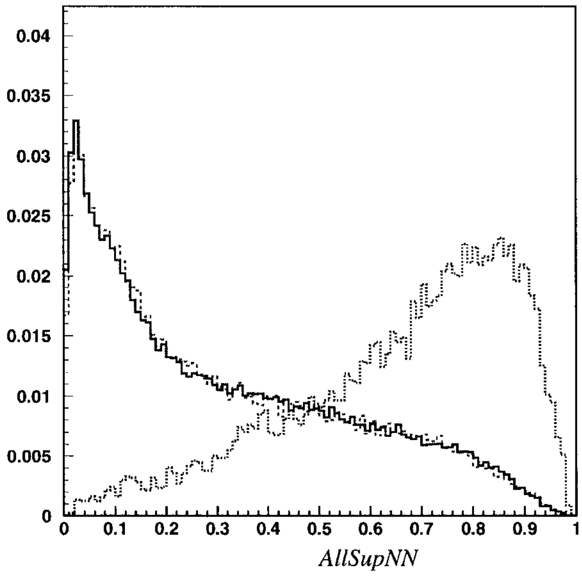

Figure 6.11: The $N2$ distributions for MC signal (dotted), $B\overline{B}$ background (dashed), and continuum background (solid). All plots are normalized to unit area.

2. "$DK_{\not{D}}$": $B^- \rightarrow DK^-$ signal with a bad D. About 16% of all generated signal events end up in this category, usually due to a badly reconstructed π^0.
3. "$D\pi_D$": $B^- \rightarrow D^0\pi^-$ with a good D^0.
4. "$D\pi_{\not{D}}$": $B^- \rightarrow D^0\pi^-$ where the D^0 decays to 3 pions, but is badly reconstructed. This constitutes about 42% of all $D^0\pi^-$, $D^0 \rightarrow \pi^+\pi^-\pi^0$ events. The bachelor candidate is usually a true kaon picked at random from the other B.
5. "DKX": $B^- \rightarrow D^{(*)0}K^{(*)-}$ and $B^0 \rightarrow D^{(*)\pm}K^{(*)\mp}$ where the D^0 decays to modes other than $\pi^+\pi^-\pi^0$. Most of these events have a badly reconstructed D^0 (although sometimes the decay mode is $K^-\pi^+\pi^0$ and all the daughters are correctly reconstructed, but with a wrong PID hypothesis for the kaon), and the bachelor kaon candidate is usually selected correctly.
6. "$D\pi X$": $B^- \rightarrow D^{*0}\pi^-$ or $D^0\rho^-$ and $B^0 \rightarrow D^{(*)\pm}\pi^{\mp}$ or $D^{(*)\pm}\rho^{\mp}$. Most of this background has a badly reconstructed D^0 (although sometimes the decay mode is $K^-\pi^+\pi^0$ and all the daughters are correctly reconstructed, with a wrong PID hypothesis for the kaon), with the bachelor kaon candidate picked at random from the event.
7. "BBC_D": Combinatorial $B\overline{B}$ background with a correctly reconstructed D.
8. "$BBC_{\not{D}}$": Combinatoric $B\overline{B}$ background with a badly reconstructed D.

9. "qq_D": Continuum background with a good D^0. This constitutes about 0.561% of all continuum background.

10. "$qq_{\not D}$": Continuum background with a bad D^0.

We do not include the charmless four-body decay $B^+ \longrightarrow K^+\pi^-\pi^+\pi^0$ decays as a type in this categorization scheme (where all four daughters of the B^+ are reconstructed, and the $\pi^-\pi^+\pi^0$ invariant mass happens to fall within our D^0 mass cut). The total branching ratio for this type is about 6×10^{-6} (from the PDG values), so after the all the cuts it would contribute only $1 - 4$ events in $180\,\mathrm{fb}^{-1}$, which is confirmed by a D^0 sideband study.

6.6.2. Choice of final event selection and fit variables

Our initial intention was to do a 5-dimension fit with the fit variables m_{ES}, ΔE, m_D and the two neural network output variables. However, we found that correlations between these fit variables in the $B\bar{B}$ background event types with the pre-selection criteria (see section 6.3.2) caused biases in the signal yield coming out of the fit. These correlation are shown in the appendix A.1. The correlations that cause the bias were mainly those between m_{ES} and other variables in the DKX and $D\pi X$ backgrounds. To eliminate these correlations, we do not use m_{ES} in the fit. Instead, we apply a tight cut on this variable, as shown below. In addition, excluding m_D from the fit has been shown to have a small effect on the expected sensitivity. Therefore, we cut hard on this variable in the selection, and do not use it in the fit. Loose cuts on ΔE, $N1$ and $N2$ provide some further reduction of the correlations and remove events far away from the signal region. More details about this are provided in the appendix A.1.

A decay $D^0/\bar{D}^0 \rightarrow K^0_S\pi^0$ with three pions is a D^0 decay CP eigenstate and was previously studied (see Ref. [62]). As this mode is not relevant to the method described in Ref. [35], it is excluded here.

These additional cuts are:

1. K^0_S veto, reject if $0.489 < m_{K^0_S} < 0.509$ GeV/c^2;
2. $5.272 < m_{ES} < 5.3$ GeV/c^2;
3. $-0.07 < \Delta E < 0.06$ GeV;
4. $1.83 < m_D < 1.895$ GeV/c^2;
5. $N1 > 0.1$;
6. $N2 > 0.1$;

With these additional final selection criteria, the final reconstructed signal MC efficiency is 11.21%.

6.6.3. Probability density function

The probability density function (PDF) used in the fit is

$$\begin{aligned} P &= N_{DK_D}(P_{DK_D} + R_{DK_{\not{D}}}P_{DK_{\not{D}}}) \\ &+ N_{D\pi_D}(P_{D\pi_D} + R_{D\pi_{\not{D}}}P_{D\pi_{\not{D}}}) \\ &+ N_{B\bar{B}}(R_{DKX}R_{D\pi X}P_{DKX} + R_{D\pi X}P_{D\pi X} \\ &+ (1 - R_{D\pi X}(1 + R_{DKX})P_{BBC_{\not{D}}}) + R_{BBC_D}P_{BBC_D}) \\ &+ N_{qq_{\not{D}}}(P_{qq_{\not{D}}} + R_{qq_D}P_{qq_D}), \end{aligned} \tag{6.7}$$

where N_j is the number of events of type j, $N_{B\bar{B}}$ is the sum of the numbers of events of type $D\pi X$, DKX and $BBC_{\not{D}}$, and R_j are defined as

1. $R_{DK_{\not{D}}}$ is the ratio of $N_{DK_{\not{D}}}/N_{DK_D}$;
2. $R_{D\pi_{\not{D}}}$ is the ratio of $N_{D\pi_{\not{D}}}/N_{D\pi_D}$;
3. $R_{D\pi X}$ is the ratio of $N_{D\pi X}/N_{B\bar{B}}$;
4. R_{DKX} is the ratio of $N_{DKX}/N_{D\pi X}$;
5. R_{BBC_D} is the ratio of $N_{BBC_D}/N_{B\bar{B}}$;
6. R_{qq_D} is the ratio of $N_{qq_D}/N_{qq_{\not{D}}}$.

The function P_j is the PDF for the events of type j. Under the assumption of no, or very small, correlation between the fit variables, for each type j, P_j can be write as the product of one-dimensional PDFs. For a PDF P_j with three fit variables:

$$P_j(\Delta E, N1, N2) = \mathcal{E}_j(\Delta E)\, \mathcal{Q}_j(N1)\, C_j(N2). \tag{6.8}$$

To extract the parameters $\hat{\theta}$ (also called floating parameters) that are described in section 4.2, we minimize the negative log of the extended likelihood

$$\mathcal{L} = \frac{e^{-\bar{N}}\bar{N}^N}{N!} \prod_{i=1}^{N} P(i), \tag{6.9}$$

here N is the number of the observed events and $\bar{N}$ is the sum of the numbers of the events for all types:

$$\begin{aligned} \bar{N} &= N_{DK_D}(1 + R_{DK_{\not{D}}}) + N_{D\pi_D}(1 + R_{D\pi_{\not{D}}}) \\ &+ N_{B\bar{B}}(1 + R_{BBC_D}) + N_{qq_{\not{D}}}(1 + R_{qq_D}). \end{aligned} \tag{6.10}$$

6.6.4. Parameterization of the probability density function

From Eq. 6.8, P_j is the product of one-dimensional functions of ΔE, $N1$ and $N2$. The parameterizations of these functions, which are obtained from Monte Carlo, are described here.

Parameterization of $\mathcal{E}_j(\Delta E)$

The functional forms for each type event j are shown in Table 6.2. The results of the fits to the MC distributions of ΔE for each type j are shown in Figs. 6.13 through 6.17. All the plots are obtained after the final event selection criteria.

Event type	$\mathcal{E}(\Delta E)$ functional form
DK_D	$G+P$
$DK_{\not D}$	$G+P$
$D\pi_D$	$G+P$
$D\pi_{\not D}$	$G+P$
$D\pi X$	$G+P$
DKX	$G+G+P$
BBC_D	G
$BBC_{\not D}$	P
qq_D	P
$qq_{\not D}$	P

Table 6.2: Functional forms of the PDFs of each event type, indicated with G = Gaussian and P = 2nd order polynomial.

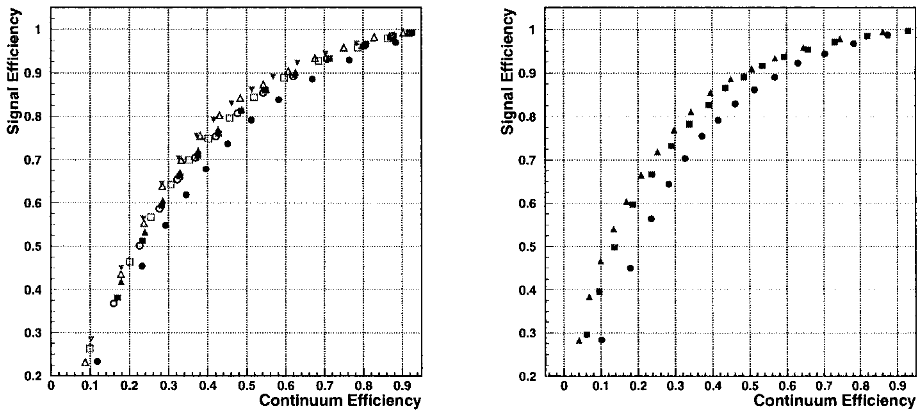

Figure 6.12: Signal efficiency vs. continuum efficiency when applying cuts on the $N2$ variable, computed with different input variables. left plot: p_{π^0} (solid circle), $\cos(\theta_{\pi^0})$ (empty circle), m_{π^0} (solid square), m_h (empty square), m_s (solid up triangle), $\cos(\theta_h)$ (empty up triangle), $\cos(\theta_s)$ (solid down triangle). right plot: All first seven π^0 variables (solid circle), adding $|\cos\theta_D|$ (solid square), and adding $\cos\theta_{BD}$ (solid triangle).

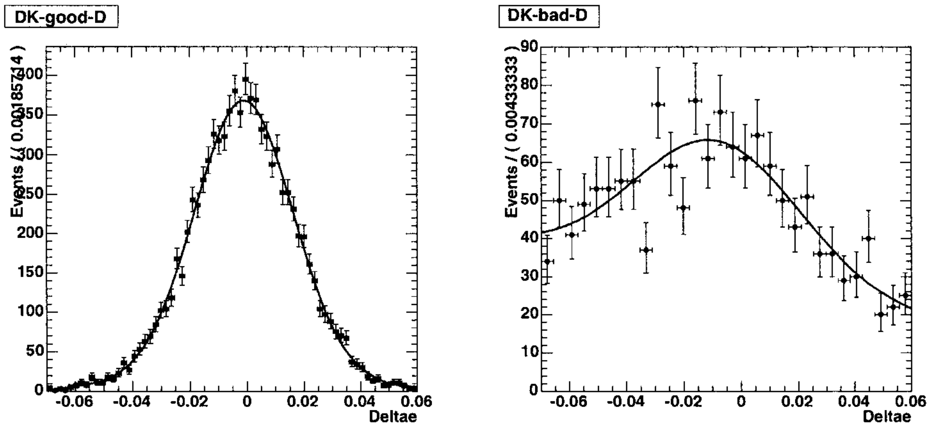

Figure 6.13: The distributions of ΔE for DK_D (left) and $DK_{\not{D}}$ (right) MC.

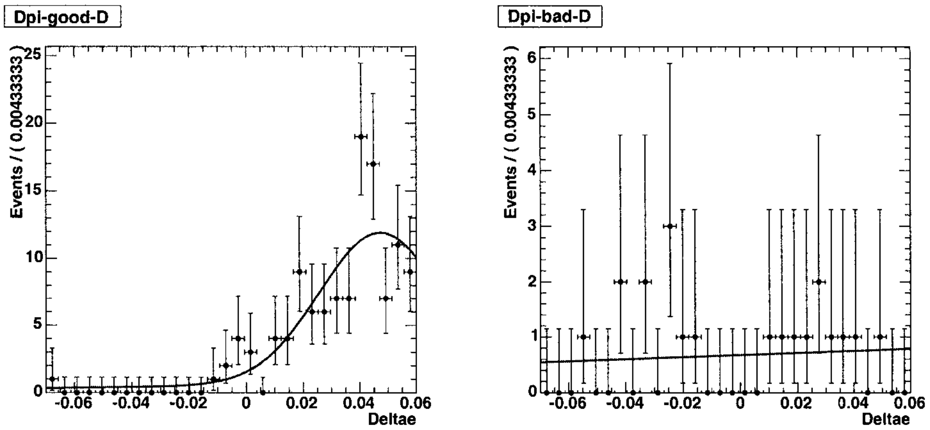

Figure 6.14: The distributions of ΔE for $D\pi_D$ (left) and $D\pi_{\not{D}}$ (right) MC.

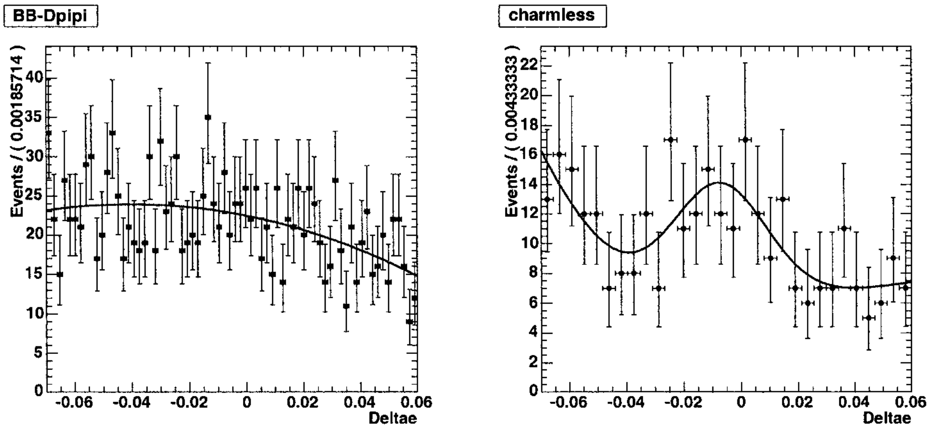

Figure 6.15: The distributions of ΔE for $D\pi X$ (left), DKX (right) MC.

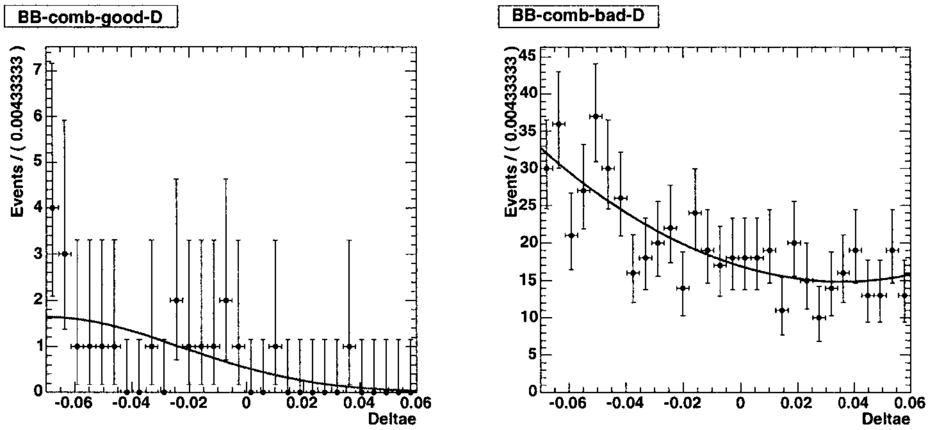

Figure 6.16: The distributions of ΔE for BBC_D (left) and $BBC_{\not{D}}$ (right) MC.

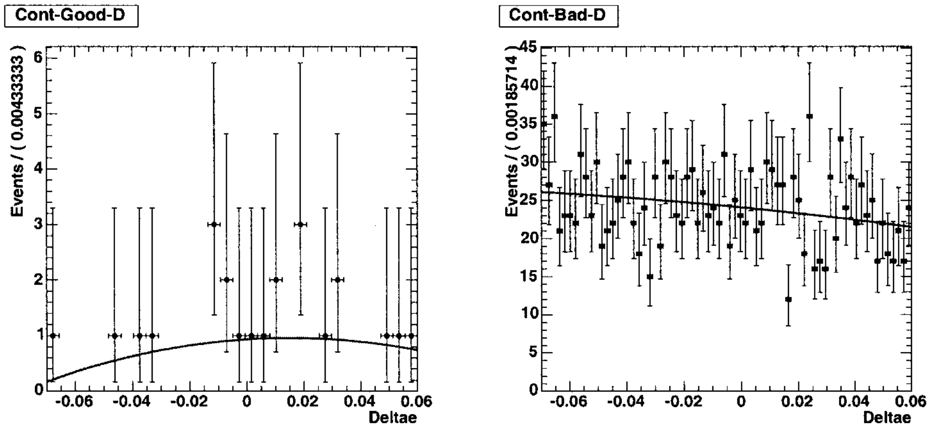

Figure 6.17: The distributions of ΔE for qq_D (left) and $qq_{\not{D}}$ (right) MC.

Parameterization of $\mathcal{Q}_j(N1)$ and $C_j(N2)$

The $N1$ and $N2$ PDFs are binned histograms obtained from the MC samples after the final event selection criteria. Figs. 6.18 through 6.27 show the $N1$ and $N2$ distributions of the various Monte Carlo event types.

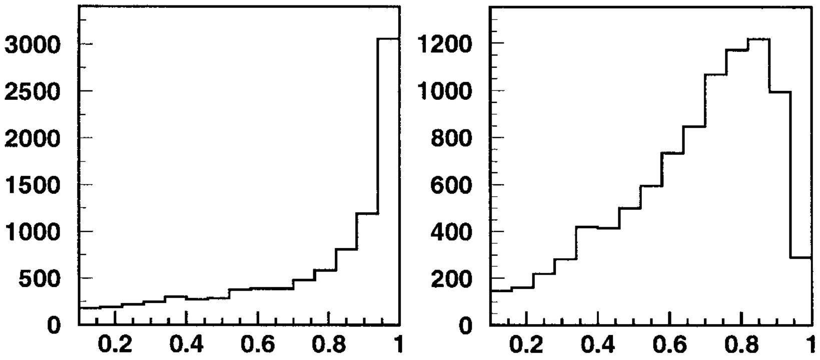

Figure 6.18: The distributions of $N1$ (left) and $N2$ (right) for DK_D MC.

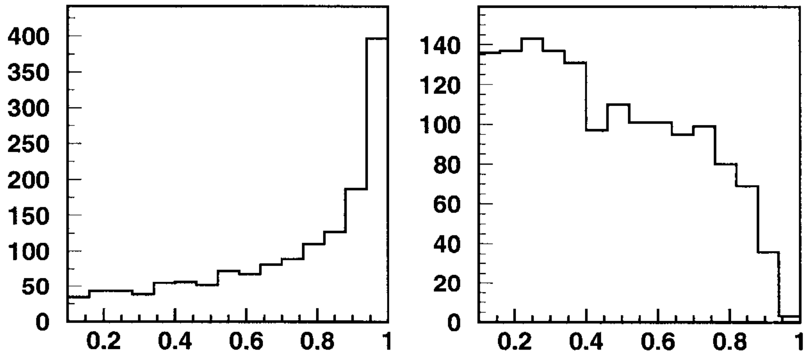

Figure 6.19: The distributions of $N1$ (left) and $N2$ (right) for $DK_{\not{D}}$ MC.

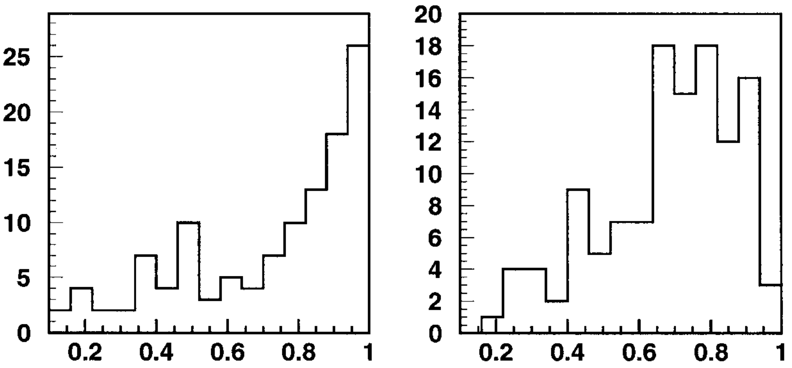

Figure 6.20: The distributions of $N1$ (left) and $N2$ (right) for $D\pi_D$ MC.

The $D\pi_{\not{D}}$, BBC_D and qq_D background are rare and have low yields in MC after the final selection criteria. For these types, we take the $N1$ or $N2$ shapes from a higher-statistics event type whose distribution is in good agreement with this low-statistic even type. Agreement is quantified using the Kolmogorov-Smirnov probability (KSP). The values of KSP are uniformly distributed between 0.0 and 1.0, for samples originating from the same distribution, with statistical fluctuations being the only source of differences between them. For any particular pair of samples, a high value of KSP indicates a high likelihood that they have the same distribution. usually, several percent is good enough to say that they have a similar distribution. Table 6.3 show the replacements and the values of KSP.

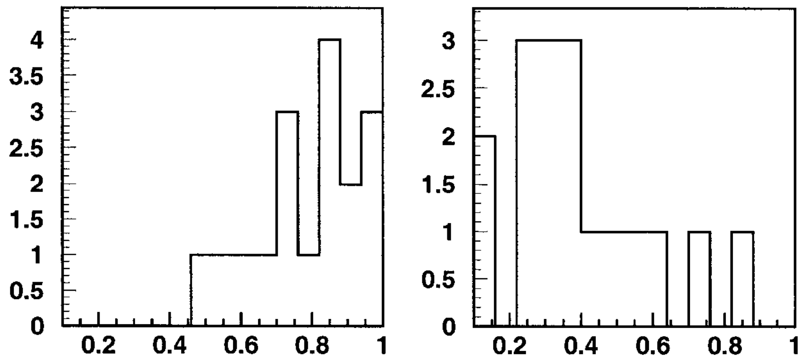

Figure 6.21: The distributions of $N1$ (left) and $N2$ (right) for $D\pi_{\not{p}}$ MC.

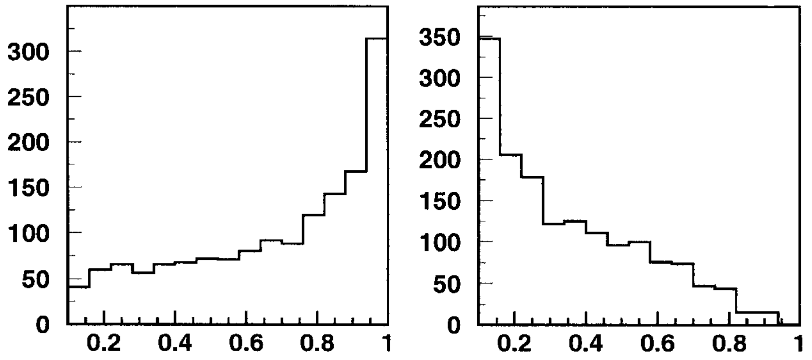

Figure 6.22: The distributions of $N1$ (left) and $N2$ (right) for $D\pi X$ MC.

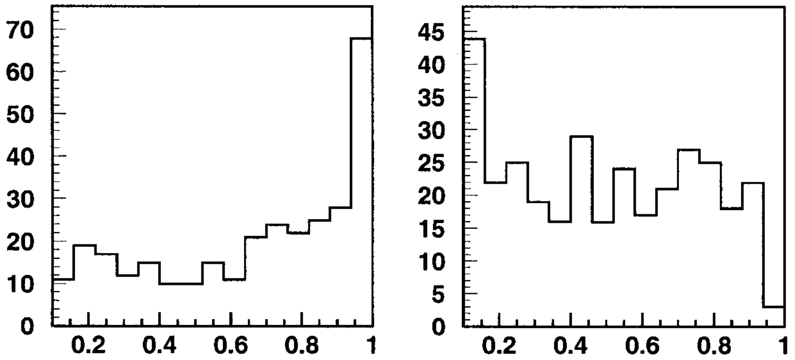

Figure 6.23: The distributions of $N1$ (left) and $N2$ (right) for DKX MC.

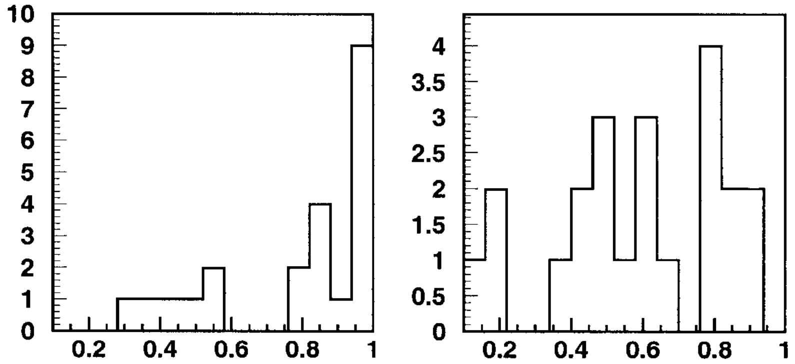

Figure 6.24: The distributions of $N1$ (left) and $N2$ (right) for BBC_D MC.

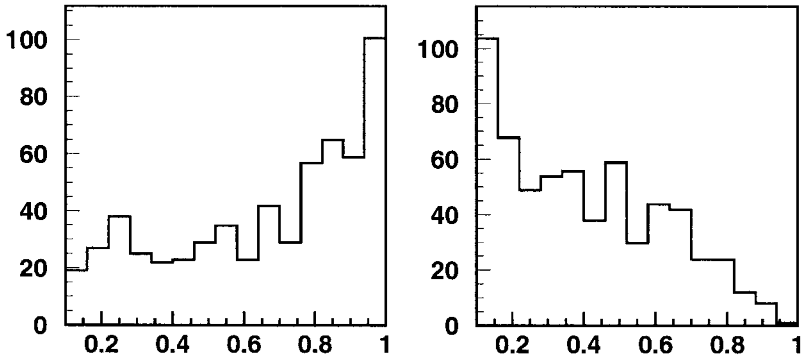

Figure 6.25: The distributions of $N1$ (left) and $N2$ (right) for $BBC_{\not{D}}$ MC.

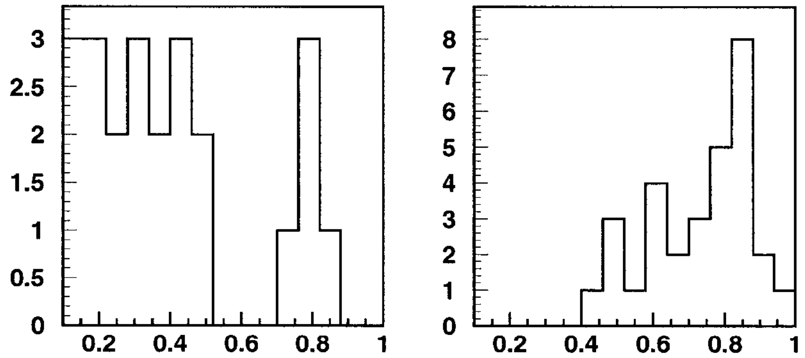

Figure 6.26: The distributions of $N1$ (left) and $N2$ (right) for qq_D MC.

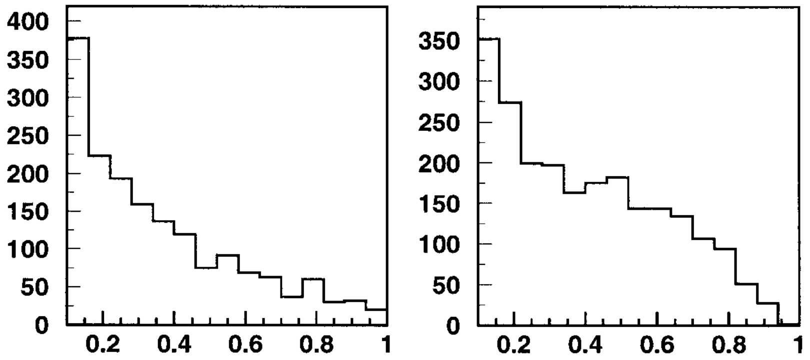

Figure 6.27: The distributions of $N1$ (left) and $N2$ (right) for $qq_{\not{p}}$ MC.

$N1$ Shape of	Taken from	KSP values of distributions
qq_D	$qq_{\not{p}}$	88.6%
BBC_D	DK_D	98.5%
$D\pi_{\not{p}}$	$D\pi X$	29.9%

$N2$ Shape of	Taken from	KSP values of the two distributions
BBC_D	$DK_{\not{p}}$	77.7%
$D\pi_{\not{p}}$	$D\pi X$	95.5%

Table 6.3: Neural net shape "replacements" and agreement between the two distributions in MC.

6.6.5. Floating parameters in the fit

The PDF parameters determined by the fit are N_{DK_D}; A_{DK_D}, which is the DK_D decay rate asymmetry, defined as $A_{DK_D} = \frac{N^-_{DK_D} - N^+_{DK_D}}{N_{DK_D}}$, here $N^{+/-}_{DK_D}$ is the number of DK_D from $B^{+/-}$; $N_{D\pi_D}$; $R_{D\pi X}$; $N_{B\bar{B}}$; $N_{qq\not{p}}$. All shapes parameters for P_j are fixed to their values or histograms obtained from MC samples. In addition, we fixed the R_j ratios to values obtained from the MC,

1. $R_{DKX} = 0.21 \pm 0.05$,
2. $R_{D\pi\not{p}} = 0.171 \pm 0.038$,
3. $R_{BBC_D} = 0.0089 \pm 0.0019$,
4. $R_{qq_D} = 0.0136 \pm 0.0028$,
5. $R_{DK_{\not{p}}} = 0.1614 \pm 0.0042$,

The error of R_{DKX} is from the measured branching ratios in the PDG [61]. All other errors are due to MC statistics.

6.6.6. Toy Monte Carlo study

We conduct a toy MC study to test the unbinned maximum likelihood fit and make sure it is not biased. Table 6.4 shows the initial values used for the floating parameters, obtained from the MC.

parameter	value
$R_{D\pi X}$	0.624
N_{DK_D}	92.2
A_{DK_D}	0.0074
$N_{D\pi_D}$	39.0
$N_{B\overline{B}}$	790.3
$N_{qq_{\not D}}$	1686.0

Table 6.4: Initial values of the floating parameters for the Toy Monte Carlo.

Fig. 6.28 through 6.33 show the extracted fit values, pulls and error for the fit parameters. There are no significant biases in these fits.

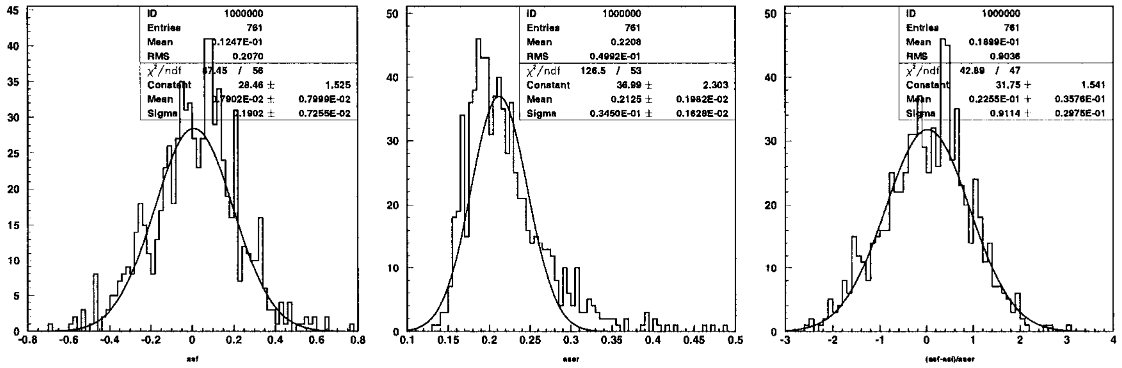

Figure 6.28: The fit value (left), error (center), and pull (right) for A_{DK_D}.

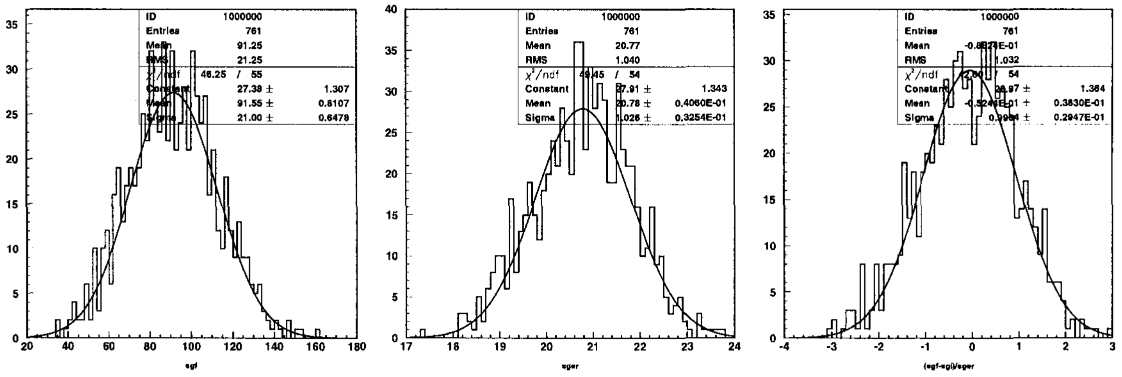

Figure 6.29: The fit value (left), error (center), and pull (right) for N_{DK_D}.

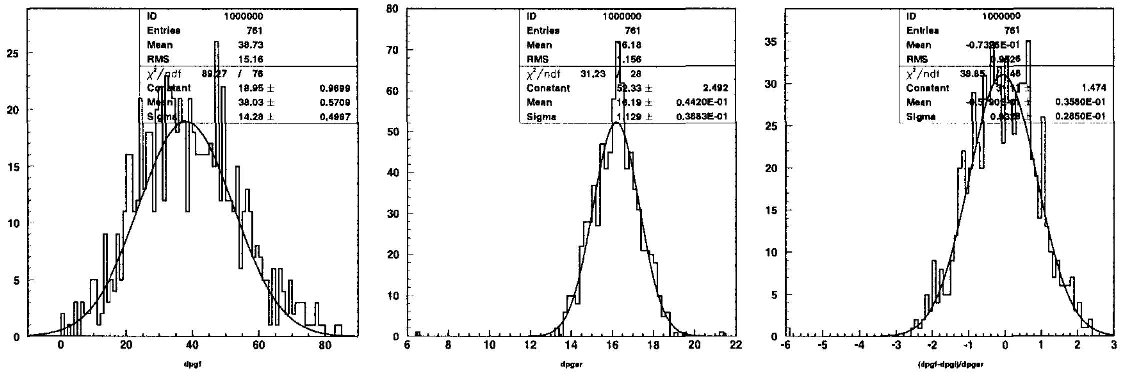

Figure 6.30: The fit value (left), error (center), and pull (right) for $N_{D\pi_D}$.

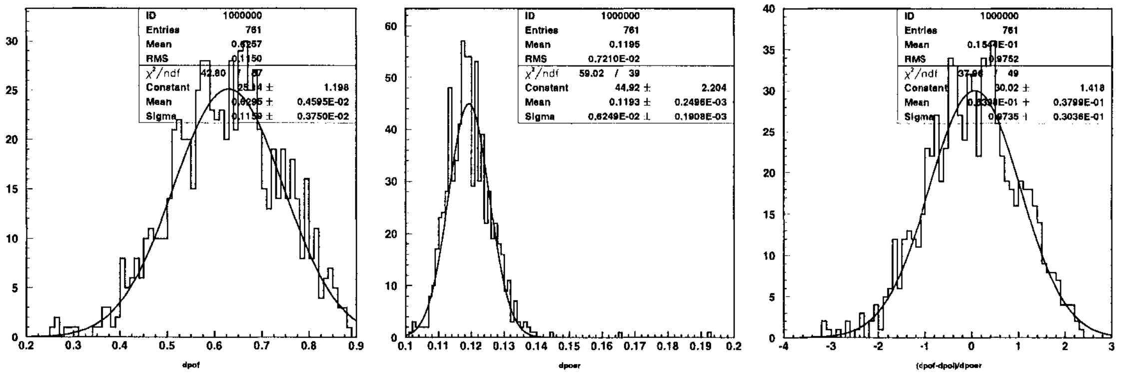

Figure 6.31: The fit value (left), error (center), and pull (right) for $R_{D\pi X}$.

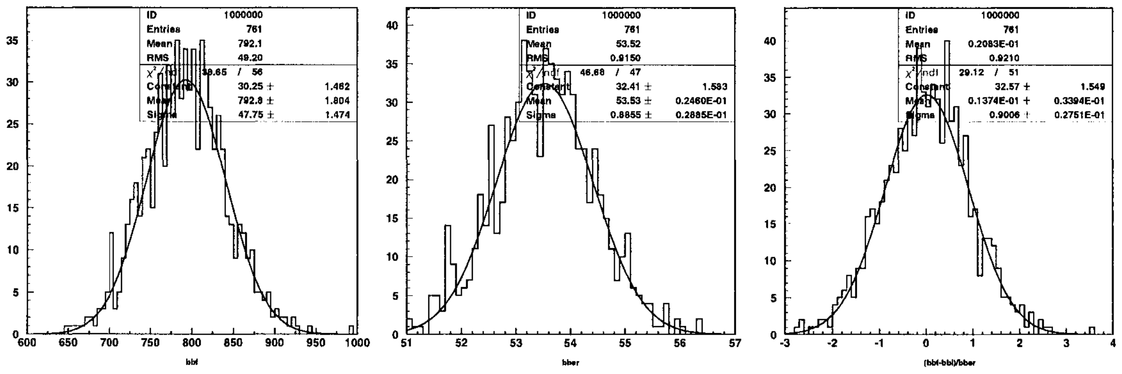

Figure 6.32: The fit value (left), error (center), and pull (right) for $N_{B\bar{B}}$.

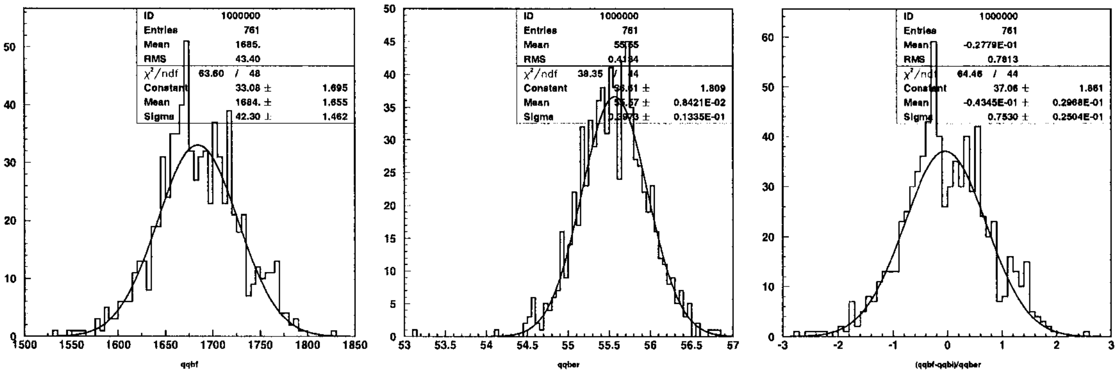

Figure 6.33: The fit value (left), error (center), and pull (right) for $N_{qq\not{p}}$.

6.7. Validation of event distributions

As our PDFs are constructed totally from MC, we need to test their validity for the use with on-peak data. To do this, we check whether the shapes obtained from MC agree well with the corresponding shapes from signal-like or off-peak data. The differences observed in these validations are all statistically insignificant and are used to evaluate systematic errors, as will be discussed in following chapters.

The procedure we used here is to compare the shapes from MC and other corresponding data samples by using KSP (Kolmogorov-Simirnov probability).

6.7.1. Continuum validation

In this validation, about 21 fb^{-1} off-peak data and 168.0 fb^{-1} continuum MC were used. The KSP values obtained by comparing the fit variable distributions of these two samples are listed in Table 6.5. Fig. 6.34 shows the distribution of these three fit variables and m_D from the continuum MC (overlaid with off-peak data). These shapes agree well with the corresponding shapes from the off-peak data.

ΔE	m_D	$N1$	$N2$
0.87	0.91	0.79	0.92

Table 6.5: KSP values by comparing the distribution of the fit variables and m_D in continuum and off-peak data.

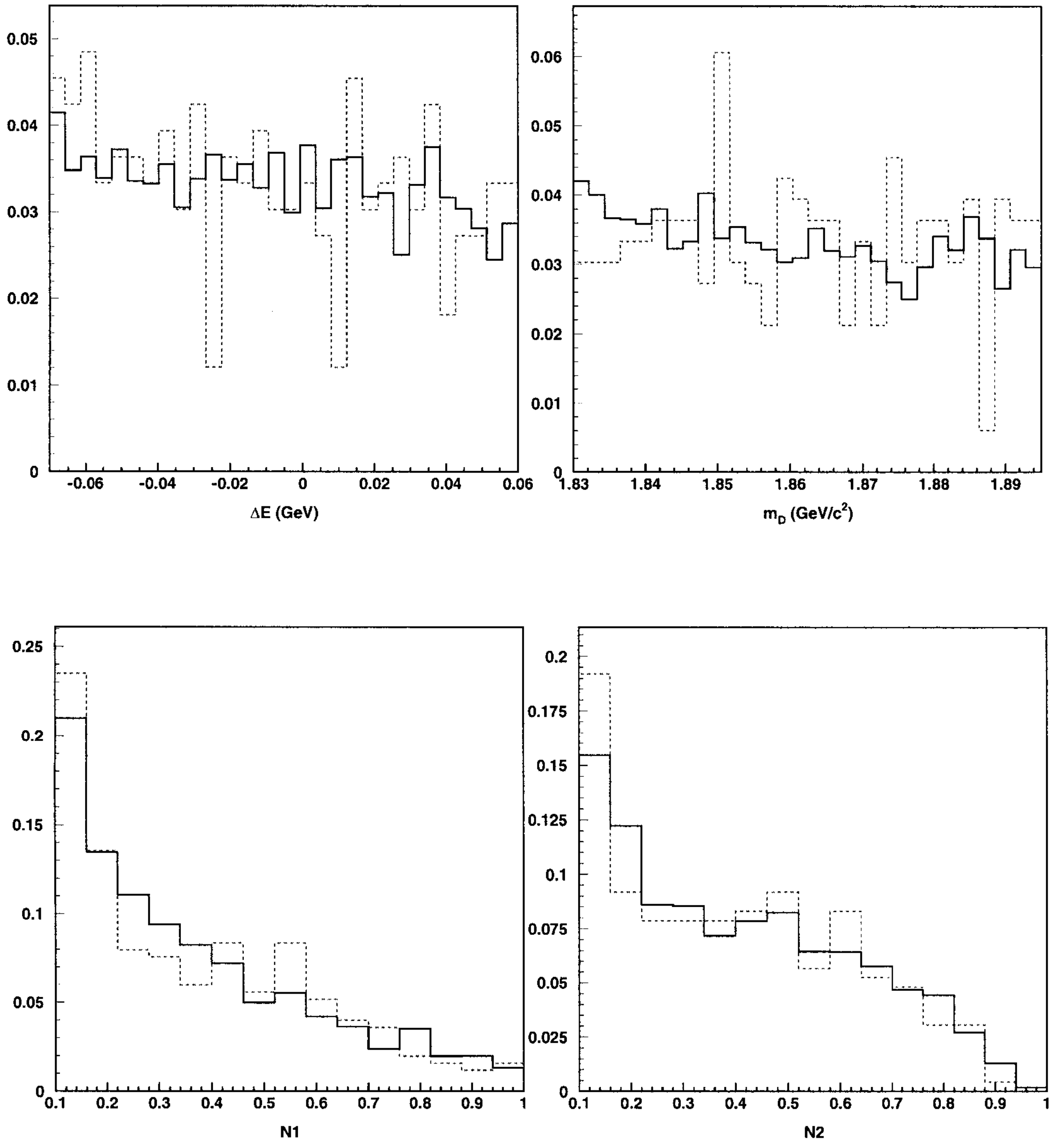

Figure 6.34: Comparison of the distributions of (from left to right, top row) ΔE, m_D, (bottom row) $N1$, and $N2$ in off-peak data (dashed) and continuum MC (solid).

6.7.2. Signal distributions validation with $B \to D\pi$ modes

Here two different D^0 decay modes, $D^0 \to K^-\pi^+\pi^0$ and $D^0 \to \pi^+\pi^-\pi^0$, are used. As they are similar to signal mode, they are used to validate the signal MC distribution.

Mode $B^- \to (K^-\pi^+\pi^0)_D\pi^-$

95,000 MC signal events and about 56 fb^{-1} on-peak data were used to reconstruct this mode. As one daughter of D is a kaon and statistics are high, this mode is very clean.

The requirements used to get a clean $B^- \to (K^-\pi^+\pi^0)_D\pi^-$ sample are

1. PidKaonMicroSelector neural net value is less than 0.5 for the bachelor "kaon";
2. $0.01 < \Delta E < 0.09\,\mathrm{GeV}$;
3. $1.845 < m_D < 1.885\ \mathrm{GeV}/c^2$;
4. $0.125 < m_{\pi^0} < 0.1425\ \mathrm{GeV}/c^2$;
5. $5.274 < m_{\mathrm{ES}} < 5.290\ \mathrm{GeV}/c^2$.

Figs. 6.35, 6.36, and 6.37 show the distributions of m_{ES}, ΔE and m_D with overlaid fits for data and MC. m_{ES} and m_D are used to reject the background in the reconstruction of this mode. Fig. 6.38 shows the distributions of $N1$ and $N2$ with data and

MC overlaid. The KSP value for the $N1$ ($N2$) distribution is 0.988 (0.345), indicating that the neural network distributions of data and MC are in good agreement.

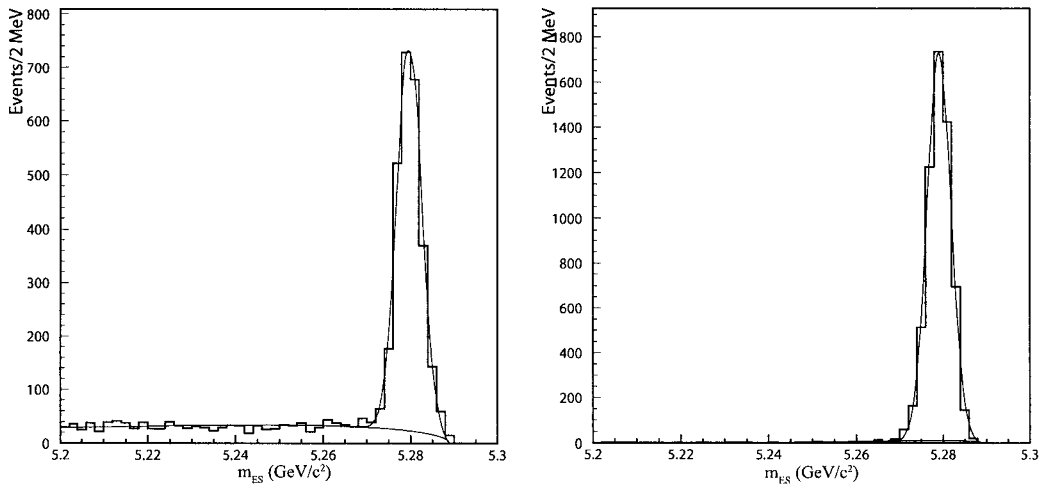

Figure 6.35: The m_{ES} distributions of $B^- \to (K^-\pi^+\pi^0)_D\pi^-$ data (left) and MC (right). The fit function (Gaussian plus ARGUS for data and signal MC) is overlaid.

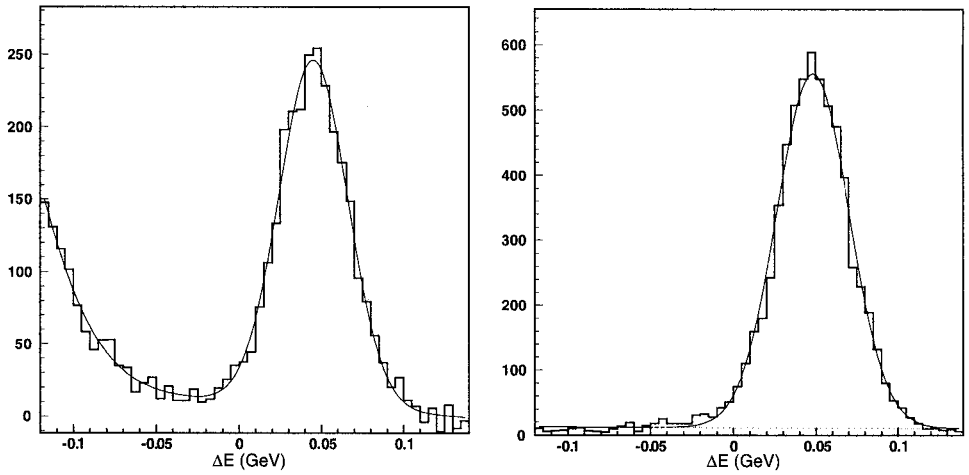

Figure 6.36: The ΔE distributions of $B^- \to (K^-\pi^+\pi^0)_D\pi^-$ data (left) and MC (right). The fit function (two Gaussians plus a first order polynomial for data, Gaussian for signal) is overlaid.

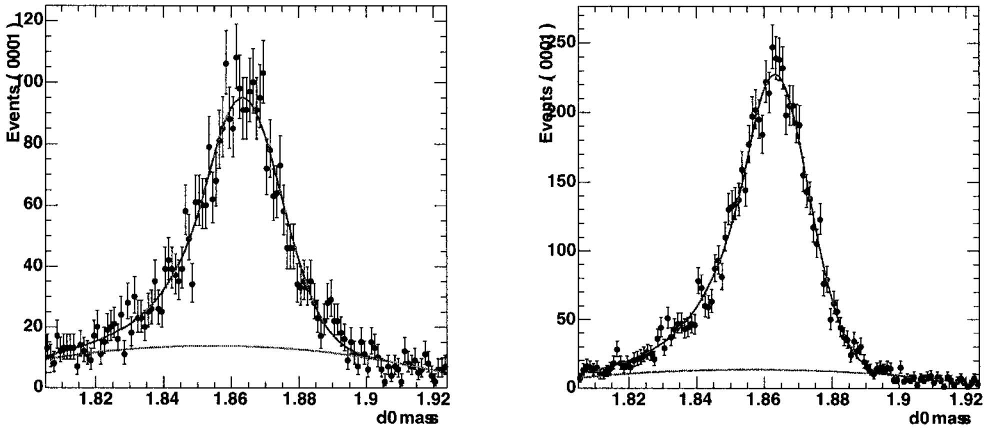

Figure 6.37: The m_{D^0} distributions of $B^- \to (K^-\pi^+\pi^0)_D\pi^-$ data (left) and truth-matched MC (right). The fit function (Crystal Ball function [59] plus 2nd order polynomial for both data and signal) is overlaid.

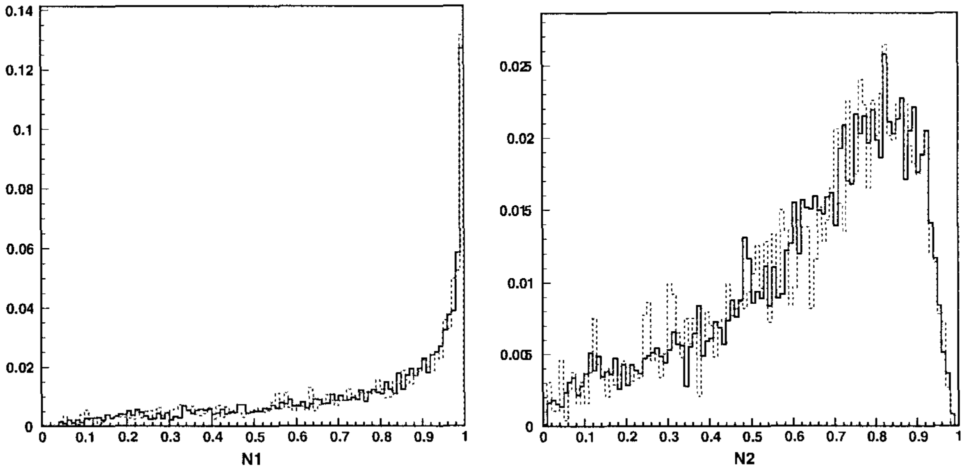

Figure 6.38: The distribution of $N1$ (left) and $N2$ (right) for $B^- \to (K^-\pi^+\pi^0)_D\pi^-$ data (dashed) and MC (solid). The histograms are made with an $m_{\rm ES}$ sideband subtraction.

As an additional validation study, we list in Table 6.6 the parameters of the functions used to fit the data and MC m_{ES}, m_D, and ΔE distributions. The data and MC m_{ES} distributions are in good agreement. The ΔE Gaussian mean in the data is shifted by -2.8 ± 0.61 MeV with respect to the MC. The m_D Crystal Ball Gaussian width in the data is 2.4 ± 0.4 Mev/c^2 broader than in MC. Although we do not use m_D in the fit, this width difference affects the signal efficiency. The efficiency and its systematic error are discussed in later chapters.

	m_{ES}(GeV/c^2)		ΔE(GeV)	
	data	MC	data	MC
mean	5.27980±0.00006	5.27910±0.00004	0.0457±0.0006	0.0483±0.0003
sigma	0.00273±0.00006	0.00266±0.00003	0.0209±0.0006	0.0209±0.0003
	m_D(GeV/c^2)			
mean	1.8634±0.0004	1.8632±0.0002		
sigma	0.0116±0.0005	0.0100±0.0002		

Table 6.6: m_{ES}, ΔE, and m_D Gaussian fit parameters for $B^- \to (K^-\pi^+\pi^0)_D\pi^-$ data and MC.

We also roughly estimated the branching ratio of this mode, 50904±79 (2464±57) events are extracted from a Gaussian plus an Argus fit to the m_{ES} distribution of the MC (on-peak data) sample (see Fig. 6.35). Given the sizes of the data and MC samples, this gives the branching ratio for $B^- \to D\pi^-$ $(5.08 \pm 0.38) \times 10^{-3}$, in a good agreement with the PDG value of $(4.98 \pm 0.29) \times 10^{-3}$.

Mode $B^- \to (\pi^+\pi^-\pi^0)_D\pi^-$

About $\sim 170\,\mathrm{fb}^{-1}$ on-peak and 15,000 $B^- \to (\pi^+\pi^-\pi^0)_D\pi^-$ MC events with 100% resonant $D \to \rho\pi$ decay were used for the study of this mode. The following cuts were used to reduce the background,

1. $5.274 < m_{\mathrm{ES}} < 5.290$ GeV/c^2,
2. $1.84 < m_D < 1.89$ GeV/c^2,
3. $N1 > 0.4$ and $N2 > 0.2$,
4. $0.01 < \Delta E < 0.09$ GeV,
5. K^0_S veto: $m_{\pi^+\pi^-} > 0.508$ GeV/c^2 or $m_{\pi^+\pi^-} < 0.489$ GeV/c^2.

As this mode has much more background than $B^- \to (K^-\pi^+\pi^0)_D\pi^-$, a different strategy is adopted here. Specifically, to avoid uncertainties in the shape of $B\bar{B}$ background that peaks in m_{ES}, the signal yield was extracted from a fit to the ΔE distribution. A Gaussian plus first-order polynomial fit finds 943±60 (1286 ± 37) events in the data (MC) sample, giving a branching ratio of $B^- \to D\pi^-$ $(4.68 \pm 0.48) \times 10^{-3}$, which is in agreement with the PDG value. Fig. 6.39 shows the ΔE fit. The parameters of the ΔE and m_D fit functions (see Fig. 6.40) are shown in Table 6.7. We do not find a shift in the ΔE Gaussian mean. As this mode is closer to the signal mode than $B^- \to (K^-\pi^+\pi^0)_D\pi^-$, in the final data fit, we did not shift the ΔE mean of the signal PDF relative to the value obtained from the signal MC. Due to background shape uncertainties, no comparison was done for m_{ES}, $N1$, and $N2$.

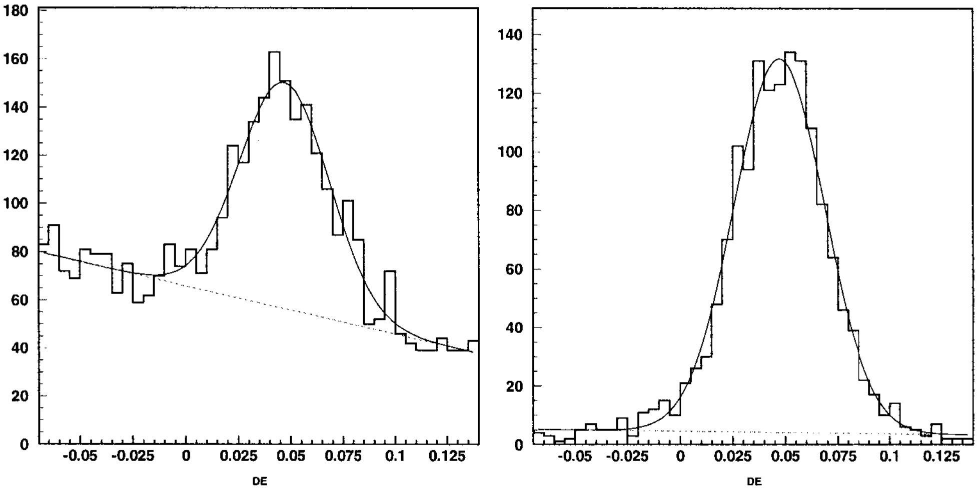

Figure 6.39: distribution of ΔE of $B^{\pm} \rightarrow (\pi^{+}\pi^{-}\pi^{0})_{D}\pi^{\pm}$ with the fit overlaid, data (left), MC (right).

	m_{D^0}		ΔE	
	data	MC	data	MC
mean	1.8628±0.0009	1.8621±0.0005	0.0471±0.0012	0.0472±0.0007
sigma	0.0125±0.0015	0.0139±0.0004	0.0214±0.0013	0.0215±0.0006

Table 6.7: Parameters extracted from the fit on m_{D^0} and ΔE from $B^{\pm} \rightarrow (\pi^{+}\pi^{-}\pi^{0})_{D}\pi^{\pm}$ on-peak data and MC.

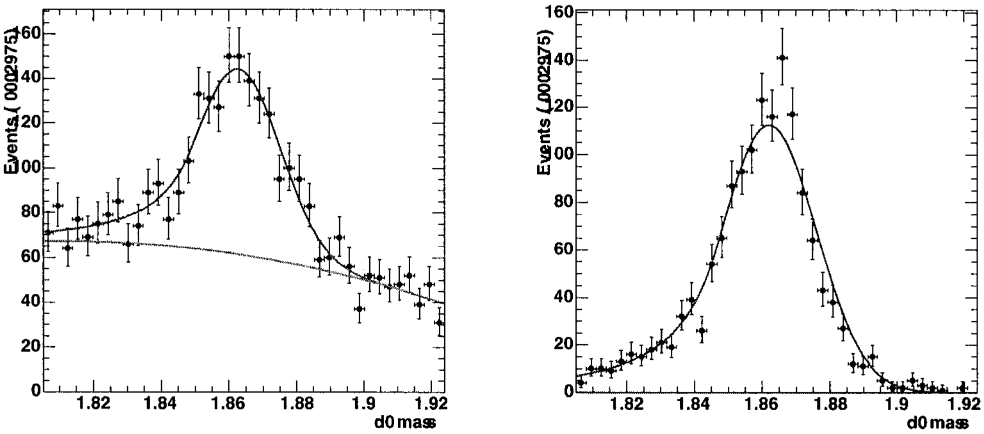

Figure 6.40: Distribution of m_{D^0} of $B^\pm \to (\pi^+\pi^-\pi^0)_D\pi^\pm$with fit overlaid, data (left), MC match (right).

6.7.3. On-peak data sideband

We used on-peak data sidebands (samples with cuts designed to eliminate the contribution of signal events) to test the agreement between the data and MC for the sum of continuum and $B\bar{B}$ backgrounds. Three sidebands are used to compare the data and MC shapes: The $m_{\rm ES}$ sideband $5.23 < m_{\rm ES} < 5.26$ GeV/c^2, the low ΔE sideband, $0.09 < \Delta E < 0.140$ GeV, and the high ΔE sideband $-0.07 < \Delta E < 0.14$ GeV. For each of these three sidebands, distributions of the other fit variables in the data and MC are overlaid, as shown in Fig. 6.41, 6.42 and 6.43, respectively. The KSP values obtained by comparing the MC and data for each of these figures are shown in Table 6.8.

The MC sample used for this comparison contains the full generic $B\bar{B}$ and continuum MC samples that are scaled to the data luminosity ($\sim 170\,\mathrm{fb}^{-1}$) with the continuum contribution reduced by 16% in order to solve a problem with the kaon yield in the continuum MC, which is 16% higher than in the off-resonance data. The plots and KSP values show good agreement between data and MC.

Sideband	ΔE	$N1$	$N2$
$5.23 < m_{\mathrm{ES}} < 5.26$	0.071	0.548	0.362
$-0.07 < \Delta E < -0.45$		0.813	0.847
$0.09 < \Delta E < 0.14$		0.998	0.048

Table 6.8: Kolmogorov-Simirnov probabilities comparing the on-peak data and MC in the side bands.

6.8. Full Monte Carlo fit

As a test of the analysis, we conducted fits to full MC samples containing both signal and background events. From Table 6.2, we see that continuum MC sample is about 170 fb^{-1}, while the $B\bar{B}$ sample is about 3 times larger and the signal MC sample is about 100 times larger. To make best use of the larger samples, we conducted 98 different fits. In each fit, a different signal sample is used. The 98 fits are divided into two sets of 33 fits each and one set of 32 fits, where each set uses a different $B\bar{B}$ sample, and all the fits within the set share the same $B\bar{B}$ sample. All 98 fits use the same continuum sample. The results of these fits, averaged over the experiments in each of the three $B\bar{B}$ sets, are listed in Table 6.9, and consistent with the true values

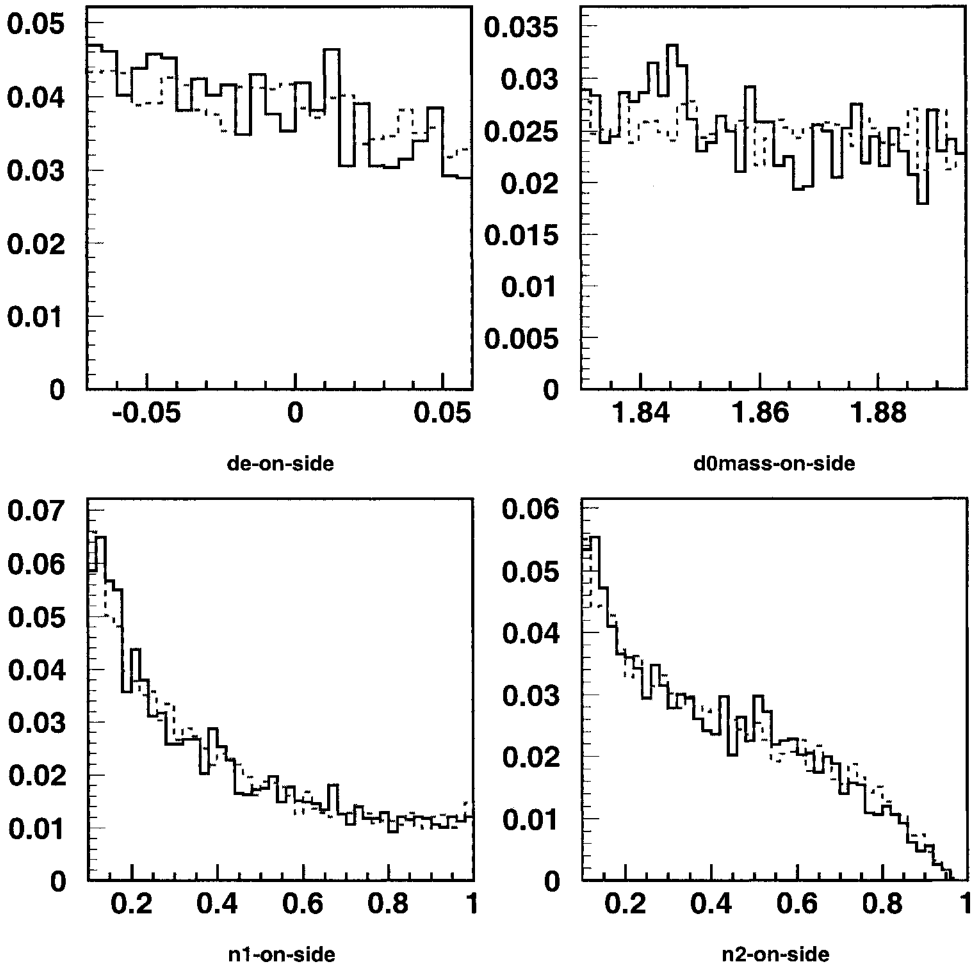

Figure 6.41: On-peak m_{ES} sideband distribution of ΔE (top left), m_D (top right) $N1$ (bottom left) and $N2$ (bottom right) with MC overlaid (dashed). All plots are normalized to unit area.

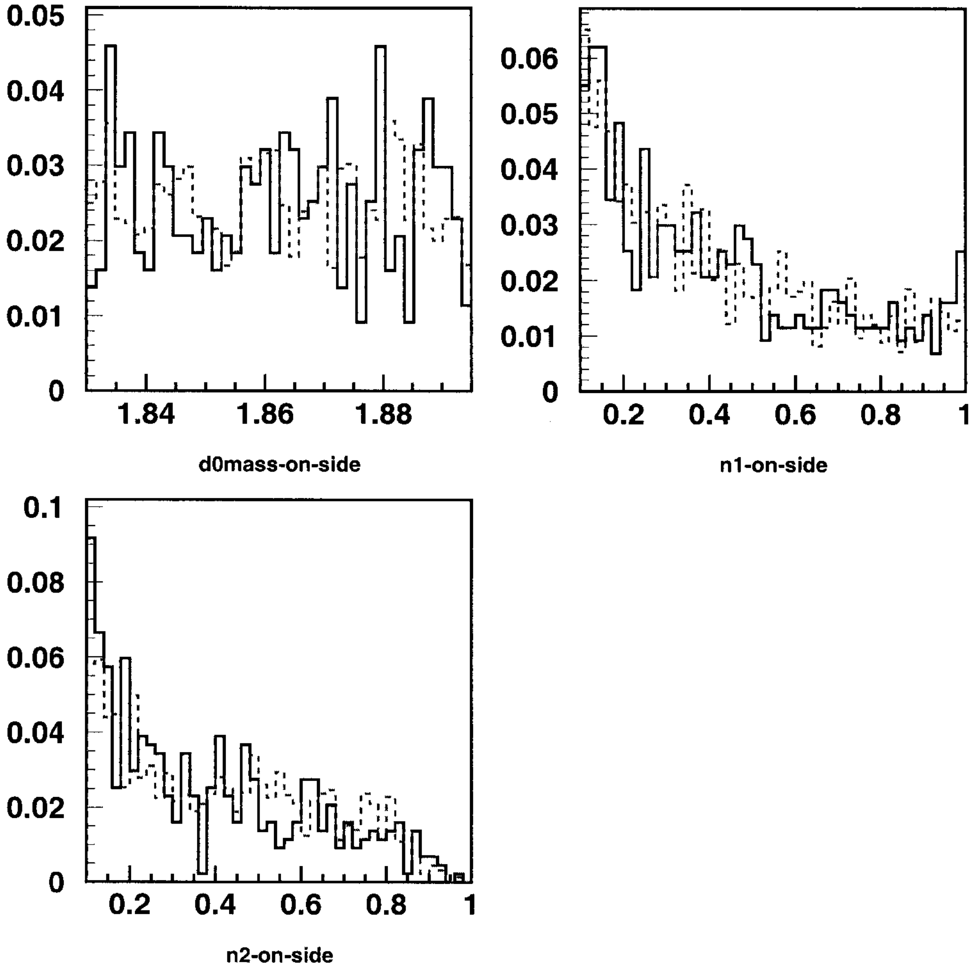

Figure 6.42: On-peak high ΔE sideband distribution of m_D (top left) $N1$ (top right) and $N2$ (bottom left) with MC overlaid (dashed). All plots are normalized to unit area.

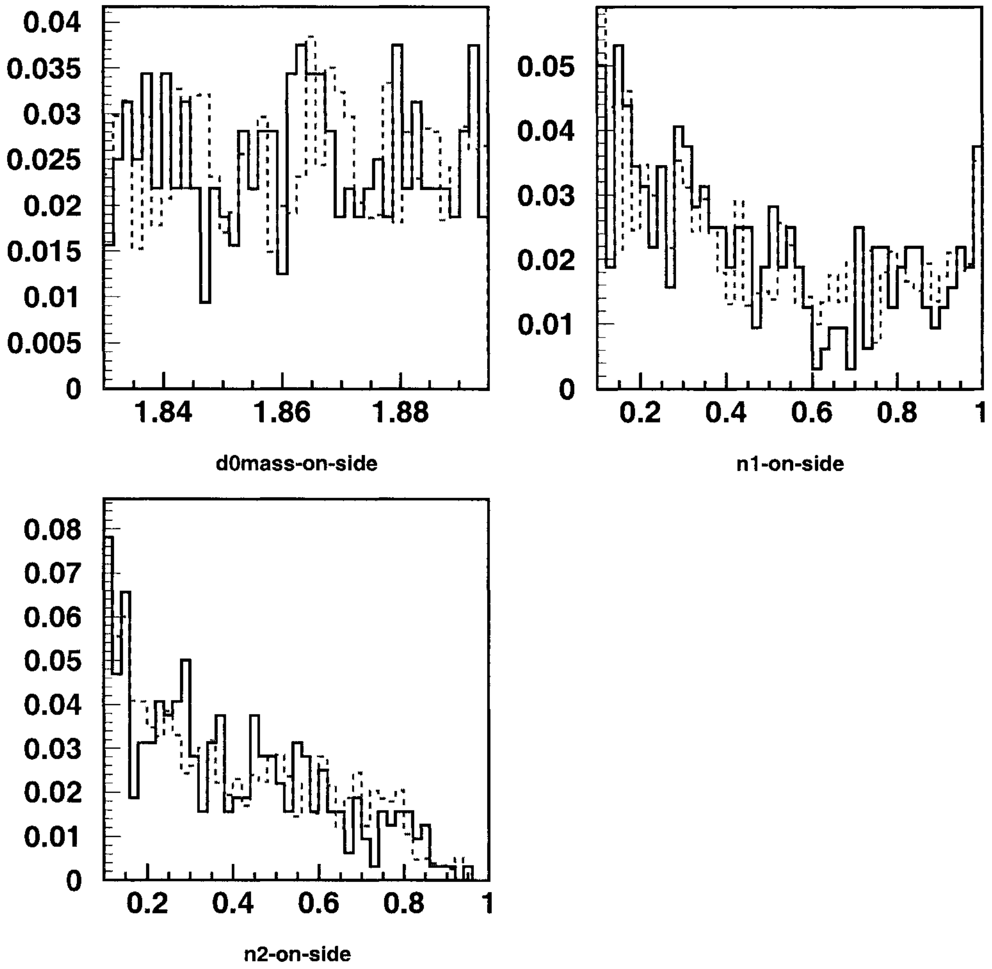

Figure 6.43: On-peak low ΔE sideband distribution of m_D (top left) $N1$ (top right) and $N2$ (bottom left) with MC overlaid (dashed). All plots are normalized to unit area.

of the floating parameters. From the value listed in this table, we can break the statistical error into three parts, writing it as as a sum in quadrature of the statistical error contributions of the signal, $B\bar{B}$ background and continuum background events:

$$\sigma^2 = \sigma_{sig}^2 + \sigma_{B\bar{B}}^2 + \sigma_{cont}^2. \tag{6.11}$$

We find $\sigma_{sig} = 10$ events, $\sigma_{cont} = 11$ events, and $\sigma_{B\bar{B}} = 15$ events. The dominant component in the statistical error is the $B\bar{B}$ events. The background increases the total error by a factor of about two compared with the no-background case.

6.9. Fit results with on-peak data

Armed with validations of the input variable shapes and MC studies, we performed a fit on the on-peak data with about 168 fb^{-1}. Table 6.10 shows the values and errors of all the parameters floating in the fit. The correlation matrix is shown in Table 6.11. With added about 39 fb^{-1} more data, a fit is done on the total about 207 fb^{-1} on-peak data. Fig. 6.44 shows the projections of the data and PDF onto the fit variable axes over the entire fit range. Projections with a signal likelihood cut, which reduces the signal yield but increases the signal-to-background ratio, are shown in Fig. 6.45. Table 6.12 and 6.13 show the final data fit results and the correlation between its fit variables.

Parameter	<True value>	<Fit value> & $< \sigma >$
Set 1		
$R_{D\pi X}$	0.6151	0.6144±0.1235
$N_{D\pi_D}$	39	24.5±15.3
A_{DK_D}	0.0141	-0.1962±0.1788
$N_{qq\not{p}}$	1686	1675.0±55.3
N_{DK_D}	91.3	108.6±20.8
$N_{BB_{\not{p}}}$	730	738.1±52.5
Set 2		
$R_{D\pi X}$	0.6323	0.6867±0.1156
$N_{D\pi_D}$	42	35.1±16.4
A_{DK_D}	0.0020	0.0227±0.1940
$N_{qq\not{p}}$	1686	1673.0±56.7
N_{DK_D}	91.1	102.1±20.9
$N_{BB_{\not{p}}}$	854	863.5±54.8
Set 3		
$R_{D\pi X}$	0.6255	0.6819±0.1254
$N_{D\pi_D}$	36	30.47±16.5
A_{DK_D}	0.0031	0.0501±0.1827
$N_{qq\not{p}}$	1686.0	1705.0±56.0
N_{DK_D}	92.0	109.0±21.2
$N_{BB_{\not{p}}}$	777.0	745.1±53.0

Table 6.9: Results of the full MC fits, averaged over about 33 fits in each set of fits. Each experiment has a different signal sample. Each set of fits has a different $B\overline{B}$ sample and a different group of 33 independent signal samples. All fits have the same continuum sample.

No.	Parameter	Value
1	$R_{D\pi X}$	0.823 ± 0.110
2	$N_{D\pi_D}$	43.2 ± 15.9
3	A_{DK_D}	-0.044 ± 0.164
4	$N_{qq\not p}$	1454.3 ± 52.9
5	N_{DK_D}	123.3 ± 22.0
6	$N_{BB_{\not p}}$	806.0 ± 53.5

Table 6.10: Results of the data fit with about 170 fb^{-1} with statistical error. See section 6.6.5 for the definitions of the variables.

No.	Parameter	$R_{D\pi X}$	$N_{D\pi_D}$	A_{DK_D}	$N_{qq\not p}$	N_{DK_D}	$N_{BB_{\not p}}$
1	$R_{D\pi X}$	1.000	-0.008	-0.000	0.195	-0.076	-0.157
2	$N_{D\pi_D}$	-0.008	1.000	0.000	-0.025	-0.198	-0.177
3	A_{DK_D}	-0.000	0.000	1.000	0.007	0.010	-0.012
4	$N_{qq\not p}$	0.195	-0.025	0.007	1.000	0.031	-0.500
5	N_{DK_D}	-0.076	-0.198	0.010	0.031	1.000	-0.332
6	$N_{BB_{\not p}}$	-0.157	-0.177	-0.012	-0.500	-0.332	1.000

Table 6.11: Correlation matrix of the data fit with about 170 fb^{-1} on-peak data.

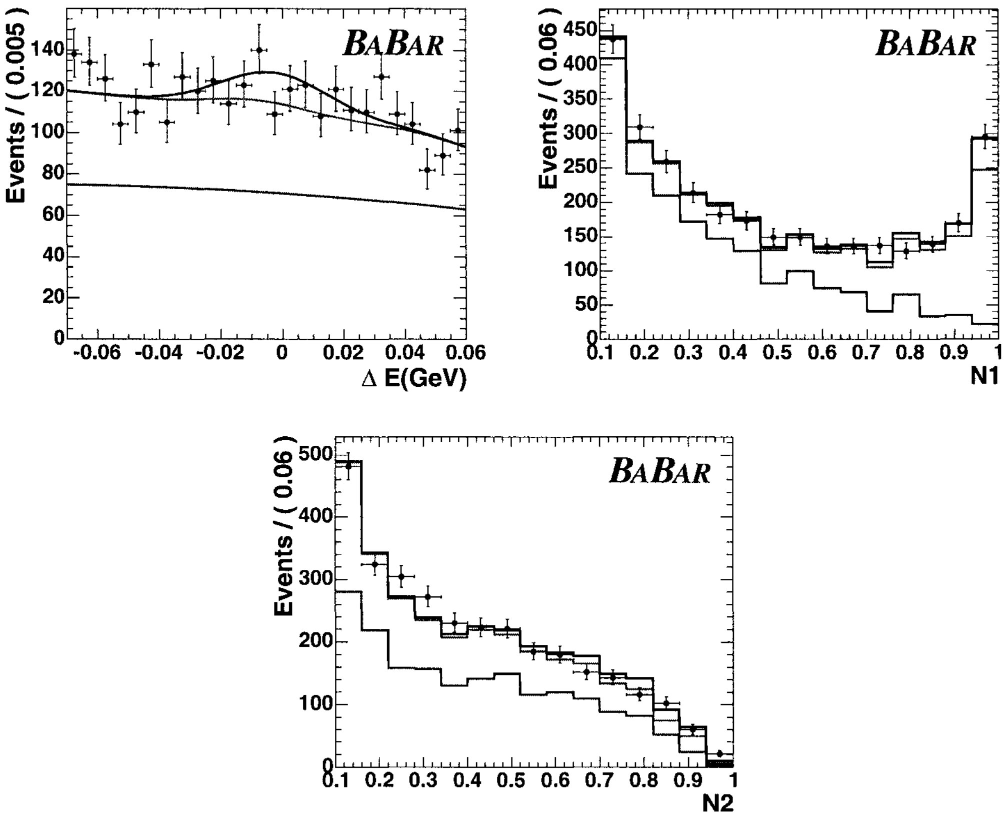

Figure 6.44: Projections of the data and PDF onto the 3 fit variable axes, clockwise, ΔE, $N1$and $N2$; bottom. The lines indicate the contributions to the PDF of (from bottom to top) continuum, all background, and all event types including signal.

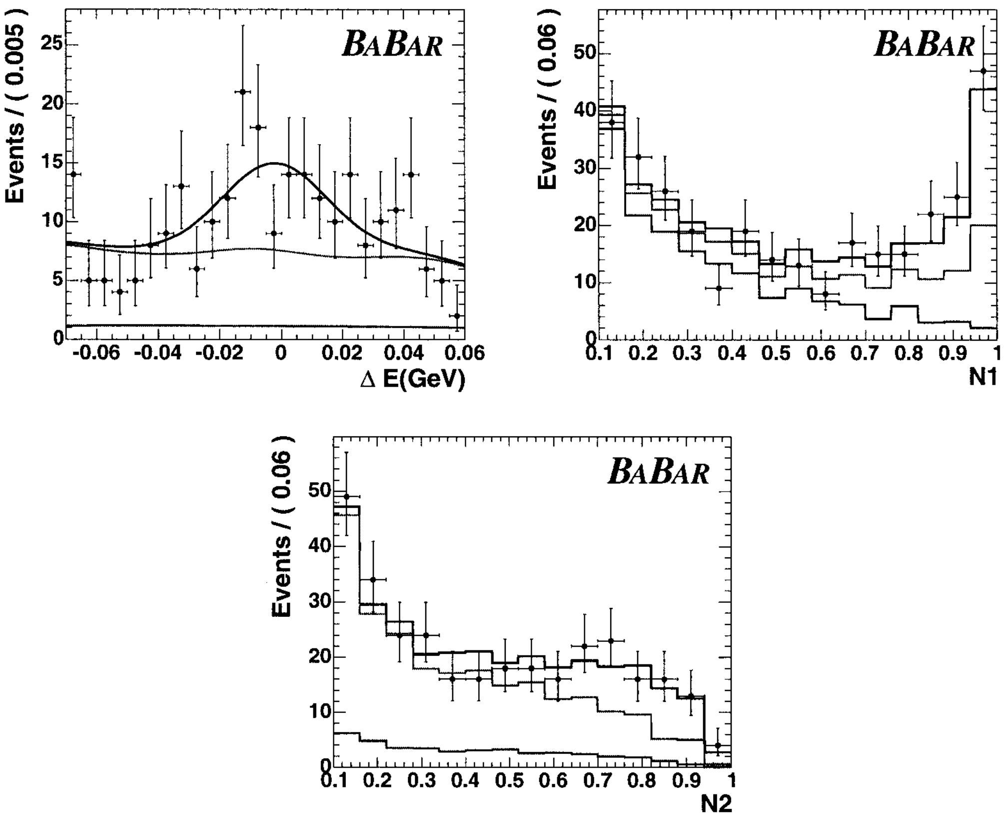

Figure 6.45: Projection of the data and PDF onto ΔE $N1$, $N2$, after a signal likelihood cut to enhance the signal to background ratio. The likelihood that we cut on is calculated using the two fit variables not been plotted. The lines indicate the contributions to the PDF of (from bottom to top) continuum, continuum plus combinatorial $B\overline{B}$ background, all backgrounds, and all event types including signal. The efficiencies of the cut applied to obtain the ΔE plot are 43% for signal, 15% for the sum of the $B\overline{B}$ backgrounds, and 1.5% for continuum.

The additional 39 fb^{-1} data seems to have low signal yield which is due to a downward fluctuation. The details can be found in Ref. [63].

No.	Parameter	Value
1	$R_{D\pi X}$	0.835 ± 0.100
2	$N_{D\pi_D}$	43.2 ± 15.9
3	A_{DK_D}	-0.044 ± 0.164
4	$N_{qq\not{p}}$	1454.3 ± 52.9
5	N_{DK_D}	123.3 ± 22.0
6	$N_{BB_{\not{p}}}$	806.0 ± 53.5

Table 6.12: Results of the data fit with $\sim 208\,\mathrm{fb}^{-1}$ on-peak data for the definitions of the variables.

No.	Parameter	1	2	3	4	5	6
1	$R_{D\pi X}$	1.000	-0.008	-0.000	0.195	-0.076	-0.157
2	$N_{D\pi_D}$	-0.008	1.000	0.000	-0.025	-0.198	-0.177
3	A_{DK_D}	-0.000	0.000	1.000	0.007	0.010	-0.012
4	$N_{qq\not{p}}$	0.195	-0.025	0.007	1.000	0.031	-0.500
5	N_{DK_D}	-0.076	-0.198	0.010	0.031	1.000	-0.332
6	$N_{BB_{\not{p}}}$	-0.157	-0.177	-0.012	-0.500	-0.332	1.000

Table 6.13: Correlation matrix of the data fit with $208\,\mathrm{fb}^{-1}$.

6.10. Systematic errors

The following subsections describe the methods used to obtain the systematic errors of this analysis. The errors are calculated for a luminosity of 168.3 fb^{-1}, and in the end are scaled for the full luminosity.

6.10.1. Variation of fixed fractions

The fixed ratios of event yields listed in section 6.6.5 are obtained from MC. In order to evaluate the systematic error due to this MC dependence, we vary each of these fixed ratios by $\pm$ half of its value, and refit the data. An exception is R_{DKX}, whose error is obtained from the PDG and is therefore reliable. In this case, we vary R_{DKX} by $\pm$ its error. In all cases, the change in the signal yield and asymmetry after the ratio is varied are taken as the systematic error (see Table 6.19).

6.10.2. Effect of Dalitz plot uncertainty on signal efficiency

The signal reconstruction efficiency depends on the Dalitz plot distribution, mostly through the π^0 momentum. The signal MC sample used to evaluate the efficiency of $(11.2 \pm 0.1)\%$ (section 6.6.2) was generated using the parameters of ref. [56], which has almost all resonant $D^0 \to \rho\pi$ decays, with just a $(2.7 \pm 1.9)\%$ non-resonant contribution. The efficiency obtained from a non-resonant phase-space $B^{\pm} \to (\pi^+\pi^-\pi^0)_D K^{\pm}$ distribution is $(13.05 \pm 0.10)\%$, where the error is due to MC statistics only. The relative difference between the two samples is $(1.97 \pm 0.1)\%$. Therefore we take a relative error of $0.019 \times 1.97/0.1121 = 0.0033$, which is 0.41 events.

6.10.3. Monte Carlo statistics

Our ΔE PDF parameters are obtained by fitting finite MC samples. To propagate the statistical errors in these MC fits to the final result while taking into account the statistical correlations between them, we follow the following procedure: Each MC fit gives a vector of N floating parameters and an $N \times N$ error matrix V. We transform the matrix and the vector to the basis in which the matrix is diagonal. In that basis, we vary the first parameter by $\sqrt{V_{11}}$, transform the vector of parameters back to the original basis, and perform the data fit again, obtaining a new result x^1_+ (where x refers to N_{DK_D} or A_{DK_D}). We then apply a $-\sqrt{V_{11}}$ variation to the first parameter, and obtain x^1_-. The procedure is repeated for all the parameters. The total systematic error due to MC statistics in this particular fit is

$$\sigma^2_{\Delta\mathrm{E\ MCstat}} = \frac{1}{2}\sum_{i=1}^{N}\left[\left(x^i_+ - x\right)^2 + \left(x^i_- - x\right)^2\right]. \tag{6.12}$$

This procedure is repeated for all MC fits used to obtain ΔE PDF shape parameters.

We use a different procedure to determine the errors associated with $N1$ and $N2$ shapes. As each bin of the shape histograms of these variables is uncorrelated with all other bins, we use shapes obtained by random fluctuations of the bin entry and its error to refit the data, and x_i (where x refers to N_{DK_D} or A_{DK_D}) is refitted result.

This experiment is the repeated N times. The total error due to this procedure is:

$$\sigma^2_{\text{NN MCstat}} = \frac{1}{N}\sum_{i=1}^{N}(x_i - x)^2 \tag{6.13}$$

Source	N_{DK_D} error (events)	A_{DK_D} error
ΔE variation	5.55	2.88×10^{-3}
$N2$ variation	7.22	1.21×10^{-2}
$N1$ variation	2.88	5.44×10^{-3}
Total error	9.55	1.35×10^{-2}

Table 6.14: Systematic errors due to finite Monte Carlo statistics.

6.10.4. Uncertainty in the charmless branching fractions

The total branching fraction of charmless $B^+ \to K^+\pi^-\pi^+\pi^0$ events in the generic MC is 6×10^{-5}. We estimate a 100% uncertainty on this value by removing these events (regardless of how they were reconstructed) from the MC sample, obtaining new PDF shapes without these events, and refitting the data. The changes in the signal yield and asymmetry are taken as the systematic errors.

6.10.5. Global detector charge asymmetry

Since we are measuring a decay rate asymmetry, it is important to account for a possible detector asymmetry. To do this, we include in the PDF a global charge asymmetry parameter that affects equally all event types. When this parameter is floating, it obtains the value $(-0.3 \pm 2.2) \times 10^{-2}$. The changes in the signal yield and asymmetry are taken as the related systematic errors.

6.10.6. Neural network shape replacements

As discussed in section 6.6.4, the neural net shapes of some low-statistics backgrounds were taken from high-statistics event types. To obtain the systematic error associated with these replacements, we undid one replacement at a time and refit the data. The results of these fits are shown in Table 6.15. The total error due to this is taken as the quadrature sum of the resulting differences in the signal yield or asymmetry.

Source	N_{DK_D} change (events)	A_{DK_D} change
$N2$, BBC_D	0.55	5.42×10^{-4}
$N2$, $D\pi_{\not{D}}$	0.83	1.73×10^{-3}
$N2$ total	1.00	1.81×10^{-3}
$N1$, BBC_D	0.09	7.72×10^{-3}
$N1$, $D\pi_{\not{D}}$	0.16	8.50×10^{-3}
$N1$, qq_D	0.41	1.81×10^{-4}
$N1$ total	0.45	1.15×10^{-2}
Total error	1.10	1.16×10^{-2}

Table 6.15: Changes in signal yield and asymmetry when removing one of the neural network shape replacements at a time.

We also tried to fit the data without any neural network replacements. Table 6.16 shows the changes, which are consistent with those of Table 6.15.

Source	N_{DK_D} change (events)	A_{DK_D} change
$N2$	1.6	1.03×10^{-3}
$N1$	0.05	8.00×10^{-3}

Table 6.16: Changes in signal yields and asymmetry with no neural network shape replacements.

6.10.7. Correlation between ΔE and $N2$ in DK_D

Table A.33 (Appendix) shows that there is some correlation between ΔE and $N2$, which is ignored in the PDF. To estimate the effect of ignoring this correlation on the signal yield and asymmetry, we repeated the data fit three times, each time taking the $N2$ shape of DK_D events from a different ΔE bin The resulting changes in the signal yield and asymmetry are listed in Table 6.17. The sum of these changes, weighted by the fraction of signal events in that bin, is taken as the systematic error.

6.10.8. Data Monte Carlo shape comparison

Comparison in the m_{ES} Sideband

In the validation plots of section 6.7.3 we generally see good agreement between MC and data distributions. To evaluate the error due to possible disagreements in

Shape taken from	N_{DK_D} change (events)	A_{DK_D} change	Fraction of events
Bin 1	3.40	6.65×10^{-4}	14.90%
Bin 2	1.13	2.83×10^{-3}	72.87%
Bin 3	8.09	1.41×10^{-2}	12.23%
Total	2.32	3.89×10^{-3}	

Table 6.17: Change in the signal yield and asymmetry when the $N2$ shape of DK_D events is taken from the different ΔE bins.

the shapes of the background and propagate the statistical errors of the validation, we use Fig. 6.41 as a measure of such disagreements in the m_{ES} sideband. The procedure for quantifying the effect is as follows:

For $n = \{N1, N2\}$ and bin i, we calculate the histogram

$$h_n(i) \equiv h_n^D(i) - h_n^{MC}(i), \tag{6.14}$$

where h_n^D (h_n^{MC}) is the data (MC) histogram of Fig. 6.41, which is already normalized to unit area. We then modify the n shape of the $D\pi X$ events by changing its histogram $s_n^{D\pi X}(i)$ in the following way:

$$s_n^{D\pi X}(i) \to s_n^{D\pi X}(i)(1 + h_n(i)). \tag{6.15}$$

In other words, we assign the entire MC-data difference to the $D\pi X$ shape.

Since the ΔE PDF is parameterized as a second order polynomial, a different procedure was used for varying this PDF. In this case, we conduct second order polynomial fits to the data and MC ΔE histograms of Fig. 6.41. These fits give the polynomial coefficients c_i^D and c_i^{MC}, where $i = \{0, 1, 2\}$. We then modify the parameters $c_i^{D\pi X}$ of the $D\pi X$ ΔE PDF:

$$c_i^{D\pi X} \to c_i^{D\pi X} + c_i^D - c_i^{MC}. \tag{6.16}$$

The fit results on data obtained with these PDF modifications are shown in Table 6.18. The change in the signal yield (asymmetry) is 6.25 events (4.5×10^{-3}) relative to Table 6.10.

parameters	value
$R_{D\pi X}$	0.794 ± 0.114
$N_{D\pi_D}$	46.5 ± 16.0
A_{DK_D}	-0.0039 ± 0.158
$N_{qq\not{p}}$	1461.9 ± 52.9
N_{DK_D}	129.6 ± 22.0
$N_{B\bar{B}}$	787.3 ± 52.9
N_{DK_D} error (events)	A_{DK_D} error
6.25	4.32×10^{-3}

Table 6.18: Data fit parameters and additional systematic error check with the difference between Data and MC from the $m_{\rm ES}$ sideband.

As a cross-check, we repeated this procedure, but this time assigning the difference to the $qq\not{p}$ PDF or the DKX PDF. The change in the signal yield (asymmetry) for

$qq_{\not{p}}$ PDF modifications is 1.5 events (2.5×10^{-3}), and for DKX PDF modifications it is 0.7 events (9.5×10^{-4}). These changes lead to smaller systematic errors than when we apply the change to the $D\pi X$ PDF. This is probably due to the fact that the $D\pi X$ component is the largest of the $B\overline{B}$ backgrounds, which have a much larger correlation with signal than does the continuum background.

Comparison of $B^- \longrightarrow (K^-\pi^+\pi^0)_D\pi^-$ NN distributions

As for decay mode $B^- \longrightarrow (K^-\pi^+\pi^0)_D\pi^-$, the neural net plots in Fig. 6.38 are for signal only. Applying the procedure described in section 6.10.8 to Fig. 6.38 and assigning the difference to the DK_D PDF, we obtain a change of 0.1 events in the signal yield and a 1.5×10^{-2} change in the asymmetry.

Comparison of $B^- \longrightarrow (K^-\pi^+\pi^0)_D\pi^-$ ΔE mean

Table 6.6 shows a difference of 2.6 MeV between the mean of the ΔE Gaussian in data and MC. To estimate the effect of this on our fit, we shift the mean values of all ΔE Gaussians by this amount relative to their original (MC) values, and repeat the fit. This gives a change of 3.4 in the signal yield and a 4.2×10^{-3} change in the asymmetry.

Comparison of $B^- \to (K^-\pi^+\pi^0)_D\pi^-$ Cut Efficiencies

Table 6.6 shows that data and MC have slightly different $m_{\rm ES}$ and m_D shapes. Although we do not use these variables in the fit, we do cut on them. Therefore, we obtained a systematic error due to the MC/data efficiency difference of these cuts. To do this, we generated about 100,000 events with the data and MC parameters of Table 6.6, corresponding to the pre-selection cuts, and calculated the data and MC efficiencies of the final cuts on the generated distributions. The same was done to evaluate the efficiencies of the neural net cuts. The ratios between the MC and data efficiencies are

$$\begin{aligned} r_{m_{\rm ES}} &= 1.0029 \pm 0.0013, \\ r_{m_D} &= 0.9981 \pm 0.0018, \\ r_{N1} &= 0.9963 \pm 0.0011, \\ r_{N2} &= 0.9987 \pm 0.0012, \end{aligned} \tag{6.17}$$

where the errors were obtained by calculating the efficiencies after changing the parameters of Table 6.6 by $\pm 1\sigma$. Combining the errors in quadrature, we obtain a total systematic error due to this signal efficiency difference of 0.28%, and also apply a total efficiency correction factor of 0.9960.

6.10.9. Tracking efficiency

Based on the studies performed by members of *BABAR* collaboration track efficiency task force group (Ref. [64]), We apply a relative efficiency correction of -0.5% per track with respect to the MC, and take the systematic error to be 1.4% per track. This decay mode has 3 tracks, so the total systematic error is 4.2% and the efficiency correction factor is 0.9851.

6.10.10. π^0 efficiency

Following the official recipe (Ref. [65]), we take the ratio between data and MC efficiencies to be 0.968311, and apply a 3.5% systematic error.

6.10.11. $B\bar{B}$ counting

The standard collaboration systematic due to $B\bar{B}$ counting is 1.1%.

6.10.12. Particle ID

To evaluate the systematic error due to the PID selection (Ref. [66]), we used the errors in the PID tables, adding in quadrature the errors of the weights of each track in our MC sample. Using this procedure, we found the systematic errors to be 0.75% for kaons and 0.69% for pions, for a total error of 1.02%.

6.10.13. Summary of the systematic errors for $B^{\pm} \rightarrow DK^{\pm}$

The systematic errors on the signal yield and asymmetry are summarized in Table 6.19. Table 6.20 lists additional systematic errors that apply to the branching fraction. Combining these two tables, the total relative systematic error on the branching fraction is 12.9%. The following subsections describe how these errors were evaluated.

Source	N_{DK_D} error (events)	A_{DK_D} error
$R_{DK_{\not{D}}}$ variation	1.40	6.51×10^{-4}
$R_{D\pi_{\not{D}}}$ variation	0.02	1.30×10^{-4}
R_{BBC_D} variation	0.93	6.06×10^{-4}
R_{DKX} variation	5.98	1.97×10^{-3}
R_{qq_D} variation	4.33	1.28×10^{-3}
Dalitz plot distribution uncertainty	0.41	NA
MC statistics	9.55	1.35×10^{-2}
Uncertainty in Charmless BR	1.04	9.32×10^{-4}
Detector charge asymmetry	0.04	9.02×10^{-3}
Neural network shape replacements	1.10	1.16×10^{-2}
$\Delta E - N2$ correlations in DK_D	2.32	3.89×10^{-3}
Data-MC shape comparison	7.12	1.62×10^{-2}
Total systematic error	14.4 (11.7%)	2.61×10^{-2}

Table 6.19: Systematic errors in the signal event yield and asymmetry.

Source	Signal BR error (%)
PID efficiency	1.0
Tracking efficiency	4.2
π^0 efficiency	3.5
$B\bar{B}$ counting	1.1
Total	5.70

Table 6.20: Additional systematic errors on the signal branching fraction.

6.11. Physics results

6.11.1. Efficiency corrections

Table 6.21 shows the corrections from the possible sources in which data and Monte Carlo have discrepancies. These correction factors are obtained from *BABAR* official recipes. With these corrections, the final Monte Carlo signal efficiency is 10.53%.

Source	correction factor
Pid efficiency	0.9893
Tracking efficiency	0.985
π^0 efficiency	0.968
Data-MC efficiency difference	0.996
Total correction	0.9395

Table 6.21: Efficiency correction factors for $B^{\pm} \to DK^{\pm}$.

6.11.2. Branching fraction and decay asymmetry measurement

The branching fraction is determined from

$$\mathcal{B}(B^{\pm} \to (\pi^{+}\pi^{-}\pi^{0})_{D}K^{\pm}) = \frac{N_{DK_D}}{N_{B\bar{B}}\,\varepsilon}, \tag{6.18}$$

where $N_{B\bar{B}}$ and ε are the number of $B\bar{B}$ events and the signal efficiency, respectively. We measure the branching fraction

$$\mathcal{B}(B^{\pm} \to (\pi^{+}\pi^{-}\pi^{0})_{D}K^{\pm}) = (5.5 \pm 1.0 \pm 0.7) \times 10^{-6} \tag{6.19}$$

and decay rate asymmetry

$$\frac{\mathcal{B}(B^{+} \to (\pi^{+}\pi^{-}\pi^{0})_{D}K^{+}) - \mathcal{B}(B^{-} \to (\pi^{+}\pi^{-}\pi^{0})_{D}K^{-})}{\mathcal{B}(B^{+} \to (\pi^{+}\pi^{-}\pi^{0})_{D}K^{+}) + \mathcal{B}(B^{-} \to (\pi^{+}\pi^{-}\pi^{0})_{D}K^{-})} = 0.02 \pm 0.16 \pm 0.02. \tag{6.20}$$

6.12. Some cross checks and additional studies

6.12.1. Fit to m_D sideband

We conducted a fit to data in the m_D sidebands $1.775 < m_D < 1.800$ GeV/c^2 and $1.920 < m_D < 1.955$ GeV/c^2. Given the signal efficiency for this cut, we expect 2.7 signal events in the fit. We find 17.0 ± 9.3 events, which is 1.5σ above the expectation, given only the statistical error of the fit.

6.12.2. Toy Monte Carlo study with the data fit parameters

We did a second toy MC study, this time with the parameters obtained from the data fit (see Table 6.10). The results of this study are in good agreement with the input parameters. Figs. 6.46 and 6.47 show the distributions of the fit parameter values and pulls for A_{DK_D} and N_{DK_D}. Fig. 6.48 compares the distribution of negative-log-likelihood values in the toy experiments to the value obtained in the data fit. The value from data fit falls well within the distribution of toy study results.

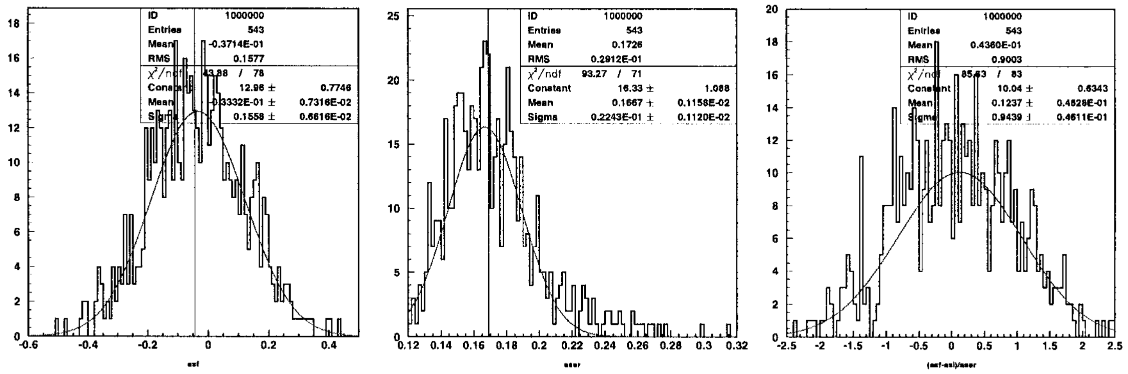

Figure 6.46: The fit value (left), error (center), and pull (right) for A_{DK_D}. Vertical lines indicate the values obtained in the data fit.

6.12.3. Significance of the signal observation

Fig. 6.49 shows a scan of the negative log likelihood as a function of the signal yield (N_{DK_D}), with all other parameters fixed. From the value of the negative log likelihood (see Fig. 6.49) at $N_{DK_D} = 0$, the significance is 5.74σ, in agreement with

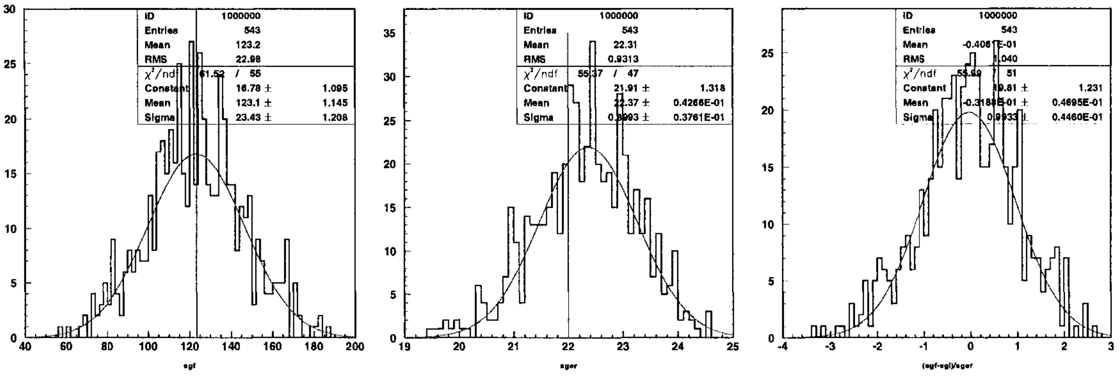

Figure 6.47: The fit value (left), error (center), and pull (right) for N_{DK_D}. Vertical lines indicate the values obtained in the data fit.

the ratio between N_{DK_D} and its statistical error.

6.12.4. Uncertainty in DKX ΔE shape

The ΔE distribution of DKX (Fig. 6.15, right), has a Gaussian component peaking around -7 MeV. It is not clear what source causes this from the existing MC samples. To estimate this peaking component effect, we fit the MC without it and used the resulting shape to fit the data. The changes in the signal yield was 3.0 events, and the change in the asymmetry was 1.7×10^{-3}. This may be compared with the systematic error obtained due to the finite MC statistics with which the ΔE shape of this event type was obtained. That error is 2.3 events for the signal yield and 2×10^{-3} for the asymmetry. We conclude therefore that no additional error is needed to account for the uncertainty in the central Gaussian of the DKX ΔE shape.

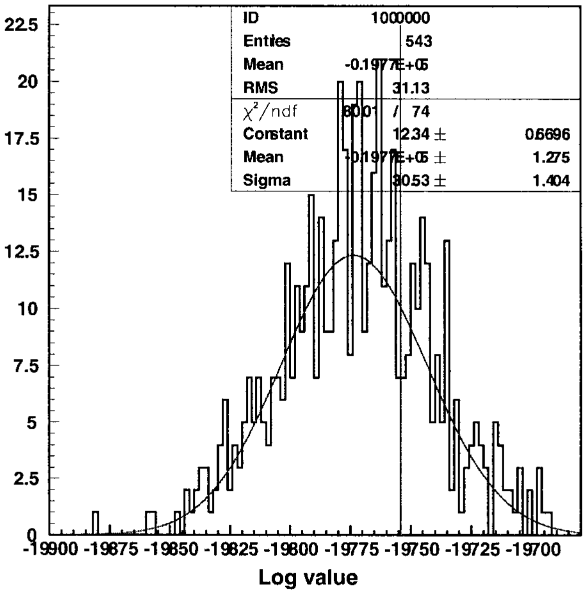

Figure 6.48: The distribution of log likelihood values for the toy fit. The vertical line indicates the data fit value.

6.12.5. Cross check on ΔE sideband for Monte Carlo data difference

The procedure of Section. 6.10.8 is repeated, using the sum of Figs. 6.42 and 6.43 instead of Fig. 6.41. This gives a change of 0.76 events in the signal yield and a 8.51×10^{-3} change in the asymmetry, consistent with the error of section 6.10.8. Since Figs. 6.42 and 6.43 contain lower statistics than Fig. 6.41, this result is used only as a cross check, but not as a systematic error.

6.12.6. Alternative candidate selections for multi-candidate events

In this $B^{\pm} \to DK^{\pm}$ analysis, a single candidate per event was chosen randomly. This selection method does not result in an accumulation of background events in any

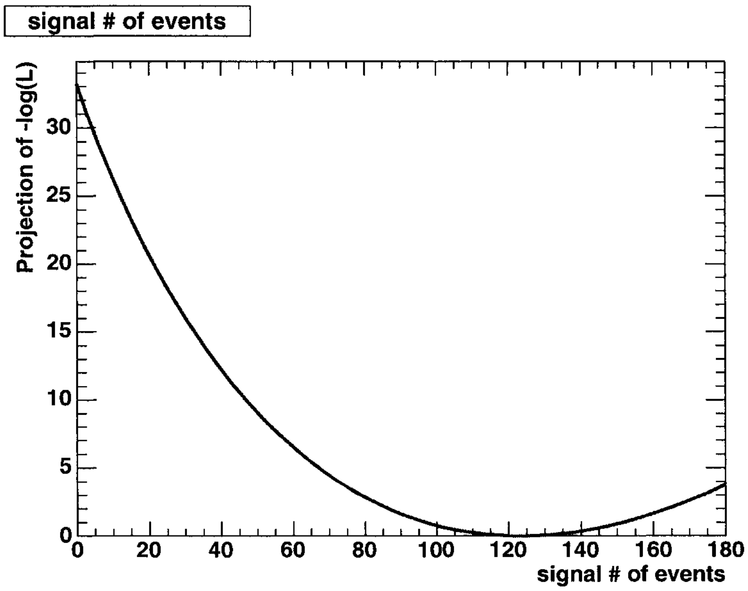

Figure 6.49: The difference between the value of the negative log likelihood as a function of N_{DK_D} and its minimum value.

variable. It therefore allowed us to test different fit variables during the development of the analysis procedure. But it does not necessarily give the most sensitive results.

Using toy MC, we explored two χ^2 selections, one based on $m_{\rm ES}$ and m_D, and the other on m_D only. In this method, we select the one candidate per event that has the smallest value of χ^2.

The cuts applied here are the same as in the main analysis (Section 6.6.2), with the same procedure as the random selection method.

Best candidate selection with $\chi^2(m_D, m_{\rm ES})$

From MC truth we determine the values of the parameters listed in Table 6.22. Comparing these parameters with the values they take with the random selection (Table 6.4), we observe that relative to the random selection, this χ^2 selection increases the signal efficiency by 16.4%, the $B\overline{B}$ background (with a fake D) by 24.9%, and the continuum background (with a fake D) by 20.8%. Thus, both the signal and background efficiencies increase, with the $B\overline{B}$ background increasing the most. To determine the effect on the analysis, we ran toy MC experiments with the input parameters of Table 6.22. The results are shown in Figs. 6.50 and 6.51. From Fig. 6.51 we see that the average relative statistical error on N_{DK_D} is about 0.219, whereas for the random selection (Fig. 6.29) this value is 0.227. Therefore, the statistical significance changes very little between the random selection and this $\chi^2(m_{\rm ES}, m_D)$ selection. In addition, the larger background (especially in $B\bar{B}$) in the χ^2 selection could result in somewhat larger systematic errors. Therefore, the $\chi^2(m_{\mathrm{ES}}, m_D)$ selection is not significantly superior to the random selection method.

parameter	value
R_{DKX}	0.2679
$R_{D\pi X}$	0.5627
N_{DK_D}	107.3
A_{DK_D}	0.0
$R_{DK_{\not{D}}}$	0.1324
$N_{D\pi_D}$	41.4
$R_{D\pi_{\not{D}}}$	0.2615
R_{BBC_D}	0.00429
$N_{B\bar{B}}$	987.3
$N_{qq_{\not{D}}}$	2037.0
R_{qq_D}	0.0128

Table 6.22: Parameter values obtained from full Monte Carlo for $\chi^2(m_{\mathrm{ES}}, m_D)$ best candidate selection.

Best candidate selection with $\chi^2(m_D)$

We used the same produce as above but calculating the χ^2 using m_D only. The input parameters are listed in Table 6.23. . Compared with the values in Table 6.4, the $\chi^2(m_D)$ selection increases the signal efficiency by 14.9%, the $B\overline{B}$ background (with a fake D) by 16.2%, and the continuum background (with a fake D) by 35.8%. The greatest increase is in the continuum. The average fit result for N_{DK_D} is 103.9 ± 22.21.

parameter	value
R_{DKX}	0.2823
$R_{D\pi X}$	0.5769
N_{DK_D}	105.9
A_{DK_D}	0.0
$R_{DK_{\not D}}$	0.1383
$N_{D\pi_D}$	41.7
$R_{D\pi_{\not D}}$	0.2266
R_{BBC_D}	0.0050
$N_{B\bar{B}}$	918.0
$N_{qq_{\not D}}$	2291.0
R_{qq_D}	0.0105

Table 6.23: Parameter values obtained from full Monte Carlo for $\chi^2(m_D)$ best candidate selection.

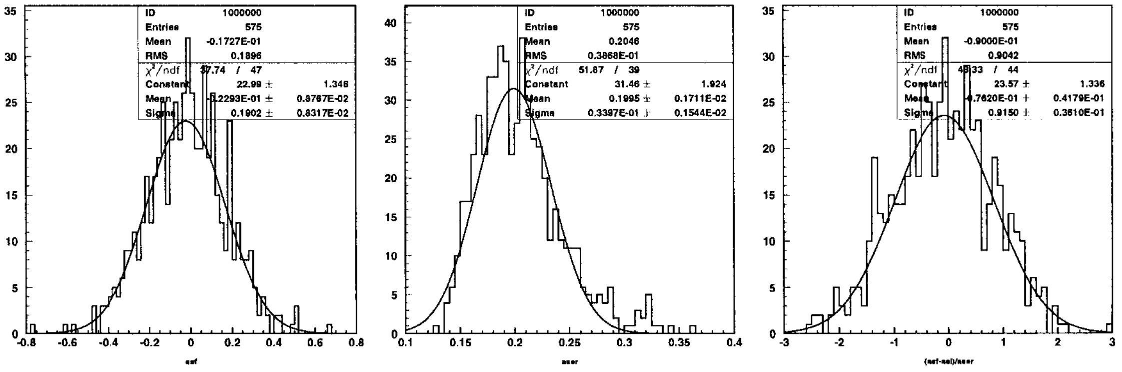

Figure 6.50: The fit value (left), error (center), and pull (right) for A_{DK_D} with χ^2 selection with m_{ES} and m_D.

The relative statistical error on N_{DK_D} is 0.214. Compared with random selection (0.227), the sensitivity is a bit improved but not significantly (about 5.7% better). We therefore conclude that the random selection is satisfactory.

6.12.7. Different fit configurations with Monte Carlo

We tried different fit configurations, using all or some of the variables m_{ES}, m_D, ΔE, $N1$ and $N2$. These are

a) 5D fit with the cuts of Section 6.3.2,

b) 5D fit with the cuts of Section 6.6.2,

c) 5D fit with the cuts of Section 6.6.2 but with a loose m_{ES} cut,

d) 4D fit (m_{ES} ΔE $N1$ and $N2$) with the cuts of Section 6.6.2,

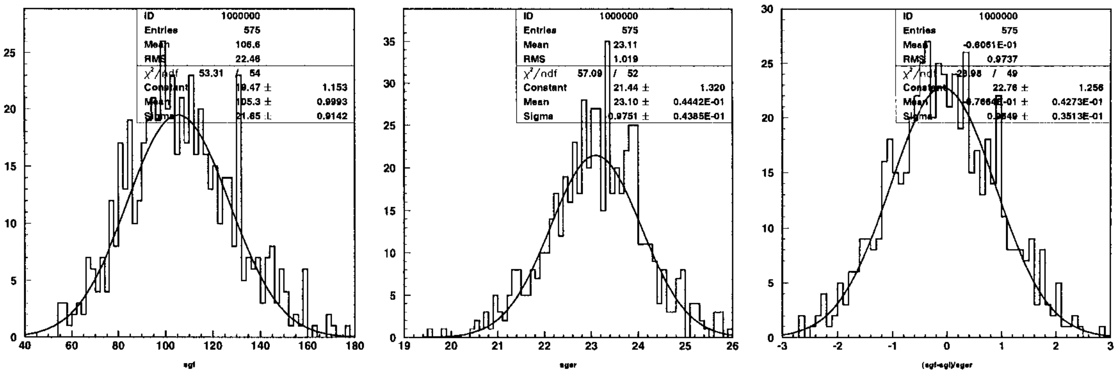

Figure 6.51: The fit value (left), error (center), and pull (right) for N_{DK_D} with χ^2 selection with m_{ES} and m_D.

e) 4D fit (m_D ΔE $N1$ and $N2$) with the cuts of Section 6.6.2,

f) 3D fit (m_{ES}, ΔE and m_D) with the cuts of Section 6.6.2 except $m_{\text{ES}} > 5.23$, $0.06 < \Delta E < 0.11$, $N1 > 0.4$ and $N2 > 0.4$.

In this section, the detail of the configurations are omitted, only the results are given.

Table 6.24 shows the bias in the N_{DK_D} with above fit configurations.

To check whether the bias is caused by the correlation between m_{ES} and other fit variables, we replaced (a) all the m_{ES} distributions, (b) only the $B\bar{B}$ m_{ES} distributions with MC PDF, and refit the MC samples with replaced m_{ES} distribution, the resulting bias in N_{DK_D} are inside 1σ range.

Configure Type	Bias in N_{DK_D} (σ)	value of 1σ
a	1.5σ	18.3
b	1.4σ	18.1
c	1.9σ	19.0
d	1.4σ	19.5
e	1.2σ	19.6
f	2.0σ	19.1

Table 6.24: MC fit bias in N_{DK_D} with different fit configurations.

Chapter 7

Conclusion

Two analyses are documented, both are on rare decays associated with charm decay of the B mesons, one is to a charmonium state,$B \longrightarrow J/\psi \eta K$, which is useful to identify the property of X(3872); the other one is to an open charm state, $B^{\pm} \longrightarrow DK^{\pm}$ with $D^0/\bar{D}^0 \longrightarrow \pi^+\pi^-\pi^0$, which can be used to extract the weak phase γ through the inteference between the two processes of $b \rightarrow c\bar{u}s$ and $b \rightarrow u\bar{c}s$ via $D^0/\bar{D}^0 \rightarrow \pi^+\pi^-\pi^0$.

The background for each analysis is different. For $B \longrightarrow J/\psi \eta K$, the J/ψ candidate can be cleanly reconstructed from leptons and gives a clean signal, the background is mainly from $B \longrightarrow J/\psi + A$ (inclusive J/ψ), where A is any combination of particles which are not for our signal modes. For $B^{\pm} \longrightarrow DK^{\pm}$, the main contributions to background are continuum and $B\bar{B}$ backgrounds; continuum background constitutes about 70%. The continuum background is flat while the $B\bar{B}$ may contribute peaking background. How to deal with the $B\bar{B}$ background is a challenge for both analyses.

For $B \rightarrow J/\psi\eta K$, we use ΔE sideband to model the distribution of the backgrond and one dimension fit on m_{ES} is used to extract the signal events. For $B^{\pm} \rightarrow DK^{\pm}$, two neural network variables are developed to suppress the background, a maximum likelihood fit is used to extract the signal yields. Though the methods used for these two analyses are quite different, both are aimed at extracting a branching fraction.

In $B \rightarrow J/\psi\eta K$ analysis, the branching fraction of charged (neutral) channel is $(10.8 \pm 2.31(\text{stat.}) \pm 2.37(\text{syst.})) \times 10^{-5}$ $((8.4 \pm 2.6 \pm 2.7) \times 10^{-5})$. The ratio between neutral and charged kaon modes is (0.77 ± 0.23), agrees with the expectation (0.5). Search for X(3872) particle was conducted in charged mode, no evidence was found with the data we used, a 90% C.L. branching fraction upper limit for $X(3872) \rightarrow \eta J/\psi$ was set, 7.7×10^{-6}. If X(3872) is a conventional charmonium state like $\psi(2S)$, the branching fraction of $\mathcal{B}(B^+ \rightarrow X(3872)K^+) \times \mathcal{B}(X(3872) \rightarrow \eta J/\psi) \sim 1.4 \times 10^{-6}$ [2], compared to the upper limit we set, no confirmative conclusion on whether X(3872) is a conventional charmonium state can be established.

For $B^{\pm} \rightarrow DK^{\pm}$, the necessary analysis techniques to suppress high background have been developed. With 207 fb^{-1} data, we got a good measurement on the branching ratio of the decay chain $B^{\pm} \rightarrow DK^{\pm}$ with $D^0/\bar{D}^0 \rightarrow \pi^+\pi^-\pi^0$, the measurement is $(5.5 \pm 1.0 \pm 0.7) \times 10^{-6}$; the decay rate asymmetry is $(0.02 \pm 0.16 \pm 0.02)$. For the further weak phase γ measurement, some members from *BABAR* will pick it up.

Appendix A

Correlation check for fit variables

A.1. Variable correlation after the pre-selection cuts

As a maximum likelihood fit is sensitive to the correlation of the variables input into the fit, we first investigate the correlations between the potential fit variables m_{ES}, ΔE, m_D, $N1$, and $N2$. This study has led to tightening of the cuts and removal of m_{ES} and m_D from the fit. Everything in this section uses the cuts of section 6.3.2.

Here we list the correlation matrixes of these variable in Tables A.1 through A.10. The correlation matrix element for variables x and y is calculated as

$$\rho_{xy} = \frac{V_{xy}}{\sqrt{V_{xx}V_{yy}}}, \tag{A.1}$$

where $V_{xy} \equiv < xy > - < x >< y >$ and the average is over all events in the sample.

In addition to this linear correlation calculation, we evaluated non-linear correlations in the following way: We divided MC events in each of the variables m_{ES},

ΔE, m_D, and $N1$, with the binning shown in Table A.11. For each bin of variable i, we made histograms of the other fit variables (variables $j \neq i$), and made Kolmogorov-Smirnov comparisons of the histograms in the different bins. A low KS probability indicates correlations between variables i and j. The KSP probabilities are summarized in Tables A.12 through A.21. In cases where the KSP probabilities are particularly low we show the plots being compared. This is done in Figures A.1 through A.5.

	m_{ES}	ΔE	m_D	$N1$	$N2$
m_{ES}	1	-0.159	-0.007	-0.013	0.012
ΔE		1	-0.003	-0.008	-0.063
m_D			1	0.012	-0.004
$N1$				1	0.035

Table A.1: Correlation matrix for DK_D MC events.

	m_{ES}	ΔE	m_D	$N1$	$N2$
m_{ES}	1	-0.133	0.043	0.068	-0.022
ΔE		1	-0.029	-0.057	0.103
m_D			1	-0.002	0.091
$N1$				1	0.048

Table A.2: Correlation matrix for $DK_{\not{D}}$ MC events.

	m_{ES}	ΔE	m_D	$N1$	$N2$
m_{ES}	1	-0.207	-0.049	-0.062	0.048
ΔE		1	- 0.014	-0.079	-0.089
m_D			1	0.045	-0.029
$N1$				1	-0.067

Table A.3: Correlation matrix for $D\pi_D$ MC events.

	m_{ES}	ΔE	m_D	$N1$	$N2$
m_{ES}	1	0.208	-0.066	0.121	-0.032
ΔE		1	-0.138	-0.018	0.055
m_D			1	0.080	-0.101
$N1$				1	-0.053

Table A.4: Correlation matrix for $D\pi_{\not{D}}$ MC events.

	m_{ES}	ΔE	m_D	$N1$	$N2$
m_{ES}	1	-0.007	0.008	0.031	-0.140
ΔE		1	-0.017	0.018	0.009
m_D			1	0.005	-0.011
$N1$				1	-0.035

Table A.5: Correlation matrix for other $D\pi X$ background MC events.

	m_{ES}	ΔE	m_D	$N1$	$N2$
m_{ES}	1	-0.0522	0.006	0.058	-0.018
ΔE		1	-0.025	-0.016	0.014
m_D			1	0.048	-0.006
$N1$				1	-0.028

Table A.6: Correlation matrix for other DKX background MC events.

	m_{ES}	ΔE	m_D	$N1$	$N2$
m_{ES}	1	-0.014	-0.002	0.038	-0.133
ΔE		1	-0.031	-0.014	-0.004
m_D			1	0.003	-0.025
$N1$				1	-0.023

Table A.7: Correlation matrix for other $BBC_{\not{D}}$ background MC events.

	m_{ES}	ΔE	m_D	$N1$	$N2$
m_{ES}	1	0.032	0.047	-0.072	-0.055
ΔE		1	0.073	-0.062	0.030
m_D			1	-0.005	-0.060
$N1$				1	-0.081

Table A.8: Correlation matrix for other BBC_D background MC events.

	m_{ES}	ΔE	m_D	$N1$	$N2$
m_{ES}	1	-0.032	0.048	-0.073	0.056
ΔE		1	-0.073	-0.062	-0.030
m_D			1	0.005	0.060
$N1$				1	0.081

Table A.9: Correlation matrix for qq_D MC events.

	m_{ES}	ΔE	m_D	$N1$	$N2$
m_{ES}	1	-0.007	$-3.1 \times 10^{-}5$	-0.024	-0.009
ΔE		1	0.0036	0.012	-0.017
m_D			1	0.010	-0.022
$N1$				1	0.008

Table A.10: Correlation matrix for $qq_{\not D}$ MC events.

Variable	Bin 1	Bin 2	Bin 3
m_{ES}(GeV)	$5.2 < m_{\text{ES}} < 5.265$	$5.265 < m_{\text{ES}} < 5.3$	$5.3 < m_{\text{ES}} < 5.3$
ΔE(MeV)	$-70 < \Delta E < -20.$	$-20 < \Delta E < 20$	$20 < \Delta E < 140$
m_D(GeV)	$1.805 < m_D < 1.853$	$1.853 < m_D < 1.877$	$1.877 < m_D < 1.924$
$N1$	$0 < N1 < 0.5$	$0.5 < N1 < 0.8$	$0.8 < N1 < 1$

Table A.11: Bins used for the KSP comparisons in Tables A.12 through A.21.

	$(m_{\rm ES})\ \Delta E$	$(m_{\rm ES})\ m_D$	$(m_{\rm ES})\ N1$	$(m_{\rm ES})\ N2$	$(\Delta E)\ m_D$
Bins 1,2	0.46102	0.43423	0.24803	0.94714	0.00004
Bins 1,3	0.33502	0.43792	0.23789	0.94592	0.59884
Bins 2,3	0.00000	0.98352	0.99999	0.99934	0.00034
	$(\Delta E)\ N1$	$(\Delta E)\ N2$	$(m_D)\ N1$	$(m_D)\ N2$	$(N1)\ N2$
Bins 1,2	0.71732	0.14083	0.37645	0.00431	0.15411
Bins 1,3	0.87929	0.00000	0.15512	0.03858	0.00114
Bins 2,3	0.44211	0.00000	0.04052	0.00264	0.50961

Table A.12: KSP tests for correlations in DK_D. In each column, $(x)\ y$ indicates that the KSP compare the histograms of variable y in bins of variable x. See Table A.11 for the bin ranges.

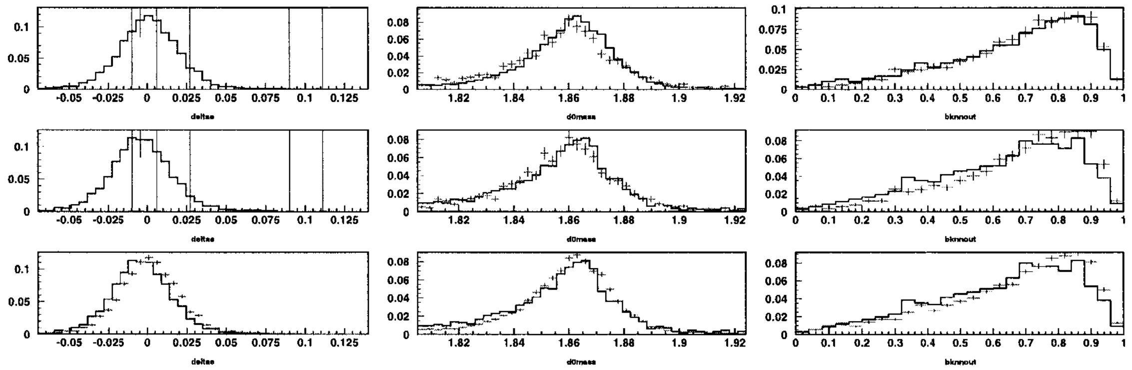

Figure A.1: DK_D plot pairs with low KS probabilities for $(m_{\rm ES})\Delta E$ (left), $(\Delta E)m_D$ (middle) and $(\Delta E)N2$ (right). Top plot is for bins 1-2, middle plot is bins 1-3, bottom plot is bins 2-3. See Table A.11 for the bin ranges.

	$(m_{\text{ES}})\ \Delta E$	$(m_{\text{ES}})\ m_D$	$(m_{\text{ES}})\ N1$	$(m_{\text{ES}})\ N2$	$(\Delta E)\ m_D$
Bins 1,2	0.00000	0.00011	0.00036	0.27794	0.00824
Bins 1,3	0.00000	0.00853	0.02549	0.68862	0.00232
Bins 2,3	0.64449	0.26339	0.53197	0.97006	0.02823
	$(\Delta E)\ N1$	$(\Delta E)\ N2$	$(m_D)\ N1$	$(m_D)\ N2$	$(N1)\ N2$
Bins 1,2	0.63190	0.23492	0.98557	0.01105	0.09839
Bins 1,3	0.00229	0.00000	0.97260	0.00000	0.96704
Bins 2,3	0.07849	0.00085	0.84767	0.14873	0.20128

Table A.13: KSP tests for correlations in $DK_{\not p}$. In each column, $(x)\ y$ indicates that the KSP compare the histograms of variable y in bins of variable x. See Table A.11 for the bin ranges.

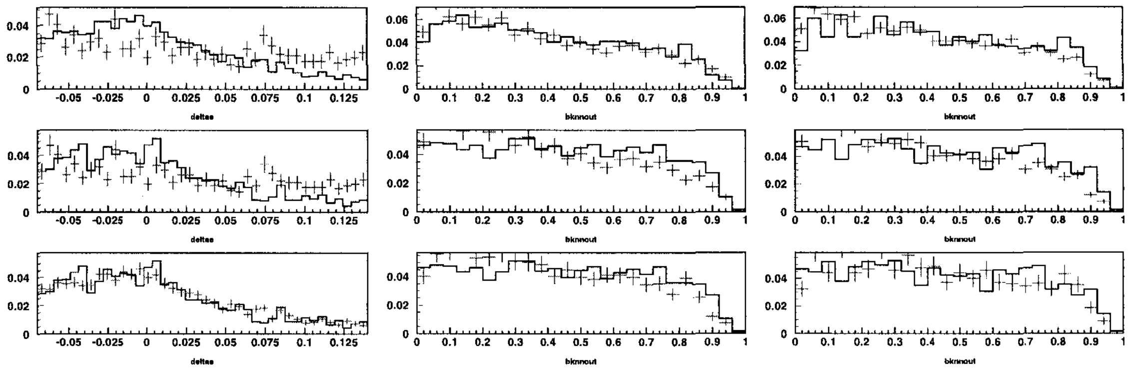

Figure A.2: $DK_{\not p}$ plot pairs with low KSP for $(m_{\text{ES}})\Delta E$ (left) , $(\Delta E)N2$ (middle) and $(m_D)N2$ (right). Top plot is for bins 1-2, middle plot is bins 1-3, bottom plot is bins 2-3. See Table A.11 for the bin ranges.

	$(m_{\text{ES}})\ \Delta E$	$(m_{\text{ES}})\ m_D$	$(m_{\text{ES}})\ N1$	$(m_{\text{ES}})\ N2$	$(\Delta E)\ m_D$
Bins 1,2	N/A	N/A	N/A	N/A	0.48713
Bins 1,3	N/A	N/A	N/A	N/A	0.94187
Bins 2,3	0.04517	0.45651	0.28163	0.99997	0.36874
	$(\Delta E)\ N1$	$(\Delta E)\ N2$	$(m_D)\ N1$	$(m_D)\ N2$	$(N1)\ N2$
Bins 1,2	0.98341	0.84903	0.98181	0.99544	0.81411
Bins 1,3	0.75658	0.92110	0.38775	0.12822	0.88331
Bins 2,3	0.66102	0.92710	0.32657	0.15735	0.94598

Table A.14: KSP tests for correlations in $D\pi_D$. In each column, $(x)\ y$ indicates that the KSP compare the histograms of variable y in bins of variable x. See Table A.11 for the bin ranges.

	$(m_{\text{ES}})\ \Delta E$	$(m_{\text{ES}})\ m_D$	$(m_{\text{ES}})\ N1$	$(m_{\text{ES}})\ N2$	$(\Delta E)\ m_D$
Bins 1,2	0.04704	0.16430	0.03519	0.73042	0.86689
Bins 1,3	0.03965	0.23904	0.96779	0.60935	0.19905
Bins 2,3	0.71791	0.92533	0.68458	0.92312	0.56582
	$(\Delta E)\ N1$	$(\Delta E)\ N2$	$(m_D)\ N1$	$(m_D)\ N2$	$(N1)\ N2$
Bins 1,2	0.48995	0.75137	0.98674	0.60836	0.98759
Bins 1,3	0.99631	0.94781	0.75944	0.51317	0.56521
Bins 2,3	0.80912	0.96379	0.99110	0.43050	0.99946

Table A.15: KSP tests for correlations in $D\pi_{\not{D}}$. In each column, $(x)\ y$ indicates that the KSP compare the histograms of variable y in bins of variable x. See Table A.11 for the bin ranges.

	$(m_{\mathrm{ES}})\ \Delta E$	$(m_{\mathrm{ES}})\ m_D$	$(m_{\mathrm{ES}})\ N1$	$(m_{\mathrm{ES}})\ N2$	$(\Delta E)\ m_D$
Bins 1,2	0.31128	0.64805	0.00004	0.00000	0.17917
Bins 1,3	0.50691	0.01341	0.00001	0.00000	0.00004
Bins 2,3	0.99900	0.21847	0.28046	0.00548	0.00030
	$(\Delta E)\ N1$	$(\Delta E)\ N2$	$(m_D)\ N1$	$(m_D)\ N2$	$(N1)\ N2$
Bins 1,2	0.75235	0.80808	0.95599	0.53301	0.34816
Bins 1,3	0.15161	0.15197	0.81675	0.17513	0.00075
Bins 2,3	0.12792	0.77201	0.34973	0.81281	0.08937

Table A.16: KSP value for correlation in $D\pi X$. $(x)\ y$ indicates that the KSP compare the histograms of variable y in bins of variable x. See Table A.11 for the bin ranges.

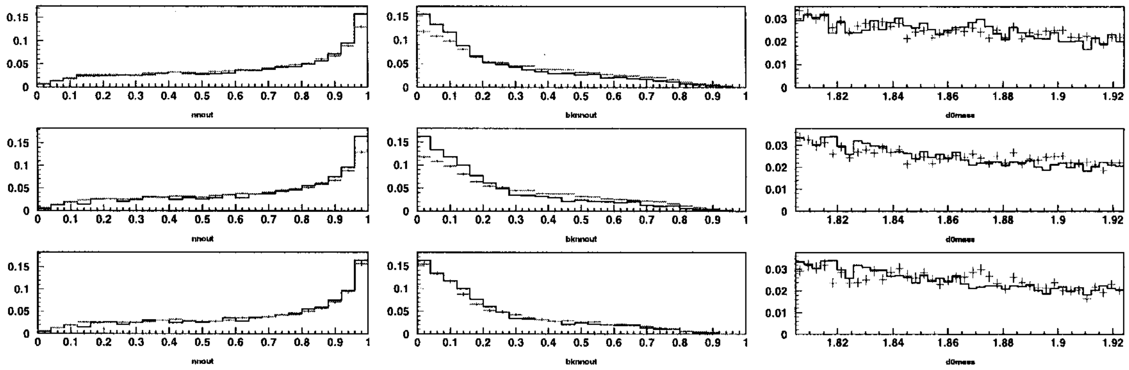

Figure A.3: $D\pi X$ plot pairs with low KSP for $(m_{\mathrm{ES}})N1$ (left), $(m_{\mathrm{ES}})N2$ (middle) and $(\Delta E)m_D$ (right). top plot is for bins 1-2, middle plot is bins 1-3, bottom plot is bins 2-3. See Table A.11 for the bin ranges.

	$(m_{\mathrm{ES}})\ \Delta E$	$(m_{\mathrm{ES}})\ m_D$	$(m_{\mathrm{ES}})\ N1$	$(m_{\mathrm{ES}})\ N2$	$(\Delta E)\ m_D$
Bins 1,2	0.17498	0.86883	0.00004	0.83127	0.44587
Bins 1,3	0.40631	0.67470	0.00014	0.89592	0.48898
Bins 2,3	0.64018	0.97473	0.41820	0.97267	0.29258
	$(\Delta E)\ N1$	$(\Delta E)\ N2$	$(m_D)\ N1$	$(m_D)\ N2$	$(N1)\ N2$
Bins 1,2	0.80953	0.66199	0.99828	0.40591	0.55844
Bins 1,3	0.46510	0.99583	0.75892	0.92588	0.99040
Bins 2,3	0.63428	0.77098	0.67266	0.71975	0.73563

Table A.17: KSP value for correlation in DKX. $(x)\ y$ indicates that the KSP compare the histograms of variable y in bins of variable x. See Table A.11 for the bin ranges.

	$(m_{\rm ES})\ \Delta E$	$(m_{\rm ES})\ m_D$	$(m_{\rm ES})\ N1$	$(m_{\rm ES})\ N2$	$(\Delta E)\ m_D$
Bins 1,2	0.45455	0.05042	0.00203	0.00000	0.74721
Bins 1,3	0.02570	0.98851	0.01675	0.00000	0.05823
Bins 2,3	0.14152	0.21257	0.98550	0.41973	0.00783
	$(\Delta E)\ N1$	$(\Delta E)\ N2$	$(m_D)\ N1$	$(m_D)\ N2$	$(N1)\ N2$
Bins 1,2	0.53011	0.67626	0.49505	0.89024	0.23089
Bins 1,3	0.05580	0.88581	0.91791	0.00911	0.02547
Bins 2,3	0.83061	0.31678	0.18642	0.27839	0.84262

Table A.18: KSP values for $BBC_{\not p}$. In each column, $(x)\ y$ indicates that the KSP compare the histograms of variable y in bins of variable x. See Table A.11 for the bin ranges.

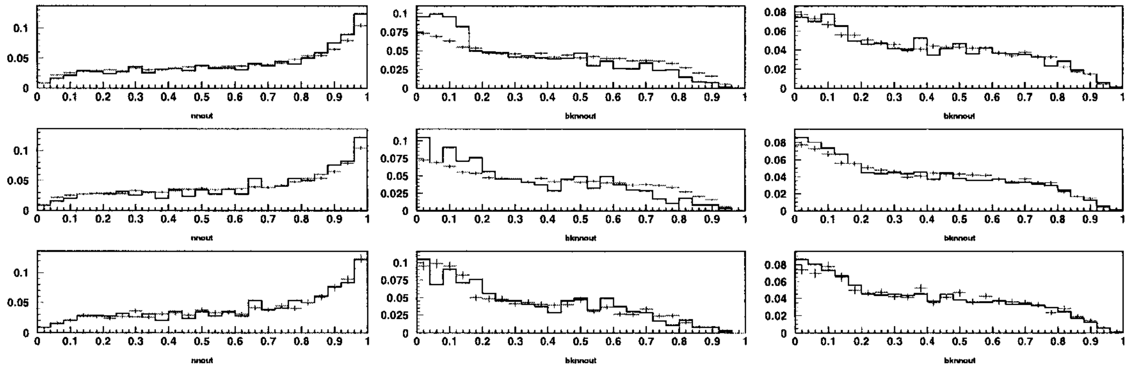

Figure A.4: $BBC_{\not p}$ plot pairs with low KSP for $(m_{\rm ES})N1$ (left), $(m_{\rm ES})N2$ (middle) and $(m_D)N2$ (right). top plot is for bins 1-2, middle plot is bins 1-3, bottom plot is bins 2-3. See Table A.11 for the bin ranges.

	(m_{ES}) ΔE	(m_{ES}) m_D	(m_{ES}) $N1$	(m_{ES}) $N2$	(ΔE) m_D
Bins 1,2	0.99716	0.31444	0.80655	0.80655	0.99681
Bins 1,3	0.98826	0.40047	0.75910	0.75910	N/A
Bins 2,3	0.89278	0.44131	0.99196	0.44131	N/A
	(ΔE) $N1$	(ΔE) $N2$	(m_D) $N1$	(m_D) $N2$	($N1$) $N2$
Bins 1,2	0.80877	0.64412	0.94397	0.94397	0.97936
Bins 1,3	N/A	N/A	0.24855	0.84749	0.91883
Bins 2,3	N/A	N/A	0.46107	0.90301	0.93245

Table A.19: KSP for BBC_D. In each column, (x) y indicates that the KSP compare the histograms of variable y in bins of variable x. See Table A.11 for the bin ranges.

	(m_{ES}) ΔE	(m_{ES}) m_D	(m_{ES}) $N1$	(m_{ES}) $N2$	(ΔE) m_D
Bins 1,2	0.26456	0.20157	0.00002	0.51418	0.89847
Bins 1,3	0.06345	0.11402	0.61756	0.07876	0.86135
Bins 2,3	0.84073	0.86051	0.09796	0.07187	0.96523
	(ΔE) $N1$	(ΔE) $N2$	(m_D) $N1$	(m_D) $N2$	($N1$) $N2$
Bins 1,2	0.90482	0.55710	0.04074	0.94575	0.78846
Bins 1,3	0.00312	0.00005	0.01631	0.00000	0.01004
Bins 2,3	0.10582	0.00023	1.00000	0.00006	0.07228

Table A.20: KSP tests for correlations in $qq_{\not{p}}$. In each column, (x) y indicates that the KSP compare the histograms of variable y in bins of variable x. See Table A.11 for the bin ranges.

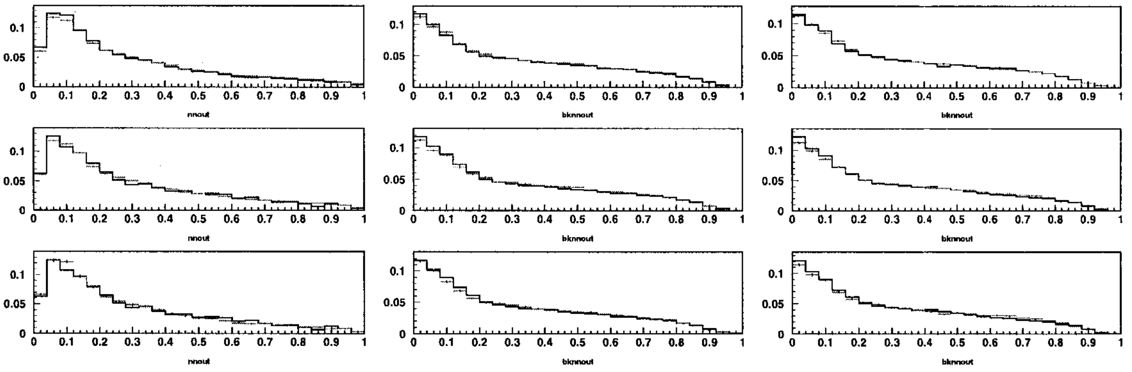

Figure A.5: $qq_{\not p}$ plot pairs with low KSP for $(m_{\mathrm{ES}})N1$ (left), $(\Delta E)N2$ (middle) and $(m_D)N2$ (right). top plot is for bins 1-2, middle plot is bins 1-3, bottom plot is bins 2-3. See Table A.11 for the bin ranges.

	$(m_{\mathrm{ES}})\ \Delta E$	$(m_{\mathrm{ES}})\ m_D$	$(m_{\mathrm{ES}})\ N1$	$(m_{\mathrm{ES}})\ N2$	$(\Delta E)\ m_D$
Bins 1,2	0.19988	0.21052	0.34146	0.69933	0.35138
Bins 1,3	0.17231	0.54168	0.99970	0.41780	0.07796
Bins 2,3	0.68727	0.96733	0.97351	0.70567	0.92490
	$(\Delta E)\ N1$	$(\Delta E)\ N2$	$(m_D)\ N1$	$(m_D)\ N2$	$(N1)\ N2$
Bins 1,2	0.75495	0.88596	0.80257	0.89224	0.30785
Bins 1,3	0.28808	0.39670	0.81145	0.80450	0.97947
Bins 2,3	0.92726	0.85680	0.93722	0.68931	0.92000

Table A.21: KSP tests for correlations in qq_D. In each column, $(x)\ y$ indicates that the KSP compare the histograms of variable y in bins of variable x. See Table A.11 for the bin ranges.

A.2. Correlation check after final cuts

The much reduced linear correlations after the final cuts are shown in Tables A.22 through A.31. Tables A.33 through A.42 show the KSP test value after the final cuts. In some of these tables we keep m_D entries, to show cases where m_D still retains significant correlations with some of the other variables.

	ΔE	$N1$	$N2$
ΔE	1	0.0013	-0.060
$N1$		1	-0.040

Table A.22: Correlation matrix for DK_D MC events after final cuts.

	ΔE	$N1$	$N2$
ΔE	1	-0.016	-0.090
$N1$		1	-0.002

Table A.23: Correlation matrix for $DK_{\not D}$ MC events after final cuts.

	ΔE	$N1$	$N2$
ΔE	1	-0.076	-0.0282
$N1$		1	-0.095

Table A.24: Correlation matrix for $D\pi_D$ MC events after final cuts.

	ΔE	$N1$	$N2$
ΔE	1	-0.140	-0.212
$N1$		1	0.164

Table A.25: Correlation matrix for $D\pi_{\not{D}}$ MC events after final cuts.

	ΔE	$N1$	$N2$
ΔE	1	-0.050	-0.020
$N1$		1	-0.001

Table A.26: Correlation matrix for $D\pi X$ MC events after final cuts.

	ΔE	$N1$	$N2$
ΔE	1	-0.031	-0.038
$N1$		1	-0.126

Table A.27: Correlation matrix for DKX MC events after final cuts.

	ΔE	$N1$	$N2$
ΔE	1	-0.006	-0.076
$N1$		1	0.009

Table A.28: Correlation matrix for $BBC_{\not{D}}$ MC events after final cuts.

	ΔE	$N1$	$N2$
ΔE	1	-0.237	0.189
$N1$		1	0.017

Table A.29: Correlation matrix for BBC_D MC events after final cuts.

	ΔE	$N1$	$N2$
ΔE	1	-0.047	-0.062
$N1$		1	-0.059

Table A.30: Correlation matrix for qq_D MC events after final cuts.

	ΔE	$N1$	$N2$
ΔE	1	-0.033	0.016
$N1$		1	0.015

Table A.31: Correlation matrix for $qq_{\not D}$ MC events after final cuts.

Variable	Bin 1	Bin 2	Bin 3
ΔE(MeV)	$-70 < \Delta E < -20.$	$-20 < \Delta E < 20$	$20 < \Delta E < 60$
m_D(GeV)	$1.83 < m_{\mathrm{ES}} < 1.853$	$1.853 < m_{\mathrm{ES}} < 1.877$	$1.877 < m_{\mathrm{ES}} < 1.895$
$N1$	$0.1 < N1 < 0.5$	$0.5 < N1 < 0.8$	$0.8 < N1 < 1$
$N2$	$0.1 < N2 < 0.5$	$0.5 < N2 < 0.8$	$0.8 < N2 < 1$

Table A.32: Bins used for the KS comparisons in Tables A.33 through A.42.

	$(\Delta E\ )m_D$	$(\Delta E)N1$	$(\Delta E)N2$	$(m_D)N1$	$(m_D)N2$	$(N1)N2$
Bins 1,2	0.0143	0.6244	0.2675	0.9836	0.0421	0.1906
Bins 1,3	0.5053	0.9902	0.0003	0.2192	0.0092	0.0011
Bins 2,3	0.7303	0.9622	0.0003	0.1439	0.0002	0.5757

Table A.33: KSP tests for correlations in DK_D. In each column, $(x)\ y$ indicates that the KSP compare the histograms of variable y in bins of variable x.

	$(\Delta E\ )m_D$	$(\Delta E)N1$	$(\Delta E)N2$	$(m_D)N1$	$(m_D)N2$	$(N1)N2$
Bins 1,2	0.0149	0.9995	0.3037	0.9505	0.6592	0.0458
Bins 1,3	0.2090	0.9034	0.0011	0.9247	0.1748	0.9229
Bins 2,3	0.7020	0.8181	0.0798	0.7873	0.6401	0.0415

Table A.34: KSP tests for correlations in $DK_{\not{p}}$. In each column, (x) y indicates that the KSP compare the histograms of variable y in bins of variable x.

	$(\Delta E)N1$	$(\Delta E)N2$	$(N1)N2$
Bins 1,2	0.9696	0.9696	0.8159
Bins 1,3	0.9584	0.9584	0.9016
Bins 2,3	0.9918	0.7071	0.9104

Table A.35: KSP for correlations in $D\pi_D$. In each column, (x) y indicates that the KSP compare the histograms of variable y in bins of variable x.

	$(\Delta E)N1$	$(\Delta E)N2$	$(N1)N2$
Bins 1,2	0.1705	0.7964	0.2755
Bins 1,3	0.7741	0.9900	0.4611
Bins 2,3	0.7381	0.5479	0.9794

Table A.36: KSP tests for correlations in $D\pi_{\not{p}}$. In each column, (x) y indicates that the KSP compare the histograms of variable y in bins of variable x.

	$(\Delta E\ )m_D$	$(\Delta E)N1$	$(\Delta E)N2$	$(m_D)N1$	$(m_D)N2$	$(N1)N2$
Bins 1,2	0.1147	0.3816	0.3188	0.7709	0.7279	0.4844
Bins 1,3	0.00003	0.1460	0.6450	0.5551	0.4134	0.9382
Bins 2,3	0.0101	0.5792	0.0226	0.8924	0.9639	0.8351

Table A.37: KSP for correlations in $D\pi X$. In each column, (x) y indicates that the KP compare the histograms of variable y in bins of variable x.

	$(\Delta E\ )N1$	$(\Delta E\ )N2$	$(N1)N2$
Bins 1,2	0.8741	0.0819	0.1414
Bins 1,3	0.9925	0.9924	0.1686
Bins 2,3	0.7209	0.2205	0.5776

Table A.38: KSP tests for correlations in DKX. In each column, (x) y indicates that the KSP compare the histograms of variable y in bins of variable x.

	$(\Delta E\ )N1$	$(\Delta E\ )N2$	$(N1)N2$
Bins 1,2	0.1690	0.4987	0.7315
Bins 1,3	0.4989	0.7567	0.4981
Bins 2,3	0.0139	0.9695	0.6819

Table A.39: KSP tests for correlations in $BBC_{\not D}$. In each column, (x) y indicates that the KSP compare the histograms of variable y in bins of variable x.

	$(\Delta E)N1$	$(\Delta E)N2$	$(N1)N2$
Bins 1,2	0.8407	0.1938	0.5095
Bins 1,3	0.3081	0.8352	0.7546
Bins 2,3	0.3457	0.7634	0.9956

Table A.40: KSP tests for correlations in BBC_D. In each column, (x) y indicates that the KSP compare the histograms of variable y in bins of variable x.

	$(\Delta E)N1$	$(\Delta E)N2$	$(N1)N2$
Bins 1,2	0.9920	0.6749	0.9801
Bins 1,3	0.9552	0.3768	0.8709
Bins 2,3	0.9451	0.8284	0.5176

Table A.41: KSP tests for correlations in qq_D. In each column, (x) y indicates that the KSP compare the histograms of variable y in bins of variable x.

	$(\Delta E)N1$	$(\Delta E)N2$	$(N1)N2$
Bins 1,2	0.8004	0.3952	0.9965
Bins 1,3	0.2151	0.8108	0.6741
Bins 2,3	0.5970	0.9902	0.9589

Table A.42: KSP tests for correlations in $qq_{\not{p}}$. In each column, (x) y indicates that the KSP compare the histograms of variable y in bins of variable x.

Bibliography

[1] *BABAR* Collaboration, B. Aubert *et al.*, Phys. Rev. Lett. **93**, 041801 (2004)

[2] *Belle* Collaboration, S.-K. Choi *et al.*, Phys. Rev. Lett. **91**, 262001 (2003)

[3] *CDFII* Collaboration,D. Acosta *et al.*, Phys. Rev. Lett. **93** (2004)

[4] *D*0 Collaboration, V. M. Abazov *et al.*, Phys. Rev. Lett. **93** (2004)

[5] *BABAR* Collaboration, B. Aubert *et al.*, $hep-ex/0406022$, (2004)

[6] F. E. Close and S. Godfrey, Phys. Lett. B **574**, 210 (2003);

F. E. Close and P. R. Page, Phys. Lett. B **579**, 119 (2004);

[7] T. Barnes and S. Godfrey, Phys. Rev. D **69**, 054008 (2004);

E. J. Eichten, K. Lane and C. Quigg, Phys. Rev. D **69**,0904019 (2004);

C. Quigg $hep-ph/0403187$ (2004);

S. L. Olsen $hep-ex/0407033$ (2004);

[8] N. A. Törnqvist, $hep-ph/0308277$ (2004);

N. A. Törnqvist, $hep-ph/040223$ (2004);

E. S. Swanson, Phys. Lett. B **588** 189 (2003);

E. S. Swanson, $hep-ph/$0406080 (2004)

[9] L. Maiani, F. Piccinini, A. D. Polos and V. Riquer, $hep-ph/$0412098 (2004);

L. Maiani, F. Piccinini, A. D. Polosa and V. Riquer Phys. Rev. Lett. **93** 212002 (2004)

[10] *Belle* Collaboration, P. Pakhlov, $hep-ex/$0412041 (2004)

[11] *Belle* Collaboration, S.-K. Choi *et. al*, $hep-ex/$0408126 (2004)

[12] J. H. Christenson, J. W. Cronin, V. L. Fitch and R. Turlay, Phys. Rev. Lett. **13**, 138 (1964)

[13] A. B. Carter and A. I. Sanda, Phys. Rev. D **23**,1567 (1981);

I. I. Bigi and A. I. Sanda, Nucl. Phys. B **193**,85 (1981);

BABAR Collaboration, B. Aubet *et al.*, Phys. Rev. Lett. **87**, 091801 (2001);

Belle Collaboration, A. Abashian *et al.*, Phys. Rev. Lett. **87**, 091802 (2001)

[14] N. Cabibbo, Phys. Rev. Lett. **10**, 531 (1963);

M. Lobayashi and T. Maskawa, Prog. Th. Phys. **49**, 652 (1973)

[15] PEP-II - An asymmetric B Factory, Conceptual Design Report, SLAC-418, LBL-5379, 1993;

BABAR Collaboration, Letter of ntent for the study of CP violation and heavy flavor physics at PEP-II, SLAC-443, 1994

[16] *BABAR* Collaboration, B. Aubet *et al.*, Nucl. Instr. and Meth. A **479** 1 (2002)

[17] S. Brandt, C. Peyrou, R. Sosnowski and A. Wroblewski, Phys. Lett. **12**, 57 (1964);

E. Fahri, Phys. Rev. Lett. **39**, 1587 (1977)

[18] R. Barlow, Nucl. Instr. and Meth. A **297**, 496 (2000)

[19] N. Isgur and J. Parton, Phys. Rev. D **31**, 2910 (1985);

T. Barnes, F. E. Close and E. S. Swanson, Phys. Rev. D **52**, 5242 (1995);

MILC Collaboration, C. W. Bernard *et al.*, Phys. Rev. D **56**, 7039 (1997);

S. Perantonis and C. Michael, Nucl. Phys. B **347**, 854 (1990);

L. A. Grffiths, C. Michael and P. E. Rakow, Phys. Lett. B **129**, 351 (1983);

X. Liao and T. Manke, $hep-lat/0210030$, (2002)

[20] E. S. Swanson, $hep-ph/0406080$, (2004)

[21] T. Barnes and S. Godfrey, Phys. Rev. D **69**, 054008 (2004)

[22] N. A. Törnqvist, Z. Phys. C **61**, 526 (1994)

[23] L. Wolfenstein, Phys. Rev. Lett. **51**, 325 (1983)

[24] F. Halzen and A. D. Martin, Quarks and Leptons: An Introductory Course in Modern Particle Physics, John Wiley and Sons, Inc., 1984, p.287

[25] P. F. Harrison and H. R. Quinn(Editors), The *BABAR* Physics Book: Physics at an Asymmetric B Factory, SLAC-R-504 (1998)

[26] *BABAR* Collaboration, B. Aubert *et al.*, Phys. Rev. Lett. **93**, 131801 (2004)

[27] M. Gronau and D. Wyler, Phys. Lett. B **265**, 172 (1991);
M. Gronau and D. London, Phys. Rev. Lett. B **253**, 483 (1991)

[28] M. Gronau, Phys. Rev. D **56** 037301 (1998)

[29] D. Atwood, I. Dunietz and A. Soni, Phys. Rev. Lett. **78**, 3257 (1997);
D. Atwood and A. Soni, Phys. Rev. D **68**, 033003 (2003);
D. Atwood and A. Soni, Phys. Rev. D **71**, 013007 (2005)

[30] R. Aleksan, T. C. Petersen and A. Soffer, Phys. Rev. D **67**, 096002 (2003)

[31] Z. Xing, Phys. Rev. D **58**, 093005 (1998);
J. Jang and P. Ko, Phys. Rev. D **58**, 111302 (1998);
M. Gronau, Phys. Lett. B **557**, 198 (2003)

[32] Y. Grossman, Z. Ligeti and A. Soffer, Phys. Rev. D **67**, 071301(R) (2003)

[33] I. Dunietz, Phys. Lett. B **270**, 75 (1991)

[34] M. Gronau, Y. Grossman, N. Shuhmaher, A. Soffer and J. Zupan, Phys. Rev. D **69**, 113003 (2004)

[35] A. Giri, Y. Grossman, A. Soffer and J. Zupan, Phys. Rev. D **68**, 0504018 (2003)

[36] A. Soffer, Phys. Rev. D **60**, 054032 (1999)

[37] J. P. Silva and A. Soffer, Phys. Rev. D **61**, 112001 (1999)

[38] *BABAR* Collaboration, B. Aubert *et al.* Phys. Rev. Lett. **93**, 131804 (2004)

[39] *BABAR* Collaboration, B. Aubert *et al.* $hep-ex/0408088$, (2004);

BABAR Analysis Document #1102, Measurement of γ in $B^{\pm} \to D^{(*)}K^{\pm}$ decay with a Dalitz analysis of $D \to K^0_S\pi^+\pi^-$.

[40] *Belle* Collaboration, K. Abe *et al.*, Phys. Rev. D **70**, (2004)

[41] G. C. Fox and S. Wolfram, Nucl. Phys. B **149**, 413 (1979)

[42] R. A. Fisher, Annals of Eugenics **7**, 179 (1936)

[43] *BABAR* Analysis Documents #102, The *BABAR* vertexing,

BABAR Analysis Documents #1061, KinFitter - A Kinematic fit with constraints.

[44] *BABAR* Analysis Documents #502, Analysis of B flavor tagging performance and study of improvements from a topological tagging algorithm; and the references in it.

[45] *BABAR* Analysis Documents #90, Cut-Based Electron Identification.

[46] A. Drescher, *et al.* Nucl. Instr. and Meth. A **237**, 464 (1985)

[47] R. Sinkus and T. Voss, Nucl. Instr. and Meth. A **391**, 360 (1997)

[48] *BABAR* Analysis Documents #60, Muon Identification in *BABAR* Experiment.

[49] *BABAR* Analysis Documents #116, Kaon Selection at the *BABAR* Experiment.

[50] A. G. Frodesen, O. Skjeggestad and H. Tofte, Probability and Statistics in Particle Physics, Universiteforlaget, 1979, p195

[51] *ARGUS* Collaboration, H, Albrecht *et al.*, Z. Phys. C **48**, 543 (1990).

[52] *BABAR* Analysis Document #113, Measurement of Branching Ratios of Charged and Neutral B mesons into Exclusive Charmonium Final States.

[53] *BABAR* Analysis Document #126, Lepton identification efficiencies and systematic errors.

[54] http://www.slac.stanford.edu/BFROOT/www/Physics/TrackEfficTaskForce/Recipe/KsTracks-Run2.html

[55] http://www.slac.stanford.edu/BFROOT/www/Physics/Tools/BetaTools/MicroNeutralKilling-RUN2.html

[56] *CLEO* Collaboration, V. V. Frolov *et al.*, $hep - ex$/0306048, 2003

[57] Stuttgart Neural Network Simulator,
http://www-ra.informatik.uni-tuebingen.de/SNNS/

[58] *BABAR* Analysis Documents #331, A search for the rare decays $B \to J/\psi \eta K$.

[59] *BABAR* Analysis Documents #18, A user guide to the RooFitTools package for unbinned maximum likelihood fitting.

[60] F. James, Minuit Function minimization and error analysis, CERN program library long writeup D506 (1994)

[61] Review of particle physics, Phys. Lett. B **592**/1-4, (2004).

[62] *BABAR* Analysis Documents #1018, Measurement of Branching Fractions and CP Asymmetries of $B^- \to D^0_{CP} K^-$ Decays with the *BABAR* Detector

[63] *BABAR* Analysis Documents #825, Study of $B^\pm \to DK^\pm$ with D undergoing singly Cabibbo suppressed decay into non-CP eigenstates.

[64] http://www.slac.stanford.edu/BFROOT/www/Physics/
TrackEfficTaskForce/TrackingTaskForce-2004.html

[65] http://www.slac.stanford.edu/BFROOT/www/Physics/Analysis/
AWG/Neutrals/validation/recipie14.html

[66] http://www.slac.stanford.edu/BFROOT/www/Physics/Tools/
Pid/PidOnMc/pidonmc.html

[67] *BABAR* Collaboration, I. Adam *et al.*, Nucl. Instr. and Meth. A **538** 281 (2005)

[68] *CLEO* Collaboration, A. Anastassov *et al.*, Phys. Rev. Lett. **84**, 1393 (2000);

BABAR Collaboration, B. Aubert *et al.*, Phys. Rev. Lett. **91**, 07801 (2003)